Development and Evaluation of Nickel and Cobalt-Based Mixed Metal Oxide Catalysts for Anion Exchange Membrane Water Electrolysis

by

Khaja Wahab Ahmed

A thesis

presented to the University of Waterloo

in fulfillment of the

thesis requirement for the degree of

Doctor of Philosophy

in

Chemical Engineering

Waterloo, Ontario, Canada, 2024

© Khaja Wahab Ahmed 2024

Examining Committee Membership

External Examiner	Professor Aimy Bazylak Mechanical and Industrial Engineering University of Toronto
Supervisor	Professor Michael Fowler Chemical Engineering University of Waterloo
Co-Supervisor	Professor Aiping Yu Chemical Engineering University of Waterloo
Internal Member	Professor Eric Croiset Chemical Engineering University of Waterloo
Internal Member	Professor Ali Kamel Chemical Engineering University of Waterloo
Internal – external Member	Professor XiaoYu Wu Mechanical and Mechatronics Engineering University of Waterloo

Author's Declaration

This thesis consists of material all of which I authored or co-authored: see Statement of Contributions included in the thesis. This is a true copy of the thesis, including any required final revisions, as accepted by my examiners.

I understand that my thesis may be made electronically available to the public.

Statement of Contributions

The body of this thesis is based on a combination of published and unpublished works.

Chapter 4 of this thesis is adapted from the published work that was co-authored by myself, my supervisor Dr. Michael Fowler, Dr. Zhongwei Chen, Dr. Meyong Je Jang (Postdoctoral fellow), and Saeed Habibpour (PhD student). I designed, developed, and conducted the experiments, analyzed the data, and wrote the complete manuscript. Dr. M. Fowler and Dr. Chen assisted with the methodology and experimental design of the experiments. Dr. Meyong Je Jang assisted in the experimental design and reviewed the manuscript, Saeed Habibpour performed the Scanning electron microscopy (SEM) analysis of the catalysts.

Ahmed KW, Jang MJ, Habibpour S, Chen Z, Fowler M. $NiFeO_x$ and $NiFeCoO_x$ Catalysts for Anion Exchange Membrane Water Electrolysis. Electrochem. 2022 Dec 14;3(4):843-61.

Chapter 5 of this work is based on published work that was co-authored by myself, my supervisor Dr. Michael Fowler, Dr. Zhongwei Chen, and Saeed Habibpour (PhD student). I designed, developed, and conducted the experiments, analyzed the data, and wrote the complete manuscript. Dr. M. Fowler and Dr. Chen assisted with the methodology and experimental design of the experiments. Saeed Habibpour performed the Scanning electron microscopy (SEM) analysis of the catalysts.

Ahmed KW, Habibpour S, Chen Z, Fowler M. Investigation of $NiCoO_x$ catalysts for anion exchange membrane water electrolysis: Performance, durability, and efficiency analysis. Journal of Energy Storage. 2024 Feb 15;79:110149.

Chapter 6 of this work is based on published work that was co-authored by myself and my supervisor Dr. Michael Fowler. I designed, developed, and conducted the experiments, analyzed the data, and wrote the complete manuscript. Dr. M. Fowler assisted with the methodology and experimental design of the experiments.

Ahmed KW, Fowler M. Performance Evaluation and Durability Analysis of $NiFeCoO_x$ Catalysts for Alkaline Water Electrolysis in Anion Exchange Membrane Electrolyzers. Catalysts. 2024 May 14;14(5):322.

Chapter 7 The work was co-authored by myself, my supervisor Dr. Michael Fowler, Aidan Dobson (Co-op student), and Saeed Habibpour (PhD student). I designed, developed, and conducted the experiments, analyzed the data, and wrote the manuscript. Dr. M. Fowler assisted with the methodology and experimental design of the experiments. Aidan Dobson performed the literature review and contributed to writing the manuscript. Saeed Habibpour performed the Scanning electron microscopy (SEM) analysis of the catalysts.

Abstract

Hydrogen production using an Anion exchange membrane (AEM) electrolyzer allows the use of non-platinum group metal (PGM) catalysts for oxygen evolution reaction (OER). Nickel and Cobalt-based oxides are active in an alkaline environment for OER and are relatively inexpensive compared to IrO_2 catalysts used in Polymer electrolyte membrane (PEM) electrolysis. This study explores the catalytic performance and stability of nickel and cobalt-based oxides, particularly $NiFeO_x$, $NiFe_2O_4$, and $NiFeCoO_x$, in OER and AEM water electrolysis.

In the first study, mixed metal oxide catalysts $NiFeO_x$ and $NiFeCoO_x$ catalysts were synthesized by coprecipitation method using NaOH. The catalysts were characterized through X-ray diffraction (XRD) and scanning electron microscopy (SEM). The $NiFeCoO_x$ catalysts demonstrated superior performance in AEM water electrolysis compared to $NiFeO_x$ and NiO, achieving the highest current density of 802 mA cm^{-2} at 2 V and 70°C using 1M KOH as the electrolyte. Electrochemical Impedance Spectroscopy (EIS) and equivalent circuit fitting were used to assess ohmic and activation resistances. Results indicated a reduction in both ohmic and activation resistances with increasing electrolyte concentration. Additionally, the performance of commercially available AEMs, Fumasep FAA-3-50, and Sustainion X-37-50 grade T, was evaluated under similar conditions. EIS results showed that the X-37-50 membrane had lower ohmic resistance compared to the FAA-3-50 membrane.

The investigation of catalytic activity and performance of nickel cobalt oxide ($NiCoO_x$) catalysts in AEM water electrolysis for hydrogen production was performed in the second study. The catalysts were synthesized with different ratios of Ni to Co and applied to a nickel foam gas diffusion layer (GDL) at the anode. Scanning electron microscopy (SEM) revealed a distinct flaky

structure of the $NiCoO_x$ catalyst, while X-ray diffraction (XRD) confirmed the presence of a $NiCo_2O_4$ spinel crystal structure. Linear sweep voltammetry (LSV) measurements for the OER in a three-electrode system indicated that $NiCoO_x$ (1:3) had the highest catalytic activity, with a current density of 238 mA cm^{-2} at 1.8 V. Tafel analysis showed that $NiCoO_x$ (1:3) had the lowest Tafel slope, indicating faster reaction kinetics and a lower overpotential for higher current densities. Chronoamperometry tests demonstrated the stability of the catalysts at different current densities, with long-term stability testing of $NiCoO_x$ (1:3) over 500 hours showing minimal voltage increase during OER, confirming its stability in prolonged operation. $NiCoO_x$ (1:3) displayed the highest activity among the tested catalysts at different temperatures, achieving current densities of 1700 mA cm^{-2} at 2.2 V and 70°C in AEM electrolysis. Nyquist plots and equivalent circuit analysis revealed that $NiCoO_x$ (1:3) had lower activation resistance compared to other catalyst compositions for AEM electrolysis. Temperature-dependent measurements showed decreased resistances (ohmic, activation, and membrane) with increasing temperature, indicating improved reaction kinetics and ion conductivity. Long-term durability tests confirmed the stable operation of the catalyst, while short-term tests verified its effectiveness at higher current densities in single-cell AEM electrolyzer operation.

In the third study, $NiCoO_x$ catalysts were modified using Fe in different proportions ranging from 2.5 to 12.5wt.%. and keeping the Ni to Co ratio to 2:1. Evaluation of the catalytic activity of $NiFeCoO_x$ catalysts was conducted by linear sweep voltammetry (LSV) and chronoamperometry (CA) experiments for the OER. The catalyst containing 5% Fe exhibited the highest catalytic activity, achieving an overpotential of 228 mV at a current density of 10 mA cm^{-2}, with activity declining with further increases in Fe content. Long-term testing for OER at 50 mA cm^{-2} demonstrated stable electrolysis operation for 100 hours. Further analysis in an AEM water

electrolyzer test revealed that the $NiFeCoO_x$ catalyst with 5% Fe at the anode demonstrated the highest current densities of 1516 mA cm^{-2} and 1620 mA cm^{-2} at 55°C and 70°C at 2.1 V, with a maximum current density of 1880 mA cm^{-2} achieved at 2.2 V and 70°C. Nyquist plot analysis of electrolysis at 55°C indicated that the $NiFeCoO_x$ catalyst with 5% Fe exhibited lower activation resistance compared to other Fe loadings, suggesting enhanced performance. This study compared the performance of $NiFeCo(OH)_x$ and $NiFeCoO_x$ catalysts for AEM water electrolysis, revealing that $NiFeCoO_x$ demonstrated significantly higher current densities at various temperatures compared to $NiFeCo(OH)_x$. The durability test conducted for 8 hours demonstrated stable AEM water electrolysis with minimal degradation, achieving an overall cell efficiency of 70.5% during operation at a higher current density of 0.8A cm^{-2}.

The final study investigated the catalytic activity and performance of $NiFeO_x$ catalysts in OER and AEM water electrolyzer. These catalysts were synthesized with varying iron content weight percentages and at the stoichiometric ratio for nickel ferrite ($NiFe_2O_4$). The stability of $NiFe_2O_4$ catalyst over a 600-hour period at 50 mA cm^{-2} was demonstrated for OER, with a degradation rate of 15 μV/h. In AEM electrolysis using the X-37 T membrane, $NiFe_2O_4$ catalyst exhibited high activity, achieving a current density of 1100 mA cm^{-2} at 45°C, increasing to 1503 mA cm^{-2} at 55°C. The performance of various membranes was assessed, with Fumatech FAA-3-50 and FAS-50 membranes showing the highest performance, indicating a strong correlation between membrane performance and conductivity. Analysis of Nyquist plots and equivalent circuit analysis revealed that ohmic resistance decreased with increasing temperature, indicating a positive effect on AEM electrolysis. FAA-3-50 and FAS-50 membranes offered lower activation and ohmic resistances, suggesting higher conductivity and faster membrane charge transfer. $NiFe_2O_4$ in an

AEM water electrolyzer demonstrated strong stability, with a voltage degradation rate of 0.833 mV/h over a 12-hour durability test.

Acknowledgments

I would like to thank my thesis supervisor, Dr. Michael Fowler, for his supervision and guidance during my PhD studies. I would also like to thank Dr. Aiping Yu for her support during my laboratory experiments. At the start of my PhD studies Dr. Zhongwei Chen also guided and reviewed my work, for which I am thankful to him. I would also like to thank Dr. Eric Croiset, Dr. Ali Kamel, and Dr. XiaoYu Wu for reviewing my proposed work and giving valuable feedback.

I would also like to thank students and postdocs in Professor Michale Fowler and Professor Aiping Yu's lab for giving me valuable feedback during the presentations. I want to thank Dr. Meyong Je Jang and Dr. Moon Park for their help in the initial part of my studies. I am also thankful to Dr. Saeed Habibpour for helping me with the morphological characterization of the catalysts.

Finally, I would like to thank my family and friends for their support during my studies. Special thanks to my Wife, Maira for supporting me and encouraging me during my PhD studies.

Table of Contents

Examining Committee Membership ii
Author's Declaration iii
Statement of Contributions iv
Abstract vi
Acknowledgments x
List of Figures xiv
List of Tables xix
List of Abbreviations xx
1 Introduction 1
1.1 Motivation 1
1.2 Thesis Objectives 4
1.3 Thesis Outline 5
2 Literature Review 7
2.1 Water Electrolysis Technologies 7
2.1.1 Alkaline Electrolyzer 7
2.1.2 PEM Electrolyzer 7
2.1.3 AEM Electrolyzer 9
2.2 Mechanism of water splitting reaction in alkaline electrolyzer 11
2.2.1 HER Mechanism 11
2.2.2 OER Mechanism 12
2.3 Thermodynamic Consideration 13
2.3.1 Theoretical Cell Voltages 13
2.3.2 Electrical Resistances 15
2.3.3 Mass Transport Resistances 15
2.3.4 Activation Loss 16
2.4 Cell Efficiencies 16
2.4.1 Efficiency 16
2.5 Anion Exchange Membrane (AEM) 17
2.5.1 AEM Performance and Stability 18
2.6 Gas Diffusion Layer (GDL) 19

2.7 AEM Water Electrolysis Catalyst 22
2.7.1 HER Catalysts. 22
2.7.2 OER Catalysts. 25
3 Experimental Methods and Techniques 34
3.1 Physiochemical Characterization 34
3.1.1 X-ray diffraction 34
3.1.2 Scanning Electron Microscopy 34
3.1.3 Energy dispersive X-ray Spectroscopy 35
3.2 Electrode Fabrication and Performance Evaluation 36
3.2.1 Preparation of Gas diffusion electrode and Membrane electrode assembly 36
3.2.2 Catalyst Testing in three-electrode System 37
3.2.3 AEM Electrolyzer Performance Test 38
4 $NiFeO_x$ and $NiFeCoO_x$ Catalysts for Anion Exchange Membrane Water Electrolysis 41
4.1 Introduction 41
4.2 Experimental 42
4.2.1 Synthesis of Catalyst 42
4.2.2 Preparation of the Membrane Electrode Assembly 43
4.2.3 AEM Electrolyzer Single-Cell Tests 44
4.3 Results 45
4.3.1 Water Electrolysis over NiO, $NiFeO_x$ and $NiFeCoO_x$. 48
4.3.2 Effect of Electrolyte Concentration 55
4.3.3 Comparison of Anion Exchange Membranes 59
4.4 Conclusion 62
5 Investigation of $NiCoO_x$ Catalysts for Anion Exchange Membrane Water Electrolysis: Performance, Durability, and Efficiency Analysis 64
5.1 Introduction 64
5.2 Experimental 67
5.2.1 Synthesis of $NiCoO_x$ catalysts 67
5.3 Results 67
5.3.1 Catalyst Evaluation in three-electrode System 70
5.3.2 AEM electrolyzer single cell tests 75
5.3.3 EIS with equivalent circuit fittings 80
5.3.4 Durability Studies 86

5.4 Conclusion 88
6 Performance Evaluation and Durability Analysis of $NiFeCoO_x$ Catalysts for Alkaline Water Electrolysis in AEM Electrolyzers 91
6.1 Introduction 91
6.2 Experimental 92
6.2.1 Synthesis of $NiFeCoO_x$ catalysts 92
6.3 Results 92
6.3.1 Oxygen Evolution Reaction 96
6.3.2 Single-cell performance with $NiFeCoO_x$ catalyst 100
6.3.3 Electrochemical Impedance Spectroscopy 105
6.3.4 Comparison of $NiFeCoO_x$ catalyst with $NiFeCo(OH)_x$ 109
6.3.5 AEM Electrolyzer Durability Test 114
6.4 Conclusion 114
7 Enhanced Performance and Stability of $NiFe_2O_4$ Catalyst in Anion Exchange Membrane Water Electrolysis: Influence of Iron Content and Membrane Selection 117
7.1 Introduction 117
7.2 Experimental 118
7.2.1 Synthesis of $NiFeO_x$ catalysts 118
7.3 Results 119
7.3.1 Oxygen Evolution Reaction 121
7.3.2 AEM electrolyzer tests with $NiFeO_x$ and $NiFe_2O_4$ catalysts 125
7.3.3 Effect of Anion exchange membranes on electrolyzer performance 127
7.3.4 EIS effect of voltage and temperature 131
7.3.5 EIS with different Anion Exchange Membranes 134
7.3.6 Durability Test 135
7.4 Conclusion 138
8 Conclusion and Future Work 140
Letters of Copyright permission 143
References 157
Appendix 188

List of Figures

Figure 2.1. (a) AEM water electrolyzer configuration with AEM transporting the OH^- to anode, (b) PEM electrolyzer with PEM where H^+ is transported to the cathode side. 10
Figure 2.2. Water electrolysis Cell potential for hydrogen production as a function of temperature [53]. 15
Figure 2.3. Comparison of different resistances during the electrolysis operation [55]. 16
Figure 2.4. Crystal structure of spinel (AB_2O_4) with octahedral and tetrahedral sites [125]. 26
Figure 2.5. Theoretical overpotential of oxygen evolution reaction vs. the difference between the standard free energy of two subsequent intermediates ($\Delta G^0_{O*} - \Delta G^0_{HO*}$) for various binary oxides [155]. 28
Figure 2.6. Structure of ABO_3 perovskite oxide [49]. 30
Figure 2.7. Theoretical overpotential of oxygen evolution reaction vs. the difference between the standard free energy of two subsequent intermediates ($\Delta G^0_{O*} - \Delta G^0_{HO*}$) for Perovskite oxide material [155]. 31
Figure 3.1. Electrolyzer used for AEM water electrolysis. (a) Anode side with water inlet and oxygen and water outlet. (b) Cathode side with hydrogen outlet. 38
Figure 3.2. The schematic of membrane electrode assembly used in this study. 39
Figure 4.1. (a) Nickel foam (b) carbon paper coated with Pt/C catalyst, (c) Nickel foam anode coated with $NiFeCoO_x$ catalyst and (d) AEM with carbon paper cathode attached on one side. The dimensions of the electrodes were 1.8 cm × 1.8 cm. 44
Figure 4.2. MEA after the electrolysis operation (a) MEA with cathode side (carbon paper) on top and (b) MEA with anode side (nickel foam) on top. The dimensions of the electrodes were 1.8 cm × 1.8 cm. 44
Figure 4.3. AEM electrolyzer configuration with AEM transporting the OH^- to the anode. 45
Figure 4.4. SEM images of (a,b) Nickel Foam without catalyst (c) $NiFeCoO_x$ coated on nickel foam and (d) Cross-section image of nickel foam coated with $NiFeCoO_x$ catalyst. 46
Figure 4.5. XRD of $NiFeO_x$, $NiFeCoO_x$ catalyst calcined at 300°C, commercial NiO is for reference. 47

Figure 4.6. Linear Sweep Voltammetry at a temperature range of 45 to 70°C. Pt/C was used at the cathode and synthesized $NiFeCoO_x$ was used at the anode. FAA-3-50 membrane with a thickness of 50 µm was used in the electrolysis operation. 49
Figure 4.7. Chronoamperometry at a voltage range of 1.5 to 2.2 V, Pt/C was used at the cathode and $NiFeCoO_x$ was used at the anode. 50
Figure 4.8. Linear Sweep Voltammetry at the temperature of 70°C. Pt/C was used at the cathode and NiO, $NiFeO_x$, and $NiFeCoO_x$ were used at anode. FAA-3-50 membrane with a thickness of 50 µm was used in the electrolysis operation. 52
Figure 4.9. Nyquist plot at a constant voltage of 1.7 V at two different temperatures of 45°C and 70°C, Pt/C was used at the cathode and $NiFeCoO_x$ was used at the anode. 55
Figure 4.10. Linear Sweep Voltammetry at a temperature of 70°C with 0.01 M to 1 M KOH concentration. Pt/C was used at the cathode and $NiFeCoO_x$ was used at the anode. 57
Figure 4.11. (a) Nyquist plot at a constant voltage of 2 V at 70°C, the concentration of electrolyte was from 0.01 M to 1 M. (b) Nyquist plot using DI water. Pt/C was used at the cathode and $NiFeCoO_x$ was used at the anode with FAA-3-50 membrane. 58
Figure 4.12. Comparison of resistances at anode, cathode, and membrane, the resistances were evaluated by using equivalent circuit fitting. The applied voltage was 2 V at 70°C. 59
Figure 4.13. Comparison of electrolysis performance using X-37-50 and FAA-3-50 membranes at different temperatures using $NiFeCoO_x$ catalyst. 61
Figure 4.14. Nyquist plot at a constant voltage of 2 V at 70°C with FAA-3-50 and X-37-50 anion exchange membranes, the concentration of electrolyte was 1 M. Pt/C was used at the cathode and $NiFeCoO_x$ was used at the anode. 62
Figure 5.1. (a) SEM images of $NiCoO_x$ (1:3) catalyst (b) Cross-sectional image of nickel foam coated with $NiCoO_x$ (1:3) catalyst (c) EDS spectra of $NiCoO_x$ (1:3). 68
Figure 5.2. XRD of $NiCoO_x$ catalyst calcined at 300ºC with different molar ratios of Ni to Co. 70
Figure 5.3. OER activity in 1M KOH. (a) Polarization curves (85% iR-corrected) of $NiCoO_x$ catalyst series and Co_3O_4. (b) Chronopotentiometry from 10 to 100 mA cm^{-2}. (c) Tafel plots in 1M KOH (d) Durability tests of $NiCoO_x$ (1:3) anode at 50 mA cm^{-2} in 1M KOH. 72
Figure 5.4. Cyclic voltammetry in non-faradaic regions at different scan rates (a) $NiCoO_x$ (1:1), (b) $NiCoO_x$ (1:2), (c) $NiCoO_x$ (1:3), (d) $NiCoO_x$ (1:5), (e) $NiCoO_x$ (2:1) and (f) Co_3O_4. 74
Figure 5.5. Double layer capacitance (C_{dl}) for $NiCoO_x$ catalyst series. 75

Figure 5.6. Chronoamperometry at a voltage range of 1.5 to 2.2 V, Pt/C was used at the cathode (a) $NiCoO_x$ (1:3) (b) $NiCoO_x$ (1:1) and (c) $NiCoO_x$ (2:1) catalysts were used at anode. 76
Figure 5.7. Linear Sweep Voltammetry at a temperature range of 45 to 70°C. Pt/C was used at the cathode and synthesized $NiCoO_x$ catalysts with varying Ni to Co ratios were used at the anode. X-37-50 T membrane with a thickness of 50 µm was used in electrolysis operation..... 79
Figure 5.8. Arrhenius plot for AEM water electrolysis over $NiCoO_x$ (1:3) catalyst at 45 to 70^{o}C. 80
Figure 5.9. Nyquist plot for the electrolysis operation conducted at 1.7 V for the $NiCoO_x$ catalyst series with different molar ratios of Ni to Co at 45^{o}C. 82
Figure 5.10. Nyquist plot at a constant voltage of 1.7 to 2 V at 45°C, 55°C and 70°C, Pt/C was used at the cathode, $NiCoO_x$ (1:3) catalyst was used at the anode. 85
Figure 5.11. Durability test at 250 mA cm^{-2} for 30 h in 1M KOH using $NiCoO_x$ (1:3) catalyst at the anode, electrolyzer was operated at 55^{o}C. (b) Short term stability at current densities of 250 mA cm^{-2} to 1000 mA cm^{-2} at 55^{o}C. 87
Figure 6.1. SEM of (a & b) Nickel Foam without any catalyst deposition (c) Cross-sectional image of $NiFeCoO_x$ (5% Fe) catalyst layer deposited on nickel foam (d) Pt/C coated on carbon paper (e) EDS of $NiFeCoO_x$ (5% Fe) catalyst. 94
Figure 6.2. XRD of $NiFeCoO_x$ catalysts with Fe content of 2.5 to 12.5% wt.%..... 96
Figure 6.3. Oxygen evolution reaction for $NiFeCoO_x$ catalyst series in 1M KOH. (a) Polarization curves (85% iR-corrected) of $NiFeCoO_x$ catalysts. (b) Overpotential of OER at 10, 50 and 100 mA/cm^2. (c) Long-term OER tests of $NiFeCoO_x$ (5%Fe) catalyst at 50 mA/cm^2..... 98
Figure 6.4. Cyclic voltammetry for the determination of C_{dl} for $NiFeCoO_x$ catalysts with varying Fe content (a) 2.5% (b) 5% (c) 7.5% (d) 10% (e) 12.5% and (f) $NiCo(OH)_x$ (5%). 99
Figure 6.5. Plot of scan rate vs current density for evaluation of electrochemical double layer capacitance (C_{dl}) of $NiFeCoO_x$ catalysts. 100
Figure 6.6. $NiFeCoO_x$ (5% Fe) catalyst activity measurement in AEM electrolyzer using chronoamperometry at 45^{o}C with voltage from 1.5 to 2.3 V..... 101
Figure 6.7. Linear Sweep Voltammetry at different temperatures using X-37-50 T membrane for AEM electrolysis (a) 45°C, (b) 55°C and (c) 70°C. The cathode was Pt/C, while the anode had $NiFeCoO_x$ catalyst with a varying Fe content ranging from 2.5% to 12.5% wt.%. 102

Figure 6.8. The trend in the activity of AEM electrolysis performance with the increase in Fe content at 2.1 V and 55^{o}C. (b) Arrhenius plot of $NiFeCoO_x$ (5% Fe) catalyst as anode for AEM water electrolysis at a temperature range of 45 - 70^{o}C. 104
Figure 6.9. EIS analysis with Nyquist plot at 1.7 V for AEM electrolysis with $NiFeCoO_x$ catalysts at 55^{o}C. 106
Figure 6.10. Effect of temperature for AEM water electrolysis with EIS analysis using Nyquist plots at three distinct temperatures (45°C, 55°C, and 70°C). $NiFeCoO_x$ catalyst with (5wt.% Fe) was used at the anode. EIS was performed at 1.7 V and 2 V. 108
Figure 6.11. XRD of $NiFeCo(OH)_x$ catalyst with 5wt.% Fe. 110
Figure 6.12. Electrolysis performance using $NiFeCoO_x$ and $NiFeCo(OH)_x$ with 5wt.% Fe at a temperature range of (a) 45^{o}C, (b) 55^{o}C, (c) 70^{o}C. 111
Figure 6.13. Comparison of Nyquist plot for $NiFeCoO_x$ and $NiFeCo(OH)_x$ catalysts with 5wt.% Fe at 55^{o}C for AEM water electrolysis. (b) AEM electrolyzer durability test at 800 mA/cm^2 for 8 h in 1M KOH, electrolyzer was operated at 55^{o}C. 113
Figure 7.1. (a) SEM of Nickel foam Anode GDL. (b) Cross-section of $NiFe_2O_4$ catalyst coated on nickel foam anode. (c) EDS of $NiFe_2O_4$ catalyst which shows the ratio of Ni to Fe of about 1:2. 120
Figure 7.2. XRD of $NiFeO_x$ and $NiFe_2O_4$ catalysts. 121
Figure 7.3. OER at room temperature in 1 M KOH with $NiFe_2O_4$ and $NiFeO_x$ catalysts (a) LSV with (85% iR-corrected). (b) Chronoamperometry at a current density range of 10 to 100 mA/cm^2 (c) Tafel plots (d) Durability test for 600 h at 50 mA/cm^2 with $NiFe_2O_4$ at the anode. 123
Figure 7.4. Cyclic voltammetry at different scan rates, the analysis was performed in non-faradic region. (a) $NiFeO_x$ (5% Fe), (b) $NiFeO_x$ (7.5% Fe), (c) $NiFeO_x$ (12.5% Fe) and (d) $NiFe_2O_4$. . 124
Figure 7.5. Double layer capacitance (C_{dl}), plot of scan rate vs current density for $NiFeO_x$ catalysts and $NiFe_2O_4$. 125
Figure 7.6. Linear Sweep Voltammetry at (a) 45°C, (b) 55°C. $NiFeO_x$ and $NiFe_2O_4$ catalysts were used at the anode. X-37-50 T membrane was used for AEM electrolysis. (c) Chronoamperometry at a voltage range of 1.5 to 2.3 V at 45^{o}C and 55^{o}C, with $NiFe_2O_4$ catalysts. 127

Figure 7.7. AEM electrolysis comparison using FAA-3-50, FAS-50, FAA-3-PK-75 and FAB PK-130 membranes at (a) 45^{o}C and (b) 55^{o}C, using $NiFe_2O_4$ catalyst at anode with 1M KOH as an electrolyte. 131
Figure 7.8. Nyquist plots for $NiFe_2O_4$ catalyst using FAA-3-50 membrane for water electrolysis at 45^{o}C and 55^{o}C. 133
Figure 7.9. Nyquist plots for AEM electrolysis operation with different membranes at 1.7 V with $NiFe_2O_4$ catalyst at 55^{o}C. 135
Figure 7.10. The durability test was at 400 mA/cm^2 for 12 h in 1M KOH using $NiFe_2O_4$ catalyst at the anode, electrolyzer was operated at 55^{o}C using X-37-50 grade T membrane. 138

List of Tables

Table 2.1. Comparison of Alkaline, PEM, and AEM water electrolyzers [8,9]. 11
Table 2.2. Oxygen evolution mechanism in Alkaline medium [49,50]. 13
Table 2.3. Oxygen evolution mechanism in Acidic medium [49,50]. 13
Table 2.4. Electrolyzer performance with commercially available membranes [59]. 32
Table 4.1. Resistances evaluated from equivalent circuit fitting. 54
Table 4.2. Commercially available membranes and their properties [59,186–190]. 60
Table 5.1. Activation energy for AEM water electrolysis with $NiCoO_x$ (1:3) catalyst at the anode and Pt/C catalyst at the cathode. 80
Table 5.2. Equivalent circuit fitting results on electrolysis operation at 45^oC and 1.7 V over $NiCoO_x$ catalyst series and Co_3O_4. 83
Table 5.3. Ohmic and Activation resistances were evaluated from the Nyquist plot. EIS was performed at a constant voltage of 1.7 to 2 V with a temperature range of 45 to 70^oC over $NiCoO_x$ (1:3) catalyst. 86
Table 6.1. Apparent Activation energy with $NiFeCoO_x$ (5% Fe) catalyst at anode for AEM water electrolysis. 105
Table 6.2. Resistances evaluated from equivalent circuit fitting, EIS was performed at 55^oC and 1.7 V. 107
Table 6.3. Equivalent circuit results for EIS analysis. The AEM electrolysis was carried out at 1.7 V and 2 V from 45^oC to 70^oC with $NiFeCoO_x$ (5wt.% Fe) anode. 109
Table 7.1. Specifications of Fumasep membranes [285,286,288,289]. 129
Table 7.2. Results from fitting an equivalent circuit during electrolysis operations at temperatures of 45°C and 55°C using FAA-3-50 membrane, with $NiFe_2O_4$ catalyst. 133
Table 7.3. Resistances evaluated from equivalent circuit fittings for AEM water electrolysis using different membranes with $NiFe_2O_4$ catalyst at 1.7 V. 135

List of Abbreviations

AEM	Anion exchange membrane
AWE	Alkaline water electrolysis
PEM	Polymer electrolyte membrane
OER	Oxygen Evolution Reaction
HER	Hydrogen Evolution Reaction
PFSA	Perfluoro sulfonic acid
EIS	Electrochemical Impedance spectroscopy
GDL	Gas diffusion layer
GDE	Gas diffusion electrode
MEA	Membrane electrode assembly
BP	Bipolar plates
CCM	catalyst-coated membrane
LHV	lower heating value
HHV	higher heating value
IEC	Ion exchange capacity
LDHs	Layered double hydroxides
keV	Kilo electron volt
EDX	Energy dispersive X-ray
SCE	Standard Calomel Electrode
RHE	Reversible hydrogen electrode
CV	Cyclic voltammetry
ECSA	Electrochemical surface area
C_{dl}	Double-layer capacitance
Cs	Smooth plane capacitance
LSV	Linear sweep voltammetry
CA	Chronoamperometry

XRD	X-ray diffraction
SEM	Scanning electron microscopy
FWHM	Full width at half Maximum
R_{ohm}	Ohmic resistance
R_{act}	Activation resistance
$R_{membrane}$	Membrane resistance
CPE	Constant phase element
PTFE	Polytetrafluroethylene
PBI	Polybenzimidazole
rGO	Reduced graphene oxide
CNTs	Carbon nanotubes
QA	Quaternary ammonium
PK	Poly-ketone
MOF	Metal-organic framework

1 Introduction

1.1 Motivation

Hydrogen is considered the fuel of the future and with the advancement of fuel cell technology, there is a renewed interest in hydrogen production by electrolysis of water [1–3]. Hydrogen is energy-dense and clean fuel and provides 140MJ/Kg upon oxidation, the only byproduct is water [4]. Hydrogen is mainly produced by steam methane reforming which can produce high-pressure hydrogen along with CO and CO_2 [5]. Hydrogen is predominantly used in making NH_3 by the Haber Bosch process, which is then used for making urea (fertilizer) [6]. In addition, hydrogen is used extensively in petrochemical processes and petroleum refining. Steam methane reforming is not a renewable route to get hydrogen and thus water electrolysis is the most sought-after route to get clean and renewable hydrogen. Climate change is also linked to burning fossil fuels and greenhouse gases. Hydrogen from renewable sources will also decrease the effect of global warming [7]. The energy source for electrolysis must be from renewable sources, such as wind turbines and photo voltaic cells to get CO_2-free H_2 from the electrolysis. This hydrogen can also be utilized for transportation purposes such as fuel cell-powered vehicles.

Alkaline water electrolysis (AWE) is a conventional water electrolysis technology, large Megawatt scale electrolysis setups are available in the market. It runs at a temperature of 60-80^{o}C, with liquid KOH as an electrolyte with a very high concentration of 20-40wt.% [8,9]. Non-noble metals such as (Ni, Co, and Mo) can be utilized as catalysts at high pH environments of AWE, which also decreases the overall cost of the catalyst. In a conventional electrolyzer a porous diaphragm is used to separate the anode and cathode compartment and to conduct water and OH^- through it. The generated oxygen and hydrogen gases can cross over through the diaphragm thus decreasing the

purity of hydrogen. The large gap between the electrodes also increases the ohmic resistance which causes a decrease in the overall efficiency of the electrolysis. The KOH electrolyte exposed to the atmosphere can combine with CO_2 to form K_2CO_3 which decreases the concentration of OH^- and decreases the ionic conductivity. The precipitation of K_2CO_3 can clog the gas diffusion electrodes and hinder the transfer of ions through the diaphragm [10,11]. The current density of water electrolysis is an important parameter that shows the hydrogen production rate at the electrode with the specific surface area. For AWE the current densities are lower compared to Polymer electrolyte membrane (PEM) water electrolysis, the lower current densities in AWEs are due to the use of a highly porous and thick diaphragm which reduces the overall efficiency of the process. PEM electrolyzers have many advantages compared to other electrolysis methods, the biggest advantages are high purity hydrogen, small footprint and compact design, application of higher current density on the electrodes, and high-pressure operation up to 200 bar [12]. The high-pressure operation allows the hydrogen to be delivered and used at high pressure and minimizes the extra cost of pressurization. These are the reasons why PEM electrolyzers are the preferred choice to produce high-purity hydrogen [13–15]. The PEM Water electrolyzer utilizes a solid electrolyte membrane made up of perfluoro sulfonic acid (PFSA) with high proton conductivity and minimizes the shortcomings of AWEs. The thickness of the membrane is in microns which reduces the ohmic resistance and the gas crossover. Due to that PEM electrolyzer can be operated at higher current densities with higher hydrogen production rates and higher energy efficiency compared to AWEs. Due to the highly acidic environment in PEM water electrolyzers, expensive noble metals such as Pt, are used for Hydrogen evolution reaction (HER), and Ir, IrO_2, Ru, and RuO_2 are used for Oxygen evolution reaction (OER) as catalysts. The high cost of the catalyst limits the overall adaptability and commercialization of PEM water electrolyzers [16].

AEM water electrolyzers are a new generation of water electrolyzers with solid polymer electrolyte membranes replacing the diaphragm and are receiving much attention due to their several advantages, such as low ohmic resistance, good gas separation and use of non-noble catalysts. The thin anion quaternary ammonium ion exchange membrane is used to conduct OH^- ions, which is cheaper than the PEM [17–19].

The AEM water electrolyzers can be used at low concentrations of electrolytes such as 1wt.% KOH or distilled water [19]. Due to less corrosive conditions, AEM water electrolyzers can use less expensive Ni and Co-based catalysts that are used in conventional AWE. In addition, due to the low concentration of the electrolyte, a buildup of K_2CO_3 precipitates by the reaction of KOH and CO_2 in the atmosphere is minimized [20,21]. For AEM water electrolyzers, similar fabrication methods can be used which are developed for PEM water electrolyzers to improve the current densities and efficiency. The AEM water electrolysis with zero gap alkaline electrolyzer has been shown to achieve higher than 500 mA cm^{-2} at a voltage lower than 1.8 V with 1 M KOH [8].

Compared to PEM water electrolyzers limited research has been conducted in this field. The HER kinetics is two to three times lower at high pHs (alkaline conditions) in AEM water electrolyzers compared to PEM water electrolyzers [22,23]. The slow kinetics of OER at the anode is the major cause of the large overpotential in water electrolysis, due to the four-electron process for the generation of gaseous oxygen. In AEM water electrolyzers due to the use of non-noble metal, the OER is also sluggish compared to PEM water electrolyzers [8]. The main challenges in the research of AEM water electrolyzer devices are to decrease the overpotential of the catalyst, which can achieve high current densities and improved hydrogen production rate, and reduce the cost of electrolyzer components including catalyst cost.

1.2 Thesis Objectives

Development of non-precious catalyst:

This objective involves the development of oxygen evolution reaction (OER) catalyst consisting of Ni Fe and Co for AEM water electrolysis. One of the objectives is to use nonprecious elements to replace iridium for the OER. Nonprecious catalysts are crucial for reducing the overall cost of electrolysis processes, making hydrogen production more economically viable.

Improvement of catalyst activity for AEM water electrolysis:

AEM water electrolysis is a promising method for hydrogen production, but it requires catalysts with high activity to facilitate the electrochemical reactions efficiently. This requires enhancing the catalytic activity of the chosen materials specifically for AEM electrolysis conditions.

The objective involves varying the iron content in the $NiFeCoO_x$ and $NiFe_2O_4$ catalysts to study the effect on catalyst performance. Different compositions of Fe were explored to understand their effect on the catalytic activity and stability for AEM water electrolysis. This variation included different weight percentage of Fe in Ni:Fe:Co in the case of $NiFeCoO_x$ and Ni:Fe in the case of $NiFe_2O_4$. In the case of $NiCoO_x$ catalysts, the Ni to Co ratio was changed and their performance was studied. Overpotential and current density were used as metrics to compare the catalyst performance.

Catalyst stability:

Catalyst stability is essential for ensuring long-term performance and reliability in electrolysis systems. This objective focuses on assessing the stability of the developed catalyst under various operating conditions, such as high current densities, and a range of different operating voltages.

Understanding how the catalyst behaves over time is crucial for predicting its lifespan and maintenance requirements.

Durability studies of AEM electrolyzer operation:

In addition to catalyst stability, the overall durability of the AEM electrolyzer system is critical for its practical implementation. This objective involves conducting durability studies to evaluate the performance and analyze the degradation rate.

1.3 Thesis Outline

Chapter 1 introduces hydrogen production using AEM electrolysis and outlines the objectives of this study. **Chapter 2** provides a literature review on water electrolysis technology, Oxygen evolution reaction (OER), and Hydrogen evolution reaction (HER) catalysts and different components of AEM electrolyzer. **Chapter 3** provides the experimental part of the work and characterization techniques used in this study.

Chapter 4 is the first study in which NiO, $NiFeCoO_x$, and $NiFeO_x$ catalysts were evaluated in AEM electrolyzers. Parameters such as the effect of temperature, Anion exchange membrane, and electrolyte concentration on AEM electrolyzer performance were studied.

Chapter 5 deals with the study in which $NiCoO_x$ catalysts composition was varied to study the effect of Ni to Co ratio on OER and AEM electrolysis was studied. In addition, Electrochemical Impedance spectroscopy (EIS) was also used to analyze different resistances associated with AEM electrolysis in different operation conditions.

In Chapter 6 $NiFeCoO_x$ catalyst was studied for OER and AEM electrolysis, the composition of the catalyst was varied by changing the Fe content. The catalyst durability was studied in OER and

AEM electrolysis. EIS and other electrochemical analyses were conducted to assess the performance of the catalyst.

In **Chapter 7** $NiFeO_x$ catalysts with Fe content ranging from 5-12.5% and $NiFe_2O_4$ catalysts were studied. The OER and AEM electrolysis performance was assessed on all the catalysts, in addition, the performance of commercially available AEM was tested. Durability tests of the catalyst for OER and AEM electrolysis were performed to evaluate the long-term performance of these catalysts.

2 Literature Review

2.1 Water Electrolysis Technologies

2.1.1 Alkaline Electrolyzer

Hydrogen production from Alkaline electrolysis is a mature technology, commercial electrolyzers are mega-watt (MW) scale. The alkaline electrolyte consists of anode and cathode immersed in a concentrated aqueous alkaline electrolyte, with a concentration of 20 -30 wt.% of KOH. In alkaline electrolyzers anode and cathode are low-cost steel or nickel alloy materials. The electrodes are separated with a thin diaphragm which helps to get zero-gap formation, the separation helps to separate the hydrogen and oxygen produced during the electrolysis. Water and hydroxide ions can pass through the diaphragm. The crossover of hydrogen and oxygen through the diaphragm is one of the issues that reduces the purity of hydrogen. Due to the low conductivity of hydroxide ions through the diaphragm, the electrolyzer can operate at lower current densities. The use of highly concentrated aqueous KOH electrolytes also poses challenges to handle the electrolyte safely [9,24,25].

2.1.2 PEM Electrolyzer

PEM water electrolysis is the most efficient and practical technology for producing hydrogen with high purity [26]. There is renewed interest in hydrogen production from water by utilizing renewable energy sources and by applying new technologies in catalysis and material science. In PEM electrolyzer IrO_2 and Pt are used at the anode and cathode as catalysts, respectively. The acidic membrane enables the electrolyzer to be operated without the use of liquid electrolytes. The membrane conducts the H^+ ions from the anode to the cathode, membrane also functions as a separator and avoids the crossover of hydrogen and oxygen. The PEM electrolyzer is usually operated at a current density of 2 mA cm^{-2} at 50 to 80^oC. As compared to an alkaline electrolyzer

the kinetics of hydrogen evolution reaction (HER) in a PEM electrolyzer is fast due to the acidic medium and high surface area of Pt electrodes. In terms of safety, the PEM electrolyzer is safer because it does not use corrosive caustic electrolytes. Due to the acidic environment in the PEM electrolyzer, specialized materials are used for the gas diffusion layer (GDL), bipolar plates (BP), and current collectors. PEM electrolyzer can also be operated at high pressure at the cathode (for hydrogen generation), while keeping the anode at atmospheric pressure [9].

A PEM electrolyzer consists of a catalyst-coated membrane (CCM) which is fabricated by spraying catalyst on the ion exchange resin membrane. The Perflurosulfonic (PFSA) membranes are usually used in PEM electrolyzers due to their high conductivity and stability in corrosive environments. The CCM is sandwiched between anode and cathode electrodes. Each catalyst layer is made up of a catalyst layer, gas diffusion layer (GDL), and BPs which transfer gas and liquid in and out of the cell and act as a current collector. Some other configurations are also used in the literature where the catalyst is coated onto the metal GDL to improve the dispersion of the catalyst and to decrease the passivation of GDL [27].

Water electrolysis in a PEM electrolyzer involves the splitting of water to hydrogen and oxygen with the application of an electric current [28]. HER takes place on the cathode side and OER takes place at the anode [29,30]. The minimum voltage required across electrodes to split water is 1.23 V based on low heating value, which results in the evolution of hydrogen and oxygen. In a real scenario, this voltage is always higher because of the overpotential at both electrodes [31,32]. To decrease the overpotential, research efforts have been directed to develop catalysts with low overpotential. As the PEM electrolyzer utilizes expensive PGM catalysts at the cathode and anode, it increases the cost of hydrogen [33–36]. Moreover, the material of construction is also expensive such as Titanium used to avoid corrosion of the components of the PEM electrolyzer.

2.1.3 AEM Electrolyzer

AEM electrolysis is one of the developing technologies that combines the knowledge attained from conventional alkaline electrolyzers and PEM electrolyzers. There are not many research articles published on AEM electrolysis and researchers are now giving more attention in this direction. One of the biggest barriers in AEM water electrolyzer technology is the instability of the AEM, low conductivity of the membrane, and slow kinetics of the catalysts. Research on AEM has been focused mainly on lab-size electrolyzer setup and development of AEM, electrocatalysts, and evaluating the operational conditions. The aim is to get high-efficiency, low-cost, and stable AEM water electrolyzers [9].

Figure 2.1a illustrates the AEM water electrolysis process and the components of the AEM water electrolyzer. AEM water electrolysis is the electrochemical splitting of water into hydrogen and oxygen in which AEM transports OH^- to complete the water splitting process. The complete reaction is the sum of both OER at the anode and HER at the cathode. The anode and cathode are connected with an external DC power supply which provides the required voltage to split water. Water is usually circulated from the anode side, but other configurations can also be used. At the cathode, water is dissociated into H^+ ion and OH^-, H^+ ions are reduced to form Hydrogen. The hydroxyl ions diffuse through AEM from cathode to anode, where OH^- ions lose electrons and O_2 and H_2O are formed. Both reactions are combined to give the overall water-splitting reaction. Figure 2.1b shows the corresponding PEM electrolyzer which works with the transport of H^+ ions. Equations 2.1 to 2.3 show the half-cell reactions at both electrodes and the overall reaction. The overall water electrolysis reaction requires 1.23 V, to produce hydrogen and oxygen at 25^{o}C. But due to the overpotential, the cell voltage is higher than 1.23 V. Extra voltage of more than 1.23 V is needed to overcome the reaction kinetics and ohmic resistances of the electrolyte and other

components of the electrolyzer [37]. In practice operational cell voltages are in the ranges of 1.85-2.05 V and at 70-90^{o}C are 1.75 V [37,38].

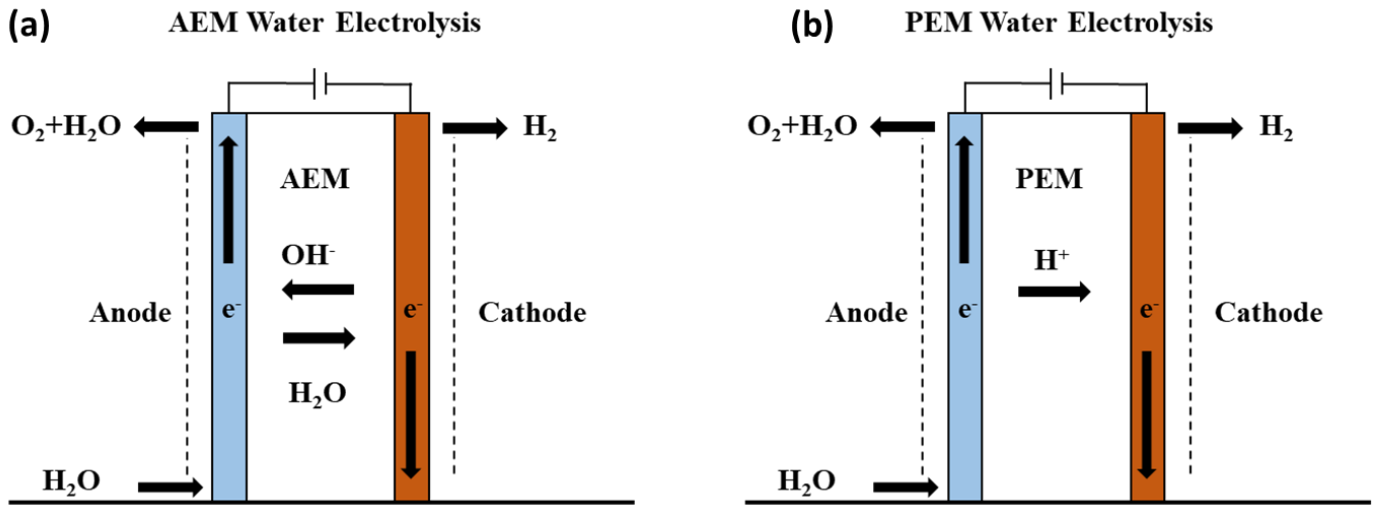


Figure 2.1. (a) AEM water electrolyzer configuration with AEM transporting the OH^- to anode, (b) PEM electrolyzer with PEM where H^+ is transported to the cathode side.

Anode	$4OH^- \rightarrow O_2 + 2H_2O + 4e^-$	E= 0.401 V	Equation 2.1
Cathode	$4H_2O + 4e^- \rightarrow +2H_2 + 4OH^-$	E= -0.828 V	Equation 2.2
Overall	$2H_2O \rightarrow 2H_2 + O_2$	E = 1.23 V	Equation 2.3

Table 2.1 shows the main difference between the three electrolyzers [8,9], the big difference between PEM and other electrolyzers is the higher current density PEM can operate. The disadvantage of a PEM electrolyzer is the use of expensive corrosion resistance components such as Pt and IrO_2 catalysts and Ti bipolar plates [39,40]. AEM electrolyzer on the other hand is set to achieve comparable higher current densities with cheap catalyst materials [41,42].

Table 2.1. Comparison of Alkaline, PEM, and AEM water electrolyzers [8,9].

	Alkaline	**PEM**	**AEM**
Electrolyte	10-30% KOH	Deionized water	1-5% KOH
Charge carrier	OH^-	H^+	OH^-
Temperature range (°C)	65-100	70-90	50-70
OER catalyst	Ni, Ni–Co alloys	IrO_2, RuO_2	Ni, Fe, Co oxides
HER catalyst	Ni, Ni–Mo alloys	Pt, Pt–Pd	Ni and Ni alloys
Current collectors	Ni	Titanium	Ni
Cell efficiency %	60-70	75-85	70-80
Current density (mA cm^{-2})	200-500	800-2500	200-1000
Cell voltage (V)	1.8-2.4	1.8-2.2	1.8-2.2
Operating pressure (bar)	1–30	30–76	1–30
Technology status	Mature	Commercial	R&D

Research on AEM systems to date has been limited to the laboratory scale with a focus on developing electrocatalysts, and membranes and understanding operational mechanisms with the general objective of obtaining high efficiency, low cost, and stable AEM devices.

2.2 Mechanism of water splitting reaction in alkaline electrolyzer

2.2.1 HER Mechanism

The reaction mechanism for HER is not completely understood as it depends on reaction conditions and the catalyst. A simple mechanism for water electrolysis is shown below [43,44]. In an alkaline medium the HER proceeds by the following reaction [45,46].

$$2H_2O + 2e^- \rightarrow H_2 + 2OH^- \qquad \text{Equation 2.4}$$

The HER completes by following the two successive steps.

The **Volmer** reaction step for HER in an alkaline medium involves the dissociation of water, which results in the formation of adsorbed hydrogen at the electrode surface M.

$$M + H_2O + e^- \rightarrow MH_{ad} + OH^- \qquad \text{Equation 2.5}$$

The reaction is completed with the desorption step **Tafel** reaction.

$$M + H^+ + e^- \rightarrow MH_{ad} \qquad \text{Equation 2.6}$$

$MH_{ad} \rightarrow 2M + H_2$ Equation 2.7

or by the **Heyrovsky reaction**:

$H_2O + MH_{ad} + e^- \rightarrow M+H_2 +OH^-$ Equation 2.8

$MH_{ad} + H^+ + e^- \rightarrow H_2 +M$ Equation 2.9

To produce hydrogen via these adsorption and desorption steps, hydrogen mustn't bind too strongly with the electrode/catalytic material. The dissociation of H_2O is a slow reaction, and it is considered the rate-limiting step. The HER in an alkaline medium requires the dissociation of a strong covalent bond of H-O which is a difficult step. Therefore, alkaline HER is considered as more complex than HER in an acidic medium [45,47].

2.2.2 OER Mechanism

For OER in alkaline conditions, the reaction involves the consumption of OH^- ions at the anode. The OH^- ions are transported through the membrane from the cathode side. OER reaction is the main reaction in water electrolysis and has higher overpotential than the HER [48]. The mechanism of oxygen evolution involves several intermediate steps, and it is kinetically unfavorable due to the four-electron process for the evolution of one mole of oxygen gas. This results in the formation of energy barriers and causes slower kinetics and high overpotential. The development of active, stable, and cost-effective OER catalysts is necessary to achieve higher electrolysis efficiencies.

The OER is not completely understood and depends on reaction conditions and catalyst. Different reaction mechanisms have been proposed for OER in alkaline and acidic medium [48]. Table 2.2 shows the OER pathways where “S” is the active site of the catalyst. In an alkaline medium, the first step of the mechanism is the adsorption of hydroxide ions on an active site. This step is proposed to take place first in each of the proposed mechanisms, followed by different intermediate steps. In an acidic medium electrochemical oxide path and oxide path are mostly considered mechanisms as shown in Table 2.3. In both acidic and alkaline conditions, the suggested

mechanistic models for the OER consist of several individual reaction steps and include various intermediate species that are absorbed onto the surface. The sum of each kinetic constraint of the intermediate step is the overpotential for the OER [49,50].

Table 2.2. Oxygen evolution mechanism in Alkaline medium [49,50].

Electrochemical oxide path
(a) $S + OH^- \rightarrow S–OH + e^-$
(b) $S–OH + OH^- \rightarrow S–O + H_2O + e^-$
(c) $2S–O \rightarrow 2S + O_2$
Oxide path
(a) $S + OH^- \rightarrow S–OH + e^-$
(b) $2S–OH \rightarrow S–O + S + H_2O$
(c) $2S–O \rightarrow 2S + O_2$

Table 2.3. Oxygen evolution mechanism in Acidic medium [49,50].

Electrochemical oxide path
(a) $S + H_2O \rightarrow S–OH + H^+ + e^-$
(b) $S–OH \rightarrow S–O + H^+ + e^-$
(c) $2S–O \rightarrow 2S + O_2$
Oxide path
(a) $S + H_2O \rightarrow S–OH + H^+ + e^-$
(b) $2S–OH \rightarrow S–O + S + H_2O$
(c) $2S–O \rightarrow 2S + O_2$

2.3 Thermodynamic Consideration

2.3.1 Theoretical Cell Voltages

Water is a very stable molecule, the splitting of water is an endothermic reaction, and energy is required to carry out the reaction. To split water into hydrogen and oxygen, equilibrium cell voltage E^o must be provided, which is the potential difference between the anode and cathode.

$$E^o = E_{anode} - E_{cathode} \qquad \text{Equation 2.10}$$

The Gibbs free energy of the reaction is related to the Equilibrium cell voltage by the Nernst equation.

$$\Delta G = nFE^o \qquad \text{Equation 2.11}$$

Where n is the number of moles of electrons transferred during the reaction, F is the Faraday constant and E^o is the equilibrium cell voltage. The standard Gibbs free energy change of the reaction is 237.2 kj/mol and the E^o is 1.23 V at 25^{o}C. This is the minimum voltage required for water electrolysis. The electrolysis of water cannot take place at room temperature without providing sufficient electrical energy. When the electrolysis takes place at adiabatic conditions, the enthalpy is provided by the electrical current. The thermoneutral voltage is required to carry out the reaction without the need of heat generation or adsorption. Even when the equilibrium potential is applied, the reactions at the anode and cathode are slow and an overpotential n is required in addition to equilibrium cell voltage to perform the reaction. This overpotential is required to overcome the activation energy barrier and other resistances during the electrolysis reaction. There are three kinds of resistances associated with electrolyzers which are electrical resistances, transport resistances, and electrochemical resistances.

The relation between temperature and electrolyzer potential is shown in Figure 2.2 [51,52]. The Figure is divided into three zones by the equilibrium voltage and thermoneutral voltage lines. Equilibrium voltage is defined as the theoretical minimum voltage to split water into hydrogen and oxygen, at a voltage lower than the equilibrium voltage the electrolysis of water cannot take place. The thermoneutral voltage is the minimum voltage required for the electrolyzer to produce hydrogen and oxygen; the electrolysis is endothermic at lower voltages than the thermoneutral voltage. At higher voltages than the thermoneutral voltage the electrolysis is exothermic [53].

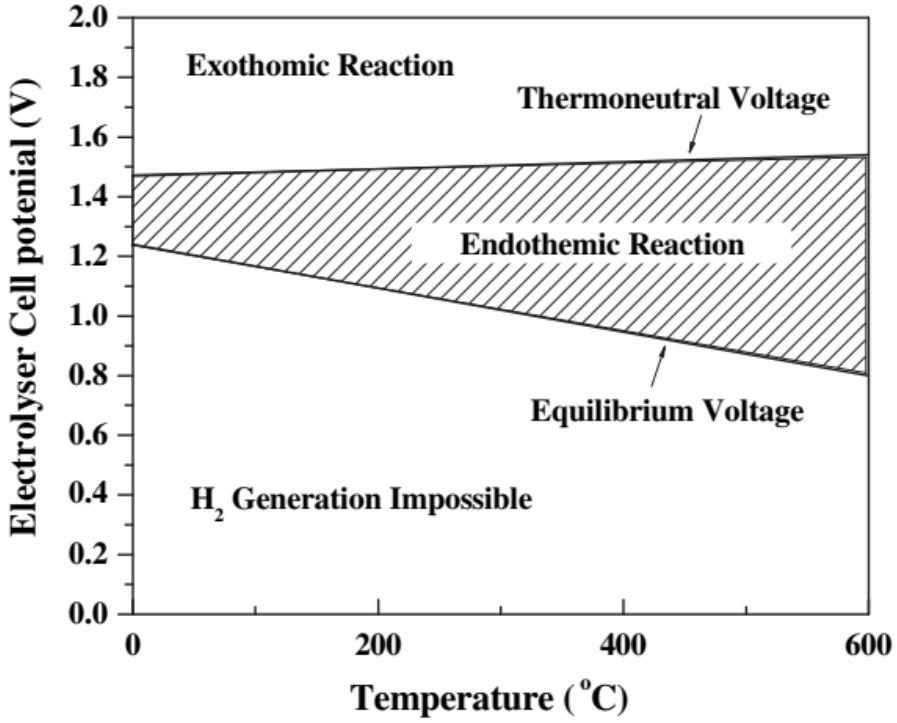


Figure 2.2. Water electrolysis Cell potential for hydrogen production as a function of temperature [53].

2.3.2 Electrical Resistances

Electrical resistances are due to ohmic losses while conducting the current through wires, separators, and electrode material. It can be calculated using Ohm's law R=E/I, where E is the potential, and I is the current. It can also be evaluated using equation R = L/(kA) where L is the length, k is the specific conductivity and A is the cross-sectional area of the metallic conductor [53,54].

2.3.3 Mass Transport Resistances

These are caused by diffusion limitations, such as the formation of bubbles that cover the electrode surfaces and resistances due to the ionic transfer through the membrane. The ion transfer is dependent on the concentration of the electrolyte and the type of membrane used for OH^- transport. An increase in mass transport resistance decreases the overall efficiency of the process [53].

2.3.4 Activation Loss

Activation losses are due to the overpotential of HER and OER at the cathode and anode, respectively. Activation losses also increase the overall resistance of the electrolyzer. The activation losses can be overcome by using the proper catalyst which reduces the activation energy of the HER and OER reaction. Figure 2.3 shows various resistances during the electrolysis process. Activation resistance due to reaction at the cathode and anode is the major cause of loss of voltage and can be minimized with the use of a highly active catalyst [55].

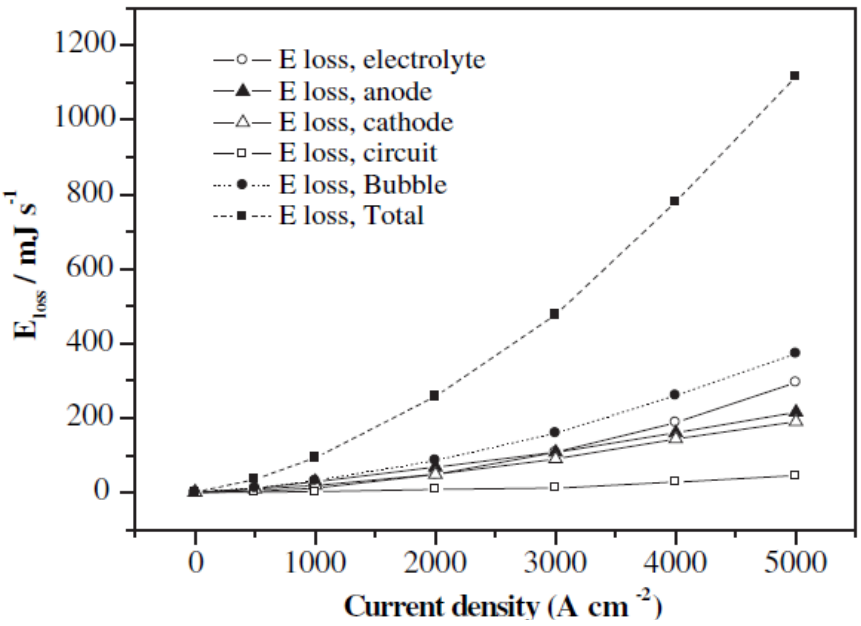


Figure 2.3. Comparison of different resistances during the electrolysis operation [55].

2.4 Cell Efficiencies

2.4.1 Efficiency

The cell efficiency can be calculated as the ratio of power input to the electrolyzer to the molar flow rate of hydrogen multiplied by the ΔH (higher heating value) or ΔG (lower heating value), the AEM electrolyzer power input was calculated by multiplying the cell voltage and current density as expressed in equation 2.12.

Cell efficiency (%) = $\frac{\text{molar flow rate of hydrogen x } \Delta H \text{ x } 100}{\text{AEM electrolyzer power input}}$ Equation 2.12

This efficiency is termed cell efficiency or energy efficiency.

Voltage efficiency is expressed as one of the major indicators of the electrolysis process, it can be calculated as the ratio of cell voltage E_{cell} to the water splitting voltages at lower heating value (LHV) and higher heating value (HHV) as shown in equations 2.13 and 2.14.

$\eta_{LHV} = 1.23/E_{cell}$ Equation 2.13

$\eta_{HHV} = 1.48/E_{cell}$ Equation 2.14

2.5 Anion Exchange Membrane (AEM)

The AEM is the main component of the electrolysis cell. It is made up of a polymer backbone and functionalized with anion exchange groups, mostly with quaternary ammonium group [56,57]. The membrane should have the properties of high ionic conductivity, good thermal and mechanical stability, gas impermeability, and long-term stability [21,58,59]. Its main role is to transport hydroxyl ions from the cathode to the anode side and to also avoid gas crossover. To be considered for commercial use AEM should be of low cost to increase its feasibility.

Membrane conductivity increases with the nucleophilic substitution of the ammonium group and by substituting methyl group to hydroxyl ions. High conductivity can be achieved with the increase in the incorporation of an anion exchange group, but it may also increase the water uptake and deteriorate the mechanical strength of the membrane [60].

The polymer backbone utilized in the literature for AEM electrolysis are polysulfone[61], poly(ether ketone) [62], poly(phenylene oxide) [63], polybenzimidazole [64], polyethylene [65], polystyrene [66], polyethylenepyrrole-co-polyethyeneketone [67,68], poly(ethylene-co-tetrafluoroethylene) [69], and poly(vinylbenzyltrimethylammonium)-b-poly(methylbutylene)

[70]. Polyphenylene base AEMs have been reported to show high current densities for AEM electrolysis [10].

2.5.1 AEM Performance and Stability

Several studies show the performance and stability of membranes. Electrochemical impedance measurement was carried out to compare different membranes, Sustainion® 37-50 showed lower resistance compared to Fumasep® FAS-50, Fumasep® FAPW, AMI 7001 and Nafion 115. There are several reports where Sustainion 37-50 is reported to be better membrane in terms of stability and performance. When it was compared with Aemion^{TM} and Tokuyama A201 membranes at different temperatures, electrolyte, and current density, the Sustainion membrane showed higher performance with 3A cm^{-2} current density with 1 M KOH at 60^{o}C [71]. Sustainion® membrane showed higher stability in the test with a degradation rate of 5µV h^{-1} for 2000 h operation at a fixed current density of 1 A cm^{-2} [58]. Tokuyama A201 showed a degradation rate of 150 µV.h^{-1} for 1000 h at 470 mA cm^{-2} [72], Fumasep® FAA-3-50 had a degradation rate of 800 µV.h^{-1} in 1000 h [73]. The comparison of AEM electrolyzer activity on different commercially available AEM shows all membranes performed well with Platinum group metal catalysts, however with the non-PGM catalysts such as Ni, Co, and Fe-based catalysts the activity decreased drastically. Among the AEM tested the membranes studied Sustainion® showed relatively higher current density in water electrolysis [59].

AEM from Aemion™ was tested for water electrolysis using Pt/C and Ir (black) as a catalyst at the cathode and anode respectively. The electrolysis performance was correlated with membrane ion exchange capacities and thickness. The membrane with ion exchange capacity of 2.1-2.5 meq $OH^{-1}g^{-1}$ and thickness of 50 µm attains the highest current density of 2A cm^{-2} at 1.82 V. FAA-3 ionomer was used and 1M KOH was used as an electrolyte at 60^{o}C [74].

The major issue with the AEM is the thermal stability at high pH [9,75]. At high temperatures, AEM degradation follows two main mechanisms of Hofmann elimination and nucleophilic substitution of hydroxide to the alkyl groups of the polymer backbone in alkaline conditions [76]. Electrochemical oxidation of the phenyl group in the polymeric ionomer on oxygen evolution catalysts has been reported as also one of the forms of degradation during AEM electrolysis [77]. It has been established that non-quaternized membrane needs a more concentrated KOH solution (3.6-6M) to achieve a higher hydrogen generation rate [91].

Short-term stability tests were performed at 0.5 A cm^{-2}, in 0.1 M KOH at 50^{o}C using Aemion™ membranes. Aemion™ ionomer was used in making the electrode. The membranes with high IEC (ion exchange capacity) of (2.1–2.5 meq OH^{-1} g^{-1}) which are AF1-HNN8-25 and AF1-HNN8-50 showed a lower rate of degradation of 2.39 mV/h and 3.21 mV/h compared to other membranes [74]. Long-term durability tests at a high current density of 1 A cm^{-2} were reported on commercial AEMs (Sustainions) using nonprecious catalysts. Sustainion grade T AEM was stable for 12000 h with a degradation rate of 0.7 mV h^{-1} [17]. The non-quaternized membrane with concentrated electrolyte has also shown long-term durability with a degradation rate of 30 μV h^{-1} for 700 h operated at 75-80^{o}C [78,79].

2.6 Gas Diffusion Layer (GDL)

(GDLs) are important parts of PEM and AEM electrolyzers, they control the diffusion of water into the catalyst layer and hydrogen and oxygen out from the catalyst layer [80,81]. Carbon paper and carbon cloths are used at the cathode while Nickel foam, Titanium, and Stainless steel felt or mesh, are used at the anode [8]. The GDL experiences a highly oxidizing and corrosive environment at the anode and needs more research efforts to optimize the properties. A catalyst coated on the gas diffusion electrode is commonly used and the electrode is called a gas diffusion

electrode (GDE). The GDLs also offer ohmic resistance due to the random pore size and shape and uneven surface in contact with the catalyst layer [82–84].

The durability and stability of the GDL depend upon the chemical and electrochemical environment, wettability, low permeability, and excess compression of the membrane, these all can cause the degradation of GDL. Carbon-based GDLs are not used at the anode because of the high concentration of OH^- at the anode that can oxidize the GDLs, therefore metallic GDLs are used at anode to avoid fast corrosion. The passivation layers formed on metallic GDLs such as Ni, Stainless steel, and Titanium protect the GDL from further oxidation but also cause an increase in interfacial contact resistance. In addition, the corrosion of metallic GDLs is reported to take place at higher voltages of 2 V or above [85]. Operating the electrolyzer at a lower voltage can reduce the corrosion of GDL but in the meantime, the hydrogen production rate will be lowered due to the lower current density operation. The corrosion of GDLs also causes the degradation of catalyst contact layers with the GDL [86].

Pore-graded GDL has been shown to improve the efficiency of electrolysis operations. The pore-graded Titanium GDL with tunable pore morphologies improves interfacial contacts, enhances mass transport, and increases activation of reaction sites. The study showed enhanced current density using the pore-graded GDL, the current density of 2.0 A cm^{-2} at 1.8 V with an efficiency of up to 81.9% at 60°C was reported using 0.1 M NaOH as an electrolyte [87].

The conductivity of the GDL also affects the performance of the electrolyzer. In one of the works modified oxidized Ni anode with graphene oxide was used as GDL. For testing electrolytic cell ternary alloy cathode is used with polystyrene-based AEM. The AEM water electrolysis current density with the modified anode was 90 mA cm^{-2} at 2 V, whereas, with the unmodified anode, it

was 60 mA cm^{-2}. The graphene oxide anode offers lower resistance and gives a higher surface area which improves the electrochemical performance [88].

GDL also functions to transport water and evolved oxygen and hydrogen gases, mass transport of liquid and gas products also impacts the stability and activity of the process. The gas bubbles formed at the electrodes should be removed to prevent them from blocking the active area of the electrode, this condition becomes more important at higher current densities. It was reported that GDLs based on the foam can have higher transport issues than the felt base GDLs, the microscopic images revealed that the bubbles were trapped in porous foam [89]. It was also reported that the accumulation of bubbles was also related to the porosity, pore diameter, and thickness of the GDLs. One of the studies showed that trapped bubbles decrease the activity in long-term operation, the electrolysis operation using an AEM electrolyzer with a flow rate of 60 ml min^{-1} was stopped after 10 hours. The flow rate of the water was not stopped and continued for another 10 minutes to remove the trapped bubbles, once the electrolysis was started again it reached the same activity as it had at the start of the operation. This study shows that the accumulation of gas bubbles negatively affects performance and bubble management needs to be performed to improve the long-term activity [90]. The other associated problem with the accumulation of bubbles is the dehydration of the catalyst layer and membrane adjacent to the GDLs. This not only causes the blockage of active surface area for both OER and HER reaction but also decreases the OH^- transport through the membrane, these processes cause long-term degradation and activity loss [8].

Stainless steel meshes have also been reported as GDLs for AEM water electrolysis at the anode. It was reported that the stainless-steel mesh with small pore size, graded pore, and smooth surface have shown higher electrochemical properties. The AEM water electrolysis using pure water at 50^oC with commercially available stainless steel meshes was studied by Xu et al. The SS10 has

the lowest pore size, and the smooth surface has a cell voltage of 2.24 V at 0.5 A cm^{-2}. In all cases, the total thickness of the GDL was 0.60 mm, obtained by pressing the stainless steel meshes. It was proposed that the higher performance was due to the improved contact area between the AEM and the SS10 mesh GDL [91].

2.7 AEM Water Electrolysis Catalyst

Water electrolysis requires a theoretical thermodynamic potential of 1.23 V, both half-cell reactions OER and HER require an electrocatalyst to decrease the overpotential and to overcome the kinetics. Catalysts are designed to reduce the overpotential of HER and OER [41,45,92]. To reduce the cost of AEM water electrolyzer, the development of non-noble metal catalysts is required for HER and OER. The main challenges in catalyst development are the activity, stability, and composition of the catalysts. Due to the low mass-specific activity of non-noble catalysts, higher loadings of the catalysts are used in MEA fabrications which may cause ohmic resistance. Transition metal oxide catalysts such as Co, Ni, and Fe are mostly used for AEM electrolysis. These catalysts are relatively lower in cost compared to Pt and IrO_2-based catalysts and are stable in alkaline conditions [9]. Table 2.4 provides the catalysts used in recent studies along with their performance and the type of membrane used [59].

2.7.1 HER Catalysts.

Under Alkaline conditions, HER reaction is slower compared to acidic pH in the PEM electrolyzer. HER kinetics are two to three times lower in alkaline conditions in AEM electrolysis compared to PEM electrolysis [22,23]. Most active non-noble catalysts for HER are the elements of the iron group, which are Nickel, Cobalt, and Iron [93,94]. Nickel-based HER catalysts have been studied as low-cost non-noble metal catalysts. Their activity is lower than Pt benchmark catalysts.

It was reported that when commercially available Ni nano powder with the loading of 2mg.cm^{-2} was used in AEM electrolysis with pure water, the electrolyzer achieved 0.3A cm^{-2} at 1.8 V [95]. In another study, Ni nanoparticles were electrodeposited onto carbon paper for HER in AEM water electrolyzer, with a feed of 1 M KOH current density of 0.15 A cm^{-2} was achieved at 1.9 V. To improve the performance of Ni-based catalysts different compositions with other transition metal oxides were also studied in the literature [96]. NiCu alloy catalysts for HER in alkaline electrolysis were prepared by Sang Hyun Ahn et al. [97]. The composition of the catalyst varied by changing the deposition potential. The activity was measured by cyclic voltammetry in a 6 M KOH at 298K. The catalyst with the composition of NiCu gave the highest activity. The HER activity of the catalyst with the composition of M_xNi_{1-x} (where M is Cr, Mo, and W and x is 0.2) was tested in alkaline and acidic conditions. Cr_xNi_{1-x} showed higher activity compared to other catalysts in the series with an overpotential of 106 mV in 1.0 M KOH at 10 mA cm^{-2} current density [41]. NiMo alloy nanowire catalyst supported on Ni foam was developed by hydrothermal method followed by thermal reduction. A hierarchical structure was obtained and showed high activity of HER in alkaline conditions. The catalysts achieved 10 mA cm^{-2} at the overpotential of 30 mV in alkaline solution with a Tafel slope of 86 mV dec^{-1} [98].

Ni_2P nanosheets supported on nickel foam were doped with Cu atoms. The Cu atom was reported to improve the physiochemical properties of Ni_2P catalysts, improve the electrical conductivity, and increase the surface-active site. The HER activity of NiCuP showed high performance with the Tafel slope of 70mVdec^{-1} for overpotential of 78 and 245mV with the current density of 10 and 100 mA cm^{-2} respectively [99]. Ni-Co microporous cathodes were developed using galvanic deposition at high current densities. HER were carried out at 30wt.% KOH solution [100].

The electrodeposition method was used to deposit Ni-Mo-Cu alloy catalyst on copper substrate. The HER activity of Ni-Mo-Cu catalyst was higher than the Ni-Mo, and the addition of Cu also resulted in a cauliflower-like structure. The increased activity was attributed to the high surface area of the Ni-Mo-Cu catalyst [101].

Commercially available Ni/(CeO_2-La_2O_3)/C have been tested with 1 M K_2CO_3 as a mild electrolyte with a pH of 10-11. For OER catalyst commercially available $CuCoO_x$ was used at the anode. The loading of the cathode catalyst increased from 0.6 to 7.4 mg.cm^{-2} and the cell potential was 2.01 to 1.89 V at 0.470 A cm^{-2} respectively with catalyst loading. This study showed that with the increase in catalyst loading the cell voltage decreased and higher current density was achieved at a lower cell voltage [72]. Nickel alloyed with Molybdenum has shown high activity with pure water [37,102]. A mixed-phase Ni-Mo catalyst with Ni rich and Ni-Mo alloy nanoparticles embedded in Mo rich oxide matrix has been developed [103].

It has been investigated in several studies that binary alloys of Nickel with Cobalt [104–108], Molybdenum [109–112], Iron [108,111,113], and W [111,114] have shown higher catalytic activity compared to pure Nickel catalysts. The improved activity was attributed to a more developed surface structure and synergistic effect. It was also proposed that when left-side elements in the transition metal group in the periodic table, with empty d-orbital, are alloyed with metals of the right side with complete internally coupled d-orbitals, the resultant metallic alloy shows lower binding energy which causes an increase in catalytic activity [115].

NiFe catalysts have been reported to have high activity for HER in an alkaline medium. Alaa Y. Faid et al. synthesized NiFe and NiCo catalysts by coprecipitation method followed by reduction in the 5% H_2-95% Ar mixture to convert the hydroxide precipitate into metallic alloy. The Raman analysis showed the presence of $NiFe_2O_4$ and $NiCo_2O_4$ spinel oxides in all the catalyst series except

the NiO catalyst, which had the rocksalt structure. The mass electrochemical activity was highest for 33mol% Ni catalyst, which was due to higher electrochemical surface area and lower crystallite size. The study did not show the catalyst performance on AEM water electrolyzer and was limited to the evaluation of the catalyst for HER in 0.1 mol.dm^3 KOH [116].

NiFeCo is also reported to have high activity in alkaline medium for HER reaction. One of the studies reported electrodeposited cathode using a bath of $CoCl_2$, $FeCl_2$, NaCl, boric acid, ascorbic acid, and saccharin, with pH adjusted to 3. Commercially available NiFeCo catalysts were used as a cathode to fabricate MEA with Sustainion ion membrane and $NiFe_2O_4$ at the anode. The AEM water electrolyzer was tested at 60^{o}C with 1 M KOH, the current densities achieved at 2 V and 1.9 V were 0.94 and 0.47 A cm^{-2} [71]. In a similar work NiFeCo cathode and NiFe as anode were used to fabricate MEA with Sustainion X-37-50 anion membrane. The current densities reported were 1.0 and 1.75 mA cm^{-2} for 1.9 V and 2 V respectively, for AEM water electrolysis operation at 60^{o}C with 1 M KOH [117].

2.7.2 OER Catalysts.

Several materials and different compositions have been used for the OER, in alkaline conditions first row transition metals showed high activity and in addition they showed good stability in alkaline environment. Ni, Fe, and Co based catalysts have been known to decrease the OER overpotential [118–120]. Transition metal oxides, hydroxides, and oxyhydroxides have been studied and their activities have been reported in the literature.

2.7.2.1 Spinel

Spinel compounds have good electric conductivity and are stable in alkaline medium for OER and at high anodic potentials. The most common spinel oxides for OER are Ni, Co, and Fe based which can also include other metals such as Cu, Zn, Mn, and Li [121–124].

Spinel materials have a cubic crystal symmetry with a general formula of AB_2O_4. Where A and B are group 2, group 13 and first row transition metal elements. The crystal structure is shown in Figure 2.4 [125], which shows two different crystallographic sites octahedral (Oh) and tetrahedral (Td) sites. Due to that, two types of spinels are formed, one is spinel, and the other is inverse spinel. The configuration for normal spinel is $(A^{2+}{}_{Td})(B^{3+}{}_{Oh})_2O_4$ with divalent cation in A^{2+} at the tetrahedral coordination. The inverse spinel has the configuration of $(A^{2+}{}_{Oh})$ $(B^{3+}{}_{Td})$ $(B^{3+}{}_{Oh})_2O_4$ with divalent A^{2+} in octahedral coordination [126].

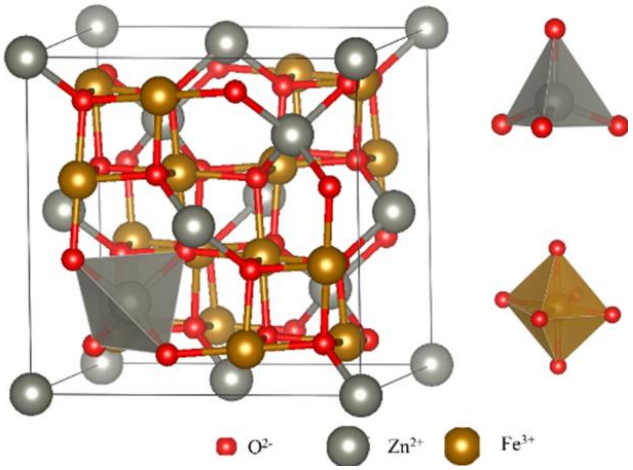


Figure 2.4. Crystal structure of spinel (AB_2O_4) with octahedral and tetrahedral sites [125].

New compositions of transition metal oxides with different morphologies are also reported. $NiCo_2O_4$ has been investigated as OER catalyst due to its higher conductivity and tunable active sites [127–129]. $NiCo_2O_4$ was also used as a support to deposit other catalysts, one such example is $Co_3O_4/NiCo_2O_4$ [130]. Other catalysts such as $Au/NiCo_2O_4$ [131] and $NiCo_2O_4$/graphene [132] were also developed. The overpotential of this series of catalysts is still higher than the benchmark catalysts.

Many research works have shown that spinel oxide based on cobaltite as a bifunctional catalyst for OER and oxygen reduction reaction for high pH conditions [133]. $Mn_xCo_{3-x}O_4$ mixed valency spinel oxides are also known to have good OER activity [134]. Cheng et al. synthesized $CoMnO_4$

by rapid room temperature synthesis method and reported that $Co_xMn_{3-x}O_4$ had high OER activity due to the high surface area and defect sites [135]. $Cu_xCo_{3-x}O_4$ was also shown to have good activity for OER [136], it was also proposed that the Mn doped $CuCo_2O_4$ could improve the activity of the cobaltite oxide doped with Cu [137].

Co-based oxides have high catalytic activity, and their performance could be enhanced by the addition of different transition metals. Fe, Ni, Mn, Zn, and Cu are reported to improve the activity of Co catalyst [138–144]. Cu-Co oxide materials have been evaluated for alkaline electrolysis and showed high activity. The ratio of Cu to Co also plays an important role and Scott et al. reported enhanced activity for $Cu_{0.7}Co_{2.3}O_4$ deposited on Ni foam [140]. $CuCo_2O_4$ catalysts fabricated on Ni foam by hydrothermal method are reported to have high OER activity [140,141].

There are also reports of doping spinel Co_3O_4 with Li, 30-40 nm particles by nitrate-assisted thermal decomposition method were synthesized. Li doping resulted in a solid solution of Co_3O_4 with Li, the OER potential also shifted to negative. This was attributed to the changes in cation distribution in the lattice and changes in the binding energy of surface oxygen. Among the series of catalysts prepared, $Li_{0.21}Co_{2.79}O_4$ showed the highest electronic conductivity and OER activity. When the same catalyst was used as anode for AEM water electrolysis, it achieved a current density of 300 mA cm^{-2} with a voltage of 2.05 V at 45 C^o [85].

Nickel has been proposed to be the most efficient catalyst for OER based on adsorption energies and bond strength of the reaction intermediates [145–148]. To further improve the activity of Ni hydroxides and oxyhydroxides, other transition metals are incorporated in lesser amounts to enhance the activity of the catalyst. The addition of transition metals as impurities into Nickel oxide improves the conductivity increases active sites and decreases the binding energy of the intermediates [149–151]. Multiple oxidation states are also possible with this method of

modification of the catalyst. Ni-Fe binary catalyst was modified with a third metal and showed higher activity compared to the Ni-Fe oxide catalyst [152–154]. Figure 2.5 shows the volcano plot for OER, the x-axis shows the energy difference between oxygen intermediates and the overpotential is on the y-axis. The catalysts that fall at the volcano's peak are considered active catalysts due to the intermediate binding energy of the intermediates. Among those materials, NiO and Co_3O_4 are the most active catalytic materials in non-platinum group materials [155].

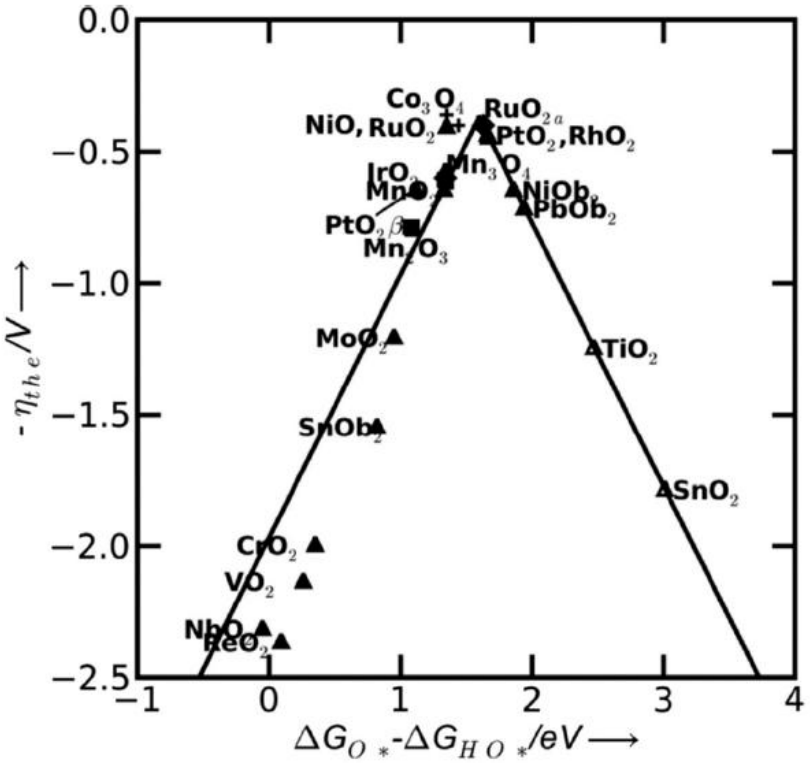


Figure 2.5. Theoretical overpotential of oxygen evolution reaction vs. the difference between the standard free energy of two subsequent intermediates ($\Delta G^0_{O*} - \Delta G^0_{HO*}$) for various binary oxides [155].

The AEM water electrolyzer performance over Ni-Fe nanoparticles as anodes was evaluated using 1 M KOH, $Ni_{0.9}Fe_{0.1}$ showed the cell voltage of 1.72 V at 0.8 A cm^{-2}. $Ni_{0.80}Fe_{0.1}$ with 10% CeO_2 had a voltage of 1.67 V with 0.4 A cm^{-2} using 0.1 M KOH. In durability testing $Ni_{0.9}Fe_{0.1}$ showed the stability of 12 h at 0.5 A cm^{-2} [156]. In another study, NiFe bimetallic anodes were fabricated using the magnetron sputtering technique. This work showed the enhancement in electrochemical

activity with the addition of Fe to Ni based catalysts. The highest performance reported was on Ni/Fe catalyst with an atomic ratio of 10/1, on this catalyst at 2 V the current density was 0.6 A cm^{-2} and 0.4 A cm^{-2} at 60^{o}C and 40^{o}C respectively [157].

2.7.2.2 Metal hydroxides

Layered double hydroxides (LDHs) of non-precious metals have been considered active catalysts for OER, due to high surface area, electron distribution, and low cost. LDHs are layered metal hydroxides that have cationic brucite like layered structures separated by interlayers of anions [158,159]. This structure enables fast diffusion of reactants and products with fast proton-coupled electron transfer. In addition, due to the high availability of catalytic active sites electrocatalytic activity for OER is high [160]. $Ni(OH)_2$, $Co(OH)_2$, NiFeOOH and NiFe LDH have been studied in detail for OER. The stability of these catalysts is one of the issues to be considered for AEM water electrolysis as they tend to dissolve when used with pure water [161].

Dongyu Xu et al. synthesized transition metal (oxy) hydroxide for OER and tested it in AEM water electrolysis. From these catalysts $NiCoO_x$:Fe shows the highest activity with the current density of 900 mA cm^{-2} at 2.4 V [161]. The catalyst was designed to be oxyhydroxide because the active sites for OER are proposed to be transition metal oxyhydroxide.

The redox activity of the layered structure comes from the intercalation of water molecules and anions. Compared to bulk LDHs, single-layered double hydroxide has been reported to have higher electrical conductivity and active sites. Single layer nanosheets of NiFe, NiCo and CoO LDHs were fabricated by liquid phase exfoliation method with high OER activity in an alkaline medium. The activity of the catalyst was in the order of NiFe > NiCo > CoO for bulk and exfoliated nanosheets [162].

High stability is also reported on LDHs electrocatalysts with low overpotentials at 10 mA cm^{-2}. A ternary catalyst based on Fe, Co, and W is reported to have a synergistic effect and favorable electronic coordination for OER, DFT calculations, and X-ray absorption spectroscopy analysis was used to propose these findings. For OER Ni foam, Au(111) and gold-plated Ni foam were used with the catalyst for OER in an alkaline medium, the gold-plated Ni foam electrode showed higher activity compared to other electrodes [163].

2.7.2.3 Perovskite

Perovskite catalysts have been considered as active OER catalysts, they are easily modifiable, low cost, and have high activity. The general structure of perovskite is ABO_3 in which A is the bigger Cation and B is the smaller cation. A can be from the lanthanide series, or an alkaline earth element, and B is from transition metal elements. B is surrounded by 6 oxygen atoms and forms BO_6 octahedral structure as shown in Figure 2.6 [49].



Figure 2.6. Structure of ABO_3 perovskite oxide [49].

In their work, Man et al. used a volcano plot as shown in Figure 2.7, which used the difference between two energy states of intermediates during the oxygen evolution reaction, represented as ($\Delta G^0_{O*} - \Delta G^0_{HO*}$). According to the Sabatier principle, surfaces with higher binding energy form

stable intermediates that do not desorb and thereby hinder the reaction, while surfaces with weak bonding to the intermediates do not retain them long enough for the reaction. The volcano plot in Figure 2.7 follows the Sabatier principle, the materials with the bonding energy in between are predicted to perform well compared to other materials. Therefore, $SrCoO_3$ and $SrNiO_3$ are materials of interest for OER [155].

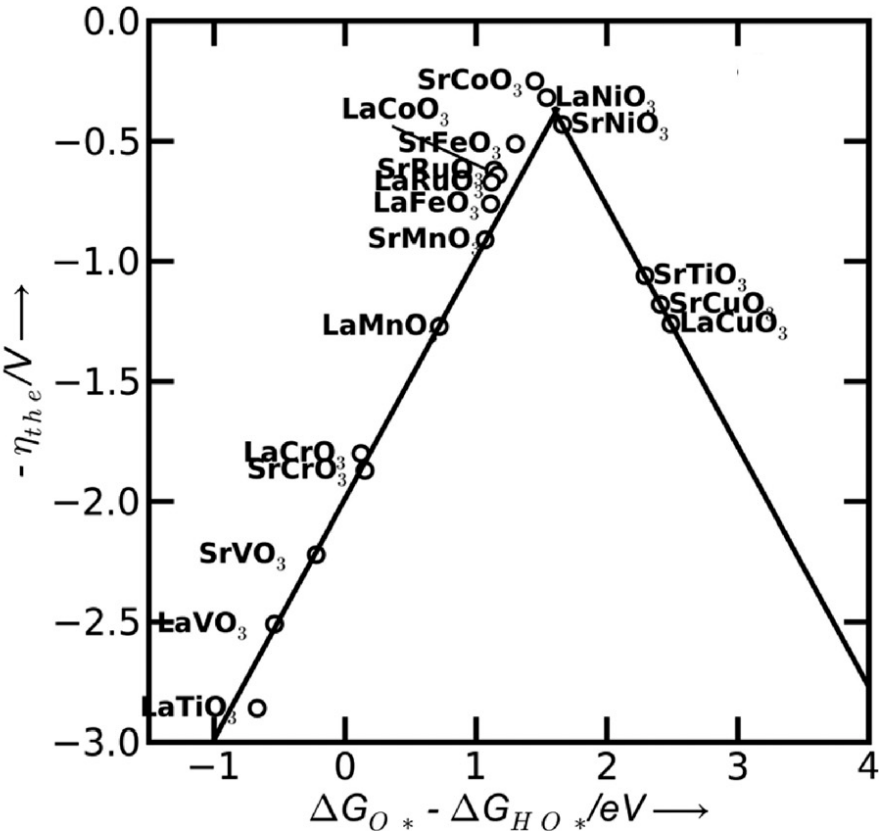


Figure 2.7. Theoretical overpotential of oxygen evolution reaction vs. the difference between the standard free energy of two subsequent intermediates ($\Delta G^0_{O*} - \Delta G^0_{HO*}$) for Perovskite oxide material [155].

Xiang Li et al. compared the OER activity of Co_3O_4, $SrCoO_3$, $CaCoO_3$ in KOH with pH range of 12.5 to 14. The results show that both $SrCoO_3$ and $CaCoO_3$ performed better than the Co_3O_4 catalyst. Co oxidation state was +4 in both perovskites while in Co_3O_4 it was +3, which also shows that the oxidation state of Co in +4 correlates with the OER results [164].

Table 2.4. Electrolyzer performance with commercially available membranes [59].

OER Catalyst	HER Catalyst	Membrane/ ionomer	Temperature (°C)	Feed	Membrane thickness (μm)	Cell voltage (V)	Current density A cm^{-2}
$NiFe_2O_4$	NiFeCo	Sustainion 37-50	60	1 M KOH	50	1.8	0.16 [71]
$NiFe_2O_4$	NiFeCo	Sustainion 37-50	60	1 M KOH	50	1.9	0.43 [71]
$NiFe_2O_4$	NiFeCo	Sustainion 37-50	60	1 M KOH	50	2	0.94 [71]
IrO_2	Pt	Sustainion 37-50	60	1 M KOH	50	1.7	1.99 [117]
IrO_2	Pt	Sustainion 37-50	60	1 M KOH	50	1.8	3.33 [117]
$CuCoO_3$	Ni/CeO_2-La_2O_3	Tokuyama A201	43	1 M KOH	28	1.7	0.29 [72]
$CuCoO_3$	Ni/CeO_2-La_2O_3	Tokuyama A201	43	1 M KOH	28	1.8	0.52 [72]
$CuCoO_3$	Pt/C	Tokuyama A201	50	10 wt.% K_2CO_3	28	1.9	0.87 [165]
$NiFe_2O_4$	NiFeCo	Tokuyama A201	60	1 M KOH	28	1.7	0.1 [71]
$NiFe_2O_4$	NiFeCo	Tokuyama A201	60	1 M KOH	28	1.8	0.26 [71]
$NiFe_2O_4$	NiFeCo	Tokuyama A201	60	1 M KOH	28	1.9	0.54 [71]
$NiFe_2O_4$	NiFeCo	Tokuyama A201	60	1 M KOH	28	2.0	0.92 [71]
$NiFe_2O_4$	NiFeCo	AEMION	60	0.1 M KOH	38	1.8	0.03 [71]
$NiFe_2O_4$	NiFeCo	AEMION	60	0.1 M KOH	38	1.9	0.07 [71]

$NiFe_2O_4$	NiFeCo	AEMION	60	0.1 M KOH	38	2.0	0.13 [71]
$NiFe_2O_4$	NiFeCo	AEMION	60	1 M KOH	38	1.8	0.13 [71]
$NiFe_2O_4$	NiFeCo	AEMION	60	1 M KOH	38	1.9	0.31 [71]
$NiFe_2O_4$	NiFeCo	AEMION	60	1 M KOH	38	2.0	0.63 [71]
Nickel Foam	Nickel Foam	FAA-30-50	60	10 wt.% KOH	55	2.0	0.03 [166]
IrO_2	Pt/C	FAA-30-50	60	1 M KOH	50	1.8	0.32 [167]
IrO_2	Pt/C	FAA-30-50	60	1 M KOH	50	1.9	0.47 [167]
IrO_2	Pt/C	FAA-30-50	60	1 M KOH	50	2.0	0.62 [167]

3 Experimental Methods and Techniques

3.1 Physiochemical Characterization

3.1.1 X-ray diffraction

X-ray diffraction is a nondestructive characterization method to investigate the crystal structure of the materials. In catalysis, XRD is used to analyze the material's crystal structure, lattice spacing, and crystallite size. The principle of XRD is based on the diffraction of X-rays by the crystal planes which act like the grating material. The interaction of X-rays with crystal structure gives secondary X-rays which are related to the interplanar spacing of the crystal. This relation is given by Bragg's law as follows.

$$n\lambda=2d\sin\theta \qquad \text{Equation 3.1}$$

Where n is an integer, λ is the wavelength of X-rays, d is the interplanar spacing of the crystal and θ is the angle of diffraction. Intensities of diffraction lines depend on the arrangement of atoms in the unit cell of the crystal lattice, this information mainly provides a distinctive description of the nature of the crystalline phases present. In actual practice, the diffraction pattern is not trivial as the catalyst contains many different phases.

3.1.2 Scanning Electron Microscopy

Scanning electron microscopy is used to investigate the morphology of solid materials. It uses a beam of electrons generated through a thermionic, Schottky, or field emission cathode that is accelerated with a voltage difference, which could be 0.1 to 50 keV (kilo electron volts). The electron beam is used to image the samples, the electrons hit the sample which is kept in the vacuum chamber and this interaction causes the release of secondary electrons, backscattered

electrons, and characteristic X-rays. The secondary and backscattered electrons are used to image the sample whereas characteristic X-rays are used in Energy dispersive X-ray (EDX) analysis.

The resolution of the image depends upon the use of an electron beam, and it can be in the range of micrometers to nanometers. In this work, SEM was used to analyze the morphology of the developed catalyst. The SEM analysis gives details about the particle size distribution and the structure of the catalyst. For powdered catalyst material, a few milligrams of the catalyst powder were mixed with ethanol/isopropanol and then the sample was put on the carbon tape, the ethanol/isopropanol evaporates quickly and gives good dispersion of powder on the carbon tape. Carbon tape was then put on the SEM sample holder which is usually made up of Aluminum. Cross-sectional images of membrane electrode assembly MEA were taken during this study, which gave insight into the thickness of the catalyst layer and membrane in the MEA.

3.1.3 Energy dispersive X-ray Spectroscopy

Energy dispersive X-ray spectroscopy (EDS) is a method to study the elemental composition of the materials. The EDS detector is present in SEM. For the analysis, the surface is bombarded with high-energy electrons and inner shell electrons are knocked out from the atom and leave a vacancy. The vacancy is then filled by electrons from higher energy level which causes the release of X-ray photons. This emission of characteristic X-rays is unique to each element. The EDS detector detects the X-rays, and the elements present in the material can be distinguished.

3.2 Electrode Fabrication and Performance Evaluation

3.2.1 Preparation of Gas diffusion electrode and Membrane electrode assembly

Catalysts were deposited onto nickel foam (thickness of 1.7 mm), which acted as the anode. Nickel foam offers high mechanical stability and porosity compared to Nickel felt type GDL. To make the catalyst slurry, 100 mg of catalyst was dispersed in a mixture of water and Nafion solution (Nafion™ 1100W from Sigma Aldrich). If the slurry was too thick, additional water was added dropwise to get the desired consistency, with the Nafion content making up 10 wt.% of the catalyst amount. The slurry was then sonicated for 30 minutes to ensure a uniform mixture. The thick catalyst slurry was then coated onto the surface of the nickel foam and pressed to form the catalyst-coated gas diffusion electrode (GDE). The anode consistently contained a loading of 25 mg cm^{-2} of catalyst, resulting in an electrode thickness of 0.80 mm.

For the cathode, a commercial Pt/C (40 wt.%, HISPEC 4000, Johnson Matthey) catalyst was used for the Hydrogen Evolution Reaction (HER). One mg of Pt was deposited onto the carbon paper (Sigracet 29BC) using airbrush, with a paper thickness of 235 µm. The catalyst ink was prepared by mixing the catalyst with water, ethanol, and Nafion solution. A typical ink composition involved dispersing 50 mg of Pt/C in 5 ml of ethanol and 1 ml of water, along with 0.22 g of Nafion solution, with the Nafion content accounting for 20 wt.% of the catalyst amount.

The membrane electrode assembly (MEA) was formed by placing an AEM (dioxide membrane Sustainion® X-37-50 grade T with a thickness of 50 µm) between the anode and cathode. The commercial AEM was initially in Cl or Br form and was activated for use in the AEM electrolyzer by soaking it in a 1.0 M KOH solution overnight (approximately 24 hours) and then rinsing it with distilled water. The activated membrane was used to construct the MEA. The total active area of

the MEA was 3.24 cm^2, with dimensions of 1.8 cm x 1.8 cm. The components were assembled into the MEA plastic casing, starting with a porous transport layer made by pressing three nickel foams to a thickness of 2 mm. Next, a nickel foam anode was inserted, followed by the AEM and the carbon paper cathode.

3.2.2 Catalyst Testing in three-electrode System

Electrochemical measurements were conducted using a potentiostatic system (VMP-3, Biologic) in a three-electrode setup with 1.0 M KOH as the electrolyte at room temperature. The working electrode consisted of nickel foam coated with an OER catalyst with an active area of 1 cm^2. The counter electrode was a graphite electrode, and the reference electrode was a Standard Calomel Electrode (SCE). To ensure uniformity, all potentials were converted to potentials versus the reversible hydrogen electrode (RHE) by applying the Nernst equation. Polarization curves for OER activity were recorded with a scan rate of 5 mV/s and 85% iR correction. For assessing the long-term stability of the catalyst, the cell was operated at a constant current density for an extended time. The double layer capacitance (C_{dl}) was calculated using cyclic voltammetry (CV) measurements at scan rates ranging from 20 to 150 mV/s in the non-faradaic region in 1.0 M KOH. To calculate the effective electrochemical surface area (ECSA), the double-layer capacitance (C_{dl}) was divided by the capacitance of a flat metal surface known as the smooth plane capacitance (Cs). The value of Cs, representing the capacitance per unit area, was 40 $\mu F/cm^2$. This ratio provides an estimation of the ECSA, which reflects the active surface area available for electrochemical reactions. To fabricate the catalyst-coated electrode, catalyst ink was prepared by mixing the catalyst with a 5 wt.% Nafion solution and ethanol. The catalyst loading on the nickel foam anode was 5 mg/cm^2.

3.2.3 AEM Electrolyzer Performance Test

The AEM water electrolyzer performance was assessed using a potentiostat connected to a 100 A Booster VMP3B-100. In the AEM electrolyzer setup, the cathode and anode are separated by an AEM. Figure 3.1a and Figure 3.1b show the AEM water electrolyzer used in this study with an inlet for water and oxygen and water outlets on the anode side, while the hydrogen outlet is on the cathode side. During the electrolysis process, hydrogen is formed at the cathode, and hydroxyl ions generated during the reaction are transported through the AEM. At the anode, the hydroxyl ions undergo oxidation, releasing oxygen gas, which is then circulated out of the electrolyzer along with the aqueous KOH solution.

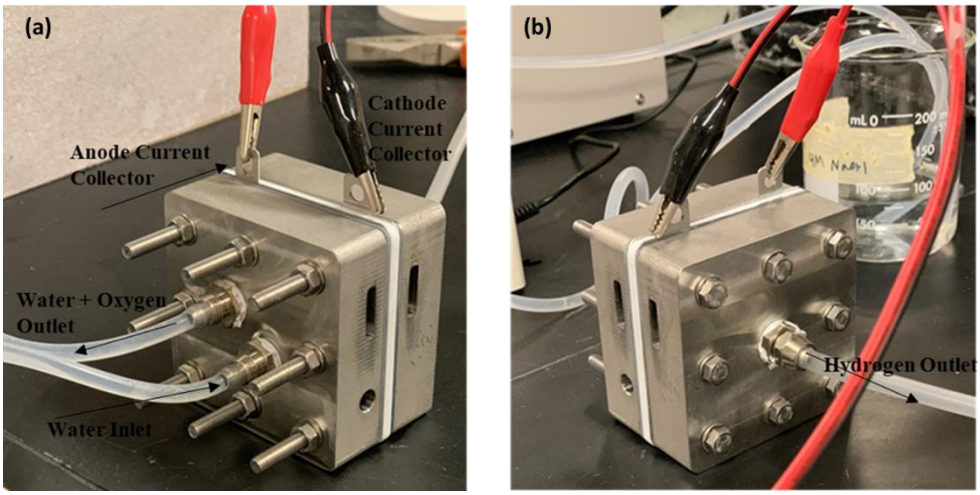


Figure 3.1. Electrolyzer used for AEM water electrolysis. (a) Anode side with water inlet and oxygen and water outlet. (b) Cathode side with hydrogen outlet.

In Figure 3.2b, the schematic of the membrane electrode assembly is depicted, where Pt/C is used on the carbon paper as the cathode, and $NiFeCoO_x$ catalyst is coated on the Nickel foam gas diffusion layer.

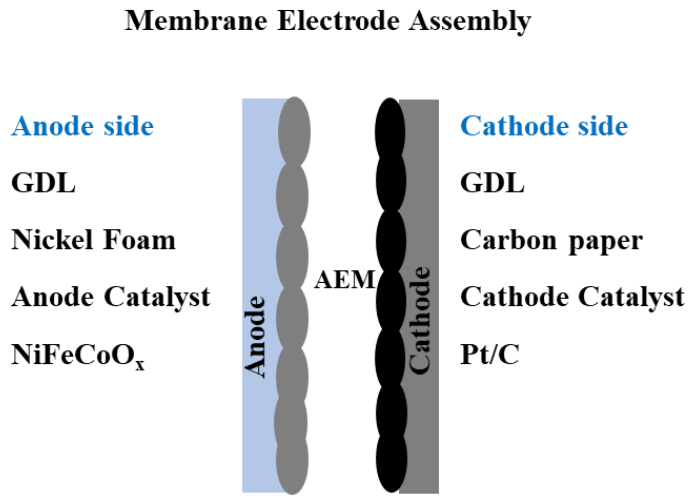


Figure 3.2. The schematic of membrane electrode assembly used in this study.

To activate the catalyst, cyclic voltammetry (CV) was performed in the voltage range of 1.3 V to 2.2 V at a scan rate of 5 mV/s. The electrolyzer operation also involved using linear sweep voltammetry (LSV) and chronoamperometry (CA). A 1M KOH electrolyte was used and circulated at a flow rate of 90 ml/min. The electrolyte and the electrolyzer were heated to the operating temperature using a hot plate, with the temperature range during electrolysis varying from 45 to 70°C. EIS measurements were conducted to determine the electrolyzer cell's impedance during the electrolysis. Potentiostatic EIS was carried out at the voltage range of 1.7 V to 2 V, with a frequency range of 100 kHz to 100 mHz. The data was analyzed using Nyquist plots and equivalent circuit fittings. The theoretical voltage required to split water is 1.23 V, but in practical cases, it is higher due to the overpotential of these reactions at both the anode and cathode.

The durability of the AEM electrolyzer was tested at constant current density. To calculate the cell efficiency, which is the ratio of power input to the electrolyzer to the power of hydrogen out, the AEM electrolyzer power was calculated by multiplying the cell voltage and current density. Cell efficiency was calculated by using equation 3.2. Faradaic efficiency was determined by measuring the quantity of hydrogen generated at room temperature.

$$\text{Cell efficiency (\%)} = \frac{\text{molar flow rate of hydrogen} \times \Delta H \times 100}{\text{AEM electrolyzer power input}} \qquad \text{Equation 3.2}$$

4 $NiFeO_x$ and $NiFeCoO_x$ Catalysts for Anion Exchange Membrane Water Electrolysis

4.1 Introduction

Anion exchange membrane (AEM) water electrolysis has the advantage of being able to operate in low concentrations of electrolytes, such as 1wt.% KOH or distilled water compared to conventional Alkaline water electrolysis (AWE), which makes it possible to use inexpensive Ni and Co-based electrocatalysts [19,168]. To improve the current density and efficiency of AEM water electrolysis, a cell structure similar to Polymer electrolyte membrane (PEM) water electrolysis is available [142,169–171].

For OER in alkaline conditions, the reaction involved the consumption of OH^- ions at the anode. The OH^- ions are transported through the membrane from the cathode side. The OER reaction is the main reaction in water electrolysis and has a higher overpotential than the HER [48]. The mechanism of oxygen evolution involves several intermediate steps, and it is kinetically unfavorable due to the four-electron process for the evolution of one molecule of oxygen gas. This resulted in the formation of energy barriers and caused slower kinetics and high overpotential [172]. Due to this, the development of active, stable, and cost-effective OER catalysts is necessary to achieve higher electrolysis efficiencies.

Several materials and different compositions have been used for the OER, in alkaline conditions, first-row transition metals showed high activity, in addition, they have good stability in alkaline environments [173]. Ni, Fe, and Co-based catalysts have been known to decrease the OER overpotential. Transition metal oxides, hydroxides, and oxyhydroxides have been studied for the OER and their activities have been reported in the literature. The general trend in the activity for these catalysts is Ni > Co > Fe [145–147,174].

The performance of AEM water electrolyzer is highly dependent on the AEM and concentration of electrolytes as well as the electrocatalysts [19]. In AEM water electrolysis, various electrolytes such as KOH, K_2CO_3, and $KHCO_3$ are used to improve performance [72]. Higher concentrations of electrolyte ensure higher ionic conductivity of the OH^-, which can be expected to improve performance. However, Deionized water can also be used as an electrolyte to prevent the corrosion of components [175].

In this study, we compared three different OER catalysts NiO, $NiFeO_x$, and $NiFeCoO_x$ for AEM water electrolysis. The effect of electrolytes was also studied by varying the concentration of KOH. Electrochemical impedance spectroscopy (EIS) was performed to investigate different resistances during the operation of the electrolyzer. In addition, two different membranes (Fumasep FAA-3-50 and Sustainion dioxide membrane X-37-50 grade T) were compared. EIS with the equivalent circuit fitting was performed to evaluate the reason for different performances under similar conditions. The catalyst performance for the electrolysis was in the order of $NiFeCoO_x$ > $NiFeO_x$ > NiO. Unlike other studies performed on these catalysts at lower current densities and in three-electrode systems, this work evaluated the catalyst at higher current densities in the AEM water electrolyzer. EIS was also measured at higher temperatures and high current densities in AEM electrolysis which are not always included in AEM electrolysis literature.

4.2 Experimental

4.2.1 Synthesis of Catalyst

The $NiFeCoO_x$ catalyst was synthesized by the coprecipitation method at room temperature. $Ni(NO_3)_2.6H_2O$, $Co(NO_3)_2.6H_2O$, and $Fe(NO_3)_3.9H_2O$ were used as a precursor of Ni, Co, and Fe, respectively. The mole fraction of Ni, Co, and Fe were 0.648, 0.324, and 0.027, respectively. Precursors were dissolved in water and kept at 25 °C. The precipitation step was carried out by

adding 1 M NaOH dropwise for 1 h until precipitation stopped. After the precipitation, the suspension was stirred for 2 h, and the catalyst suspension was centrifuged to get the solid catalyst. The solids obtained after centrifuging were washed with plenty of water to remove excess NaOH. The solid obtained after washing was dried in an oven overnight and then calcined/annealed in the furnace at 300 °C for 5 h to convert the catalyst into oxide form. $NiFeO_x$ catalyst was also developed by the same method with Ni and Fe mole fractions of 0.85 and 0.15. All the chemicals used in the synthesis were from Sigma Aldrich, Saint Louis, MI, USA.

4.2.2 Preparation of the Membrane Electrode Assembly

NiO, $NiFeO_x$, and $NiFeCoO_x$ catalysts were deposited on the nickel foam (thickness 1.7 mm), which is used as the anode. The catalyst slurry was made by dispersing 100 mg of catalyst in water and Nafion solution (Nafion™ 1100 W from Sigma Aldrich), an additional amount of water was added dropwise using a micropipette to get the proper consistency, and the Nafion content was 10 wt.% of the catalyst amount. The slurry was sonicated for 30 minutes to remove any agglomeration of particles. The catalyst slurry was then pasted on the surface of nickel foam and hot pressed to get the catalyst-coated gas diffusion electrode (GDE). The catalyst loading at the anode was 25 mg cm^{-2} for all electrolyzer testing and the final thickness of the electrode was 785 μm. Figure 4.1a, b shows nickel foam which is a gas diffusion layer (GDL) at the anode side, and carbon paper coated with Pt/C catalyst which is used at the cathode side. Nickel foam coated with the catalyst and AEM on top of carbon paper is shown in Figure 4.1c, d. The dimensions of the GDLs are 1.8 cm × 1.8 cm. Figure 4.2a, b shows the Membrane electrode assembly (MEA) from the cathode side and anode side, with AEM sandwiched in between them.

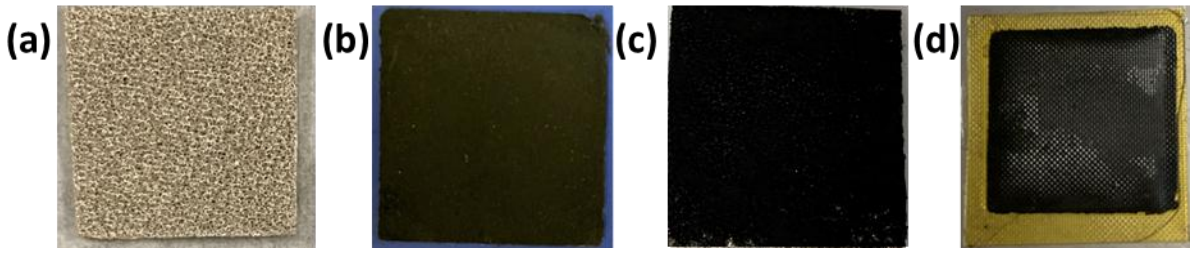


Figure 4.1. (a) Nickel foam (b) carbon paper coated with Pt/C catalyst, (c) Nickel foam anode coated with $NiFeCoO_x$ catalyst and (d) AEM with carbon paper cathode attached on one side. The dimensions of the electrodes were 1.8 cm × 1.8 cm.

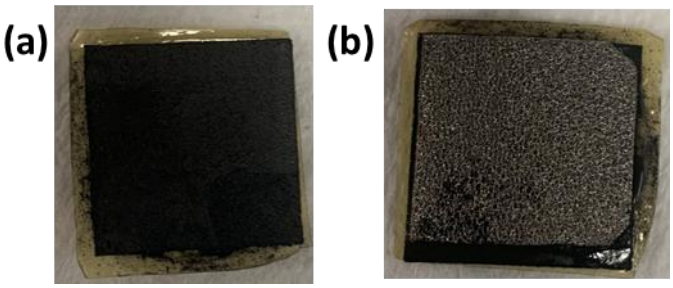


Figure 4.2. MEA after the electrolysis operation (a) MEA with cathode side (carbon paper) on top and (b) MEA with anode side (nickel foam) on top. The dimensions of the electrodes were 1.8 cm × 1.8 cm.

4.2.3 AEM Electrolyzer Single-Cell Tests

Half-cell reactions at the anode and cathode are shown in Equations (1) and (2), and the overall reaction in AEM electrolyzer is shown in Equation (3). The theoretical voltage required to split water is 1.23 V, in practical cases, it is higher than 1.23 V due to the overpotential of these reactions at the anode and cathode.

Figure 4.3 shows a schematic of the AEM electrolyzer, in which the anode and cathode are separated by a thin polymeric AEM. In this work, the KOH aqueous solution is circulated from the anode side only. The reduction of water takes place at the cathode to form hydrogen, the OH^- transports through the AEM and oxidizes to give O_2 at the anode.

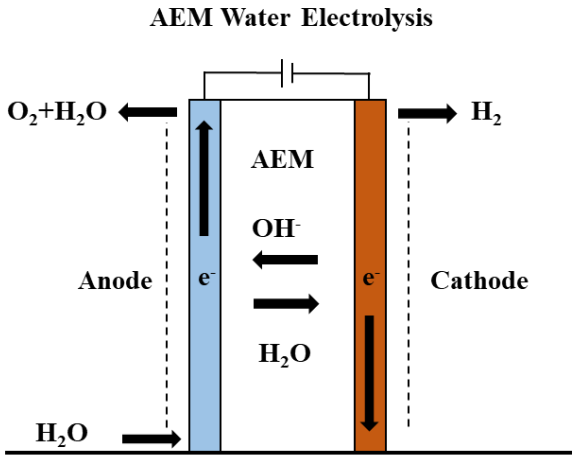


Figure 4.3. AEM electrolyzer configuration with AEM transporting the OH^- to the anode.

Anode $4OH^- \rightarrow O_2 + 2H_2O + 4e^-$ E = 0.401 V

Cathode $4H_2O + 4e^- \rightarrow 2H_2 + 4OH^-$ E = −0.829 V

Overall $2H_2O \rightarrow 2H_2 + O_2$ E = 1.23 V

4.3 Results

The morphology of the catalyst coating and nickel foams was performed by scanning electron microscope (SEM, Leo 1550, Zeiss, Jena, Germany). The morphology of nickel foam which acts as a GDL at the anode was analyzed by SEM. Figure 4.4a, b shows nickel foam before it was coated with the catalyst layer. The pore size was in the range of 100 to 500 µm. Figure 4.4c shows nickel foam coated with $NiFeCoO_x$ catalyst; the catalyst layer was pressed with nickel foam to get a compact layer of catalyst on top of the nickel foam. From SEM it was observed that the catalyst layer completely covered the nickel foam. There were some cracks in the catalyst layer which were due to the high loading of the catalyst. Figure 4.4d shows the cross-sectional image of a catalyst-coated nickel foam gas diffusion electrode (GDE), the overall thickness of GDE was 785 µm.

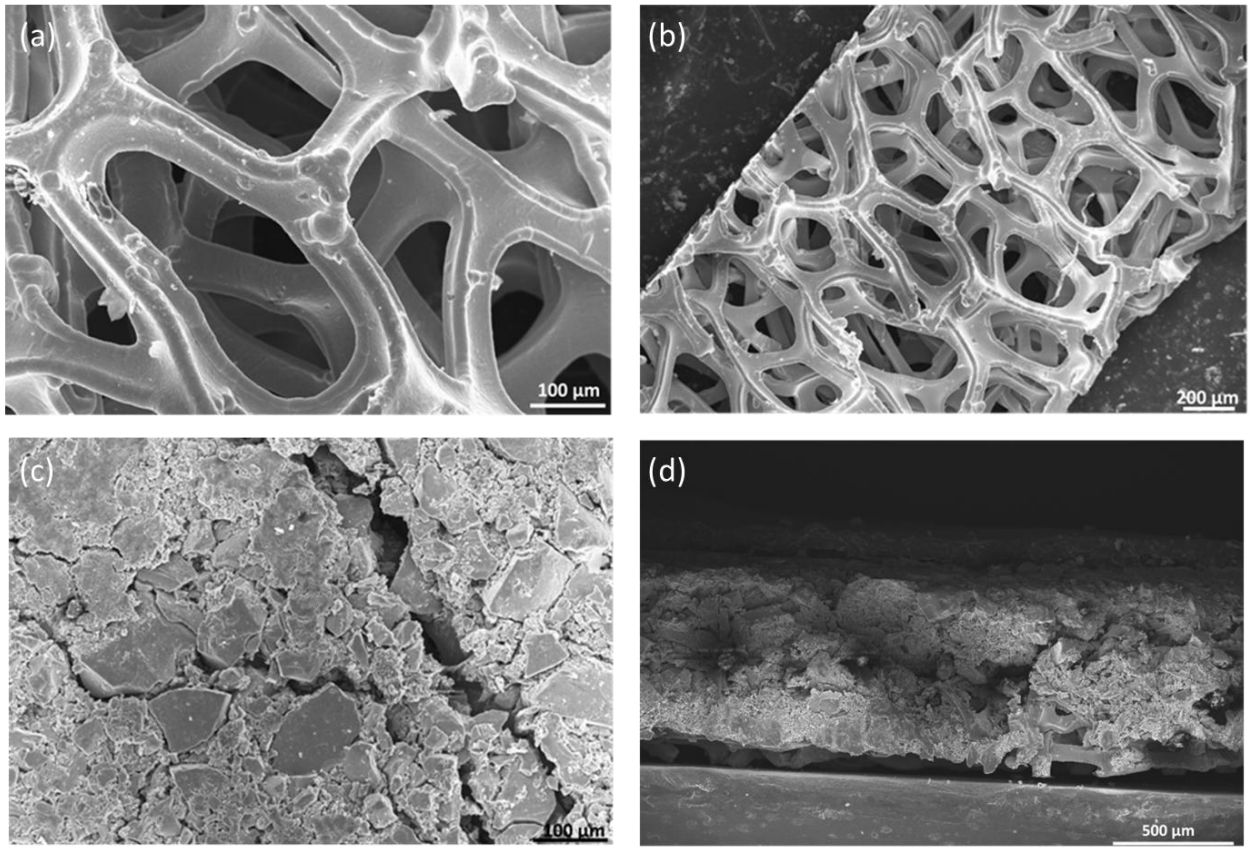


Figure 4.4. SEM images of (a,b) Nickel Foam without catalyst (c) $NiFeCoO_x$ coated on nickel foam and (d) Cross-section image of nickel foam coated with $NiFeCoO_x$ catalyst.

X-ray diffraction studies were performed (Rigaku Miniflex 600) using Cu-Kα radiation (λ = 1.54184 Å). Catalysts were analyzed by XRD, commercial NiO and $NiFeO_x$ (15% Fe) show mainly NiO phase with five distinct peaks at 2θ which are at 37.36, 43.36, 60, 75.54 and 79.56, which are assigned to (111), (200), (220), (311) and (222), respectively. All peaks are indexed to NiO (JCPDS card no. 78-0643) as shown in Figure 4.5. The dashed lines are the corresponding JCPDS standard. NiO has a rock salt structure with a lattice constant of 4.17 Å. Due to the low concentration of Fe in the $NiFeO_x$ catalyst peaks related to $NiFe_2O_4$ or Fe_2O_3 were not observed. The XRD of $NiFeCoO_x$ catalyst which has 2.7 wt.% Fe and Ni to Co molar ratio of 2:1, showed $NiCo_2O_4$ spinel crystal structure with a most intense peak at 2θ 36.8 assigned to (311), all peaks are indexed to $NiCo_2O_4$ (JCPDS card no. 20-0781).

Equation 4.1 is the Scherrer-Debye equation, which is used to calculate the crystallite size, where λ is the wavelength of the X-ray, β is the full width at half Maximum (FWHM) peak intensity in radian, and θ is the diffraction angle and k is the Scherrer's constant, which is 0.94 for crystalline nanoparticles. The calculated crystallite sizes for NiO, $NiFeO_x$, and $NiFeCoO_x$ were 17, 4, and 6 nm, respectively.

$$D = \frac{k\lambda}{\beta \cos\theta} \qquad \text{Equation 4.1}$$

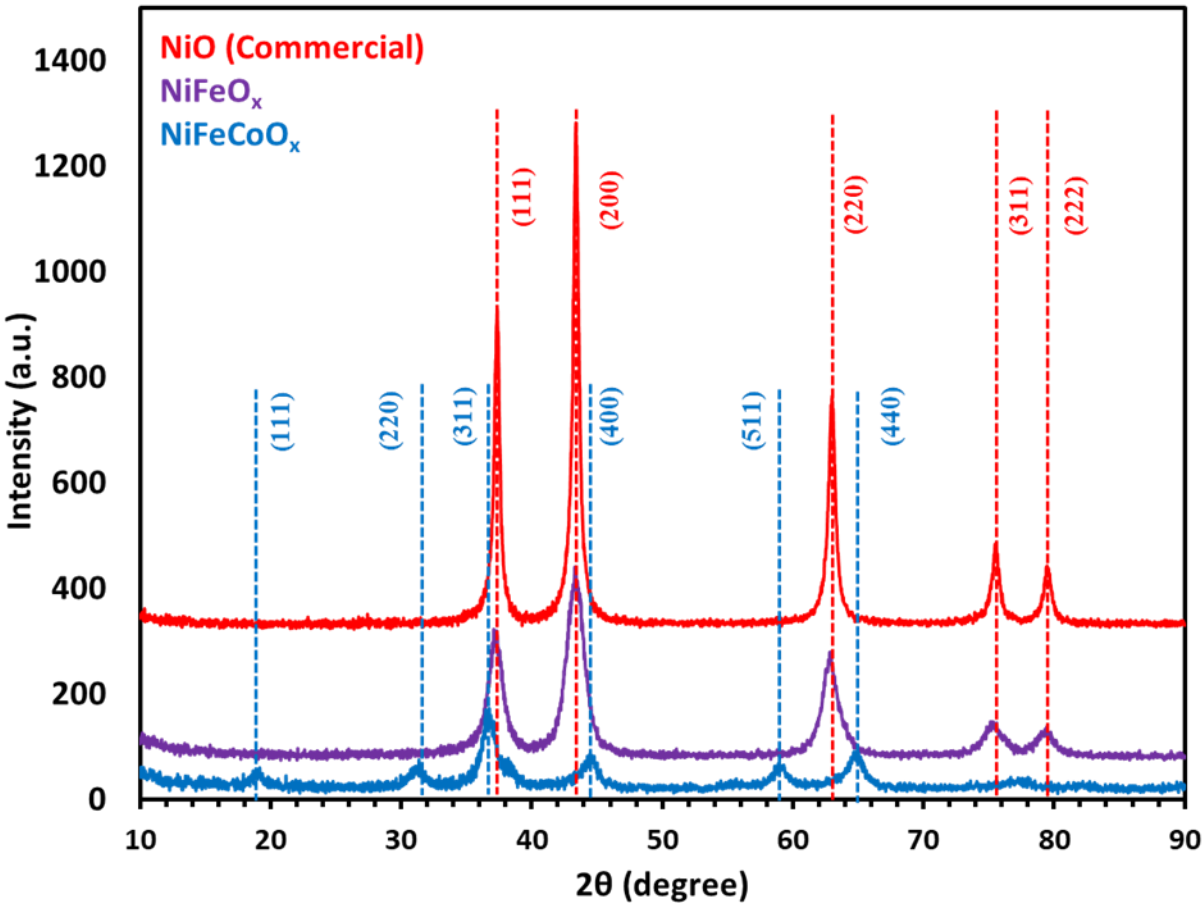


Figure 4.5. XRD of $NiFeO_x$, $NiFeCoO_x$ catalyst calcined at 300°C, commercial NiO is for reference.

4.3.1 Water Electrolysis over NiO, $NiFeO_x$ and $NiFeCoO_x$.

Three different OER catalysts, commercial NiO, lab-made $NiFeO_x$, and $NiFeCoO_x$ were tested for AEM water electrolysis operation with Pt/C catalyst for the HER at the cathode. The polarization curve was taken at a temperature range of 45 °C to 70 °C. LSV was used as a preferred method to evaluate the activity of the catalyst.

$NiFeCoO_x$ showed the highest activity among all the catalysts tested, the catalyst showed a current density of 802 mA cm^{-2} at 2 V with the temperature of the electrolyte and the electrolyzer at 70 °C.

Figure 4.6 shows polarization curves using $NiFeCoO_x$, at 70 °C when the voltage was further increased to 2.2 V, the current density increased to 1100 mA cm^{-2}, which is an enhancement of about 37% in current density. The current density also increased with the increase in electrolyte temperature, for electrolysis operation at 45 °C and 55 °C at 2 V. The current density was 532 and 656 mA cm^{-2}, which increased to 802 mA cm^{-2} at 70 °C, which is an increase of 53% and 22% in the current density. The increase in temperature decreases the overpotential at the cathode and anode side for OER and hydrogen evolution reaction (HER). Moreover, the conductivity of the electrolyte also increases with the temperature and improves the overall activity of the electrolysis [19]. In another study, electrolysis performance was evaluated from 30 °C to 50 °C, at the current density of 470 mA cm^{-2}. The electrolyzer potential decreased with the increase in temperature [72]. The effect of temperature was also investigated with a novel integrated inorganic membrane electrode assembly at the temperature range of 50–70 °C, the performance of the electrolyzer improves with the increase in temperature. The enhancement in the performance was mainly due to the higher conductivity of OH^- and the reduction in the overpotential of the catalyst [176].

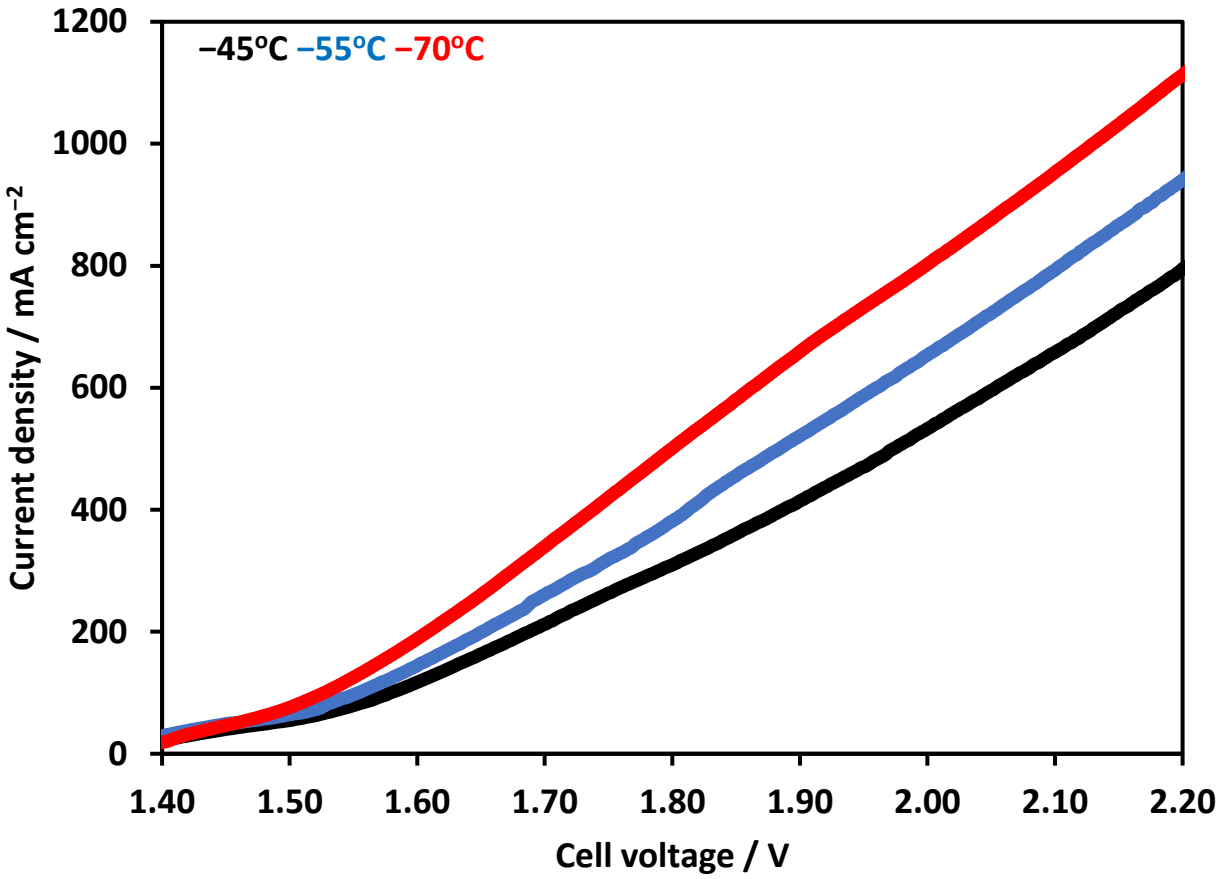


Figure 4.6. Linear Sweep Voltammetry at a temperature range of 45 to 70°C. Pt/C was used at the cathode and synthesized $NiFeCoO_x$ was used at the anode. FAA-3-50 membrane with a thickness of 50 µm was used in the electrolysis operation.

Chronoamperometry was used to analyze the activity of the catalyst at constant voltage for a fixed time. Figure 4.7 shows the chronoamperometry at 70 °C. The voltage increased from 1.5 V to 2.2 V with a time step of 60 s. The electrolysis operation was stable during the analysis and had minimum current fluctuations at the fixed voltage. At 2.2 V the maximum current density was 1140 mA cm^{-2}.

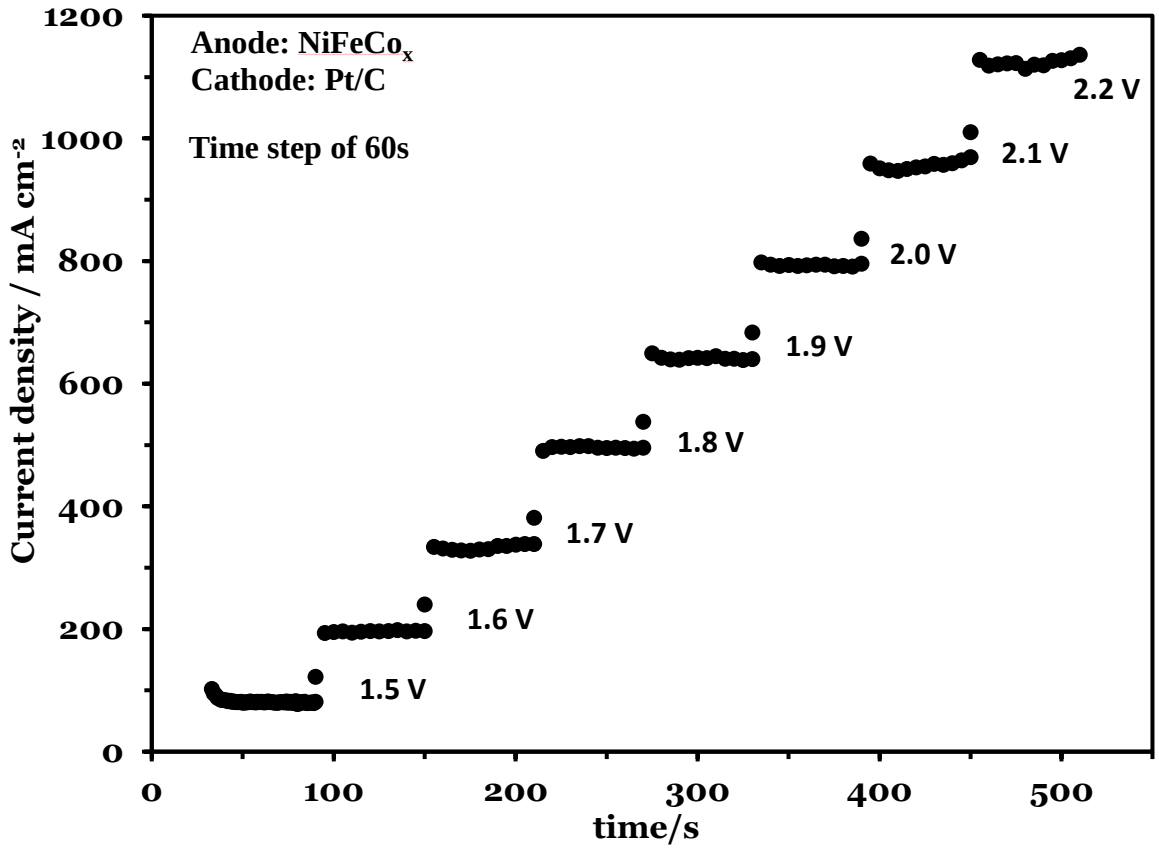


Figure 4.7. Chronoamperometry at a voltage range of 1.5 to 2.2 V, Pt/C was used at the cathode and $NiFeCoO_x$ was used at the anode.

Figure 4.8 shows the LSV of NiO, $NiFeO_x$, and $NiFeCoO_x$ catalysts at 70 °C using 1 M KOH electrolyte. $NiFeCoO_x$ had a higher current density followed by $NiFeO_x$ and NiO, the current density with $NiFeO_x$ catalyst was 551 and with NiO was 509 mA cm^{-2}. When comparing the performance of NiO and $NiFeO_x$, there was not much enhancement due to the addition of Fe in the $NiFeO_x$ catalyst. In this study, a relatively high loading of Fe was used which might have decreased the performance of the $NiFeO_x$ catalyst. NiFe-based catalysts are reported to have higher catalytic activity in basic electrolyte medium [177,178]. Nickel is proposed to be an active site for OER and

Fe is considered to improve the conductivity of the catalyst. In other research works, the addition of Fe is linked to stabilize Ni in Ni^{2+} form [179].

Emily Cossar et al. studied the AEM water electrolysis performance over Ni-Fe nanoparticles as anodes using 1 M KOH, $Ni_{0.9}Fe_{0.1}$ showed the cell voltage of 1.72 V at 0.8 A cm^{-2}. $Ni_{0.80}Fe_{0.1}$ with 10% CeO_2 had a voltage of 1.67 V with 0.4 A cm^{-2} using 0.1 M KOH. In durability testing, $Ni_{0.9}Fe_{0.1}$ showed stability of 12 h at 0.5 A cm^{-2} [156]. In another study, NiFe bimetallic anodes were fabricated using the magnetron sputtering technique. The work showed the enhancement in electrochemical activity with the addition of Fe to Ni-based catalysts. The highest performance was on Ni/Fe catalyst with an atomic ratio of 10/1, on that catalyst at 2 V the current density was 0.6 A cm^{-2} and 0.4 A cm^{-2} at 60 °C and 40 °C, respectively [157]. Dongyu Xu et al. synthesized transition metal (oxy) hydroxide for OER and tested it in the AEM electrolyzer. Among the catalysts $NiCoO_x$:Fe showed the highest activity with a current density of 900 mA cm^{-2} at 2.4 V [161]. The catalyst was designed to be oxyhydroxide because the active sites for OER are proposed to be transition metal oxyhydroxide.

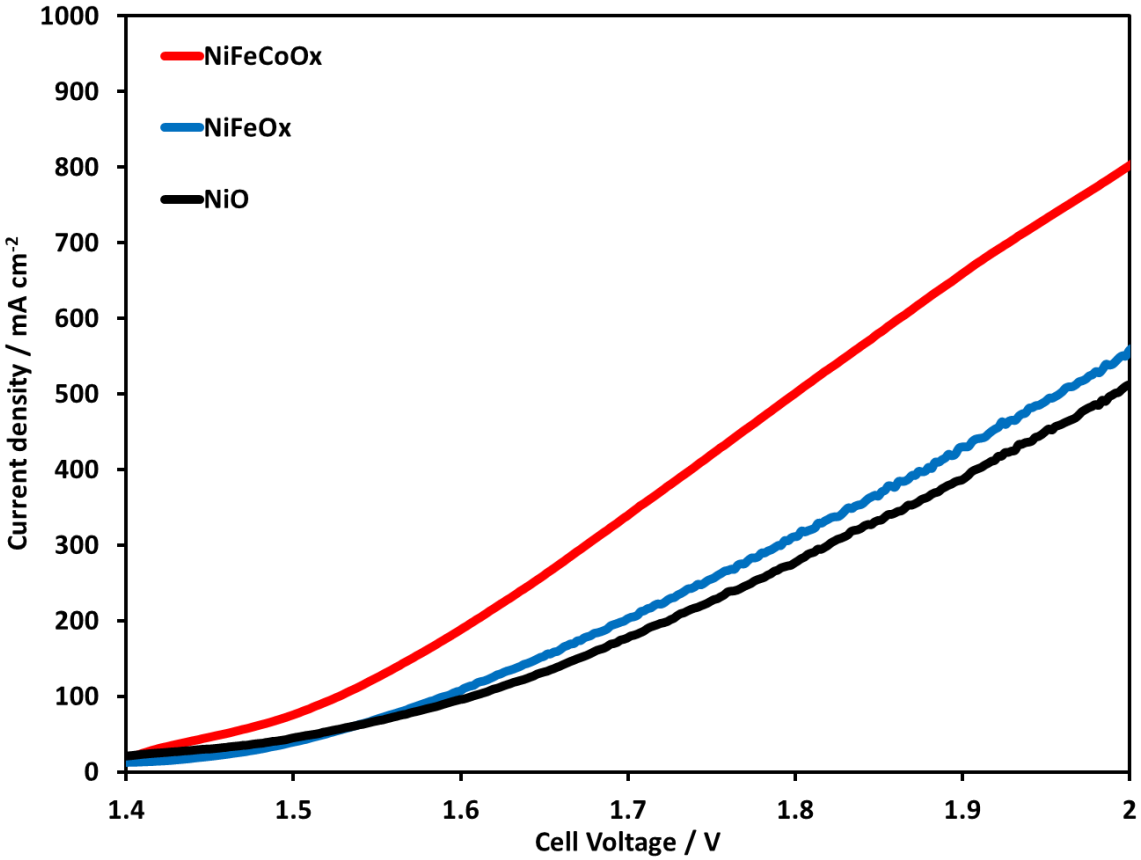


Figure 4.8. Linear Sweep Voltammetry at the temperature of 70°C. Pt/C was used at the cathode and NiO, $NiFeO_x$, and $NiFeCoO_x$ were used at anode. FAA-3-50 membrane with a thickness of 50 µm was used in the electrolysis operation.

EIS measurements were carried out to get the impedance of the electrolyzer cell during the operation. Potentiostatic EIS was performed at the voltage range of 1.7 V to 2 V, with a frequency range of 100 kHz to 100 mHz, the data was analyzed by Nyquist plots and equivalent circuit fitting. Figure 4.9 shows the Nyquist plot for electrolysis operation performed at 1.7 V at two different temperatures of 45 °C and 70 °C. The first x-intercept is at a high-frequency region and shows the ohmic resistance (R_{ohm}), the second intercept at the *x*-axis subtracted by the first intercept gives the activation resistance (R_{act}). As can be seen in Figure 4.9, the diameter of the semicircle for the Nyquist plot at 45 °C is higher which shows that there is higher activation resistance at this temperature compared to 70 °C operation. To further evaluate the contribution of different

components to the resistance, the equivalent circuit fitting is performed. The circuit given in Figure 4.9 shows the whole electrolyzer element, where L is the inductance due to the wires, R1 is the ionic resistance due to the AEM, R2, and R3 are the activation resistance due to the anode and cathode, respectively. Q1 and Q2 at anode and cathode are the constant phase element (CPE) and are used to simulate resistors, capacitors, and inductors, and capture the effects of surface roughness, porosity, reactivity, and surface inhomogeneity that are due to the electrical double layer [180]. EC-Lab software was used to fit the Nyquist plot with randomized simplex method and the results are given in Table 4.1.

Equivalent circuit results are tabulated in Table 4.1. As the electrolyzer was operated at a higher temperature of 70 °C, the ohmic resistance decreased from 0.125 to 0.105 Ω. This was mainly due to the increase in the conductivity of OH^- at higher temperatures, which also resulted in a decrease in membrane resistance. The ohmic losses are due to the resistance in the flow of electrons from different components of the electrolyzer, such as the anode, cathode, and membrane.

The total activation resistance at the anode and cathode were also evaluated using equivalent circuit fitting. With the increase in temperature, the total activation resistance at both electrodes decreased from 0.186 to 0.116 Ω. This is mainly due to the improvement of reaction kinetics of OER and improved conductivity of OH^- with the increase in temperature. The membrane resistance also decreased with the increase in temperature and there was a reduction of about 33%, when the temperature was increased from 45 to 70 °C. One of the reasons for the decrease in ohmic resistance is the decrease in the membrane resistance with the temperature. It was reported that the membrane resistance decreased from 75.3 to 52.5 $m\Omega.cm^2$ for polycarbazole-based anion exchange membrane (QPC-TM) [181].

The EIS measurement at a voltage of 1.9 V was performed by Immanuel Vincent et al., the ohmic resistance was reported to decrease with the increase in temperature. The reported ohmic resistance at 1.9 V was 17.8, 16, 15.8, and 15.6 mΩ at 30, 40, 50, and 60°C [182]. In PEM electrolysis, an increase in temperature is also reported to decrease the ohmic contact, one of the reasons being the thermal expansion of the components which causes the decrease in interfacial contact resistance [183,184]. The interfacial contact resistance decreases with the thermal expansion due to the increased compression pressure in the PEM electrolyzer [185].

Table 4.1. Resistances evaluated from equivalent circuit fitting.

Resistance	Temperature	
	45°C	70°C
R_{ohm}	0.125	0.105
$R_{membrane}$	0.102	0.068
R_{anode}+ $R_{cathode}$	0.186	0.116

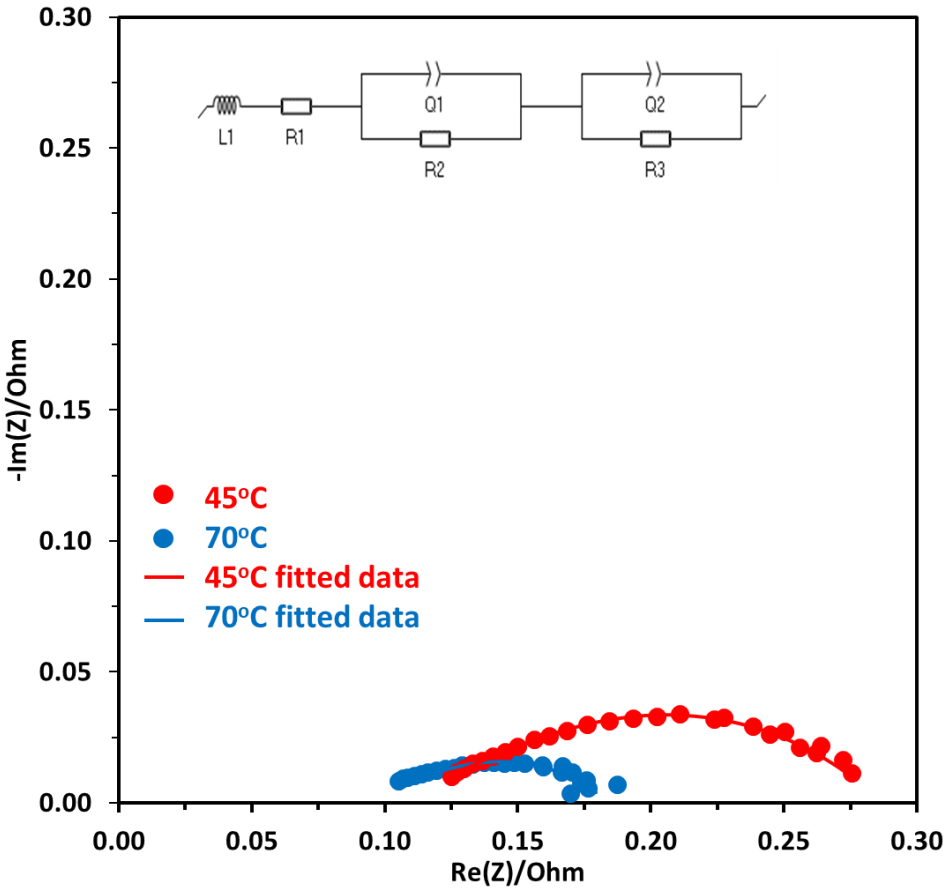


Figure 4.9. Nyquist plot at a constant voltage of 1.7 V at two different temperatures of 45°C and 70°C, Pt/C was used at the cathode and $NiFeCoO_x$ was used at the anode.

4.3.2 Effect of Electrolyte Concentration

The concentration of the electrolyte is an important parameter that needs to be understood in detail to optimize the electrolysis conditions. It is desirable to operate the electrolyzer at low electrolyte concentrations or only with water. However, using only water or using low concentrations of electrolyte can significantly affect the performance of the electrolyzer, due to the decreased conductivity of OH^- ions.

In this work, the electrolyzer was tested at three different concentrations of KOH. The molarity of KOH was 0.01, 0.1, and 1 M used in this study, all other parameters were the same as mentioned earlier. Briefly, 25 mg/cm^2 $NiFeCoO_x$ catalyst at the anode side and 1 mg_{Pt}/cm^2 Pt/C were used at

the cathode, the anion membrane was 50 µm Faumsep FAA-3-50. Figure 4.10 shows the LSV curves, the highest activity was achieved when 1 M KOH was used, and the electrolyzer reached the current density of 951, 681, and 513 mA cm^{-2} for 1 M, 0.1 M, and 0.01 M electrolyte at 2.1 V. The current density increased to about 39% when electrolyte concentration increased from 0.01 M to 0.1 M, and there was an increase of 85% in current density when KOH concentration increased from 0.01 to 1 M. It was also observed that at 0.01 M concentration, the polarization curve did not remain linear after 1.9 V and slightly bent downwards. This is the indication that at a higher voltage, more OH^- is required for the OER, but due to the lower concentration of OH^-, the current density did not remain linear and started to decrease. This trend was not observed for 0.1 M and 1 M concentration electrolyzer performance. Electrolysis with DI water has shown lower current density compared with other results obtained with KOH, the highest current density achieved was 254 mA cm^{-2} at 2.1 V. At 2.3 V, which is considered high for electrolysis, the current density was 400 mA cm^{-2}.

An increase in pH is reported to improve the conductivity of AEM, which reduces the ohmic resistance and increases the activity of AEM water electrolysis operations [86]. Higher pH is reported to decrease the overpotential of the reaction. At lower concentrations of KOH, there is a lower number of OH^- available, which causes slower reaction kinetics of OER [19]. In other research works, DI water was used in AEM electrolyzer with a current density of 399 mA cm^{-2} at 1.8 V [175].

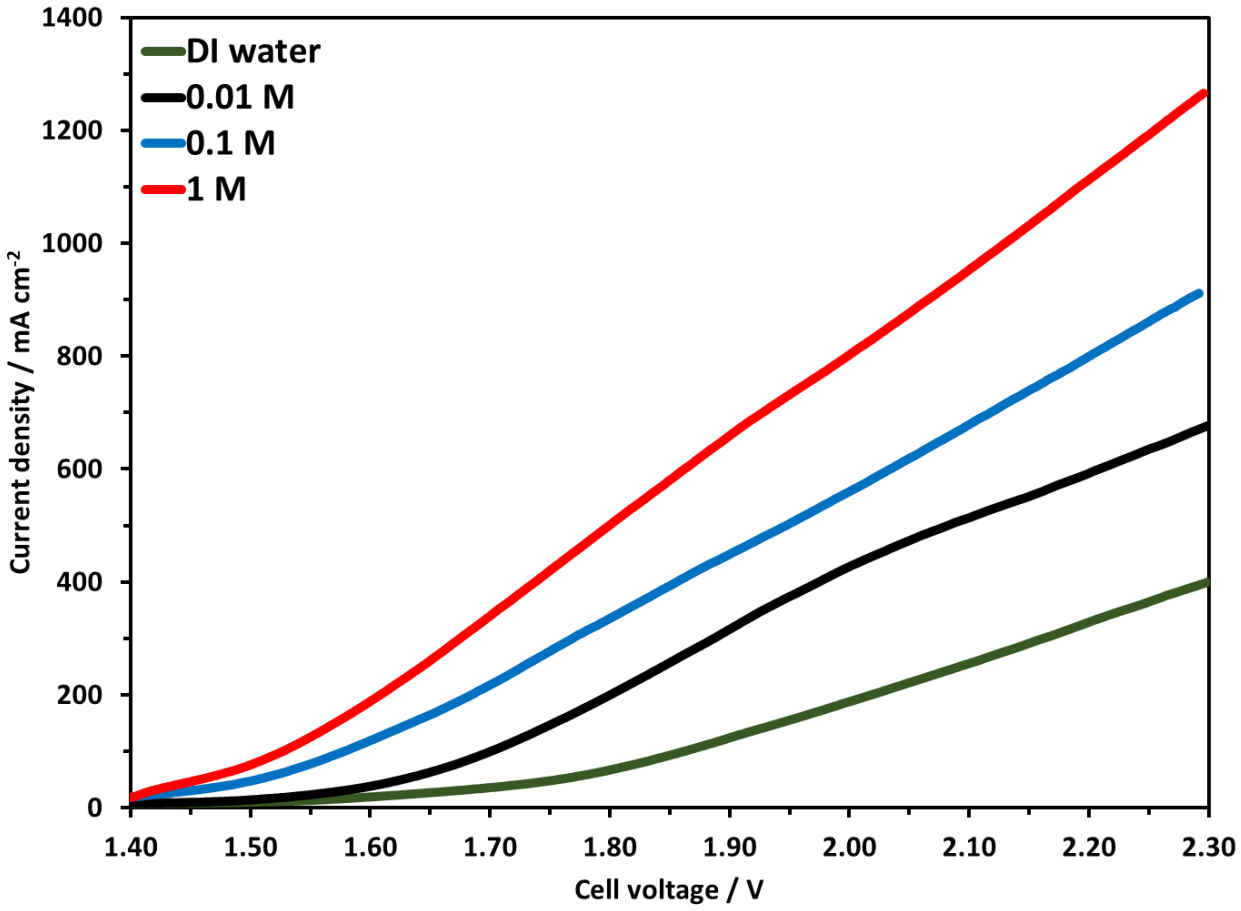


Figure 4.10. Linear Sweep Voltammetry at a temperature of 70°C with 0.01 M to 1 M KOH concentration. Pt/C was used at the cathode and $NiFeCoO_x$ was used at the anode.

Nyquist plot for KOH concentration of 0.01 M to 1 M and DI water are shown in Figure 4.11a, b. The EIS was performed at 2 V and 70°C for all electrolyte concentrations. There is a big difference between the DI water Nyquist plot, which has a higher x-intercept and a bigger diameter, which are indicative of ohmic resistance and activation resistance, respectively. The ohmic resistance for DI water-fed electrolyzer was very high at 0.56 Ω. For the KOH-fed electrolyzer, the ohmic resistance decreased with the increase in concentration. Lower ohmic resistance with increased KOH concentration was due to the increased conductivity of the anion exchange membrane.

For comparison, the ohmic resistance using 1 M KOH was 0.12 Ω, which was 4.66 times lower compared to the DI water-fed electrolyzer. For EIS measurement at 1.5 V, ohmic resistance is

reported to decrease from 170.4 to 18 mΩ, when the concentration of KOH increased from 0 to 1 M KOH [182]. The decrease in ohmic resistance was attributed to the increase in the conductivity of the membrane.

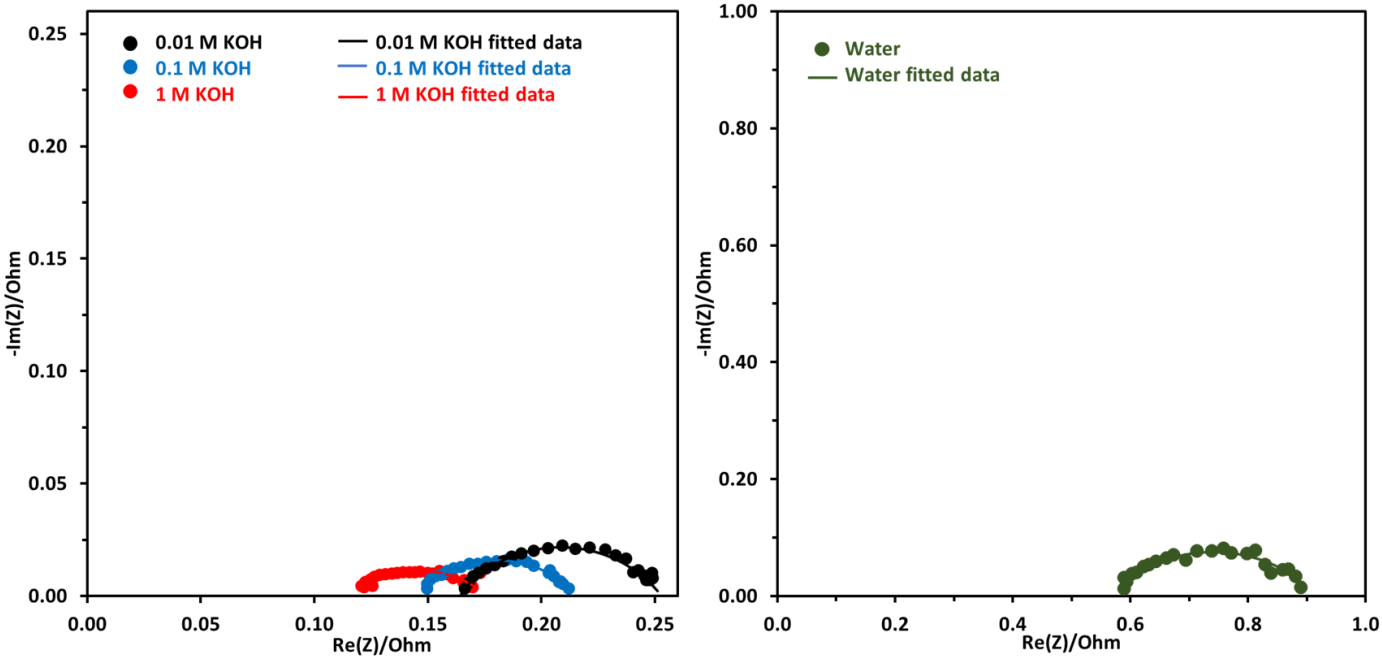


Figure 4.11. (a) Nyquist plot at a constant voltage of 2 V at 70°C, the concentration of electrolyte was from 0.01 M to 1 M. (b) Nyquist plot using DI water. Pt/C was used at the cathode and $NiFeCoO_x$ was used at the anode with FAA-3-50 membrane.

To evaluate individual resistances due to the components of the electrolyzer, equivalent circuit fitting was performed with the same circuit as discussed earlier. The results from the equivalent circuit fitting are shown in a bar graph in Figure 4.12. The Figure shows the activation resistance at the anode and cathode along with membrane resistance, the resistances as a function of electrolyte are shown along with DI water. In all cases, DI water shows the highest resistances at each component of the electrolyzer, followed by 0.01 M and 0.1 M KOH. These results showed that two main components that can control the activity of the electrolyzer are the anion exchange membrane and the anode catalyst. For the membrane, a lower thickness and higher conductivity

can reduce these resistances. For the resistance at the anode, where an oxygen evolution reaction takes place, there is still room for improving the OER catalyst to reduce the overpotential of the catalyst. Another trend that was observed was membrane resistance and activation resistance at the anode decreased with the increase in KOH concentration, but activation resistance at the cathode did not change much with the increase in KOH concentration.

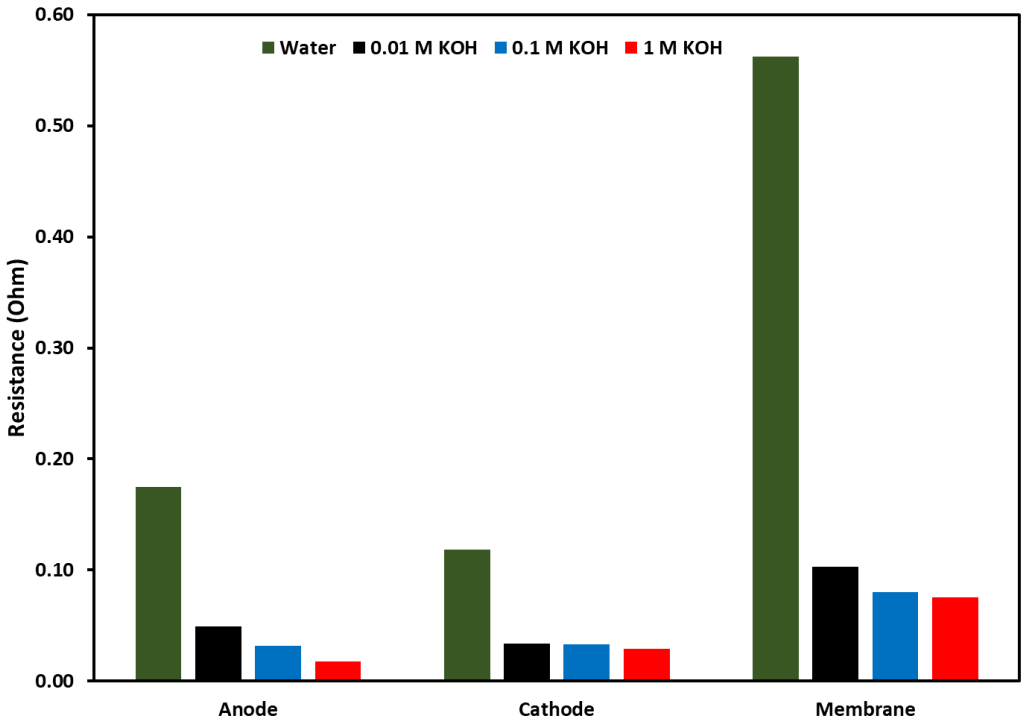


Figure 4.12. Comparison of resistances at anode, cathode, and membrane, the resistances were evaluated by using equivalent circuit fitting. The applied voltage was 2 V at 70°C.

4.3.3 Comparison of Anion Exchange Membranes

Commercially available membranes are widely used in AEM electrolysis research, which are Sustainion® 37-50 (dioxide membrane), Tokuyama A201, Fumasep® FAA-3, Orion™, and Aemion™. These AEM need to be pretreated because they are usually shipped in bromide and chloride forms. The AEM can be activated by keeping the membrane in the KOH solution for

about 24 to 48 h. Table 4.2 provides the properties of the commercially available membrane [59,186–190].

Table 4.2. Commercially available membranes and their properties [59,186–190].

Membrane	Thickness (μm)	Conductivity ($ms.cm^{-1}$)
Sustainion® 37-50 (dioxide membrane)	50	70
Fumasep® FAA-3	45-50	40-45
Fumasep® FAB-PK-130	110-140	42
Tokuyama A201	28	-
Aemion™	50	80
Orion™	50	60

Membranes from Fumatech, such as the FAA3 type, are polyaromatic polymers with ether bonds and quaternary ammonium groups present at the main chain. The reported electrolysis work with these membranes in the presence of a noble metal catalyst (Pt/C cathode and IrO_2 anode) showed the activity of 1.5 A cm^{-2} at 2 V with 1 M KOH at 50 °C [191]. The durability testing of the FAA3-40 membrane showed a lifetime of 31 h, due to poor mechanical stability caused by the excessive swelling of the membrane [19]. Whereas, the FAA3-50 membrane shows the stability of 1000 h, with the $NiMnO_x$ anode and Pt/C cathode catalyst [73]. Sustainion membranes X-37-50 from dioxide materials are based on 4-vinylbenzyl chloride-co-styrene [58,59,192]. The membranes take some water for crosslinking which reduces the swelling of the membrane during the electrolysis operation [59].

For the comparison of electrolyzer activity commercially available Dioxide membrane X-37-50 was used, and the MEA preparation method was similar as mentioned earlier. The operation was performed at three temperatures of 45, 55, and 70 °C as shown in Figure 4.13a–c. The X-37-50 MEA had a higher current density at each temperature compared to the FAA-3-50 membrane with the same thickness of 50 μm. At 2.2 V the current density for X-37-50 MEA was 1390, 1590, and 1815, for FAA-3-50 MEA it was 794, 937, and 1121 mA cm^{-2} at 45, 55, and 70 °C, respectively.

Higher activity could be correlated with the X-37-50 higher conductivity compared to the FAA-3-50 membrane.

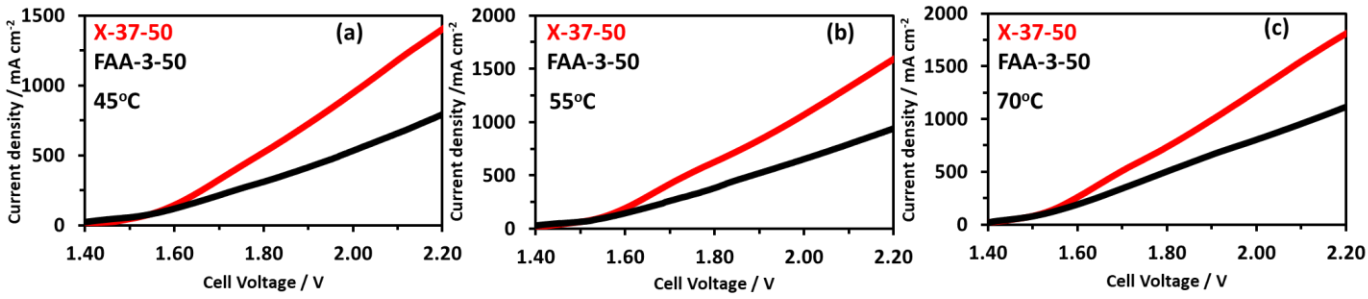


Figure 4.13. Comparison of electrolysis performance using X-37-50 and FAA-3-50 membranes at different temperatures using $NiFeCoO_x$ catalyst.

Figure 4.14 shows EIS results at 70 °C for both membrane electrode assemblies at 2 V. There is a big difference between both results. The ohmic resistance for the X-37-50 was 0.064 Ω and for FAA-3-50 it was 0.12 Ω. This shows that the conductivity of the X-37-50 is higher in similar conditions, higher conductivity decreases the resistance caused by the membrane. This also demonstrated that the X-37-50 membrane has better charge transfer ability between the catalyst layer and the membrane compared to FAA-3-50. The diameter of the semicircle which is indicative of activation resistance is also lower for X-37-50, the corresponding activation resistance was 0.037 and 0.054 Ω. These results showed that lower ohmic resistance and activation resistance resulted in higher performance for X-37-50.

There are a few studies where Sustainion X-37-50 is reported to be a better membrane in terms of stability and performance. Electrochemical impedance comparison at different membranes showed Sustainion® 37-50 had lower resistance compared to Fumasep® FAS-50, Fumasep® FAPW, AMI 7001, and Nafion 115. Sustainion® membrane had higher stability in the test with a degradation rate of $5\mu V.h^{-1}$ for 2000 h operation at a fixed current density of 1 A cm^{-2} [57]. Tokuyama A201

had a degradation rate of 150 µV.h^{-1} for 1000 h at 470 mA cm^{-2} [72], Fumapsep® FAA-3-50 had a degradation rate of 800 µV h^{-1} in 1000 h [73].

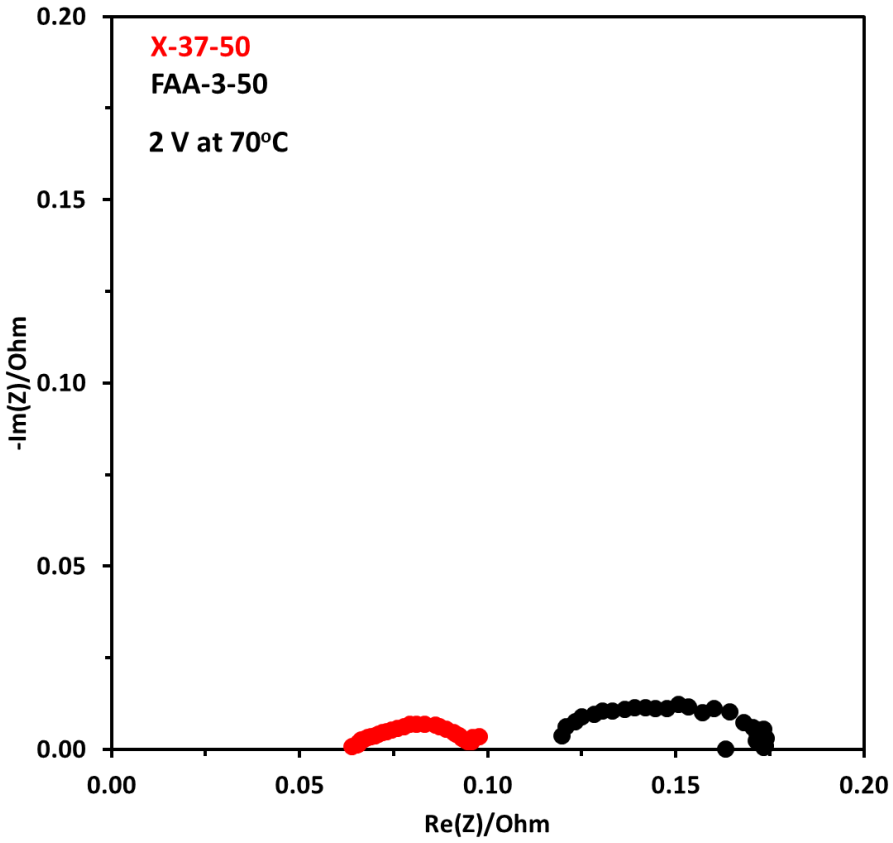


Figure 4.14. Nyquist plot at a constant voltage of 2 V at 70°C with FAA-3-50 and X-37-50 anion exchange membranes, the concentration of electrolyte was 1 M. Pt/C was used at the cathode and $NiFeCoO_x$ was used at the anode.

4.4 Conclusion

NiO, $NiFeO_x$, and $NiFeCoO_x$ catalysts were tested for AEM water electrolysis using Fumasep FAA-3-50 membrane, $NiFeCoO_x$ showed higher performance than other catalysts, due to the promotion effect of Co and Fe in Ni-based catalysts. The highest activity at 2 V with $NiFeCoO_x$ catalysts was 802 mA cm^{-2} at 70°C. The performance of the AEM electrolyzer was found to be highly dependent on the electrolyte concentration, the activity was 954 mA cm^{-2} at 2.1 V with 1 M KOH whereas with DI water it was 254 mA cm^{-2} at 70°C. EIS results showed that there is a

decrease in ohmic resistance with the increase in electrolyte concentration, mainly due to the increased conductivity of the membrane. The membrane conductivity increased due to more OH^- ions being available at higher concentrations of KOH. The activation resistance of the anode also decreased with the increase in electrolyte concentrations, which is due to the availability of more OH^- ions at higher pH, which improved the reaction kinetics of OER. A comparison of the FAA-3-50 and X-37-50 membranes, which have the same thickness of 50 μm showed higher AEM electrolyzer performance with the X-37-50 membrane. For comparison, the highest activity on FAA-3-50 and X-37-50 membrane was 1121 and 1815 mA cm^{-2} at 2.2 V, 70°C, which shows X-37-50 had 1.62 times higher current density at the same operating conditions. EIS results showed that the X-37-50 membrane had lower ohmic resistance than the FAA-3-50 membrane.

5 Investigation of $NiCoO_x$ Catalysts for Anion Exchange Membrane Water Electrolysis: Performance, Durability, and Efficiency Analysis

5.1 Introduction

Given the urgent need to shift away from fossil fuels and address the challenges of global warming and climate change, hydrogen is considered as a highly promising fuel option for the future [27]. It offers the potential to reduce carbon emissions and pollution associated with conventional fossil fuels. The electrolysis of water using Proton Exchange Membrane (PEM) electrolyzers is widely recognized as an efficient technology for producing hydrogen by utilizing renewable energy sources [26,169]. However, the use of expensive and scarce catalysts such as Iridium and Platinum, as well as Titanium construction materials due to the acidic environment, contributes to the high cost of hydrogen production in PEM electrolyzers [193].

Anion exchange membrane (AEM) water electrolyzer represents a new type of water electrolyzer with a polymeric AEM. These electrolyzers share a compact design similar to PEM electrolyzers, making them suitable alternatives [25]. One notable advantage of AEM water electrolyzers is the ability to utilize non-precious transition metal oxide catalysts due to the relative stability of these catalysts in a basic medium. This feature helps reduce the overall cost of the electrolyzer system [9].

One of the main components of an AEM water electrolyzer is the anion exchange membrane. The membrane is composed of a polymer backbone functionalized with anion exchange groups. In most cases, the ion exchange groups are quaternary ammonium salts [56,57]. The main role of the membrane is to transport hydroxyl ions from the cathode to the anode and to avoid the crossover

of hydrogen and oxygen gas. To be considered for a practical water electrolysis process AEM should have high conductivity, thermal and mechanical stability, impermeability to gases, and long-term durability [8]. Ionomers are the anion-functionalized groups that are used as binders for the catalyst at the electrodes. They also improve the conductivity of the membrane and facilitate the exchange of water and ions at the surface of the catalyst [194].

Dioxide membrane X-37-50 T from Sustainion® has been shown to have high conductivity and stability for AEM water electrolysis [58]. Commercial AEM dioxide X-37-50 T is composed of polytetrafluroethylene (PTFE) supported styrene and vinyl benzyl chloride co-polymers with imidazolium and pyridinium groups [190,195]. Quaternary ammonium groups are also utilized as functional groups in AEM due to their low cost, high conductivity, and easier to synthesize method [196–199]. Quaternary groups are relatively easier to degrade by nucleophilic substitution and Hofmann elimination reaction in alkaline conditions [200–202]. Imidazolium functional groups as present in dioxide membrane X-37-50 T are more stable than the quaternary ammonium groups due to their resonance structure [203,204]. In addition to AEM, highly KOH-doped ion solvation membranes based on polybenzimidazole (PBI) have also been considered for AEM electrolysis and short-term durability [205,206].

In AEM water electrolysis the presence of electrolytes such as KOH and NaOH increases the conductivity of the solution and reduces the corrosion of the catalyst [207]. Compared to PEM electrolyzer AEM water electrolyzer has been reported to have lower current density and energy efficiency due to the higher overpotential of oxygen evolution reaction (OER) catalysts [208]. Significant effort has been focused on the development of OER catalysts with low overpotentials [209]. To address this challenge, significant advancements have been made in the development of

oxygen-evolving anodes with low overpotentials. Platinum group metals such as IrO_2 and RuO_2 have been reported to have lower overpotentials [210,211].

$NiCo_2O_4$ is one of the favorable metal oxide materials for OER in alkaline medium, due to its high electrical conductivity, high number of catalytically active sites, and relatively lower cost compared to the IrO_2 and RuO_2 catalysts [127,212]. Co_3O_4 and $NiCo_2O_4$, have a spinel structure and are extensively studied as non-platinum catalysts due to their ability to exhibit comparable catalytic efficiency to platinum-based catalysts. These materials demonstrate enhanced stability, reduced corrosiveness, and high electrocatalytic activity, particularly in alkaline conditions [213–215]. The catalysts with a spinel structure, such as $NiCo_2O_4$, have received significant interest due to their favorable mixed metal valence states (Ni^{3+}/Ni^{2+} and Co^{3+}/Co^{2+}), which offer excellent redox active sites for OER [216]. This characteristic contributes to their high catalytic activity and stability, making them highly desirable for various applications. In the spinel structure Nickel occupies the octahedral sites and cobalt occupies the octahedral and tetrahedral sites [217]. Ni doping has been shown to enhance the activity of Co_3O_4 catalyst [122].

$NiCo_2O_4$ catalysts have been shown to have high activities in three-electrode systems, there are few studies for AEM water electrolysis on $NiCo_2O_4$ catalyst as OER catalyst. $NiCo_2O_4$ catalyst with hollow spherical morphology has been shown to have higher OER activity with a current density of 10 mA cm^{-2} at 1.63 V [218]. In AEM water electrolysis $NiCoO_x$:Fe at the anode showed good activity with a current density of 900 mA cm^{-2} at 2.39 V and 50°C in water using a Pt black cathode. It was reported that the catalyst performed better than IrO_x catalyst under similar conditions [161].

In this study, $NiCoO_x$ mixed metal oxide catalysts were synthesized using different Ni to Co ratios. The OER was performed using three electrode systems and complete water electrolysis was

performed using AEM electrolyzer. Electrochemical impedance spectroscopy (EIS) was performed to evaluate different resistances due to the electrolyzer components. Long-term and short-term durability testing was also performed using $NiCoO_x$ at the anode.

5.2 Experimental

5.2.1 Synthesis of $NiCoO_x$ catalysts

$NiCoO_x$ catalyst was synthesized by the coprecipitation method at room temperature. $Ni(NO_3)_2.6H_2O$ and $Co(NO_3)_2.6H_2O$ were used as a precursor of Ni and Co, respectively. The molar ratio of Ni and Co was varied to get a series of $NiCoO_x$ catalysts. The molar ratio of Ni:Co was changed from 1:1, 1:2, 1:3, 1:5, and 2:1, in addition, Co_3O_4 catalyst was also synthesized using the same synthesis method. Precursors were dissolved in water and kept at 25^{o}C. The precipitation step was carried out by adding 1 M NaOH dropwise for 1 h until precipitation stops. After the precipitation, the suspension was stirred for 2 h, and the catalyst suspension was centrifuged. The solid catalyst obtained after centrifuge was washed with water to remove excess NaOH. The solid obtained after washing was dried in an oven overnight and then calcined in the furnace at 300^{o}C to convert the catalyst into oxide form.

5.3 Results

Scanning electron microscopy (SEM, Leo 1550, Zeiss) was used to analyze the morphology of $NiCoO_x$ catalyst and nickel foam coated catalyst which acts as GDL at the anode. Figure 5.1a shows $NiCoO_x$ (1:3) which has a distinct flaky structure, this morphology has been observed in other studies [219]. Figure 5.1b shows a cross-sectional image of nickel foam coated with $NiCoO_x$ catalyst; a thin layer of catalyst was pressed on top of nickel foam to get a compact layer of catalyst on top of the nickel foam. It was observed that the catalyst layer completely covered the nickel foam from the top side and due to the higher loading of the catalyst, the particles also penetrated

inside the nickel foam, the catalyst particles reached about half the width of the nickel foam GDL. The overall thickness of Gas diffusion electrode (GDE) was 800 μm. The pore size of nickel foam was in the range of 100 to 500 μm. The ratio of Ni to Co in $NiCoO_x$ (1:3) catalysts was confirmed from the energy dispersive spectroscopy (EDS) spectrum as shown in Figure 5.1c. During SEM sample preparation gold was sputtered to improve the conductivity of the sample for the analysis. Au and Nb have similar characteristic X-ray energy for Lα, which are 2.120 and 2.166 keV. Due to that, the software picks up Nb instead of Au in the EDS analysis. Figures A5.1 to A5.5 in the appendix show the EDS spectrum of other catalysts in the series.

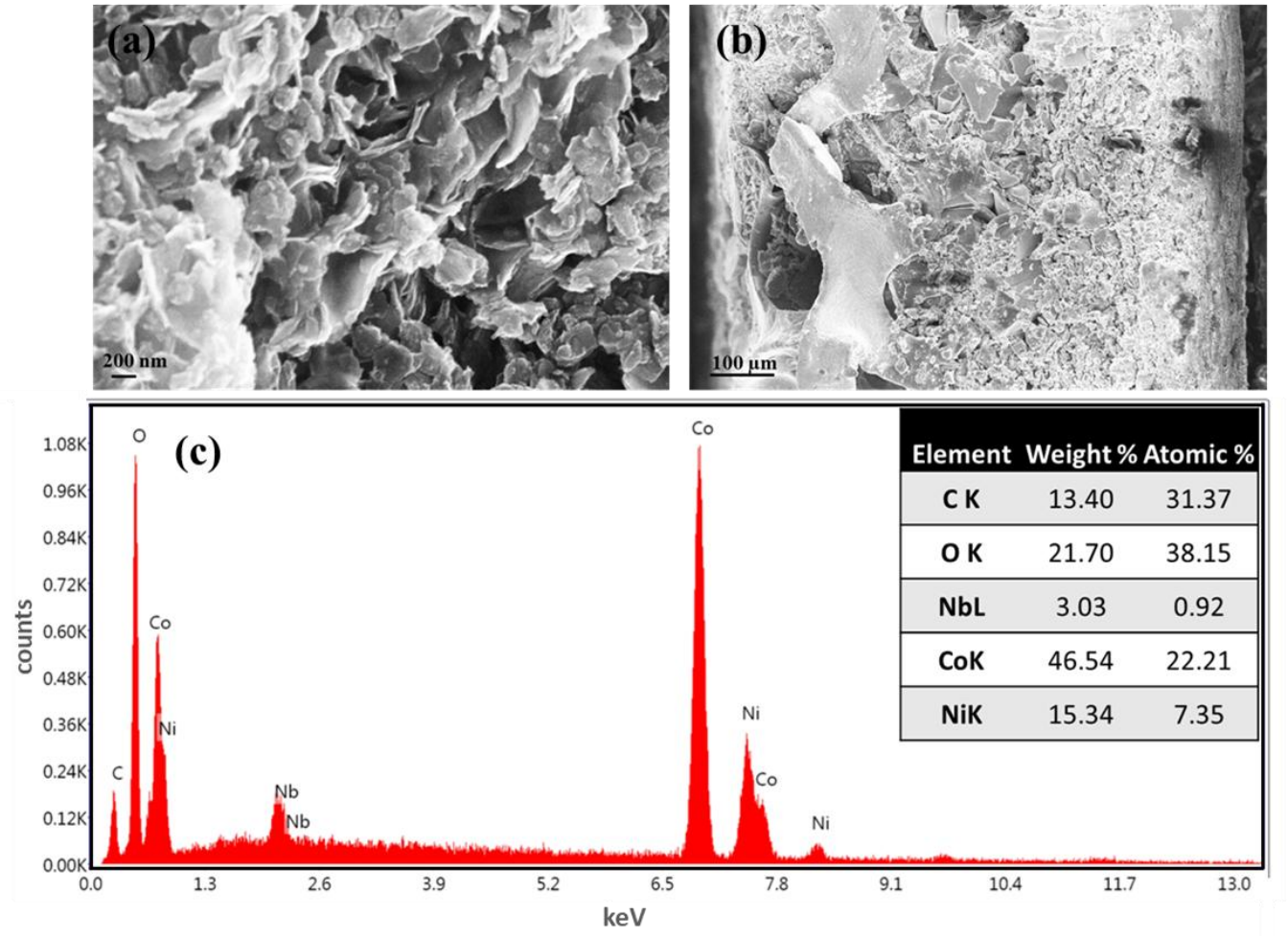


Figure 5.1. (a) SEM images of $NiCoO_x$ (1:3) catalyst (b) Cross-sectional image of nickel foam coated with $NiCoO_x$ (1:3) catalyst (c) EDS spectra of $NiCoO_x$ (1:3).

X-ray diffraction studies were performed on (Rigaku Miniflex 600) using Cu-Kα radiation (λ = 1.54184 Å). Commercial NiO shows mainly NiO phase with five distinct peaks at 2θ which are at 37.36, 43.8, 60, 75.54, and 79.56, which are assigned to (111), (200), (220), (311), and (222) respectively. All peaks are indexed to NiO (JCPDS card no. 78-0643) as shown in Figure 5.2.

The XRD of $NiCoO_x$ catalyst with Ni to Co molar ratio of 1:1, 1:2, 1:3,1:5 shows distinct XRD peaks which confirms $NiCo_2O_4$ spinel crystal structure with a most intense peak at 2θ 37 assigned to (311), all peaks are indexed to $NiCo_2O_4$ (JCPDS card no. 20-0781). No peak due to NiO was observed due to the lower Ni mole fraction in these catalysts. These catalysts are mixed metal oxide catalysts with varying proportions of $NiCo_2O_4$ and Co_3O_4. By stoichiometric ratio 1:2 is $NiCo_2O_4$ but other catalysts with 1:3, 1:5 have both $NiCo_2O_4$ and Co_3O_4 phases. The catalyst with 1:1 ratio, stoichiometrically contains $NiCo_2O_4$ and NiO. Although NiO peak was not observed for this catalyst, the intensity of peaks attributed to $NiCo_2O_4$ at 2θ 37, 45, and 56 decreased for this catalyst due to the presence of NiO. For catalysts with a higher ratio of Co there is a small peak at 2θ 38.6 assigned to (222) (JCPDS card no.74-1657), this peak confirms the presence of Co_3O_4.

The catalyst with 2:1 ratio shows broad peaks centered at 36.8 and 43.8, the broad peaks are due to the presence of both NiO and $NiCo_2O_4$ in the catalyst, and the broader peaks are formed by overlapping of NiO peak at 2θ 37.36 and $NiCo_2O_4$ peak at 2θ 36.8. The other peak also resulted due to the overlapping of NiO 2θ 43.8 and $NiCo_2O_4$ peak at 2θ 45 [220]. Due to the higher molar ratio of Ni, this catalyst had NiO and $NiCo_2O_4$ phases in the catalyst.

Scherrer-Debye equation was used to calculate the crystallite size of the catalyst, where λ is the wavelength of X-ray, β is the full width at half Maximum (FWHM) peak intensity in radian, and θ is the diffraction angle and k is the Scherrer's constant, which is 0.94 for crystalline nanoparticles

as shown in equation 5.1. The calculated crystallite sizes for $NiCoO_x$(1:3) catalyst were in the range of 3.5 to 4 nm.

$$D = \frac{k\lambda}{\beta \cos\theta}$$ Equation 5.1

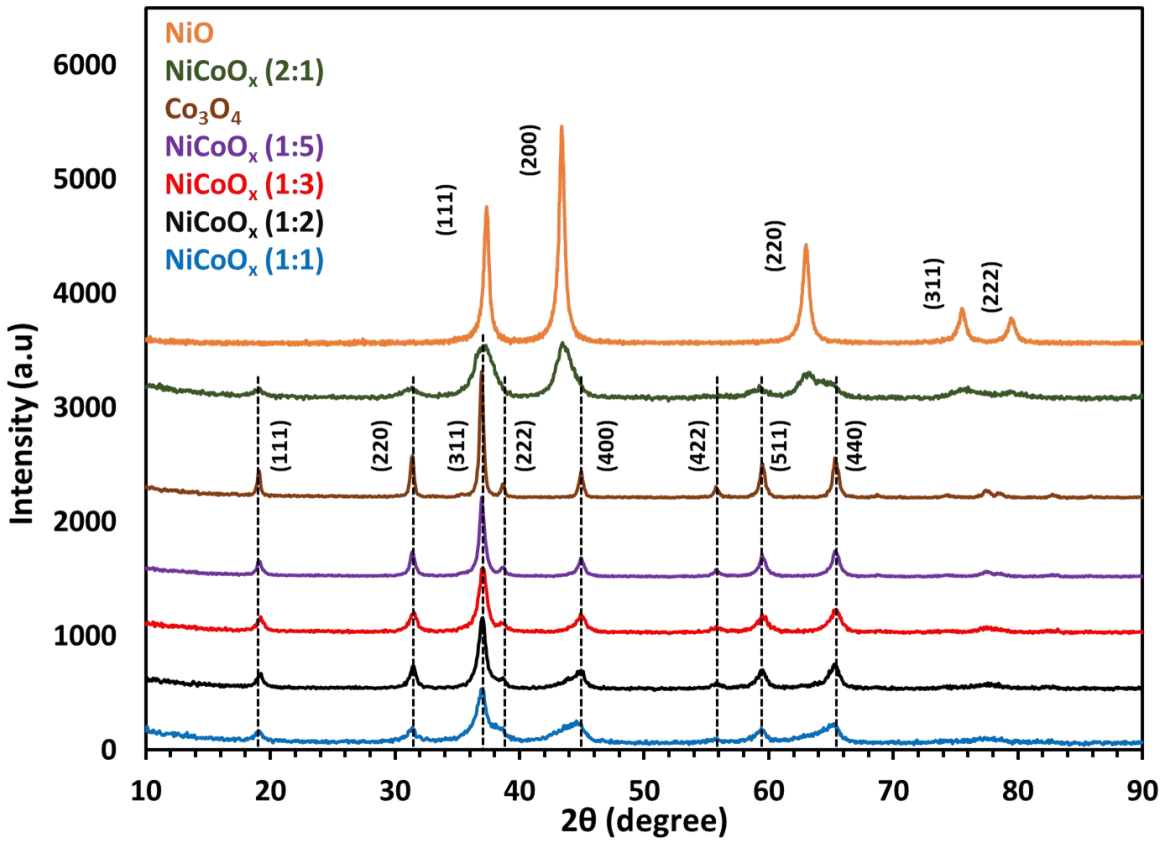


Figure 5.2. XRD of $NiCoO_x$ catalyst calcined at 300°C with different molar ratios of Ni to Co.

5.3.1 Catalyst Evaluation in three-electrode System

Linear sweep voltammetry was performed in 1M KOH to evaluate the catalytic activity of the $NiCoO_x$ catalyst coated on Nickel foam. $NiCoO_x$ (1:3) showed the highest catalytic activity with a current density of 238 mA cm^{-2} at 1.8 V, $NiCoO_x$ (2:1) showed the least activity with a current density of 67 mA cm^{-2} as shown in Figure 5.3a. There is a self-redox peak at 1.45 V (V vs RHE) which is indicative of Ni^{2+} to Ni^{3+} oxidation [153,154]. Short-term stability of the catalyst was

tested for 10 hours by chrono potentiometry at the current density of 10 to 100 mA cm^{-2}, at each current density the stability of the catalyst was tested for 1 h as shown in Figure 5.3b. The $NiCoO_x$ (1:1) and $NiCoO_x$ (1:3) catalysts exhibited the lowest overpotentials of 346 mV and 355 mV, respectively, at a current density of 10 mA cm^{-2}. At a higher current density of 100 mA cm^{-2} the same catalyst showed an overpotential of 776 mV and 760 mV. During this stability testing, the catalyst was stable at each current density and the activity did not decrease.

To compare the activity of the catalyst Tafel plots were used as shown in Figure 5.3c. $NiCoO_x$ (1:3) has the least Tafel slope of 79 mV/dec whereas $NiCoO_x$ (1:1) exhibits the Tafel slope of 101 mV/dec. A smaller Tafel slope is indicative of faster reaction kinetics of the reaction on the catalyst. In other words, a lower Tafel slope shows that the catalyst offers lower overpotential for higher current density. Tafel slope of 110 mV/dec, 111 mV/dec, 121 mV/dec and 122 mV/dec were calculated for $NiCoO_x$ (1:2), Co_3O_4, $NiCoO_x$ (1:5) and $NiCoO_x$ (2:1) respectively. These results showed that catalysts with Ni:Co ratios of 1:3 and 1:1 are the most active catalysts.

Different studies have reported overpotential over $NiCo_2O_4$ catalysts for OER, an overpotential of 0.457 V was reported in 1M KOH for $NiCo_2O_4$ film [221]. For $NiCo_2O_4$ hexagonal plates an overpotential of 0.637 V in 1M KOH was reported [222]. A composite of graphene and $NiCo_2O_4$ has shown an overpotential of 0.27 V in 1M NaOH at a current density of 4-6 mA cm^{-2} [223]. $NiCo_2O_4$ nanorods at the current density of 140 mA cm^{-2} had an overpotential of 0.27 V in 1 M NaOH [224]. MnO_x nanoflakes deposited on $NiCo_2O_4$ nanowires have an overpotential of 342 mV at 10 mA cm^{-2} [225].

The stability of the catalyst during the prolonged reaction is desirable with high activity. A long-term stability test was performed on $NiCoO_x$ (1:3) catalyst for 500 h Figure 5.3d. The test was performed in a three-electrode setup using a catalyst coated on nickel foam as a working electrode

and graphite electrode as a counter electrode and SCE as a reference electrode. The test was performed at a current density of 50 mA cm^{-2} with a starting voltage of 1.78 V (vs RHE). The voltage increases by 1.83 V during the 500-h operation. The rate of increase of the voltage during the operation was 0.11 mV/h. This long-term stability testing ensures that the catalyst is not only active at higher current density but also stable in longer electrolysis operations.

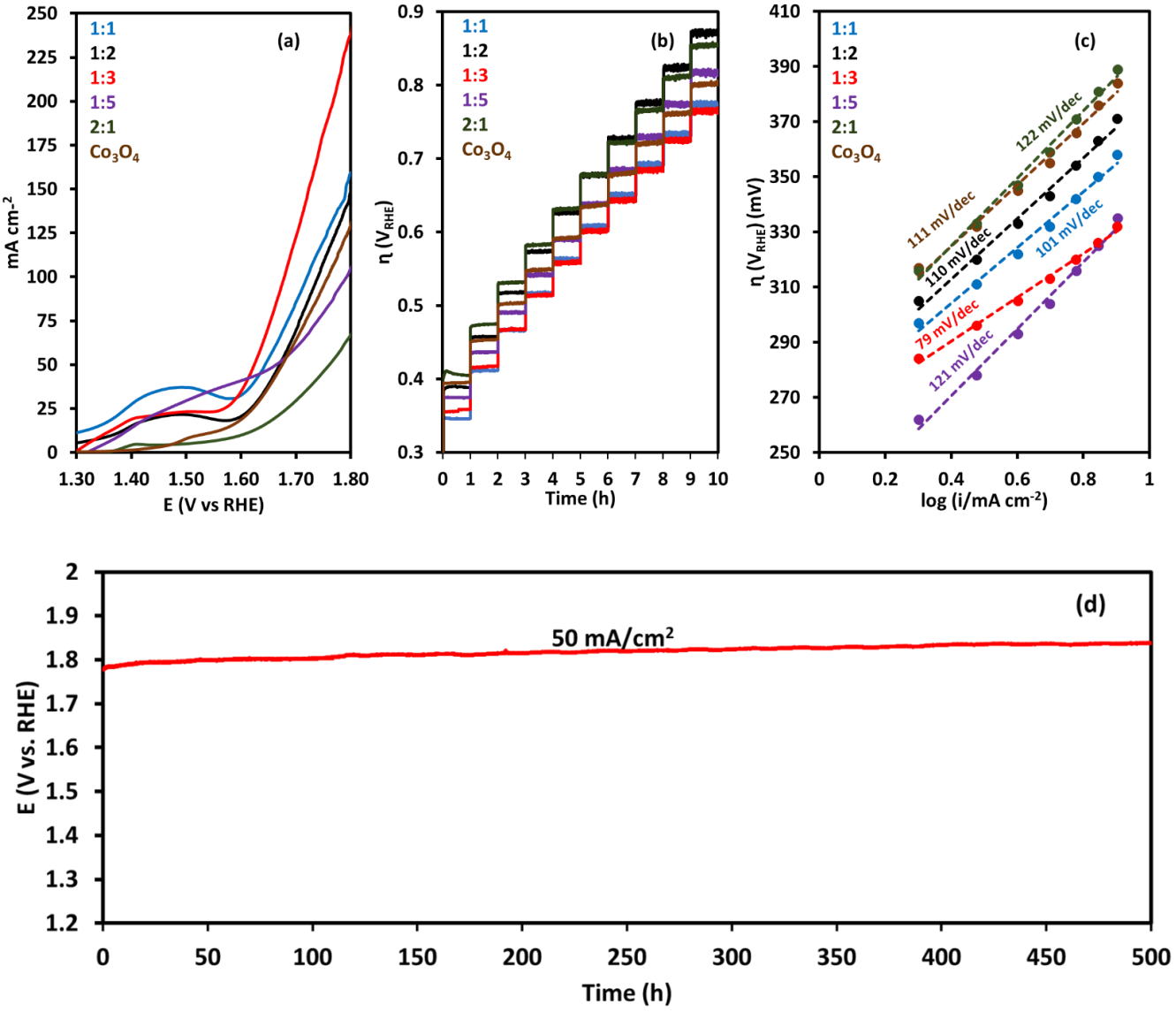


Figure 5.3. OER activity in 1M KOH. (a) Polarization curves (85% iR-corrected) of $NiCoO_x$ catalyst series and Co_3O_4. (b) Chronopotentiometry from 10 to 100 mA cm^{-2}. (c) Tafel plots in 1M KOH (d) Durability tests of $NiCoO_x$ (1:3) anode at 50 mA cm^{-2} in 1M KOH.

The double layer capacitance C_{dl} was measured by performing CV in the non-faradic region from 0.967 V to 1.167 V. $C_{dl} = i_c/v$ where i_c is the charging current due to capacitance and *v* is the scan rate. Figure 5.4 a-f shows the plot of scan rate vs current density in the non-faradic region. Figure 5.5 shows the double-layer capacitance (C_{dl}) for $NiCoO_x$ catalyst series. The value of ECSA was 55 cm^2, 70 cm^2, 90 cm^2, 145 cm^2, 67.5 cm^2 and 52.5 cm^2 for $NiCoO_x$ (1:1), $NiCoO_x$ (1:2), $NiCoO_x$ (1:3), $NiCoO_x$ (1:5), $NiCoO_x$ (2:1) and Co_3O_4 catalysts respectively.

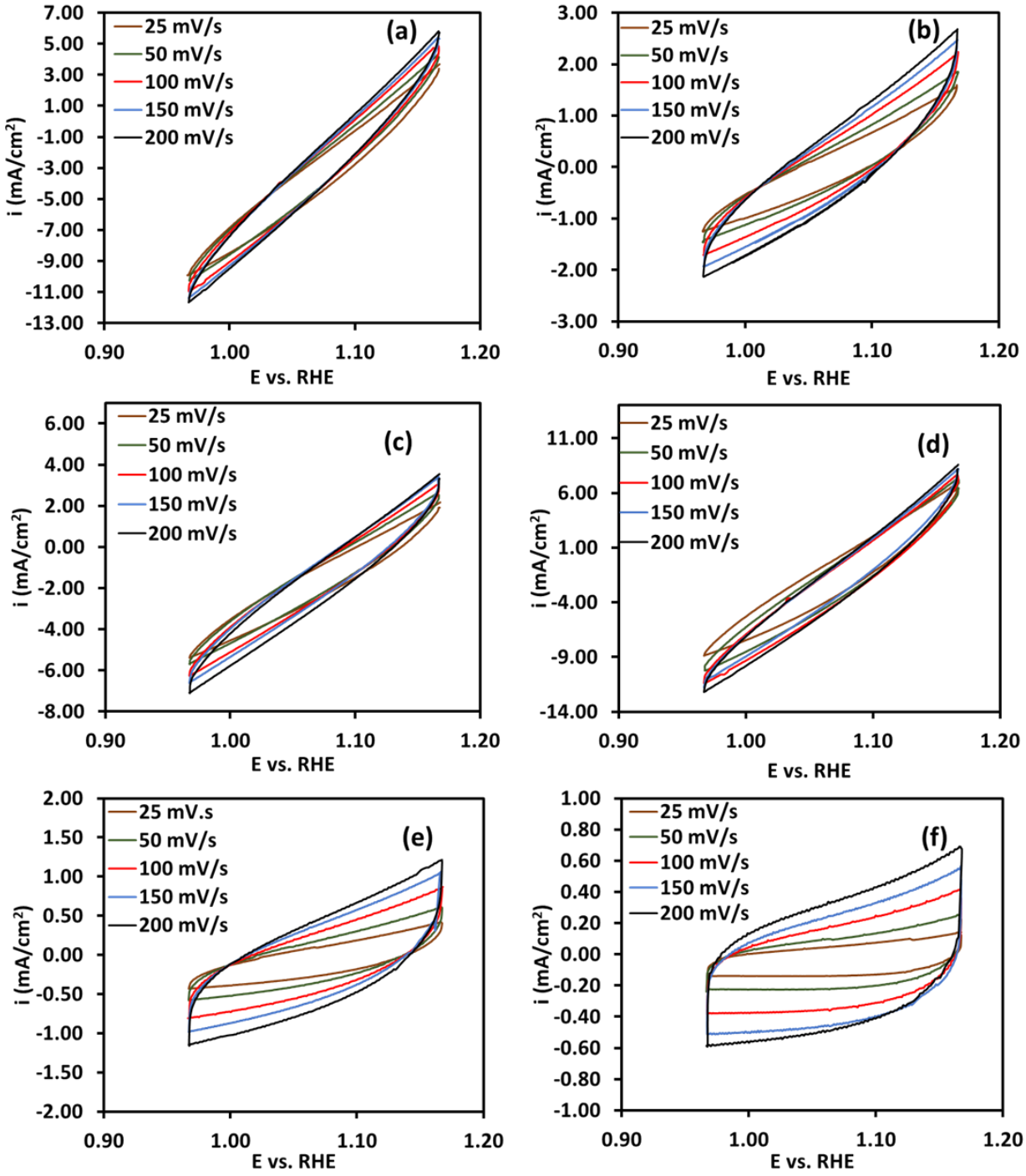


Figure 5.4. Cyclic voltammetry in non-faradaic regions at different scan rates (a) $NiCoO_x$ (1:1), (b) $NiCoO_x$ (1:2), (c) $NiCoO_x$ (1:3), (d) $NiCoO_x$ (1:5), (e) $NiCoO_x$ (2:1) and (f) Co_3O_4.

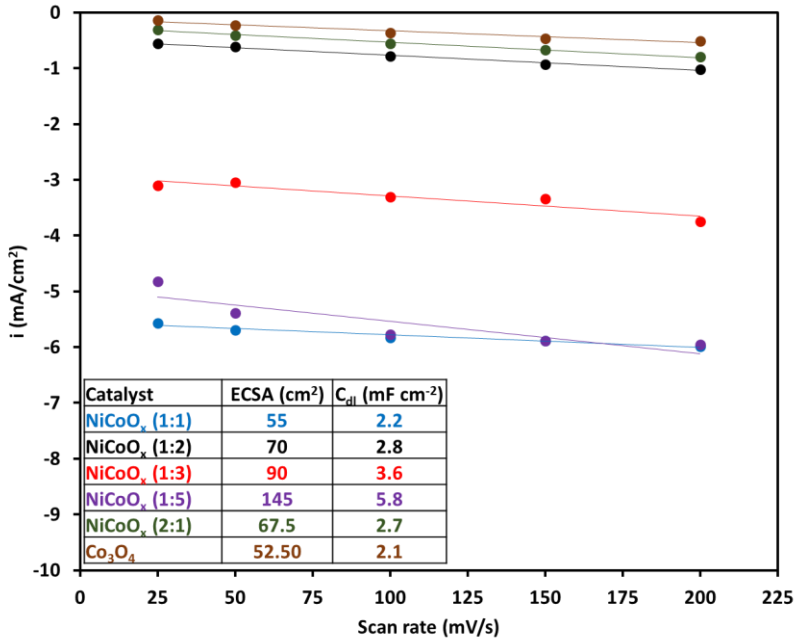


Figure 5.5. Double layer capacitance (C_{dl}) for $NiCoO_x$ catalyst series.

5.3.2 AEM electrolyzer single cell tests

Single-cell tests were performed with $NiCoO_x$ catalyst at the anode and Pt/C at cathode using Ni foam and carbon paper GDL respectively with Dioxide membrane X-37-50 T with a thickness of 50 µm. Dioxide membrane Sustainion® X-37-50 T is based on 4-vinylbenzyl chloride-co-styrene with imidazolium and pyridiniums groups and is supported on PTFE [58,192]. Chronoamperometry (CA) was used to measure the activity of the catalyst at constant voltage for one minute. Figure 5.6 shows the chronoamperometry at 45°C, 55°C, and 70°C, the voltage was increased from 1.5 V to 2.2 V in time steps of 60 seconds. Figure 5.6a shows the CA results on $NiCoO_x$ (1:3) catalyst, the current density increased from 12.3 mA cm^{-2} to 1684 mA cm^{-2} when the voltage is increased in steps from 1.5 V to 2.2 V at 55°C. The activity also increased when the operation was performed at a higher temperature of 70°C, the highest current density at 2.2 V was 1684 mA cm^{-2}. Figure 5.6b shows CA results on $NiCoO_x$ (1:1), the highest current density achieved on this catalyst at 2.2 V was 1267 mA cm^{-2} at 55°C, and the current density increased to

1510 mA cm^{-2} at 70°C which is 19% increase in the current density. Figure 5.6c shows CA for $NiCoO_x$ (2:1) compared to others, this catalyst showed lower current density at the same operational conditions. The current density at 55°C and 70°C at 2.2 V was 616 mA cm^{-2} and 661 mA $cm^{-2,}$ respectively. In all cases, electrolysis operation was stable with minimal current fluctuations at the fixed voltage.

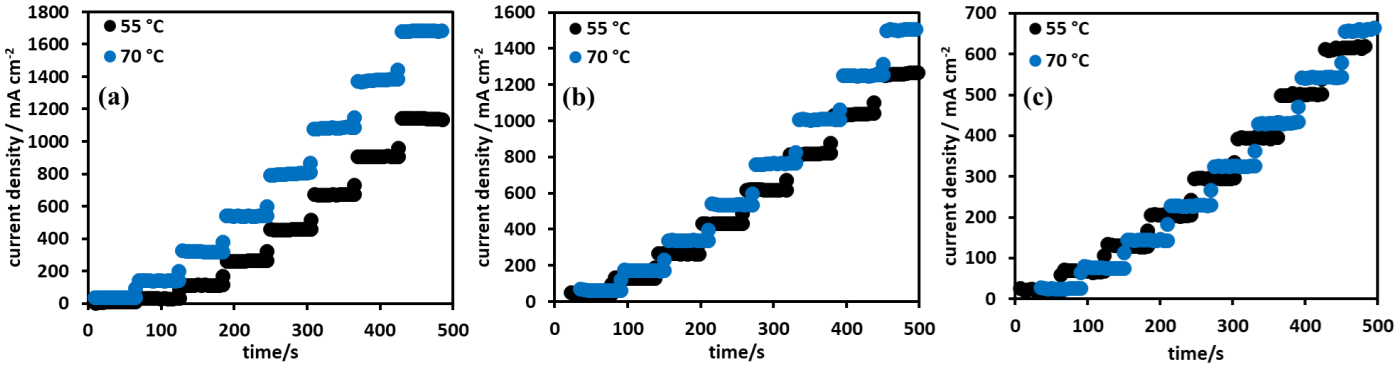


Figure 5.6. Chronoamperometry at a voltage range of 1.5 to 2.2 V, Pt/C was used at the cathode (a) $NiCoO_x$ (1:3) (b) $NiCoO_x$ (1:1) and (c) $NiCoO_x$ (2:1) catalysts were used at anode.

The polarization curves in Figure 5.7a show the relationship between the applied cell voltage and the current density in AEM electrolyzer at 45°C, which provides information about the efficiency and stability of the electrochemical reaction at the anode and cathode. The polarization curves at 45°C provide insights into how the different $NiCoO_x$ catalysts perform at these conditions. Linear sweep Voltammetry was performed from 1.3 to 2.2 V, and the current density on $NiCoO_x$ (1:3) catalyst was 735 mA cm^{-2} at 2 V which further increased to 1107 mA cm^{-2} at 2.2 V. The second highest activity was observed on $NiCoO_x$ (1:1) catalyst with the highest current density of 576 mA cm^{-2} and 884 mA cm^{-2} at 2 V and 2.2 V, respectively. $NiCoO_x$ (1:2), $NiCoO_x$(1:5) and $NiCoO_x$(2:1) have the current density of 753 mA cm^{-2}, 689 mA cm^{-2} and 510 mA cm^{-2} respectively at 2.2 V. Among all the catalysts $NiCoO_x$ (1:3) showed the highest performance. Figures 5.7b and 5.7c show the results of single-cell tests performed at 55°C and 70°C, respectively. The activity of all the

catalysts increased with the increase in temperature, which is expected due to the improvement in reaction kinetics and the decrease in overpotential for OER and HER [19,226]. The conductivity of the electrolyte (KOH or NaOH) also increases with the temperature which results in higher activity [74,191]. The trend in the activity of the catalyst remained the same and $NiCoO_x$ (1:3) had the highest current density of 1406 mA cm^{-2} and 1700 mA cm^{-2} at 2.2 V at 55ºC and 70ºC. The activity of this catalyst series is very high compared to our earlier study on NiO catalysts in similar electrolysis operating conditions [220]. This shows that the $NiCo_2O_4$ catalysts are more active compared to NiO catalysts in water electrolysis.

Nickel is considered to be the most effective catalyst for the OER due to the adsorption energies and bond strength of reaction intermediates on its surface [145–148]. The activity of Ni hydroxides and oxyhydroxides can be enhanced by adding small amounts of other transition metals. The incorporation of transition metals into metal oxides or hydroxides can change the way, the metallic phases interact with one another, specifically by altering the d-d intermetallic bonding. This could lead to a reduction in the amount of energy required for the intermediates to adsorb and result in weaker adsorption of the intermediates and faster reaction kinetics [227,228]. Adding transition metals as impurities to nickel oxide has been shown to increase the material's conductivity and decrease the amount of energy required for intermediates to bind to the catalyst [149–151].

The addition of nickel to cobalt oxide introduces new redox couples and facilitates electron transfer processes, leading to enhanced electrocatalytic performance. The synergistic effect of the two metals results in improved catalytic activity, stability, and conductivity, making $NiCo_2O_4$ a promising material for various electrochemical applications [127,224,229,230]. The molar ratio of Ni to Co is an important parameter to alter the activity of the OER. It has been reported that the OER over Nickel cobalt oxide catalyst with Ni/Co ratio of 1:2 showed higher activity compared

to other compositions of the catalyst. The higher performance is evident through lower overpotential and smaller Tafel slopes [231]. The AEM water splitting with $NiCo_2O_4$@MnO_x catalyst deposited on stainless steel mesh has an overpotential of 500 mV at 200 mA cm^{-2} [225].

Anion exchange membrane has a very high influence on the overall performance of the electrolyzer, the conductivity, stability, and thickness of the membrane are important parameters that affect performance. Z. Liu et al. compared the performance of different membranes for AEM electrolysis at 60^oC using $NiFe_2O_4$ catalyst at the cathode and NiFeCo catalyst at the anode. Linear sweep voltammetry results at a cell potential of 1.9 V showed 1A cm^{-2}, 0.5 A cm^{-2}, 0.16 A cm^{-2}, 0.11 A cm^{-2} and 0.1 A cm^{-2} for Sustainion dioxide membrane, Fumatech FAS-50, Fumatech FAPQ, AMI-7001 and Nafion 115, respectively. A stability test with dioxide membrane was also performed at a current density of 1A cm^{-2} for 2000 h at a cell voltage of 1.9 V [58].

Other catalyst compositions and membranes have been reported for AEM electrolysis. Carbon nanofiber-supported OER catalysts $NiMn_2O_4$ and $NiCo_2O_4$ have been studied using FAA-3-50 membrane with 6M KOH electrolyte, the current density in a single cell test was 181 and 303 mA cm^{-2} respectively [232]. $CuCoO_3$ OER catalyst was studied with Pt/C cathode using Tokouyama A201 membrane (thickness 28 μm) at 50^oC using 10M K_2CO_3 as electrolyte. The highest current density achieved was 0.82 A cm^{-2} at 1.9 V. High current density was reported using IrO_2 catalyst at the anode and Pt catalyst at the cathode using the dioxide X-37-50 membrane, with a current density of 2A cm^{-2} [117]. In non-precious catalysts, $NiFe_2O_4$ catalyst has been studied more compared to other catalysts for AEM electrolysis. A high current density of 1.5 mA cm^{-2} was reported on $NiFe_2O_4$ catalyst with Pt/C catalyst at the cathode. The electrolysis was performed at 60^oC using 1M KOH electrolyte [233]. Our best-performing catalyst has achieved the current densities of 1406 mA cm^{-2} and 1700 mA cm^{-2} at 2.2 V at 55^oC and 70^oC, respectively. Compared

to the other studies reported in similar operation conditions, our results are comparable and showed high activity.

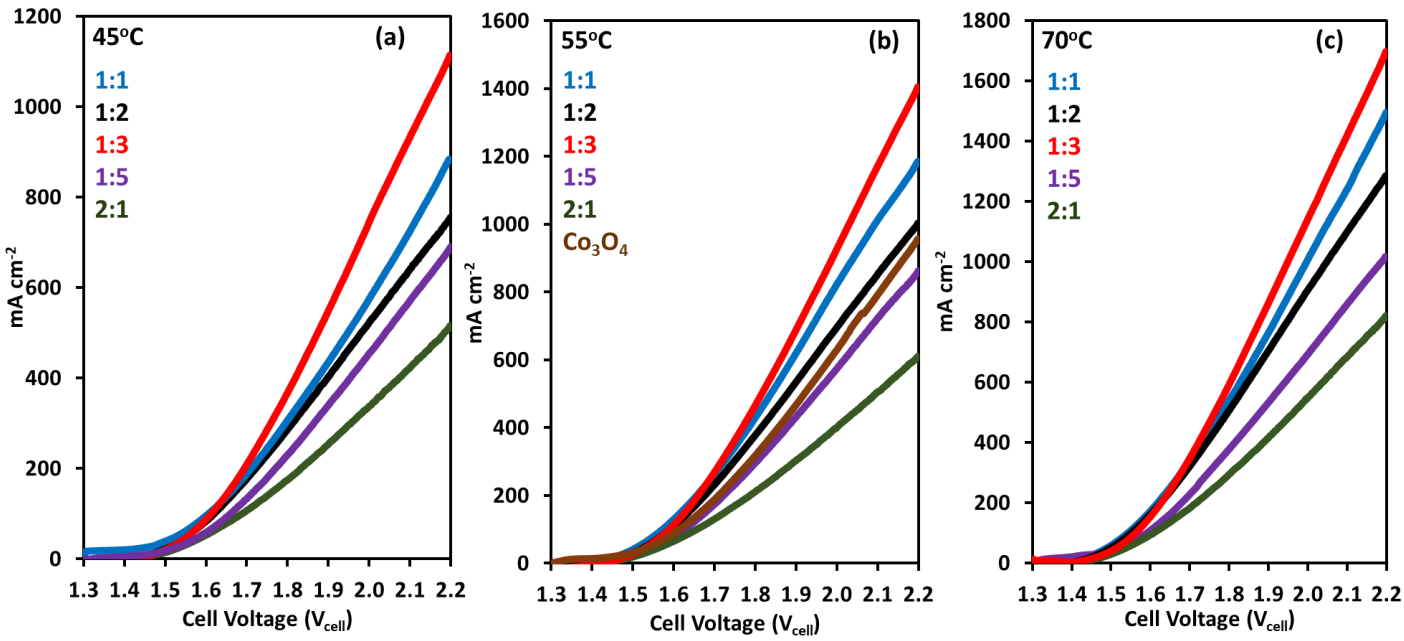


Figure 5.7. Linear Sweep Voltammetry at a temperature range of 45 to 70°C. Pt/C was used at the cathode and synthesized $NiCoO_x$ catalysts with varying Ni to Co ratios were used at the anode. X-37-50 T membrane with a thickness of 50 µm was used in electrolysis operation.

The apparent activation energy for AEM water electrolysis was calculated for $NiCoO_x$ (1:3) catalyst at a temperature range of 45°C to 70°C. The Arrhenius plot in Figure 5.8, which correlates the logarithm of current density with the reciprocal of temperature, was used for this analysis. The apparent activation energy was determined at different voltages ranging from 1.7 to 2 V, and it was observed to fall within the range of 19.09 to 14.61 kJ/mol. As shown in Table 5.1, the relationship between activation energy and voltage was examined, revealing a decrease in apparent activation energy with increasing voltage. This can be attributed to the higher concentration of reactants at the electrode surface, which results from increased voltage. Consequently, the elevated potential energy of the reactants aids in surpassing the activation energy barrier, facilitating the reaction [234].

Table 5.1. Activation energy for AEM water electrolysis with $NiCoO_x$ (1:3) catalyst at the anode and Pt/C catalyst at the cathode.

Voltage (V)	Activation energy (kj/mol)
1.7	19.09
1.8	16.82
1.9	15.32
2	14.61

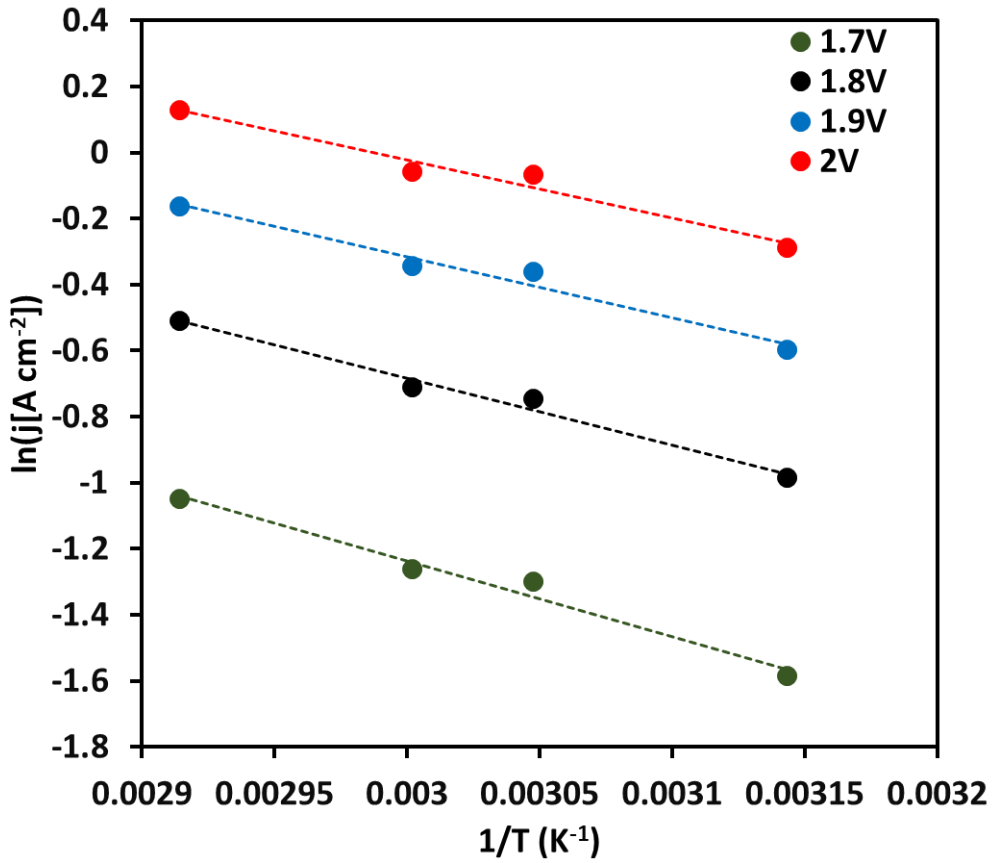


Figure 5.8. Arrhenius plot for AEM water electrolysis over $NiCoO_x$ (1:3) catalyst at 45 to 70°C.

5.3.3 EIS with equivalent circuit fittings

EIS was conducted to measure the impedance of the AEM water electrolyzer during electrolysis. Potentiostatic EIS was performed with a constant potential applied to the cell at a voltage range of 1.7 V to 2 V and a frequency range of 100 kHz to 100 mHz. The data obtained from the EIS measurements was analyzed using Nyquist plots and equivalent circuit fitting. This technique

enables the investigation of the cell's impedance, providing information on the kinetic and transport processes, as well as the resistance of the electrolyte and MEA. The Nyquist plot offers a graphical representation of the impedance characteristics of the cell. Through equivalent circuit fittings, parameters such as capacitance, resistance, and inductance can be evaluated, which helps in optimizing the electrolyzer performance [235].

Figures 5.9a and 5.9b show the Nyquist plot for the electrolysis operation that was conducted at 1.7 V for the $NiCoO_x$ catalyst series at 45°C. The $NiCoO_x$ (1:3) catalyst has a lower activation resistance compared to the other catalysts, which is evident from the smaller diameter of the semicircle in the Nyquist plot. The ohmic resistance (R_{ohm}), on the other hand, can be obtained from the x-intercept at the high-frequency region, and it represents the resistance due to the flow of ions through the electrolyte. By subtracting the first x-intercept from the second x-intercept, the activation resistance (R_{act}) can be obtained, which represents the resistance associated with the rate-determining step of the reaction [236]. The smaller diameter of the semicircle for the $NiCoO_x$ (1:3) catalyst indicates that this catalyst has a lower activation resistance and therefore, a more efficient oxygen evolution reaction catalyst compared to the other catalysts.

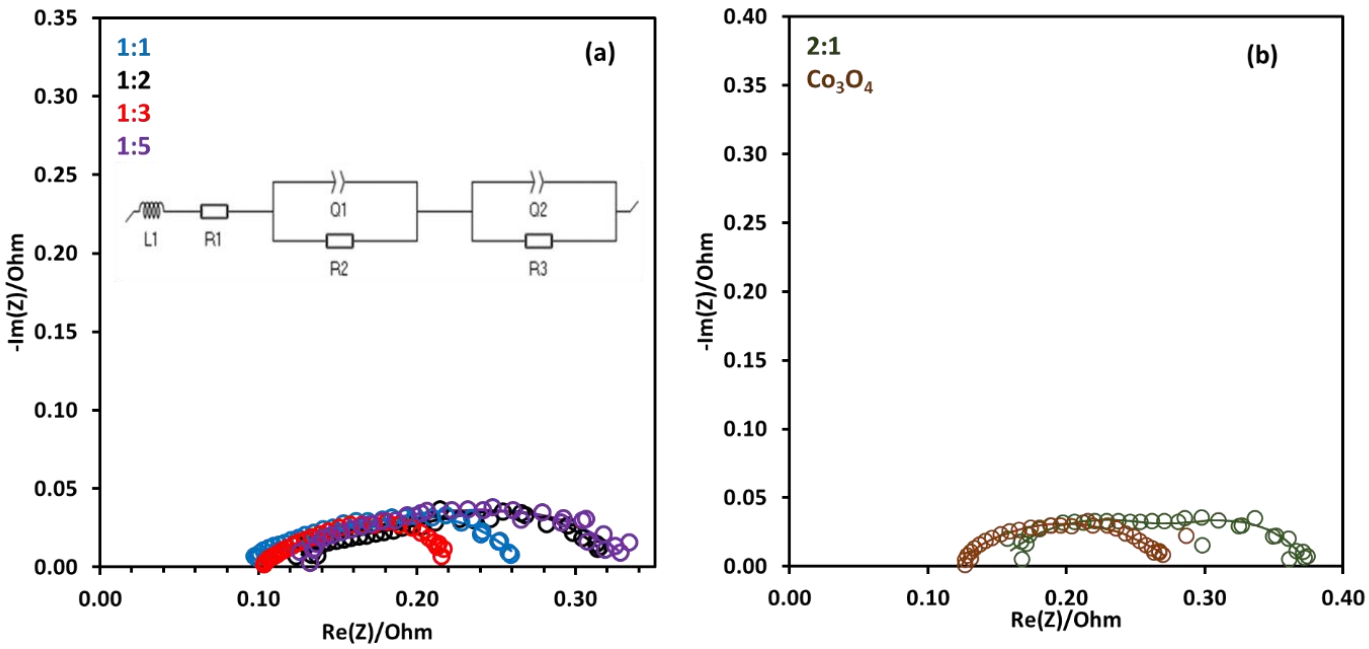


Figure 5.9. Nyquist plot for the electrolysis operation conducted at 1.7 V for the $NiCoO_x$ catalyst series with different molar ratios of Ni to Co at 45°C.

An equivalent circuit fitting was used to analyze the performance of the electrolyzer cell. This method involves fitting the impedance data obtained from the EIS measurements to a mathematical model of the cell, which includes different components that contribute to the resistance. The inset in Figure 5.9a shows the electrolyzer elements where L is the inductance due to the wiring, ionic resistance due to the AEM (R1), activation resistance at the anode and cathode (R2, R3), and a constant phase element (CPE) (Q2, Q3) at the anode and cathode, which can be used to simulate resistors, capacitors, and inductors [237].

The Nyquist plot obtained from the EIS measurements is fitted to the equivalent circuit model using the Randomize simplex method, and the results of the fitting are presented in Table 5.2. The software EC-Lab was used to perform the equivalent circuit fitting. Ohmic resistance (R_{ohm}) represents the resistance encountered by the electric current as it passes through the electrolyte and other conductive components of the system. Lower values of ohmic resistance indicate better

conductivity and reduced energy losses within the system. Among the catalyst compositions listed, $NiCoO_x$ (1:3) exhibits the lowest ohmic resistance 0.103 Ω, suggesting it has better conductivity compared to other compositions. Activation resistance (R_{anode}+$R_{cathode}$) is associated with the kinetics of the electrochemical reactions occurring at the anode and cathode. It represents the resistance encountered during the electrochemical reactions at the electrode surfaces. Lower values of activation resistance indicate faster reaction kinetics and enhanced catalytic activity. In this case, $NiCoO_x$ (1:3) demonstrates relatively low activation resistance of 0.124 Ω, whereas Co_3O_4 and $NiCoO_x$ (1:1) exhibits 0.178 Ω and 0.185 Ω, which shows that these catalysts have favorable catalytic activity compared to other catalyst compositions. Membrane resistance ($R_{membrane}$) refers to the resistance offered by the ion-conductive membrane used in the electrochemical system. It represents the hindrance faced by ions as they pass the membrane. Lower values of membrane resistance indicate better ion conductivity through the membrane. Electrolysis operation using $NiCoO_x$ (1:1) exhibits the lowest membrane resistance of 0.087 Ω.

Table 5.2. Equivalent circuit fitting results on electrolysis operation at 45°C and 1.7 V over $NiCoO_x$ catalyst series and Co_3O_4.

Catalyst	Ohmic resistance R_{ohm}	Activation resistance R_{anode}+ $R_{cathode}$	Membrane resistance $R_{membrane}$
$NiCoO_x$ (1:1)	0.100	0.185	0.087
$NiCoO_x$ (1:2)	0.127	0.212	0.113
$NiCoO_x$ (1:3)	0.103	0.124	0.102
$NiCoO_x$ (1:5)	0.127	0.229	0.112
$NiCoO_x$ (2:1)	0.153	0.277	0.140
Co_3O_4	0.125	0.178	0.104

To investigate the impact of temperature on different resistances involved in AEM electrolysis operation, a potentiostatic EIS was carried out on an electrolyzer with $NiCoO_x$ (1:3) catalyst in the

voltage range of 1.7 V to 2 V, at temperatures ranging from 45°C to 70°C as shown in Figure 5.10. Equivalent circuit fitting was not performed on these Nyquist plots and resistances were evaluated directly from the plot from the x-intercepts. Table 5.3 shows that increasing the temperature of the AEM electrolyzer results in a decrease in ohmic resistance, which can enhance the overall efficiency of the electrolysis process. This can be explained by the rise in OH^- ion conductivity at higher temperatures, which decreases the resistance in the electron flow through the electrolyzer components. This finding supports the notion that elevating the temperature can reduce the ohmic resistance and promote the efficiency of the water electrolysis [181].

Table 5.3 shows that as the temperature rose from 45 to 70°C, the total activation resistance at both the anode and cathode decreased, from 0.103 to 0.056 Ω at 1.7 V and from 0.038 Ω to 0.023 Ω at 2 V. This decrease in activation resistance can be attributed to the improved reaction kinetics of OER and the increased conductivity of OH^- ions at higher temperatures [182]. The increased mobility of reactant ions and the higher reactivity of the catalyst at elevated temperatures result in a higher rate of OER. Moreover, the improved OH^- ion conductivity leads to a reduction in the resistance of electron flow through the anode and cathode. Increasing the voltage from 1.7 V to 2 V further decreased the activation resistance at each temperature. Specifically, the activation resistance at 45°C, 55°C, and 70°C was reduced by 63%, 65%, and 59%, respectively, upon increasing the voltage to 2 V. The higher voltage facilitated the transfer of OH^- and electrons through the membrane and electrodes by overcoming resistances. Furthermore, the membrane resistance decreased with the temperature increase, which can be attributed to the enhanced conductivity of the electrolyte at higher temperatures. The ohmic resistance did not change with the increase in the voltage from 1.7 to 2 V, there is a slight decrease in ohmic resistance with the increase in temperature.

Ji Eun Park et al. studied EIS for AEM water electrolysis at 1.9 V using Pt/C and IrO_2 catalysts at cathode and anode, respectively. The electrolysis temperature was from 50 to 60°C and 1M KOH was used as an electrolyte, it was reported that the ohmic resistance decreased with the increase in temperature. They proposed that the decrease in ohmic resistance was due to the increase in ionic conductivity of the electrolyte and membrane [238]. Similar results were observed when AEM water electrolyzer temperature increased from 30°C to 60°C at 1.9 V. The ohmic resistance was decreased from 17.8 mΩ cm^{-2} to 15.6 mΩ cm^{-2}. Charge transfer resistance also decreased from 23 mΩ cm^{-2} to 11.4 mΩ cm^{-2} at temperatures of 40°C and 60°C respectively. The charge transfer resistance was decreased due to the increased conductivity of the ions within the membrane at higher temperatures. The increase in conductivity can elevate the concentration of OH^- ions at the catalyst interface, which promotes faster reaction kinetics [182].

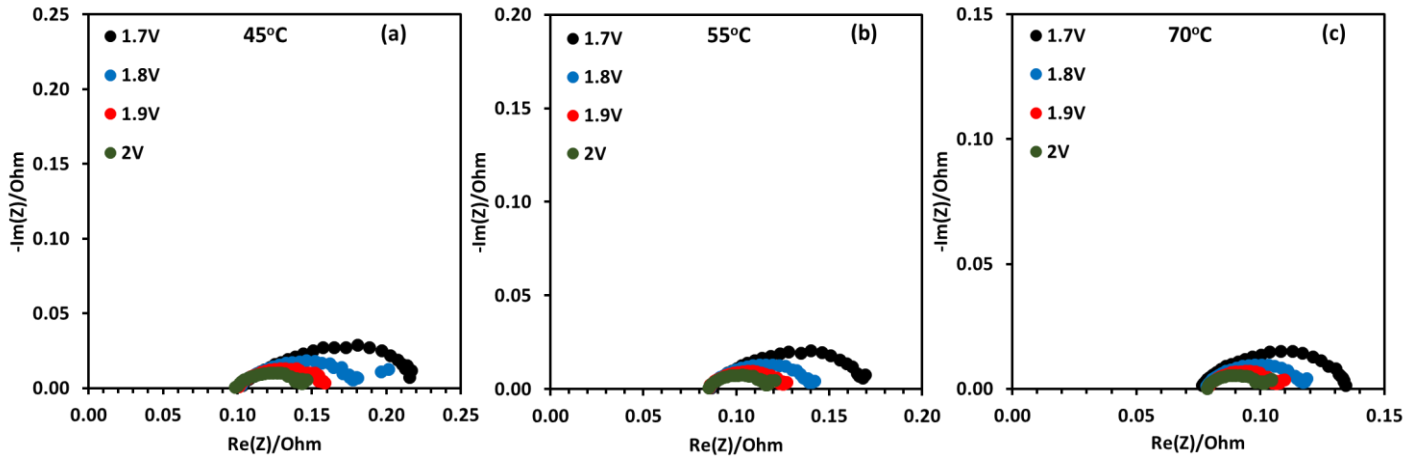


Figure 5.10. Nyquist plot at a constant voltage of 1.7 to 2 V at 45°C, 55°C and 70°C, Pt/C was used at the cathode, $NiCoO_x$ (1:3) catalyst was used at the anode.

Table 5.3. Ohmic and Activation resistances were evaluated from the Nyquist plot. EIS was performed at a constant voltage of 1.7 to 2 V with a temperature range of 45 to 70^{o}C over $NiCoO_x$ (1:3) catalyst.

Temperature	Ohmic resistance $R_{ohm\ (\Omega)}$	Activation resistance $R_{anode}+ R_{cathode\ (\Omega)}$
	1.7 V	
45^{o}C	0.112	0.103
55^{o}C	0.078	0.09
70^{o}C	0.078	0.056
	1.8 V	
45^{o}C	0.112	0.065
55^{o}C	0.078	0.063
70^{o}C	0.078	0.039
	1.9 V	
45^{o}C	0.112	0.047
55^{o}C	0.078	0.046
70^{o}C	0.078	0.028
	2 V	
45^{o}C	0.112	0.038
55^{o}C	0.078	0.031
70^{o}C	0.078	0.023

5.3.4 Durability Studies

To test the durability of the AEM electrolyzer, the long-term test was performed at a constant current density of 250 mA cm^{-2} for 30 h using 1M KOH with $NiCoO_x$ (1:3) catalyst at the anode and Pt/C at the cathode. The flow rate of electrolyte was maintained at 90 ml/min during the operation. The cell efficiencies were determined by measuring the flow rate of hydrogen during the initial 1-hour stability test at a current density of 250 mA cm^{-2}. At this operating condition, the cell efficiency was 70%, which was determined using equation 5.2.

Cell efficiency (%) = $\frac{\text{molar flow rate of hydrogen x } \Delta H \text{ x } 100}{\text{AEM electrolyzer power input}}$ Equation 5.2

Throughout the stability testing, the electrolyzer's performance remained stable. A degradation rate of 0.68 mV/h was observed during the test, starting from an initial voltage of 1.732 V. After 30 hours of continuous operation, the voltage increased to 1.752 V, as shown in Figure 5.11a. Additionally, the Faradic efficiency was calculated during the first hour of operation, and the efficiency was 81%. These results indicated the stable operation of AEM electrolyzer for longer operation time with minimal increase in voltage. Short-term durability tests were conducted to evaluate the performance of the electrolyzer at lower and higher current density ranges as shown in Figure 5.11b. The tests were carried out for 10 minutes, and the current density ranged from 250 mA cm^{-2} to 1000 mA cm^{-2}. The voltage did not vary significantly during each operation. At a current density of 1000 mA cm^{-2}, the voltage was 2.1 V, indicating that the electrolyzer was able to operate effectively at higher current densities.

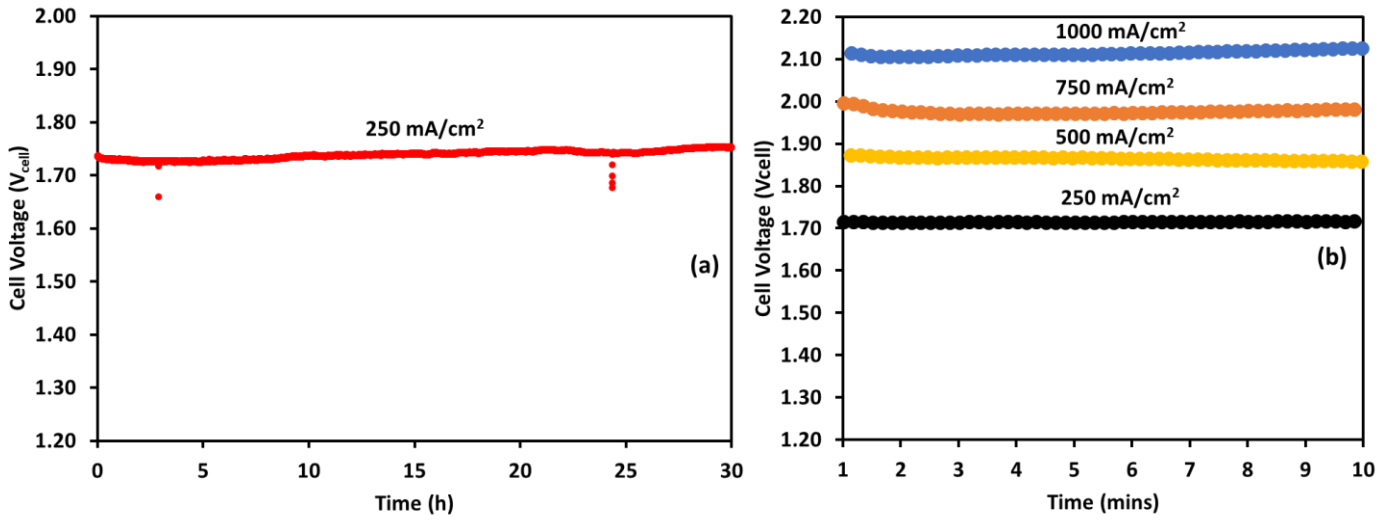


Figure 5.11. Durability test at 250 mA cm^{-2} for 30 h in 1M KOH using $NiCoO_x$ (1:3) catalyst at the anode, electrolyzer was operated at 55°C. (b) Short term stability at current densities of 250 mA cm^{-2} to 1000 mA cm^{-2} at 55°C.

There are many possible causes for the increase in voltage during the long-term AEM electrolysis. One of the main reasons is the durability of the AEM, as the membrane must be stable in an alkaline environment for prolonged testing. There are several mechanisms for AEM degradation, such as Hofmann elimination, SN_2 mechanism, radical induced hydrolysis of aryl ether-containing polymers, or crosslinking of quaternized polymers [196,239]. The degradation reaction mechanism via Hofmann and SN_2 mechanism with quaternary ammonium and imidazolium functional groups are summarized in the literature [239].

In one of the studies, the durability of FAS-50 membrane from Fumatech and Dioxide membrane X-37-50 was compared at a current density of 1 A cm^{-2}. FAS-50 membrane had a voltage increase of 0.4 mV h^{-1} for 180 hours of AEM electrolysis. While AEM electrolysis using X-37-50 membrane had a degradation rate of 5 μV h^{-1} for 2000 h stability test. It was concluded that the FAS-50 membrane had low alkaline stability compared to the X-37-50 membrane [58]. Deactivation can also be caused by changes in catalyst morphology or detachment of the catalyst due to the corrosive and oxidative environment of the electrolysis operation [240]. Furthermore, the catalyst can leach into the electrolyte solution causing loss of active sites or a void in the catalyst layer [241].

5.4 Conclusion

The experimental data and analysis conducted in this study provide valuable insights into the performance of different $NiCoO_x$ catalysts for AEM water electrolysis. Among the catalysts investigated, $NiCoO_x$ (1:3) demonstrated the highest catalytic activity for OER with a current density of 238 mA cm^{-2} at 1.8 V in three electrode systems. It also exhibited the lowest Tafel slope of 79 mV/dec, indicating more efficient electrochemical reaction kinetics. The other catalysts showed slightly lower activity with Tafel slopes ranging from 101 to 122 mV/dec. Furthermore,

$NiCoO_x$ (1:3) demonstrated excellent stability over a 10-hour chrono potentiometry test without any performance decrease. The long-term stability testing for 500 hours also showed stable performance with minimal voltage increase, indicating its potential for long-lasting applications in AEM water electrolysis. Comparing the different catalysts for AEM water electrolysis, $NiCoO_x$ (1:3) catalyst with a Ni to Co molar ratio of 1:3 outperformed the other catalysts in catalytic activity with the highest current density of 1700 mA cm^{-2} at 2.2 V. It also showed better electrochemical kinetics and stability compared to other catalysts.

The EIS and equivalent circuit fitting analysis of different catalyst compositions in AEM water electrolyzer reveal distinct performance characteristics. Among the catalyst compositions studied, $NiCoO_x$ (1:3) demonstrates superior performance with lower activation resistance and membrane resistance compared to $NiCoO_x$ (1:1), $NiCoO_x$ (1:2), $NiCoO_x$ (1:5), $NiCoO_x$ (2:1), and Co_3O_4 catalysts. This indicates enhanced catalytic activity and conductivity, suggesting $NiCoO_x$ (1:3) as a promising catalyst for AEM water electrolysis. The effect of temperature on the AEM electrolyzer was investigated, and it was found that increasing the temperature resulted in decreased ohmic resistance, activation resistance, and membrane resistance. The improved reaction kinetics, higher OH^- ion conductivity, and increased mobility of the ions at higher temperatures contribute to the overall efficiency of the electrolysis process.

During the 30-hour long-term durability test, the electrolyzer showed stable operation and maintained a relatively low degradation rate of 0.68 mV/h. The small increase in voltage from 1.732 V to 1.752 V over the test duration indicates minimal performance degradation. The cell efficiency, calculated during the initial hour of stability testing, was approximately 70%, demonstrating efficient hydrogen production at a current density of 250 mA cm^{-2}. Furthermore, the faradic efficiency reached around 80%, indicating the effective conversion of electrical energy

to hydrogen. The short-term durability tests conducted at lower and higher current density ranges show the effective performance of the catalyst. The voltage remained constant during each operation, highlighting the stability of the system.

6 Performance Evaluation and Durability Analysis of $NiFeCoO_x$ Catalysts for Alkaline Water Electrolysis in AEM Electrolyzers

6.1 Introduction

With the advancement in AEM, more research is now focused on nonprecious OER catalysts for AEM water electrolyzer and AEM fuel cells. Three main classes of OER catalysts have been widely studied for OER, which are spinel such as ($NiFe_2O_4$), perovskites such as $SrCoO_3$, and mixed metal oxide catalysts $LaNiCoO_x$ [242–244]. It was reported that in the spinel catalyst's structure, which contains Ni and Fe have higher OER activity. This is because Ni and Fe can have synergistic effects on the OER process, resulting in improved activity compared to catalysts containing only one of these elements. Several studies have identified Ni-Fe spinel compounds as promising electrocatalysts for the OER [244–246].

Mixed oxide catalysts containing both Ni and Fe have been found to have superior OER activity compared to pure Ni electrodes or other bimetallic mixed oxides. The modification of Ni-Fe bimetallic catalyst with a third metal has shown higher activity compared to the bimetallic OER catalyst [152–154]. The activity of monometallic metal oxide films for the OER can vary depending on the specific metal used. Previous studies have suggested that nickel (Ni) is the most active of the group 3d metals for the OER [174]. More recent research has indicated that the high apparent activity of Ni oxide samples may be due to contamination with trace amounts of iron (Fe) [177].

In this work, $NiFeCoO_x$ mixed metal oxides were synthesized with increasing Fe content. The activity of these catalysts was tested in three electrode systems and an AEM electrolyzer for water

electrolysis. AEM electrolyzer operation was also analyzed by Electrochemical Impedance spectroscopy (EIS) with $NiFeCoO_x$ catalysts at the anode. In addition, $NiFeCo(OH)_x$ catalyst was also synthesized, and the activity was compared with $NiFeCoO_x$ catalyst. The catalyst durability was also tested in a three-electrode system and AEM electrolyzer.

6.2 Experimental

6.2.1 Synthesis of $NiFeCoO_x$ catalysts

For the catalyst synthesis, Nickel nitrate ($Ni(NO_3)_2$), cobalt nitrate $Co(NO_3)_2 \cdot 6H_2O$, and iron nitrate $Fe(NO_3)_2$ were utilized as precursors for Ni, Co, and Fe, respectively. By maintaining a Ni to Co molar ratio of 2:1, the Fe concentration varied from 2.5 to 12.5 wt.% per metal basis. All three precursors were dissolved in water at 25 °C, 1 M NaOH was then added dropwise for 60 minutes during the precipitation phase, followed by 2 hours of stirring. The resulting catalyst suspension underwent centrifugation to isolate the solid catalyst, which was thoroughly washed to remove excess NaOH. The washed solids were dried in an oven overnight and subsequently subjected to calcination at 300°C for 5 h in a furnace to convert the catalyst into its metal oxide form.

6.3 Results

The morphology of nickel foam and GDL was analyzed by scanning electron microscopy (SEM, Leo 1550, Zeiss). Figures 6.1a and 6.1b show nickel foam without any catalyst coating, which shows pore size ranges of 100 to 500 μm. Figure 6.1c illustrates a cross-sectional view of nickel foam coated with $NiFeCoO_x$ catalyst. It shows a thin layer of catalyst on the surface of the nickel foam. The thickness of the GDE was around 790 μm, the cross-sectional image showed that the top surface of the GDE is covered with the catalyst layer, and due to the applied pressure during the fabrication process particles also deposited within the structure of nickel foam.

Figure 6.1d shows the Pt/C coated Carbon paper cathode, the total loading of the catalyst was 1mg/cm^2 of Pt and it covers the carbon paper completely. Some cracks were due to the heat treatment during the deposition of the catalyst. Figure 6.1e shows the EDS spectra of $NiFeCoO_x$ 5wt.% catalyst, which confirms the ratio of Ni to Co and Fe content of 5wt% with respect to the total metal content of the catalyst. Figures A6.1 to A6.5 in the appendix section show the EDS spectrum of $NiFeCoO_x$ catalyst series. All the EDS results confirm the total Fe content in each catalyst.

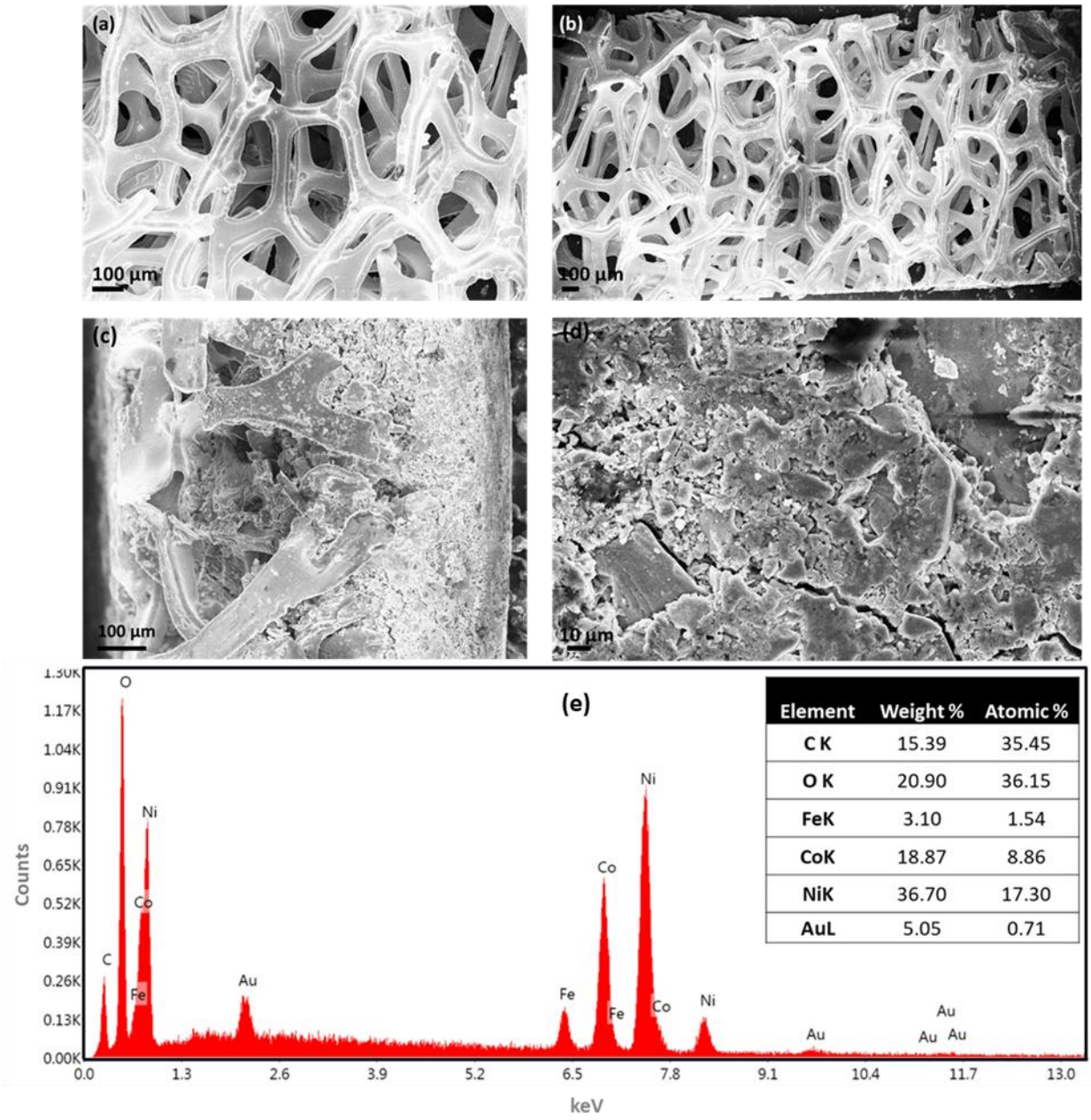


Figure 6.1. SEM of (a & b) Nickel Foam without any catalyst deposition (c) Cross-sectional image of $NiFeCoO_x$ (5% Fe) catalyst layer deposited on nickel foam (d) Pt/C coated on carbon paper (e) EDS of $NiFeCoO_x$ (5% Fe) catalyst.

X-ray diffraction (XRD) investigations were carried out using the Rigaku Miniflex 600 instrument, employing Cu-Kα radiation with a wavelength of 1.54184 Å. XRD of $NiFeCoO_x$ (2.5 -12.5 wt.% Fe) catalysts, which have Ni to Co molar ratio of 2:1, showed $NiCo_2O_4$ spinel crystal structure with a most intense peak at 2θ 36.8 assigned to (311) Figure 6.2. The peaks were indexed to

$NiCo_2O_4$ (JCPDS card no. 20-0781). Due to the low loading of Fe in $NiFeCoO_x$ catalysts diffraction peaks for $NiFe_2O_4$ and Fe_2O_4 were not observed. Some peaks corresponding to $NiCo_2O_4$ were not distinct due to the 2:1 ratio of Ni to Co, indicating the presence of $NiO/NiCo_2O_4$ phases in the catalyst. In Figure 6.2 XRD of NiO is added for the comparison, Nickel oxide had five distinct peaks centered at 2θ 37.36, 43.36, 60, 75.54, and 79.56 and assigned to (111), (200), (220), (311) and (222) respectively. Peaks are indexed to NiO (JCPDS card no. 78-0643).

In a co-precipitated $NiFeO_x$ catalyst with 15% Fe loading, there was no XRD peak observed for $NiFe_2O_4$ or Fe_2O_3 [220]. For the XRD of $Ni/NiFe_2O_4$ catalyst, no XRD peak due to $NiFe_2O_4$ was observed at the Fe mol% of 10 to 15%. At a higher mol% of 25 the XRD at peak at $2\theta \approx 35°$ observed, further increase in the Fe mol% to 50 results in the appearance of Fe_2O_3 diffraction peaks [247].

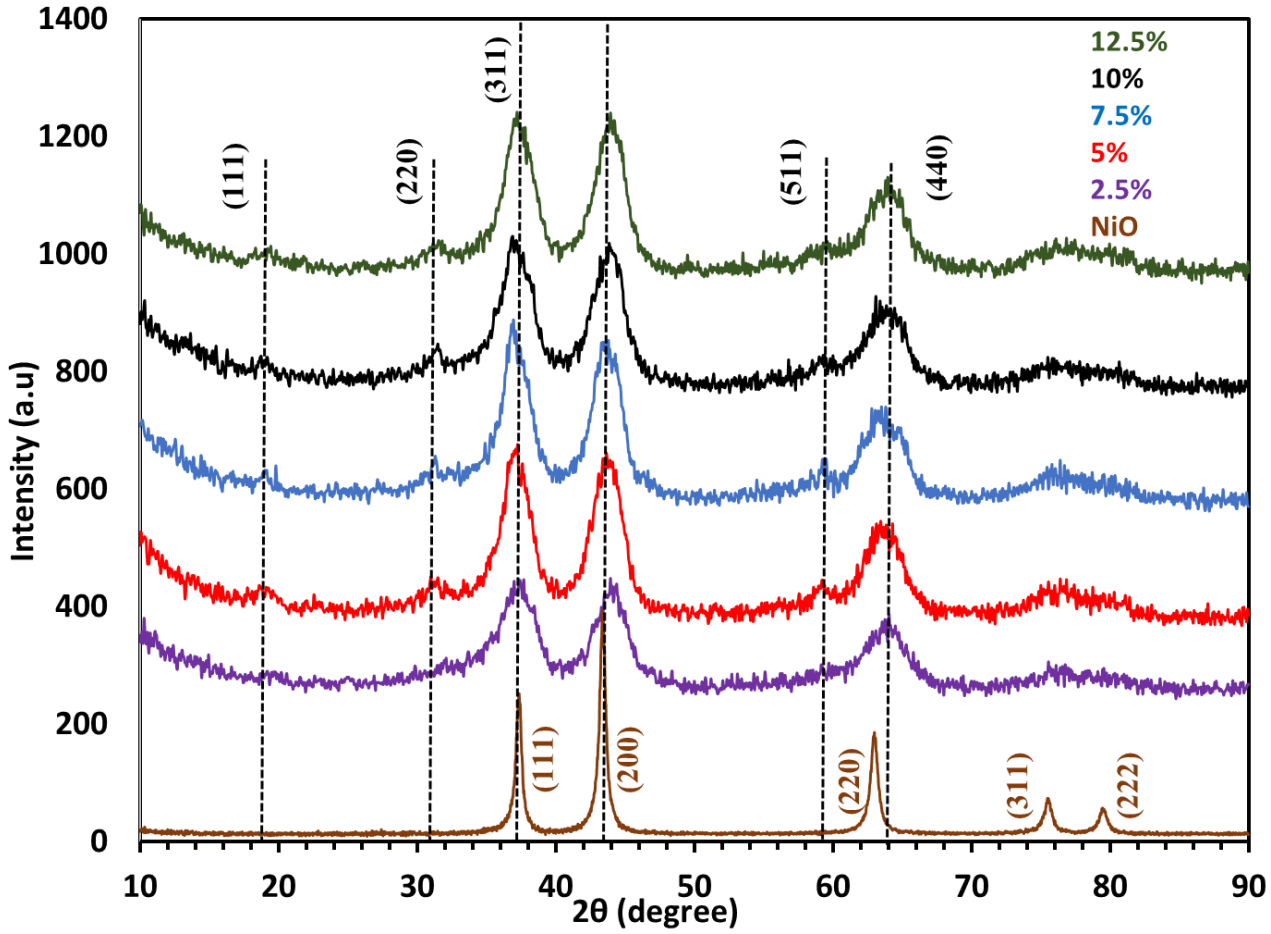


Figure 6.2. XRD of $NiFeCoO_x$ catalysts with Fe content of 2.5 to 12.5% wt.%.

6.3.1 Oxygen Evolution Reaction

To evaluate the catalytic activity of the $NiFeCoO_x$ catalysts, LSV was performed in 1M KOH. $NiFeCoO_x$ (5%Fe) showed the highest catalytic activity with an overpotential of 228 mV at a current density of 10 mA cm^{-2} Figure 6.3a, in all cases catalyst was coated on Nickel foam. The catalytic activity increased in the order of 5%>7.5%>2.5%>10%>12.5% with respect to total Fe content. The trend shows maximum activity at 5% and 7.5% Fe content, which decreases after further addition of Fe content to 10% and 12.5% Fe. Similar results were reported for $NiFeO_x$ electrocatalysts, where the OER activity improved till 15% Fe content, and with a further increase in Fe content to 30% the OER activity decreased [244]. Higher Fe content in NiFe layered double

hydroxides (LDH) material is reported to decrease the OER activity due to the formation of FeO_xH_y segregated phase which decreases the electrical conductivity of the catalysts [248].

NiO catalysts have shown comparatively lower activity in terms of oxygen evolution reaction OER [249], there is a self-redox peak at 1.45 V (V vs RHE) which is indicative of Ni^{2+} to Ni^{3+} oxidation. With the increase in Fe content higher than 5% Fe the peak became less prominent. In earlier work, it has been proposed that the addition of Fe in NiO materials promotes charge transfer and increases the valence state of Ni. This made further oxidation of the catalyst relatively difficult, causing the disappearance of Ni^{2+} to Ni^{3+} peak at 1.45 V. This partial charge transfer between Ni and Fe has been linked to improved OER activity [250]. Figure 6.3b shows the overpotential at current densities of 10, 50, and 100 mA cm^{-2}. At 10 mA cm^{-2} the overpotential did not change much with the increase in Fe content in $NiFeCoO_x$ catalyst series with $NiFeCoO_x$ (5% Fe) catalyst had an overpotential of 228 mV at 10 mA cm^{-2}. At higher current densities of 50 mA cm^{-2} and 100 mA cm^{-2} the overpotential of $NiFeCoO_x$ (5% Fe) was 406 and 495 mV, which is the lowest among other catalysts and with further increase in Fe content to 12.5% it increased to 458 mV and 558 mV for 50 mA cm^{-2} and 100 mA cm^{-2} respectively.

A long-term stability test was performed on $NiFeCoO_x$ (5% Fe) catalyst for 100 h Figure 6.3c. The OER catalyst stability test was performed at a current density of 50 mA/cm^2. During the 100-h operation, the voltage increased from 1.741 V to 1.79 V (vs RHE). The rate of voltage increase over 100 h stability period was 0.49 mV/h. This test helped to analyze the stability of the catalyst for prolonged OER at a relatively higher current density.

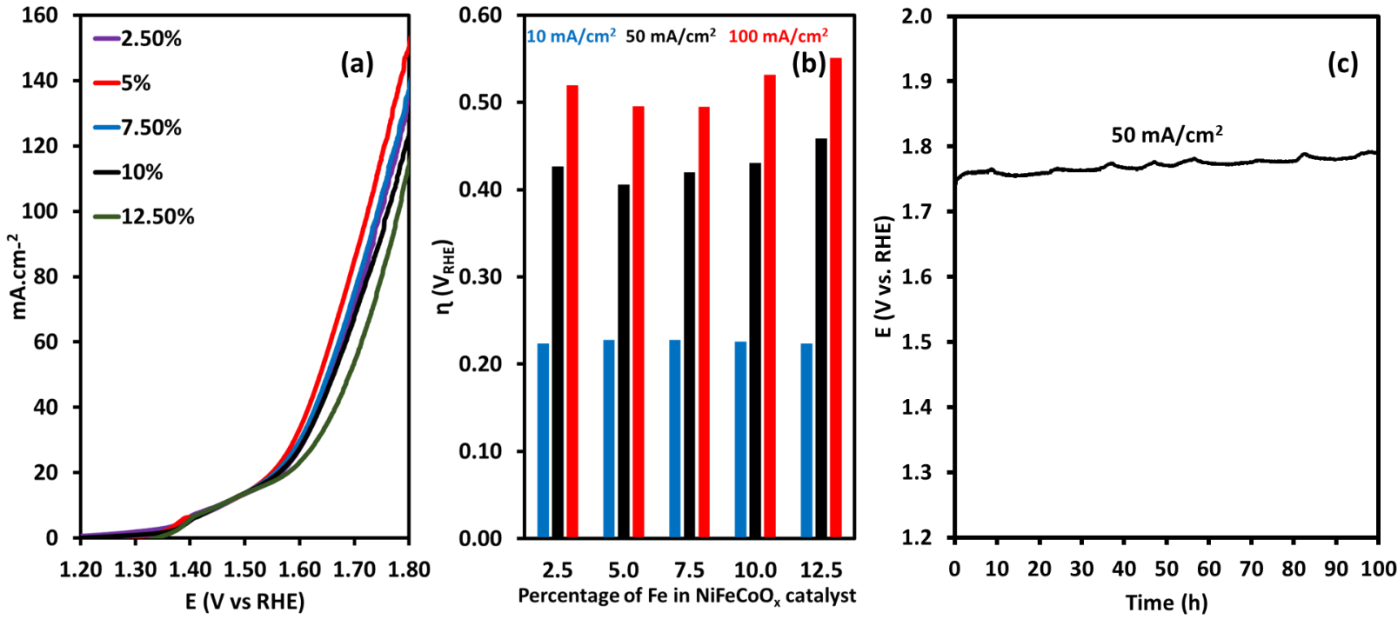


Figure 6.3. Oxygen evolution reaction for $NiFeCoO_x$ catalyst series in 1M KOH. (a) Polarization curves (85% iR-corrected) of $NiFeCoO_x$ catalysts. (b) Overpotential of OER at 10, 50 and 100 mA/cm^2. (c) Long-term OER tests of $NiFeCoO_x$ (5%Fe) catalyst at 50 mA/cm^2.

The determination of double-layer capacitance (C_{dl}) involved conducting cyclic voltammetry (CV) in the non-faradic region, specifically ranging from 0.967 V to 1.167 V. The plots in Figure 6.4 a-f depict the relationship between scan rate and current density in the non-faradic region. C_{dl} was calculated from the slope of the scan rate vs the current density plot as shown in Figure 6.5. The Table in Figure 6.5 shows the values of C_{dl} and ECSA for $NiFeCoO_x$ catalysts. The calculated values for the ECSA were 172.5 cm^2, 127.5 cm^2, 132.5 cm^2, 135 cm^2, and 132.5 cm^2 for $NiFeCoO_x$ catalysts with Fe concentrations of 2.5%, 5%, 7.5%, 10%, and 12.5%, respectively.

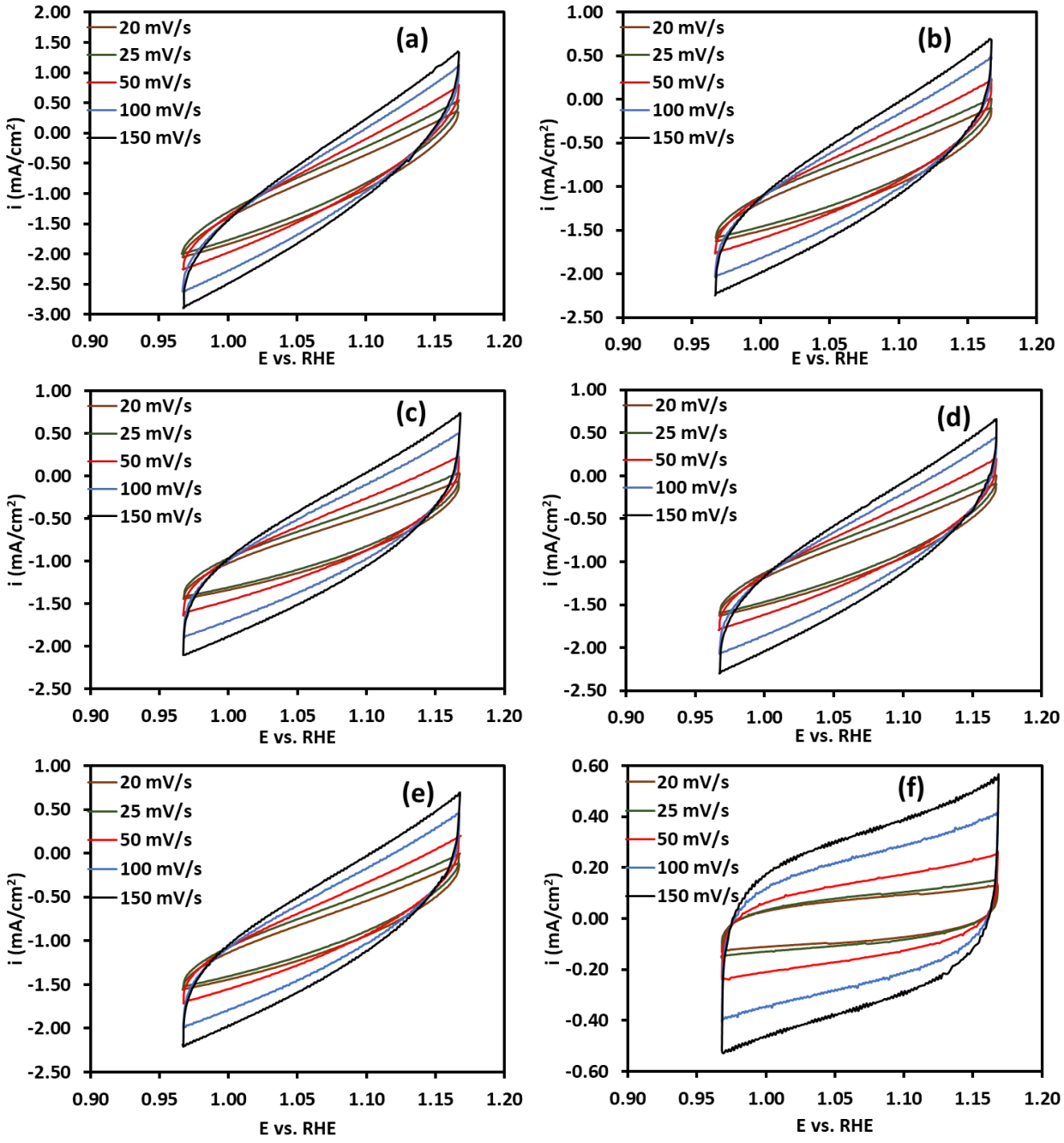


Figure 6.4. Cyclic voltammetry for the determination of C_{dl} for $NiFeCoO_x$ catalysts with varying Fe content (a) 2.5% (b) 5% (c) 7.5% (d) 10% (e) 12.5% and (f) $NiCo(OH)_x$ (5%).

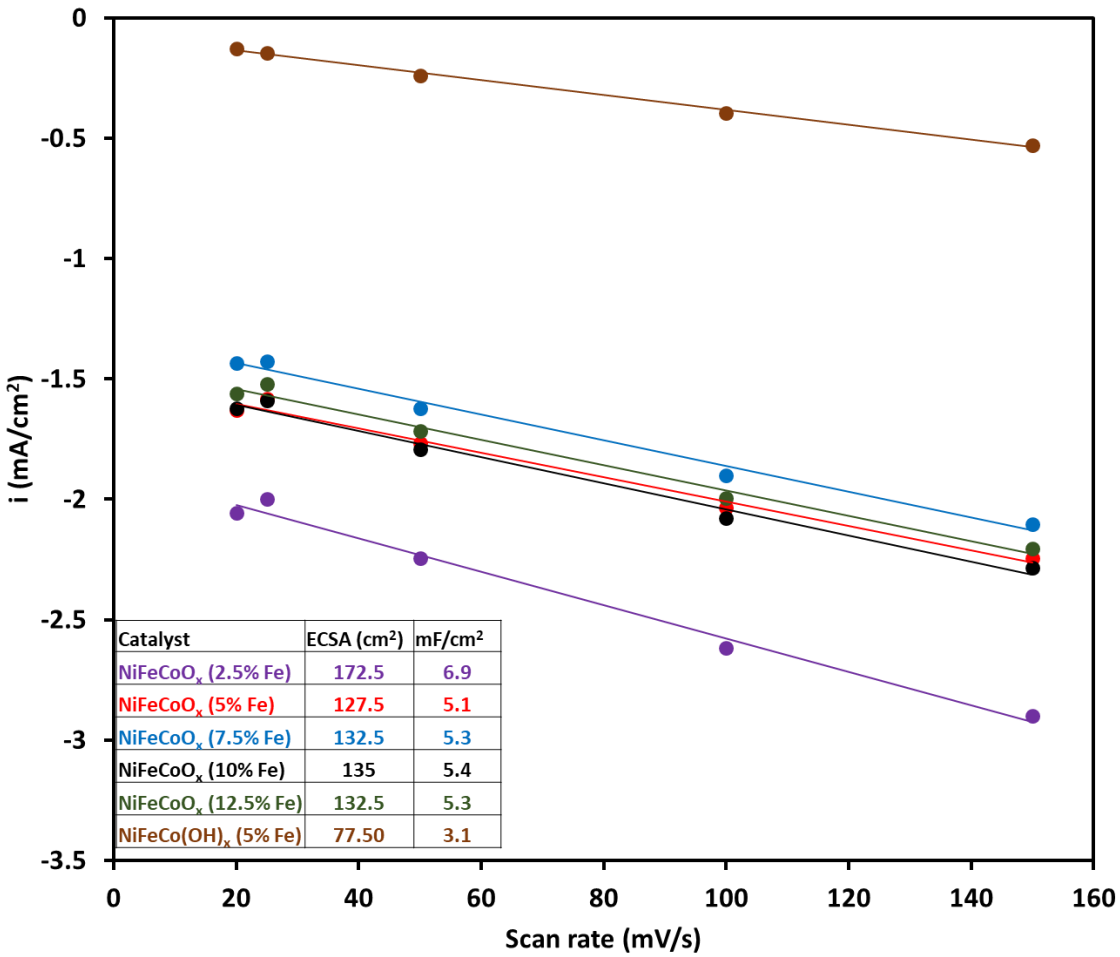


Figure 6.5. Plot of scan rate vs current density for evaluation of electrochemical double layer capacitance (C_{dl}) of $NiFeCoO_x$ catalysts.

6.3.2 Single-cell performance with $NiFeCoO_x$ catalyst

The activity of the catalyst in AEM electrolyzer was tested using chronoamperometry. Figure 6.6 shows the activity of the catalyst at 45°C, with voltage ranges from 1.5 V to 2.2 V. The voltage was constant for one minute at each voltage, the electrolyzer performance was monitored and there was very little variation in current density at a fixed voltage. At a voltage of 2.2 V, the maximum current density was 1675 mA cm^{-2}.

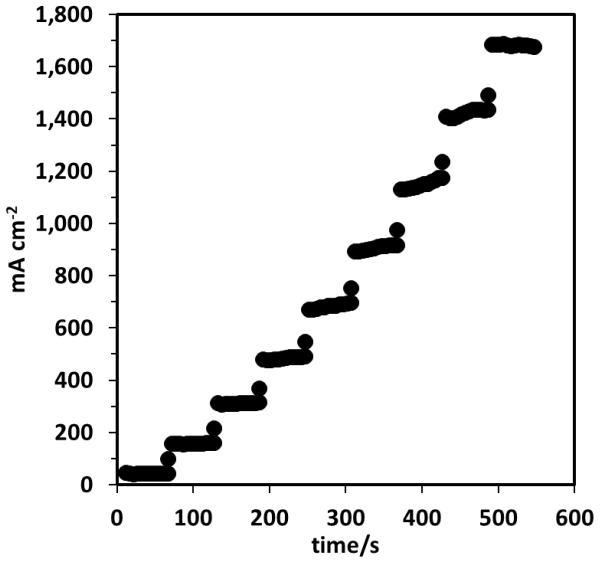


Figure 6.6. $NiFeCoO_x$ (5% Fe) catalyst activity measurement in AEM electrolyzer using chronoamperometry at 45°C with voltage from 1.5 to 2.3 V.

Figure 6.7a shows polarization curves with the series of $NiFeCoO_x$ catalysts at 45°C. The Ni to Co ratio in all the catalysts was 2:1 with Fe content changes from 2.5 to 12.5%. The catalyst with 5% Fe content showed the highest activity of 1128 mA cm^{-2} at 2.1 V. Other catalysts also exhibited increased activity, with the catalyst containing 7.5 wt.% Fe achieving a current density of 832 mA cm^{-2} at the same voltage. As the percentage of iron (Fe) exceeds 7.5 wt.%, a reduction in activity was observed, particularly at concentrations of 10 and 12.5 wt.%.

AEM water electrolysis is usually performed at higher temperatures than 45°C, the reason is to improve the reaction kinetics and to increase the conductivity of the electrolyte. Figures 6.7b and 6.7c show the AEM electrolysis performance at 55°C and 70°C. The trend in activity was the same with 5% Fe having the highest current density of 1516 and 1620 mA cm^{-2} at 55°C and 70°C respectively at 2.1 V. With the 7.5 wt.% Fe catalyst, the highest activities were 1048 and 1340 mA cm^{-2} at 55°C and 70°C, respectively. The AEM electrolyzer tests were repeated for reproducibility, the tests were repeated three times with the new MEA with the same catalyst composition. Figure

A 6.6 in the appendix section shows the AEM electrolysis at 45°C using $NiFeCoO_x$ 5% Fe catalyst at the anode and Pt/C at the cathode. The error bar shows the standard deviation among the measured current density.

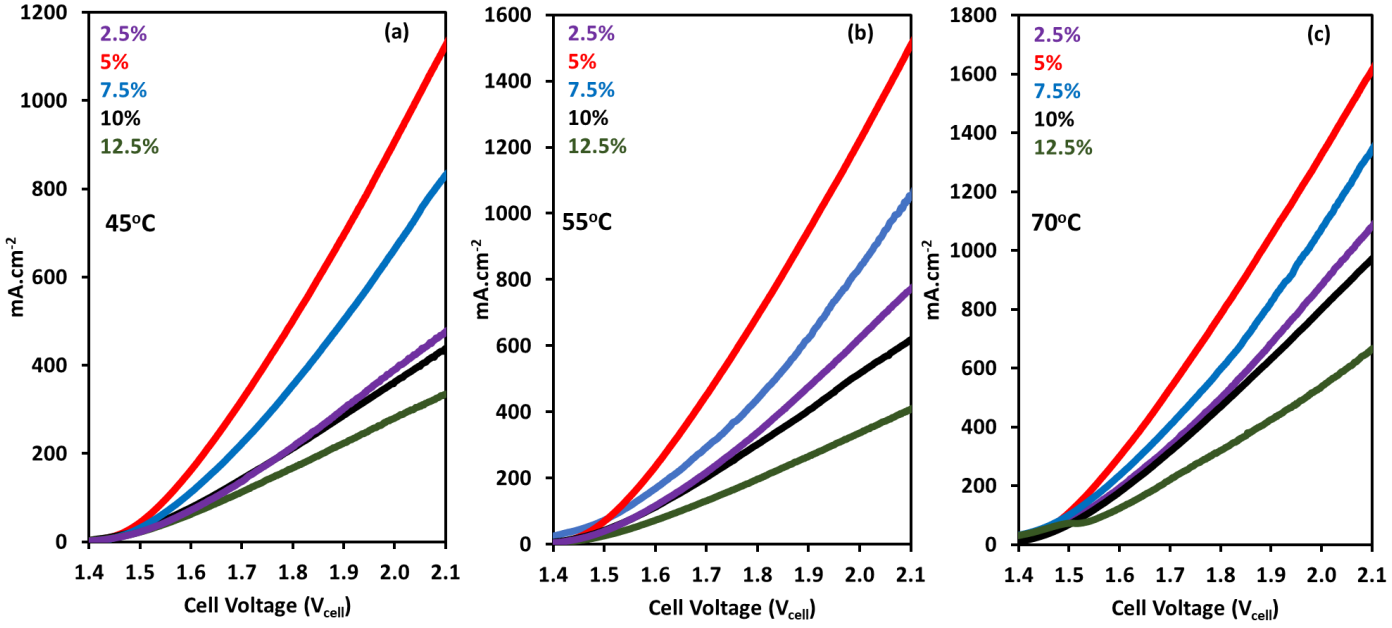


Figure 6.7. Linear Sweep Voltammetry at different temperatures using X-37-50 T membrane for AEM electrolysis (a) 45°C, (b) 55°C and (c) 70°C. The cathode was Pt/C, while the anode had $NiFeCoO_x$ catalyst with a varying Fe content ranging from 2.5% to 12.5% wt.%.

The formation of a spinel phase, such as $NiCo_2O_4$, can contribute to enhancing the activity in electrocatalysis, particularly for the oxygen evolution reaction. Fe oxides can also promote the formation of the $NiCo_2O_4$ spinel phase, which is known to be a good oxygen evolution electrocatalyst [251]. The optimum percentage of Fe in Ni based catalyst for OER has been shown to vary in different studies. For $NiO/NiFe_2O_4$ based mixed oxide catalyst, the OER activity was reported to be maximum at 10 mol% of Fe with 90% of Ni. Increasing the Fe content to 20 mol% the activity of the OER decreased to half. It was proposed that the formation of amorphous Fe_2O_3 could be the reason for lower activity with the increase in Fe content [247]. In another study, it was shown that the addition of Fe in a Ni hydroxide catalyst enhanced the overall performance of

alkaline water electrolysis, with higher Fe content the performance is reported to decrease [147]. The Nickel Iron oxide with a sputtered catalyst with 1.9% Fe was reported to have a lower overpotential than the 5.6% Fe catalyst for OER [252].

In this work addition of Fe in $NiCoO_x$ catalyst has shown to have a promotional effect on the overall activity of the catalyst when the Fe content was 5 to 7.5%. The increased activity is linked to the improved conductivity of the catalyst and also due to the decrease of the overpotential of the OER catalyst. The NiO catalyst's performance for OER has been demonstrated to be enhanced by a Fe content between 10 and 20%. Co aids in the formation of Ni^{3+}, and it was suggested that Fe would stabilize Ni in the Ni^{2+} Oxidation state [245]. In another study, trimetallic $Ni_{0.6}Co_{0.2}Fe_{0.2}$ was reported to have a current density of 1.5 A/cm^2 at 2 V. The enhancement in the activity of the catalysts was due to the $Ni(OH)_2$ to NiOOH transformation at a relatively lower temperature [253].

Figure 6.8a shows a bar graph, which illustrates a clear electrolysis activity trend with the change in Fe content under the condition of 2.1 V at 55^{o}C. At 2.5 wt.% Fe the catalyst activity is higher than the 10 and 12.5% Fe, which means that higher Fe content retards the overall activity. The optimum Fe content was at 5 and 7.5%, which shows the highest activity among the series of catalysts. For comparison when the Fe content increased from 2.5 to 5% the current density increased by 96%.

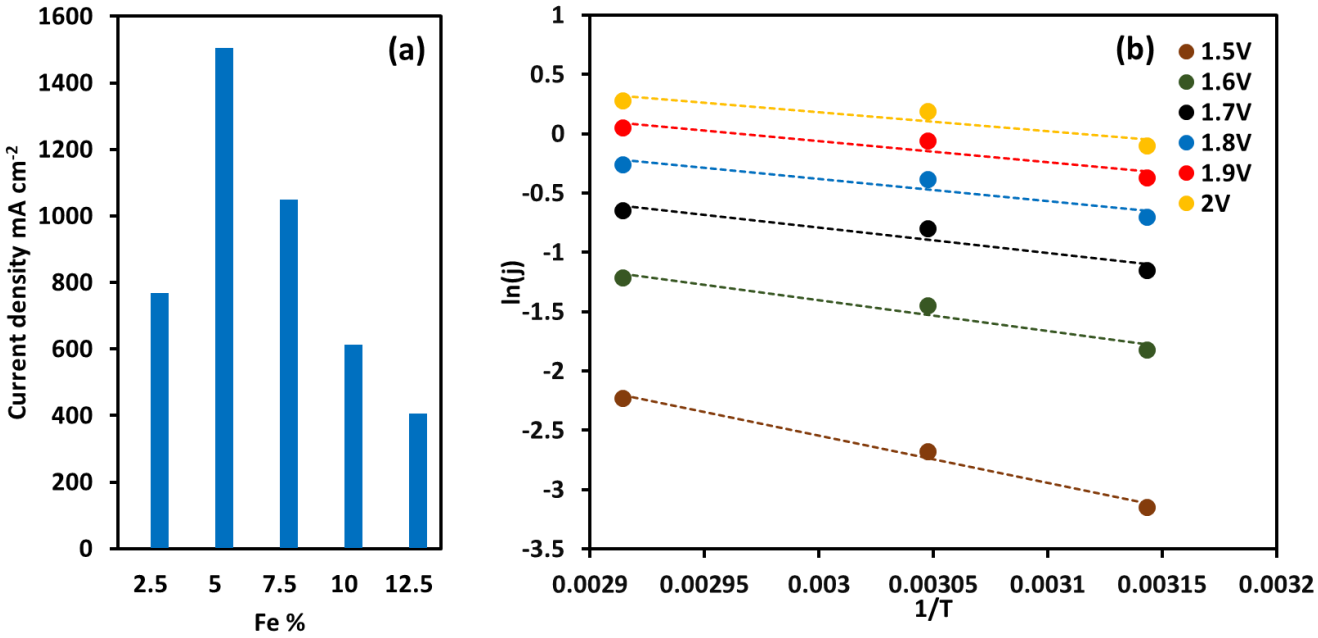


Figure 6.8. The trend in the activity of AEM electrolysis performance with the increase in Fe content at 2.1 V and 55ºC. (b) Arrhenius plot of $NiFeCoO_x$ (5% Fe) catalyst as anode for AEM water electrolysis at a temperature range of 45 - 70ºC.

Arrhenius plot was used to calculate the apparent activation energy for AEM water electrolysis by plotting the logarithm of current density and reciprocal temperature as shown in Figure 6.8b. The apparent activation energy was calculated at a voltage range of 1.5 to 2.2 V and a temperature range of 45 to 70ºC. The apparent activation energy was 33.09 to 12.40 kj/mol for $NiFeCoO_x$ catalyst with 5% Fe content. Table 6.1 shows the apparent activation energy at each current density, the activation energy decreased with the increase in the voltage. In electrochemical reactions, such as OER, as voltage increases, the potential energy of the reactants also increases. This increase in potential energy can be used to overcome the activation energy barrier required for the reaction to occur, making it easier for the reaction to take place [254,255].

Table 6.1. Apparent Activation energy with $NiFeCoO_x$ (5% Fe) catalyst at anode for AEM water electrolysis.

Voltage (V)	Activation energy kj/mol
1.5	33.09
1.6	21.66
1.7	17.63
1.8	15.62
1.9	14.94
2	13.36
2.1	12.57
2.2	12.40

6.3.3 Electrochemical Impedance Spectroscopy

EIS is a robust technique employed for investigating the operational characteristics of electrolyzer cells, especially in the context of AEM water electrolysis cells [256,257]. By this analysis, the impedance of the electrolyzer during the electrolysis operation can be measured. In addition, the impedance at the cathode and anode, resistance due to electrolyte and membrane can also be evaluated [236]. The data obtained from the EIS measurements can be analyzed by Nyquist plots, which allow for the visualization of the impedance characteristics of the cell. The Nyquist plot can be used to identify the different components of the impedance, such as the charge-transfer resistance and the Warburg impedance [258].

Figure 6.9 illustrates the Nyquist plot obtained during the electrolysis operation at 55°C, performed at a voltage of 1.7 V, for the $NiFeCoO_x$ catalyst series. On the Nyquist plot, the x-intercept at the high-frequency region signifies the ohmic resistance (R_{ohm}), and the activation resistance (R_{act}) can be determined by subtracting the first x-intercept from the second x-intercept. The Nyquist plot in

Figure 6.9 illustrates that the semicircle diameter for $NiFeCoO_x$ with a 5% loading is smaller than that of the other catalysts with different Fe loadings. This suggests that the activation resistance for this catalyst is comparatively lower when compared to other catalysts.

To gain further insight into the performance of the electrolyzer cell, equivalent circuit fitting was used to analyze the contributions of different components to the impedance. An equivalent circuit is shown in Figure 6.9, with different electrolyzer components. Where (L) is inductance, ionic resistance, R1 is the ionic resistance, R2 and R3 are the activation resistance and Q2 and Q3 are the constant phase element (CPE) (Q2, Q3) at the electrodes [254]. Due to the non-uniform nature of the electrodes, CPE was used instead of capacitive elements Q [259].

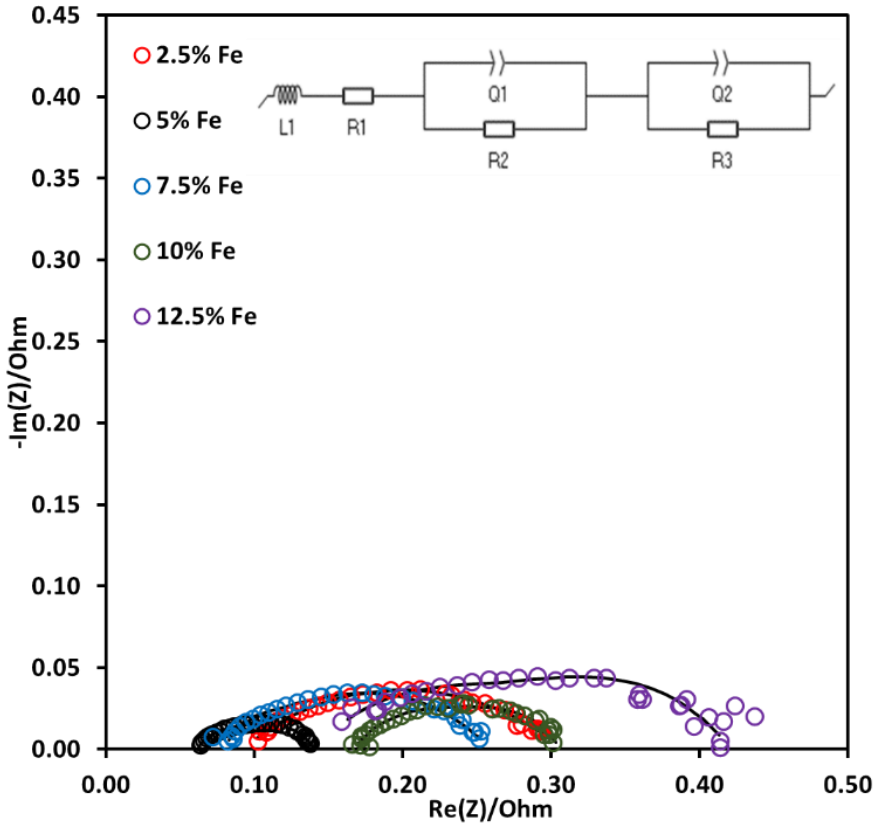


Figure 6.9. EIS analysis with Nyquist plot at 1.7 V for AEM electrolysis with $NiFeCoO_x$ catalysts at 55°C.

Table 6.2. Resistances evaluated from equivalent circuit fitting, EIS was performed at 55^{o}C and 1.7 V.

Catalyst Fe%	Ohmic resistance	Activation resistance
	R_{ohm} (Ω)	R_{anode}+ $R_{cathode}$ (Ω)
2.5	0.102	0.218
5	0.064	0.074
7.5	0.083	0.180
10	0.166	0.139
12	0.159	0.284

Table 6.2 shows the activation resistance and ohmic resistance evaluated from the Nyquist plots for the catalyst series during AEM electrolysis. The Nyquist plots showed the same trends as was observed in the performance testing, the activation resistance and ohmic resistance increased in the same order that is 5%Fe < 7.5%Fe < 2.5% Fe < 10% Fe < 12.5% Fe. The lower activation resistance (0.074 Ω) and ohmic resistance (0.064 Ω) for $NiFeCoO_x$ (5% Fe) catalyst resulted in higher performance for the AEM electrolysis. The lower ohmic resistance for $NiFeCoO_x$ (5% Fe) was due to the increased conductivity of the catalyst due to the addition of Fe. Higher loading of Fe greater than 5% resulted in the decrease of conductivity of the catalyst and increased ohmic resistance. Similarly higher Fe content in the catalyst resulted in increased activation resistance, which means that OER at the anode has a lower overpotential on $NiFeCoO_x$ (5% Fe) than other catalysts in the series. These results clearly showed that the addition of Fe in the range of 5-7.5% in $NiCoO_x$ catalyst increased the catalyst conductivity, leading to a reduction in ohmic resistance. Activation resistance was also lower for 5-7.5% Fe content catalysts and these catalysts have shown higher current densities in single-cell performance.

Potentiostatic EIS was also used to study the effect of temperature on different resistances involved in AEM electrolysis operation. EIS was performed on $NiFeCoO_x$ (5% Fe) catalyst from 45 to 70^{o}C

at 1.7 V and 2 V as shown in Figure 6.10. Equivalent circuit fitting results in Table 6.3 suggest that as the temperature of the AEM electrolyzer increases, the ohmic resistance decreases, which can improve the overall efficiency of the electrolysis process.

The results in Table 6.3 show that with an increase in temperature from 45 to 70°C, the total activation resistance at the anode and cathode decreased from 0.096 to 0.065 Ω at 1.7 V and from 0.051 to 0.029 Ω at 2 V. With the increase in the voltage from 1.7 to 2 V, the activation resistance decreased at each temperature. The activation resistance at 45°C, 55°C and 70°C decreased by 46.8%, 47.3%, and 55.3% by increasing the voltage to 2 V.

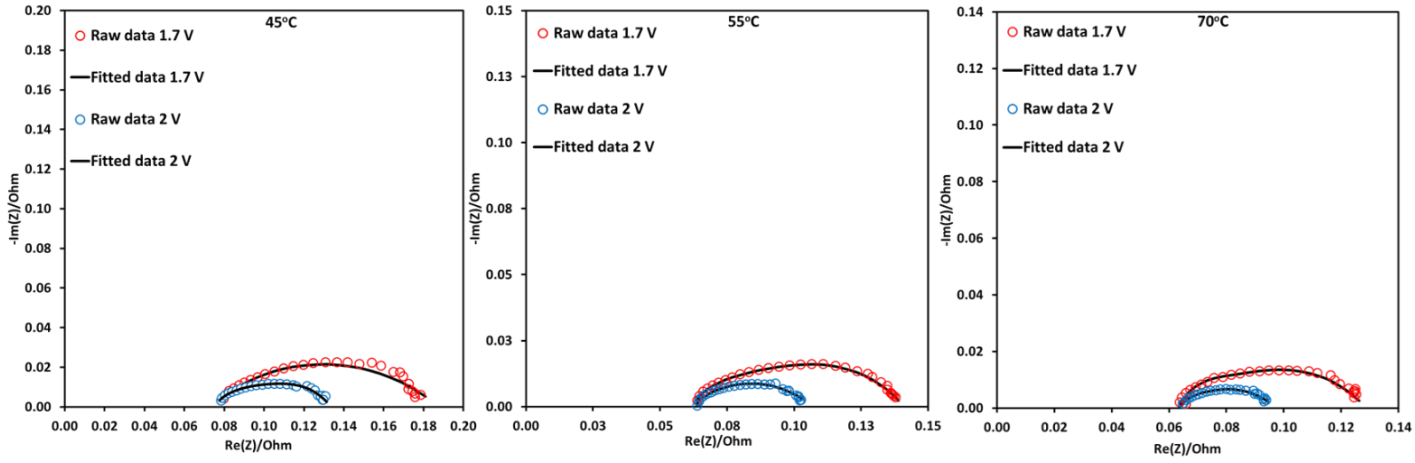


Figure 6.10. Effect of temperature for AEM water electrolysis with EIS analysis using Nyquist plots at three distinct temperatures (45°C, 55°C, and 70°C). $NiFeCoO_x$ catalyst with (5wt.% Fe) was used at the anode. EIS was performed at 1.7 V and 2 V.

Table 6.3. Equivalent circuit results for EIS analysis. The AEM electrolysis was carried out at 1.7 V and 2 V from 45°C to 70°C with $NiFeCoO_x$ (5wt.% Fe) anode.

Temperature	Ohmic resistance R_{ohm} (Ω)	Activation resistance R_{anode}+ $R_{cathode}$ (Ω)	Membrane resistance $R_{membrane}$ (Ω)
	1.7 V		
45°C	0.080	0.096	0.072
55°C	0.064	0.074	0.060
70°C	0.060	0.065	0.058
	2 V		
45°C	0.078	0.051	0.071
55°C	0.064	0.039	0.060
70°C	0.061	0.029	0.060

6.3.4 Comparison of $NiFeCoO_x$ catalyst with $NiFeCo(OH)_x$

Ni based hydroxide-based materials have shown good stability in alkaline conditions and are known to have high OER activity. Ni, Fe, and Co based Layered double hydroxide materials are also reported to have high OER activity [248,260,261]. In this study, the synthesis method for the $NiFeCo(OH)_x$ is similar to the $NiFeCoO_x$ with the only difference being that it was not annealed at high temperature, the catalyst was dried at room temperature for one day. The loading of the Fe was 5% and the performance of the catalyst was compared with the $NiFeCoO_x$ (5% Fe) catalyst. The XRD pattern of $NiFeCo(OH)_x$ revealed peaks that corresponded to reflections of a hydrotalcite-like structure Figure 6.11, with distinct peaks at 2θ which are at 10.4, 21, 34, 38.5 and 60 which were assigned to (003), (006), (012), (015), and (110) reflections and are indexed to (JCPDS: 00-035-0965).

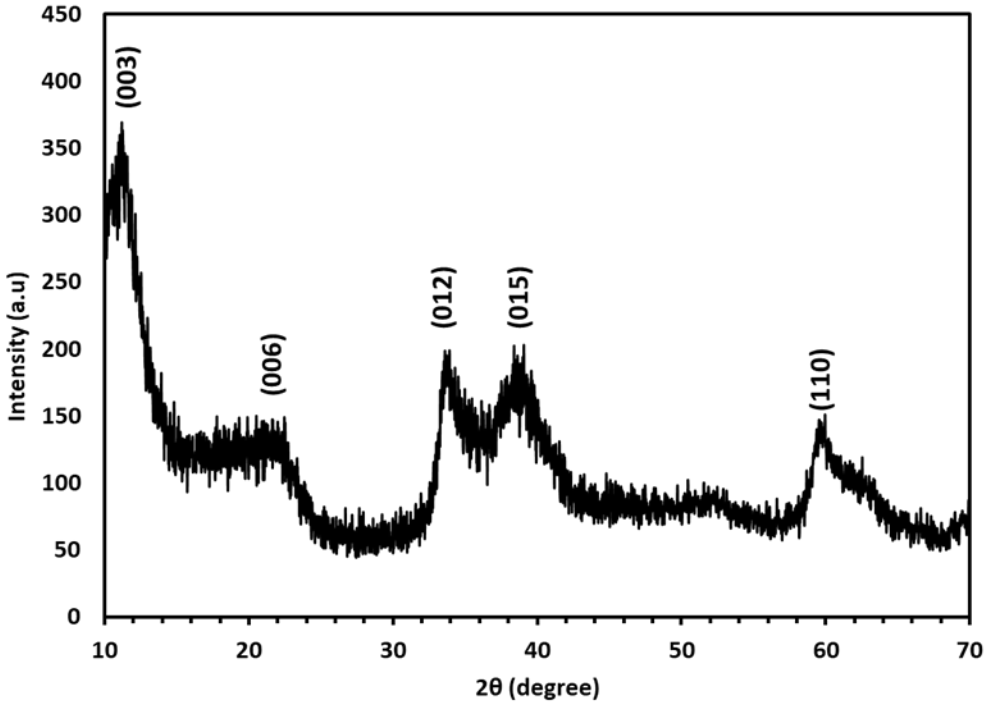


Figure 6.11. XRD of $NiFeCo(OH)_x$ catalyst with 5wt.% Fe.

To compare the electrolyzer activity of $NiFeCo(OH)_x$ and $NiFeCoO_x$, a dioxide membrane X-37-50 T was employed, and the MEA preparation method followed the previously described procedure. The operation was conducted at three temperatures (45°C, 55°C, and 70°C), as depicted in Figure 6.12 a-c. At each temperature, the $NiFeCo(OH)_x$ catalyst exhibited a lower current density compared to $NiFeCoO_x$, with both catalysts having the same loading of 25 mg cm^{-2}. At a voltage of 2.2 V, the current density for $NiFeCo(OH)_x$ was 514 mA cm^{-2} at 45°C, 588 mA cm^{-2} at 55°C, and 617 mA cm^{-2} at 70°C. In contrast, for the $NiFeCoO_x$ catalyst, the current density was higher, reaching 1311 mA cm^{-2} at 45°C, 1800 mA cm^{-2} at 55°C, and 1880 mA cm^{-2} at 70°C. The activity of $NiFeCo(OH)_x$ is higher as it achieves a current density of higher than 500 mA cm^{-2} at each temperature but compared to $NiFeCoO_x$ the activity was 2.5 times lower at 45^{o}C. At relatively higher temperatures of 55^{o}C and 70^{o}C, the $NiFeCo(OH)_x$ activity was 3 times lower than the

$NiFeCoO_x$ catalyst. The hydroxide form of OER catalyst is reported to show higher activities in literature. However, their low electronic conductivity can be a limitation for the OER. This means that the electrons may have difficulty moving through the material, which can slow down the reaction and decrease the efficiency of the electrolysis process [260]. The hydroxyl group present in the catalyst results in oxygen defects, it is reported that the presence of oxygen defects can change the properties of materials, including energy levels and conductivity. It also leads to an increase in the number of reactive and surface-active sites. However, an overabundance of oxygen vacancies causes a deformation in the metal-oxygen bond, which decreases the electron transfer between the catalyst surface and the intermediate in the oxygen evolution reaction [248].

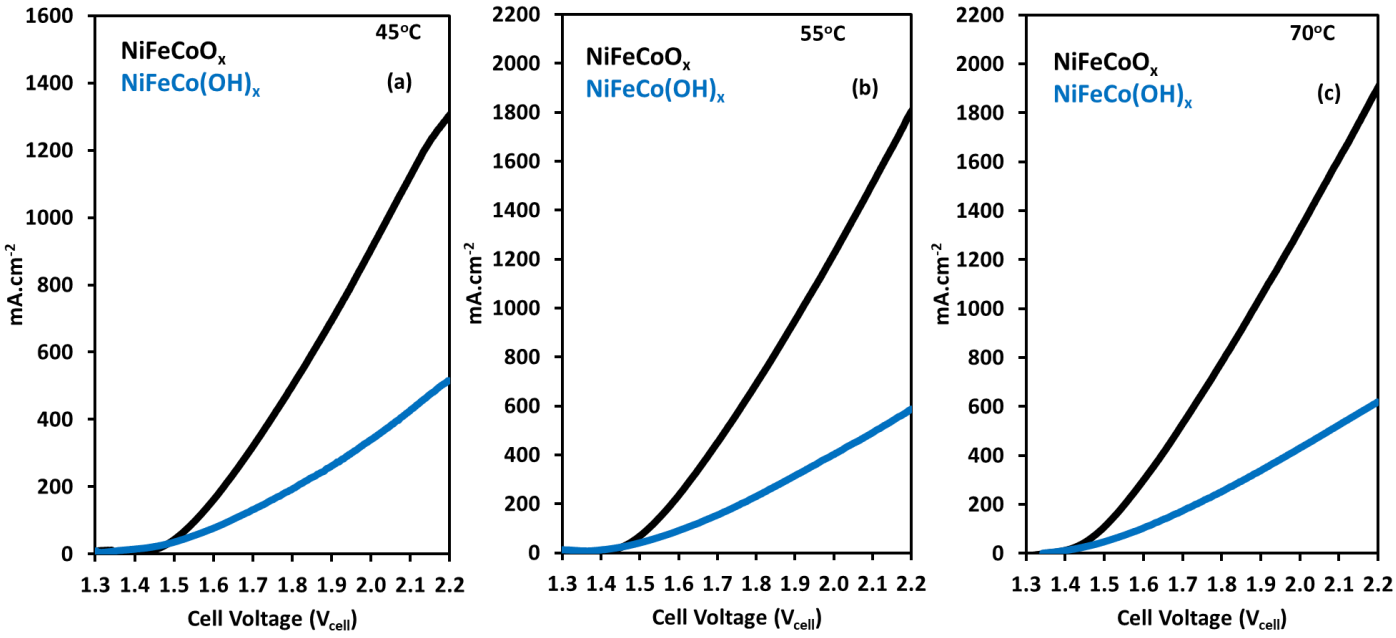


Figure 6.12. Electrolysis performance using $NiFeCoO_x$ and $NiFeCo(OH)_x$ with 5wt.% Fe at a temperature range of (a) 45°C, (b) 55°C, (c) 70°C.

Modifications to nickel hydroxide catalysts to improve their performance in the OER typically focus on several key areas. Heteroatom doping, such as the incorporation of Fe and Co into the catalyst, can enhance the conductivity of the material and promote charge transfer, thereby

improving its OER performance [262–264]. Heteroatomic doping, specifically Fe-doping, is a promising method for improving the activity of nickel-based (oxy)hydroxide catalysts in the OER. Studies have found that the intentional and/or incidental incorporation of Fe into nickel (oxy)hydroxide can significantly enhance the catalytic activity of the material. It was reported that the introduction of Fe into nickel (oxy)hydroxide catalysts affects the electronic structure of the material and promotes partial charge transfer activation on the Ni atoms. Fe-doping in nickel (oxy)hydroxide catalysts has been found to result in optimal adsorption energy for oxygen intermediates, making the OER more efficient. Other research has also suggested that the Fe ions, rather than the Ni sites, may be the active sites for the generation of O_2 from intermediate species on $Ni_{1-x}Fe_xOOH$ catalysts [265].

Another strategy to improve the activity of NiFe-based Layered Double Hydroxides (LDHs) in the OER is the ternary metal catalyst. This can affect the conductivity and structure of the binary catalyst (NiFe hydroxide), leading to enhanced OER activity. For instance, Ternary NiFeCo mixed metal oxide film has been found to exhibit enhanced OER activity compared to reference NiFe LDH catalysts. This approach can create new active sites and change the electronic structure of the catalyst leading to improved performance in OER [245,261]. Some synergism has been reported between Ni and Co in $Ni(Co)O_xH_y$ catalyst for OER, which is more active than the corresponding CoO_xH_y catalyst. The OER activity was reported to increase 3 times by co-deposition of Fe in $Ni(Co)O_xH_y$ [151].

The Lower conductivity of layered double hydroxides (LDHs) has been a barrier to their use as catalysts in the OER. To overcome this limitation, researchers have attempted to combine LDHs with conductive materials such as reduced graphene oxide (rGO) and carbon nanotubes (CNTs) or to grow LDHs on conductive substrates such as nickel foam or carbon fiber cloth. This approach

aims to enhance the conductivity of the catalysts, making them more efficient in the OER process [266,267].

Figure 6.13a shows EIS results at 55°C for $NiFeCo(OH)_x$ (5% Fe) catalyst using the X-37-50 T membrane. The ohmic resistance at 1.7 and 2 V were 0.225 Ω and 0.218 Ω, and the activation resistance was 0.244 Ω and 0.2 Ω determined from equivalent circuit fittings. When these EIS results are compared with $NiFeCoO_x$ (5% Fe) for electrolysis operation, the ohmic resistances were 3.5 and 3.4 times higher for $NiFeCo(OH)_x$ catalyst. This could be due to the low conductivity offered by this catalyst which offered higher resistance in electron transport. The conductivity also affects the overall performance of the electrolyzer, and this catalyst achieves lower current density than $NiFeCoO_x$ catalyst during water electrolysis at the same conditions. Activation resistances were also 3.29 and 5.1 times higher compared to $NiFeCoO_x$ catalyst. This explains the lower performance of hydroxide catalysts for water electrolysis compared to the other $NiFeCoO_x$ series of catalysts.

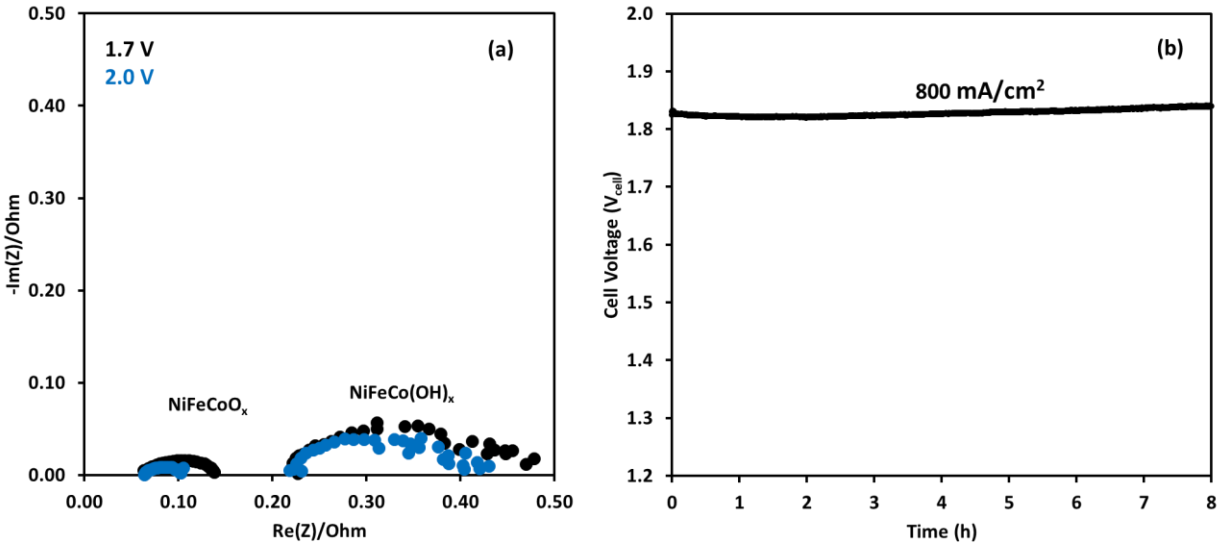


Figure 6.13. Comparison of Nyquist plot for $NiFeCoO_x$ and $NiFeCo(OH)_x$ catalysts with 5wt.% Fe at 55°C for AEM water electrolysis. (b) AEM electrolyzer durability test at 800 mA/cm^2 for 8 h in 1M KOH, electrolyzer was operated at 55°C.

6.3.5 AEM Electrolyzer Durability Test

A durability test was performed for water electrolysis with $NiFeCoO_x$ (5%Fe) OER catalyst at 800 mA/cm^2 for 8 h. Cell efficiencies were determined within the first hour of the stability test. The cell efficiency was 70.5% at this high current density operation. During the stability testing, the voltage did not increase much during the analysis. The degradation rate observed during the test was 2.3 mV/h, and the initial voltage at the start of the test was 1.825 V and after 8 hours it reached 1.839 V, as shown in Figure 6.13b. Faradic efficiency was also calculated within the first 60 minutes of the operation, with an efficiency of 87%.

One of the factors that affect the electrolyzer's performance for longer runs is the stability of AEM. Some of the commercially available membranes tested for durability testing were not stable even at very low current density, FAA-3 membrane was reported to degrade within 10 h of the operation at 20 mA cm^{-2}. With aryl ether-free HMT-PBI AEM showed stability for 200 h at a current density of 25 mA cm^{-2} [268]. Higher current density AEM stability tests were reported with FAS-50 and Sustainions X-37-50 membranes at 60^oC, both membranes showed stability for 180 h and 2000 h at 1 A cm^{-2} [58].

6.4 Conclusion

In this study, the catalytic activity of $NiFeCoO_x$ catalysts in AEM water electrolysis was investigated. $NiFeCoO_x$ catalysts exhibited a well-defined $NiCo_2O_4$ spinel crystal structure. The electrochemical analysis in the three-electrode system revealed that the catalytic activity of the $NiFeCoO_x$ catalysts varied with the Fe content. Specifically, the catalyst with 5% Fe content exhibited the highest catalytic activity, achieving an overpotential of 228 mV at a current density of 10 mA cm^2. The long-term stability testing for 100 hours showed stable performance with a slight voltage increase, which shows the stability of $NiFeCoO_x$ catalyst anode for the OER. As

the Fe content increased beyond the optimal concentration, the catalytic activity gradually decreased. This observation suggests that there is an optimal Fe concentration for maximizing the catalyst's performance, beyond which the presence of excess Fe might negatively affect the catalytic activity due to the decrease in the conductivity of the catalyst and increase in the overpotential of the catalyst. This finding emphasizes the importance of careful control over the catalyst composition to achieve optimal performance. The single-cell tests conducted under practical operating conditions further supported the superior electrochemical activity of the $NiFeCoO_x$ catalyst with 5% Fe content. This catalyst consistently demonstrated the highest current densities of 1516 mA cm^{-2} and 1620 mA cm^{-2} at 55°C and 70°C respectively at 2.1 V, highlighting its stability and suitability for real-world applications. $NiFeCoO_x$ consistently exhibited higher current density than $NiFeCo(OH)_x$ catalyst at each temperature, with the former achieving 2.5 times higher activity at 45°C and three times higher activity at 55°C and 70°C. These results indicate that $NiFeCoO_x$ outperforms $NiFeCo(OH)_x$ in terms of electrolyzer activity, particularly at elevated temperatures.

EIS coupled with equivalent circuit fitting analysis of various catalyst compositions in AEM water electrolyzers shows performance characteristics. The catalyst study during AEM electrolysis revealed that $NiFeCoO_x$ (5% Fe) exhibited superior performance, attributed to its lower activation and ohmic resistances. Increasing the temperature demonstrated a steady decrease in overall resistances, enhancing electrolysis efficiency. Higher voltage further lowered activation resistance, emphasizing the importance of voltage and temperature in optimizing AEM electrolysis.

The durability test of $NiFeCoO_x$ (5%Fe) OER catalyst in water electrolysis showed promising results. The catalyst demonstrated stable performance throughout the 8-hour AEM electrolysis at 800 mA cm^{-2}, suggesting its reliability and durability in high current density operations. The cell

efficiency measured during the initial hour of the stability test was 70.5%, highlighting the catalyst's efficiency in facilitating water electrolysis and hydrogen generation. The faradic efficiency of the system was measured to be 87% during the first hour of operation, indicating efficient electrochemical reactions during water electrolysis.

These findings have important implications for the development of efficient and sustainable hydrogen production. By optimizing the composition of $NiFeCoO_x$ catalysts, it is possible to enhance the electrochemical performance of alkaline water electrolysis systems, thereby facilitating the production of hydrogen in a more environmentally friendly and economically viable manner.

7 Enhanced Performance and Stability of $NiFe_2O_4$ Catalyst in Anion Exchange Membrane Water Electrolysis: Influence of Iron Content and Membrane Selection

7.1 Introduction

Despite their advantages over AWE and PEM systems, there are still several key challenges in utilizing AEM electrolyzers for hydrogen generation. AEM electrolyzers show lower current density and energy efficiency when compared to PEM water electrolyzers [269]. These limitations can be largely attributed to high overpotentials found in Oxygen evolution reaction (OER). One primary focus for AEM electrolyzer research is the development of catalysts with low overpotential. Noble metal oxides are effective for this purpose, however, as in PEM they are scarce and expensive to use. This has led to a focus on the use of transition metal oxide catalysts. More specifically, spinel-structured first-row transition metal oxides have received the most attention due to their efficiency as an electrocatalyst, and their relative abundance [270–272]. $NiFe_2O_4$ based catalysts show significant promise and potential for this application. One reason is due to the polyvalent redox pairs present (Ni^{2+}/Ni^{3+} and Fe^{2+}/Fe^{3+}), which can act as redox active sites for oxygen evolution [273]. Additionally, it possesses high stability as well as corrosion resistance, which helps mitigate a major concern in the long-term operation of AEM electrolyzer [270]. Furthermore, it is abundant and high in reserve, resulting in low costs, especially when compared to noble metal-based catalysts [273].

$NiFe_2O_4$ based catalyst has been reported to have good activity for OER and AEM water electrolysis. $NiFe_2O_4$ nanoparticles, sized at 10 nm, showed high activity in OER, achieving a current density of 10 mA cm^{-2} at an overpotential of 290 mV, with a Tafel slope of 42 mV dec^{-1}

[270]. Furthermore, $NiFe_2O_4$ nanorods have also shown excellent performance. With mesoporous $NiFe_2O_4$ nanorods catalyst reaching 10 mA cm^{-2} with an overpotential of 342 mV and a Tafel slope of 44 mV dec^{-1} [271]. Furthermore, doping or mixing $NiFe_2O_4$ with various materials has shown significant performance increases. $NiO/NiFe_2O_4$ biphasic nanorods achieve 10 mA cm^{-2} at a reduced 302 mV, with a slightly lower Tafel slope of 42 mV dec^{-1}, and also increased specific surface area when compared to standard $NiFe_2O_4$ nanorods [272]. A $NiFe_2O_4@Co_3O_4$ heterostructure catalyst achieved 10 mA cm^{-2} at an overpotential of 251 mV with a low Tafel slope of 36 mV dec^{-1} [274]. Similarly high performance can be found in AEM systems utilizing $NiFe_2O_4$ as an anode electrocatalyst.

In this study $NiFeO_x$ and $NiFe_2O_4$ catalysts were synthesized, in $NiFeO_x$ catalysts the Fe content was changed from 5 to 12.wt.% of total metal content. The OER was performed in three electrode systems and complete water electrolysis was performed using AEM electrolyzer. Electrochemical impedance spectroscopy (EIS) was performed to evaluate different resistances due to the electrolyzer components. Long-term and short-term durability testing was also performed using $NiFe_2O_4$ at the anode. In addition, several anion exchange membranes (AEMs) were tested, and their performance was compared for AEM water electrolysis.

7.2 Experimental

7.2.1 Synthesis of $NiFeO_x$ catalysts

$NiFeO_x$ catalysts were synthesized by the coprecipitation method at room temperature. $Ni(NO_3)_2$ and $Fe(NO_3)_2$ were used as a precursor of Ni and Fe respectively. The Fe content varied from 5wt.% to 12.5wt.% for $NiFeO_x$ catalysts and for $NiFe_2O_4$ catalysts Ni to Fe ratio was kept at 1:2. Both precursors were dissolved in deionized water at room temperature. 1M NaOH was used for the precipitation and was added drop by drop until complete precipitation. The precipitate was then

washed with water to remove excess NaOH and centrifuged to collect the solid catalyst. The catalyst was then dried in an oven at 100^{o}C overnight to remove water. For both catalysts $NiFeO_x$ and $NiFe_2O_4$, calcination was performed at 500^{o}C for 5 h.

7.3 Results

SEM and EDS analysis were carried out using (SEM, Leo 1550, Zeiss). Figure 7.1a shows the morphology of nickel foam anode GDL, Nickel foam had a pore size in the range of 100 to 500 μm, which provides easier access to water and oxygen at the anode to transport. The cross-sectional image showed the total width of the catalyst-coated nickel foam, which has a thickness of 740 μm as shown in Figure 7.1b. The $NiFe_2O_4$ catalyst layer was dense, and catalyst particles were distributed within the matrix of the nickel foam. Figure 7.1c shows the EDS of $NiFe_2O_4$, which clearly shows the Ni to Fe ratio of approximately 1:2. The EDS of other catalysts are presented in Figures A7.1 to A7.3 in the appendix section. In all cases, catalyst composition is confirmed from the EDS analysis.

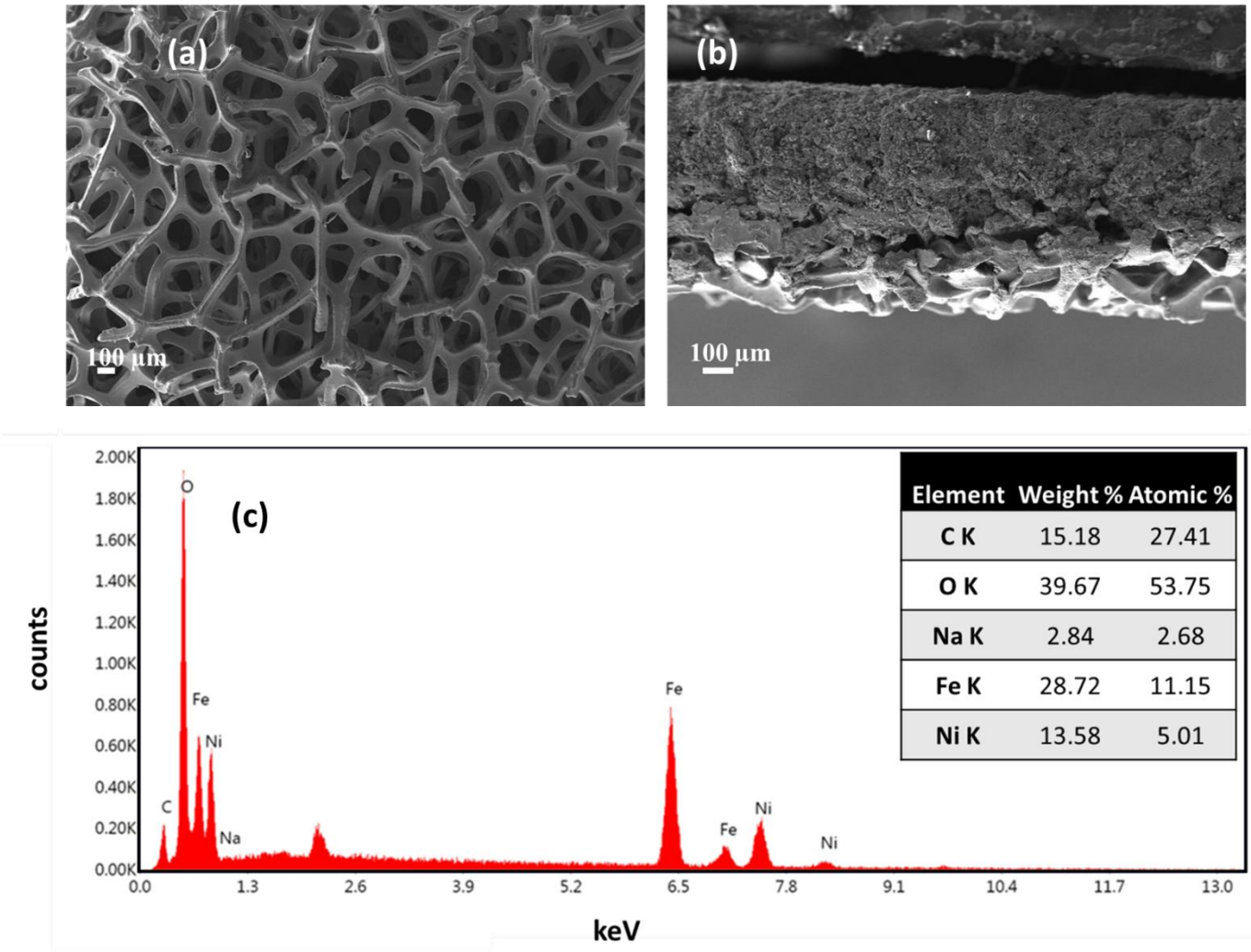


Figure 7.1. (a) SEM of Nickel foam Anode GDL. (b) Cross-section of $NiFe_2O_4$ catalyst coated on nickel foam anode. (c) EDS of $NiFe_2O_4$ catalyst which shows the ratio of Ni to Fe of about 1:2.

Catalysts were analyzed by XRD (Rigaku Miniflex 600) using Cu-Kα radiation (λ = 1.54184 Å). $NiFeO_x$ samples with varying Fe concentrations of 5%, 7.5%, and 12.5% exhibit the NiO phase, characterized by five distinctive peaks at 2θ values of 37.36, 43.36, 63, 75.54, and 79.56. These peaks are assigned to the crystallographic planes (hkl) of (111), (200), (220), (311), and (222), respectively. The diffraction peaks have been matched and indexed to NiO using the JCPDS card number 78-0643, as depicted in Figure 7.2.

$NiFe_2O_4$ catalyst showed the typical diffraction pattern of $NiFe_2O_4$, with the main peak centered at 2θ 18.6, 30.5, 35.5, 37.5, 43.6, 54.3, 57.5 and 63.2 which are assigned to (111), (220), (311), (222), (400), (422), (511) and (440) respectively. The XRD data includes dashed lines representing the JCPDS standard for $NiFe_2O_4$. The JCPDS card number 22-1086 was used to match the diffraction lines of $NiFe_2O_4$.

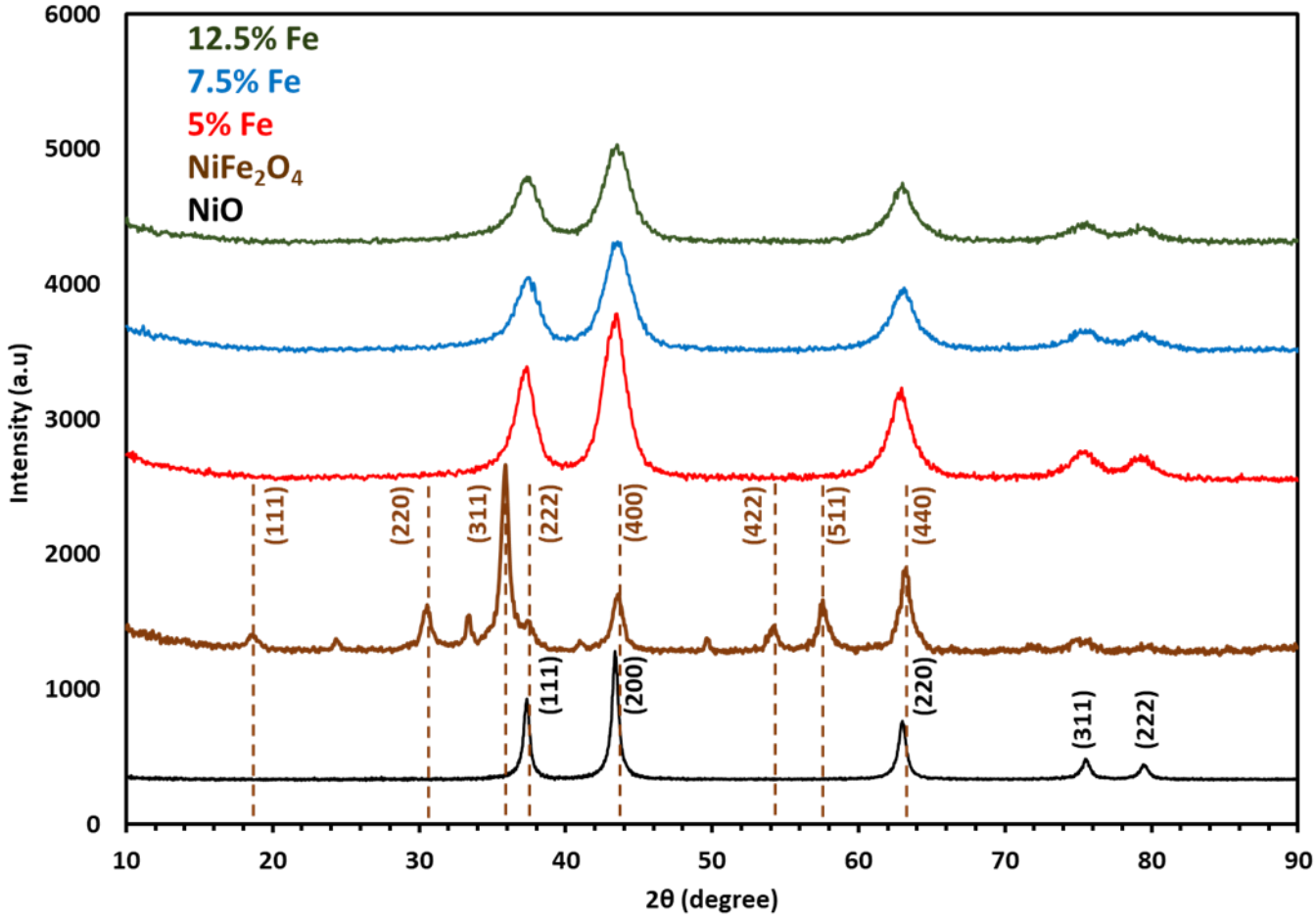


Figure 7.2. XRD of $NiFeO_x$ and $NiFe_2O_4$ catalysts.

7.3.1 Oxygen Evolution Reaction

To evaluate the catalytic activity of the $NiFeO_x$ catalyst, Linear sweep voltammetry was performed in 1M KOH. $NiFe_2O_4$ showed the highest catalytic activity with a current density of 135 mA cm^{-2}

at 1.8 V (Figure 7.3a). Figure 7.3b shows chrono potentiometry at the current density of 10 to 100 mA cm^{-2}. At each voltage, the operation was performed for 1 hour which shows the short-term stability of the catalyst at these conditions. The lowest overpotential was 409 mV and 416 mV for $NiFeO_x$ (5%) and $NiFe_2O_4$ catalysts, respectively. The highest overpotential was on $NiFeO_x$ (12.5%) which was 457 mV, followed by the overpotential of 419 mV over $NiFeO_x$ (7.5%). The catalyst performance was stable at a higher current density of 100 mA cm^{-2}, the overpotential were 852 mV and 858 mV for $NiFeO_x$(5%) and $NiFe_2O_4$, respectively. In both cases, the overpotential increased about two times compared to the OER performed at 10 mA cm^{-2}. These results showed that the catalysts are stable at high current density operation and well suited for AEM electrolysis. Several other studies using $NiFe_2O_4$ catalyst reported comparable results, $NiFe_2O_4$/N-graphene nanocomposite had an overpotential of 340 mV at 10 mA cm^{-2} [275]. $NiFe_2O_4$-12Pi has an overpotential of 332 mV at 10 mA cm^{-2}, and the same study determined the overpotential of pristine $NiFe_2O_4$ to be 443 mV at 10 mA cm^{-2} [276].

Tafel plots, as depicted in Figure 7.3c, were used to compare the efficiency of different catalysts. These plots represent the correlation between overpotential η and current density (i) in a logarithmic scale. The Tafel slope (b), derived from the linear segment of the plot, is indicative of the catalyst's activity. $NiFe_2O_4$ has a Tafel slope of 124 mV/dec and $NiFeO_x$ (12.5%) has a Tafel slope of 169 mV/dec. The Tafel slope of $NiFeO_x$ (5%) and $NiFeO_x$ (7.5%) were 144 mV dec^{-1} and 150 mV dec^{-1} respectively, which are in the same range. These results showed that $NiFe_2O_4$ catalyst is a relatively more active catalyst among the series of catalysts.

To test the activity and stability of $NiFe_2O_4$ catalysts for OER, a durability test was performed for 600 h as shown in Figure 7.3d. The test was performed at a current density of 50 mA/cm^2 the initial voltage was 1.739 V (vs RHE), during the 600-h operation, the voltage increased to 1.748 V. The

degradation rate or the voltage increase rate was 15 µV/h during the 600 h OER test. The stability of $NiFe_2O_4$ is reported in the literature with different compositions. A $NiO/NiFe_2O_4$ catalyst held at 100 mA cm^{-2} for 450 h showed considerable stability, although exact changes in voltage over the test were not provided [277]. S-$NiFe_2O_4$/IF showed good durability and minimal changes in voltages over 100 h at both 100 mA cm^{-2} and 500 mA cm^{-2} [278].

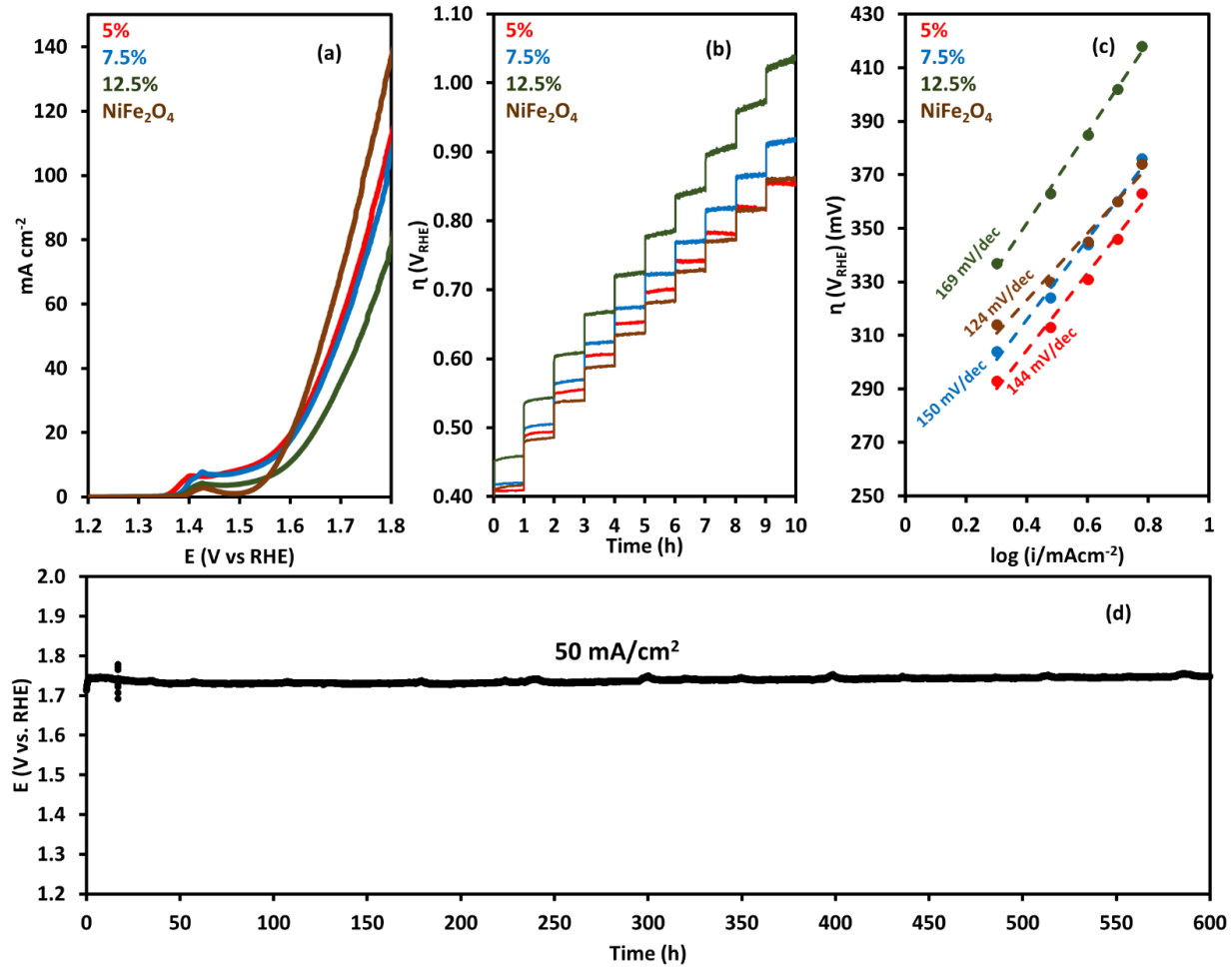


Figure 7.3. OER at room temperature in 1 M KOH with $NiFe_2O_4$ and $NiFeO_x$ catalysts (a) LSV with (85% iR-corrected). (b) Chronoamperometry at a current density range of 10 to 100 mA/cm^2 (c) Tafel plots (d) Durability test for 600 h at 50 mA/cm^2 with $NiFe_2O_4$ at the anode.

Figure 7.4 a-d shows the CV plot, the scan rate was from 25 to 250 mV/s and the voltage range was 0.967 V to 1.167 V (non-faradic region for water electrolysis). C_{dl}, the double layer

capacitance was calculated from the slope of scan rate vs current density plot as shown in Figure 7.5. The Electrochemical surface area (ECSA) was 75 cm^2, 77.5 cm^2, 82.5 cm^2, and 82.5 cm^2 for $NiFeO_x$ (5%Fe), $NiFeO_x$ (7.5%), $NiFeO_x$ (12.5% Fe), and $NiFe_2O_4$ catalysts respectively.

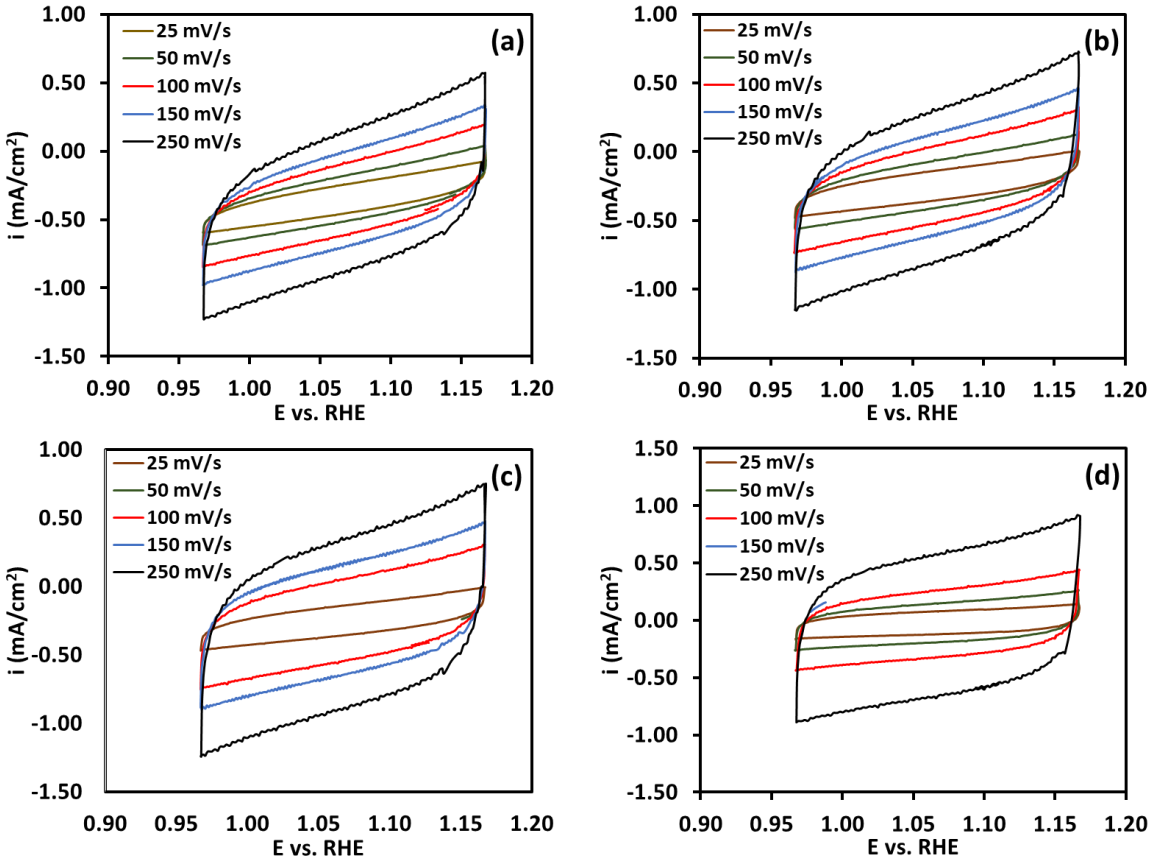


Figure 7.4. Cyclic voltammetry at different scan rates, the analysis was performed in non-faradic region. (a) $NiFeO_x$ (5% Fe), (b) $NiFeO_x$ (7.5% Fe), (c) $NiFeO_x$ (12.5% Fe) and (d) $NiFe_2O_4$.

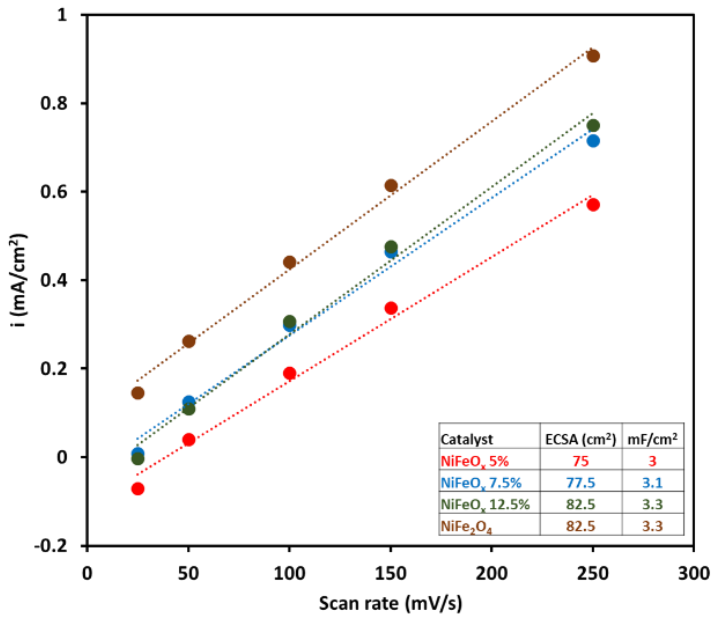


Figure 7.5. Double layer capacitance (C_{dl}), plot of scan rate vs current density for $NiFeO_x$ catalysts and $NiFe_2O_4$.

7.3.2 AEM electrolyzer tests with $NiFeO_x$ and $NiFe_2O_4$ catalysts

Single-cell tests were performed with $NiFeO_x$ catalyst at the anode and Pt/C at cathodes using Ni foam and carbon paper GDL respectively using (dioxide membrane X-37-50 grade T). The AEM X-37-50 T from Sustainion® exhibits high conductivity and stability in AEM water electrolysis [58,192]. The membrane comprises co-polymers of styrene and vinyl benzyl chloride supported by polytetrafluoroethylene (PTFE), incorporating imidazolium and pyridinium groups for ion exchange. Figure 7.6a shows polarization curves using $NiFe_2O_4$ catalyst and $NiFeO_x$ catalysts with Fe wt.% of 5wt.%, to 12.5wt.% at 45°C. $NiFe_2O_4$ showed the highest activity of 1100 mA cm^{-2} at 2.2 V. Other catalysts also showed good activity for AEM electrolysis, at the same voltage catalyst with 12.5 wt.% Fe had a current density of 921 mA cm^{-2}. The current density decreased to 842 mA cm^{-2} and 561 mA cm^{-2} for catalyst with Fe content of 7.5wt.% and 5wt%. Figure 7.6b shows the polarization curves at 55°C, for all the catalysts the activity increased with the increase in temperature. It follows the same trend in the activity of the catalysts for 45°C electrolysis

operation. $NiFe_2O_4$ shows the highest current density of 1503 mA cm^{-2} which is an increase of 36%. Current densities were 1098 mA cm^{-2}, 994 mA $cm^{-2,}$ and 885 mA cm^{-2} for the catalysts with 12.5wt.%, 7.5wt.%, and 5wt.% Fe content.

$NiFe_2O_4$ catalyst shows high current densities in AEM water electrolysis as reported in the literature. A current density of 1000 mA cm^{-2} was achieved at 1.85 V for AEM electrolysis using $NiFe_2O_4$ as the anode catalyst and Raney Nickel as the cathode catalyst in 1 M KOH solution, using a Sustainion X-37-50 T membrane at 60ºC, [279]. Additionally, a system using $NiFe_2O_4$ at the anode and 30 wt.% PtNi/ECS (Engineered Catalyst Support, carbon) at the cathode had a current density of 1000 mA cm^{-2} at 60ºC in 0.1M NaOH, using a GT72-10 with PTFE reinforcement with a thickness of 30 μm [280].

Temperature is an important factor in the performance of an AEM electrolyzer, that must be considered during catalyst performance analysis. Increased temperature results in lower overpotentials for any given current density, as well as increase the efficiency of the electrolyzer [281]. Furthermore, kinetics improved due to the reduced energy requirement for splitting water molecules as there is additional energy present within the system. Increased ionic conductivity at higher temperatures also plays a large role in increasing performance due to the increase in mobility of OH^- ions, increasing their availability for the redox reaction [282].

Chronoamperometry (CA) was used to measure the activity of the catalyst at a constant voltage. Figure 7.6c shows the chronoamperometry at 45ºC, and 55ºC, the voltage range was from 1.5 V to 2.3 V in time steps of 60 seconds. Figure 7.6c shows the CA results on the $NiFe_2O_4$ catalyst, the current density increased from 32 mA cm^{-2} to 1179 mA cm^{-2} when the voltage was increased in steps from 1.5 V to 2.3 V at 45ºC. The activity also increased when the operation was performed at a higher temperature of 55ºC, the highest current density at 2.3 V was 1568 mA cm^{-2}.

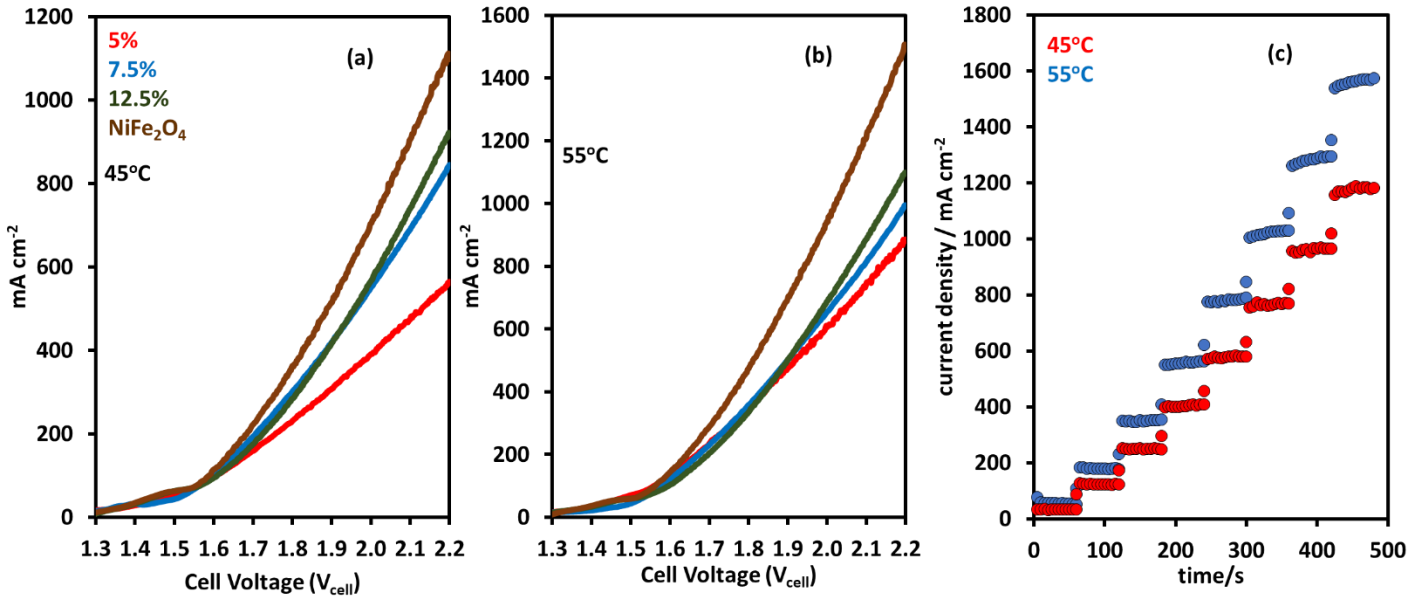


Figure 7.6. Linear Sweep Voltammetry at (a) 45°C, (b) 55°C. $NiFeO_x$ and $NiFe_2O_4$ catalysts were used at the anode. X-37-50 T membrane was used for AEM electrolysis. (c) Chronoamperometry at a voltage range of 1.5 to 2.3 V at 45°C and 55°C, with $NiFe_2O_4$ catalysts.

7.3.3 Effect of Anion exchange membranes on electrolyzer performance

Anion exchange membranes have a significant impact on the performance of AEM water electrolyzers, due to their critical role in their operation. The specific membrane choice can also play a large role in determining the performance of a system. Several characteristics determine the performance of a specific membrane, however, specifically predicting and ranking these membranes require experimental results and they are often system specific [59]. Maximizing ionic conductivity and stability while reducing specific resistance is essential to increase performance and viability. Mechanical stability frequently comes at the cost of lowering ionic conductivity [283]. This is because thinner membranes frequently exhibit better OH^- transfer and lower mass transport resistance [71]. The membrane manufacturer Fumatech offers various membranes with different characteristics and performances. Out of these membranes, the following are relevant to this study: FAA-3-50, FAS-50, FAA-3-PK-75, and FAB-PK-130.

The Fumasep FAA-3-50 is a membrane based on a brominated polysulfone backbone and uses quaternary ammonium (QA) side chain groups [284]. All mentioned Fumatech membranes come with a Br^- counter ion, however, this can be altered as specified in their technical data sheet. This membrane is comparatively thin, at 45-55 µm, It has very low specific area resistance at 0.6-1.5 Ω cm^2 and has a high specific conductivity of 3-8 mS cm^{-1} [285]. Table 7.1 shows the specifications of Fumasep membranes, the conductivities and area-specific resistance of the membranes were reported in Cl^- form. Fumasep FAS-50 membrane is composed of a propriety hydrocarbon resin and composition is not available. This membrane is similar to the FAA-3-50 in terms of performance specifications, with a thickness of 45-55 µm, specific area resistance of 0.6-1.5 Ω cm^2, and a high specific conductivity of 3-8 mS cm^{-1} [286]. FAA-3-PK-75 is also based on a polysulfone backbone with the same QA sidechains, alongside a poly-ketone (PK) reinforcement [287]. It has a thickness of 70-80 µm. This thickness, alongside its high specific area resistance of 1.2-2.0 Ω cm^2, results in a lower specific conductivity of 4.5-6.5 mS cm^{-1} [288]. The final membrane examined is the FAB-PK-130, composed of PK reinforced hydrocarbon resin [289]. This membrane was designed for high mechanical stability and stability in acidic and basic environments. The FAB-PK-130 is a much thicker membrane of 110-140 µm and as a result, has a very high specific area resistance of 5.0-9.0 Ω cm^2. This results in low specific conductivities of 1.0-2.5 mS cm^{-1}. The conductivity of Fumasep FAA-3-50 and X-37-50 membranes in KOH has been reported to be 40 and 80 mS cm^{-1} respectively, which is considerably higher than when the membrane's conductivity is reported in chloride [59].

Table 7.1. Specifications of Fumasep membranes [285,286,288,289].

Membrane	Thickness (μm)	Specific Conductivity in Cl^- (ms cm^{-1})	Specific Area resistance (Ω cm^2)
FAA-3-50	45-55	3-8	0.6-1.5
FAS-50	45-55	3-8	0.6-1.5
FAA-3-PK-75	70-80	4.5-6.5	1.2-2
FAB PK-130	110-140	1-2.5	5-9

To compare electrolyzer activity with different AEM, commercially available Fumasep membranes FAA-3-50, FAS-50, FAA-3-PK-75, and FAB PK-130 were used. The AEM electrolysis was performed at 45 and 55ºC with 1 M KOH, using $NiFe_2O_4$ catalyst at the anode and Pt/C catalyst at the cathode. FAA-3-50 MEA showed the highest current density of 1020 mA cm^{-2} at 2.2 V as shown in Figure 7.7a. FAS-50 MEA showed similar activity with a current density of 915 mA cm^{-2}. The activity with FAA-3-PK-75 was also high with a current density of 723 mA cm^{-2}, but the activity is slightly lower compared to other membranes. The lowest activity was with the FAB PK-130 membrane with a current density of 178 mA cm^{-2}.

At 55ºC the current density increased for each membrane but the trend in activity was the same as 45ºC Figure 7.7b. The MEA with FAA-3-50 and FAS-50 achieve the current density of 1174 mA cm^{-2} and 1161 mA cm^{-2} at 2.2 V. For FAA-3-PK-75 membrane current density increased to 857 mA cm^{-2} which is about 18% increase compared to 45ºC operation. The current density did not increase for FAB PK-130 membrane with the temperature rise, which means that this membrane is the least active for AEM electrolysis compared to other membranes used in this study.

The activities of the different membranes follow the trends predicted by their specific conductivity. The conductivity of the membrane strongly influences the overall activity of an AEM electrolyzer, as it allows easier passage of ions with minimal resistance, resulting in greater current densities. The higher specific conductivity of the FAA-3-50 and FAS-50 resulted in higher activity when

compared to FAA-3-PK-75 and FAB PK-130. This is corroborated by the results, where the FAA-3-50 and FAS-50 membranes show higher activity at 2.2 V and similar activities at 55^{o}C. Similarly, the comparatively lower conductivity of the FAA-3-PK-75, 1.5 ms cm^{-1} which is approximately 19% lower compared to FAA-3-50 and FAS-50, resulted in a notably reduced activity. The current density of 723 mA cm^{-2} achieved by the FAA-3-PK-75 membrane is lower than the current densities of the FAA-3-50 and FAS-50 of 1020 mA cm^{-2} and 915 mA cm^{-2} respectively, showing an approximate decrease in activity of 29% and 21%. The reduced conductivity of the FAB PK-130 resulted in a decrease in activity compared to all other membranes.

Studies with Fumatech membranes for AEM water electrolysis are reported in the literature. A Fumatech FAS-50 using $NiFe_2O_4$ anode catalyst and a NiFeCo cathode, in 1 M KOH solution at 60^{o}C, achieved a current density of 250 mA cm^{-2} at 1.8 V and 900 mA cm^{-2} at 2 V [290]. The same catalysts and solution using a FAA-3-50 membrane, achieved a similar 240 mA cm^{-2} at 1.8 V, current densities at 2 V were not provided. This is similar to the trends observed in this study but with higher current densities, with very similar results between FAS-50 and FAA-3-50. There is less literature available on FAA-3-PK-75 membranes for use in AEM applications. However, using a FAA-3-PK-75 membrane with an IrO2 anode catalyst and a Pt/C cathode catalyst, in a 1M KOH solution at various conditions, achieved current densities ranging from 293-983 mA cm^{-2} at 1.8 V depending on specific testing conditions [291].

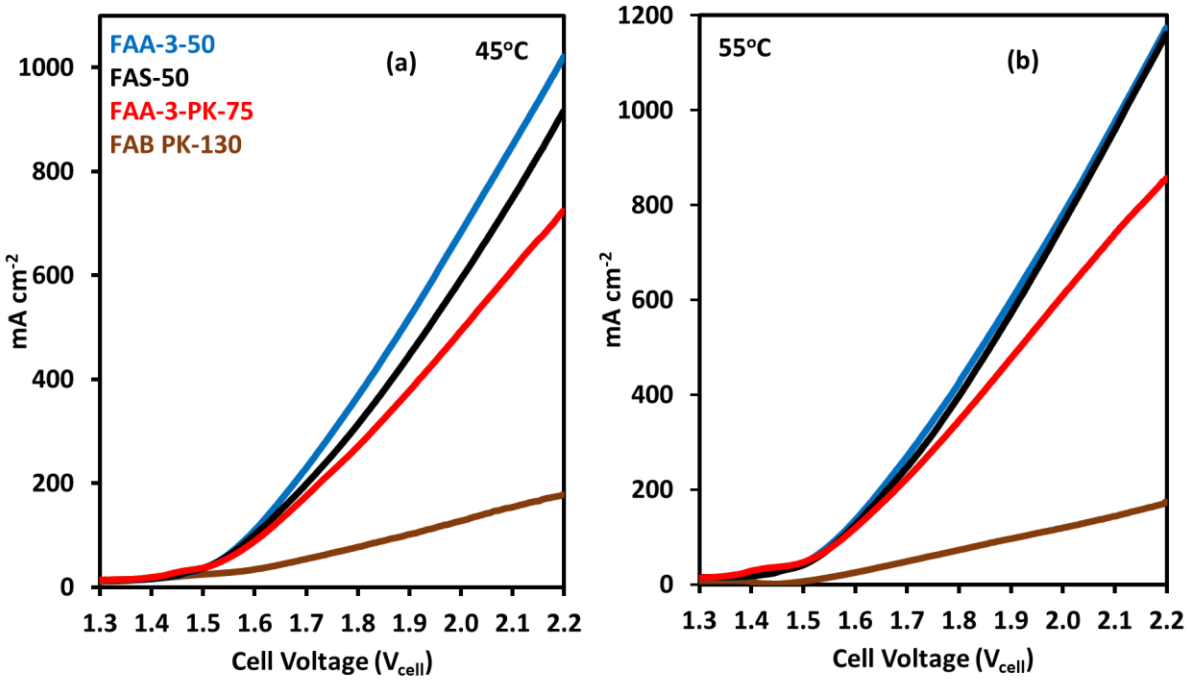


Figure 7.7. AEM electrolysis comparison using FAA-3-50, FAS-50, FAA-3-PK-75 and FAB PK-130 membranes at (a) 45°C and (b) 55°C, using $NiFe_2O_4$ catalyst at anode with 1M KOH as an electrolyte.

7.3.4 EIS effect of voltage and temperature

EIS analysis was performed on AEM electrolyzer cell operation at constant voltage, the analysis was performed at a temperature range of 45°C and 55°C. EIS analysis is performed to analyze the impedance associated with the electrolysis process. This analysis can provide information on the kinetic and mass transport processes that take place at cathode and anode. With this analysis resistance of electrolyte and membrane electrode assembly can also be evaluated [292].

Figure 7.8a shows the Nyquist plot for the EIS analysis performed at 45°C. The AEM electrolysis was carried out using $NiFe_2O_4$ catalyst at the anode and Pt/C at the cathode. At 2 V the diameter of the semicircle in the Nyquist plot is smaller compared to 1.7 V operation, which shows that it has lower activation resistance compared to AEM electrolysis at low voltages. In the Nyquist plot,

the (high-frequency region) x-intercept shows the ohmic resistance and the second x-intercept shows the total resistance, which has the contribution from ohmic resistance, activation resistance, and mass transport resistance [293]. Figure 7.8b shows a similar trend but the ohmic and activation resistances are relatively lower at 55^{o}C. The Nyquist plot obtained from the EIS analysis is fitted to the equivalent circuit and the results are presented in Table 7.2. An equivalent electrical circuit is shown in Figure 7.8a, which represents the components of the AEM electrolyzer. All the equivalent circuit components were the same as shown in earlier chapters.

Table 7.2 shows that with the increase in temperature of the AEM electrolyzer, there is a decrease in ohmic resistance, which can enhance the overall efficiency of the electrolysis process. The ohmic resistance decreased due to the improved conductivity of hydroxyl ions with the increase in temperature [294]. Table 7.2 shows that as the temperature rose from 45 to 55^{o}C, the activation resistance at both the anode and cathode decreased, from 0.101 Ω to 0.075 Ω at 2 V and from 0.055 Ω to 0.031 Ω at 2 V. With the increase in temperature, the reaction kinetics of the AEM electrolysis became faster as it overcomes the kinetic barrier of the reactions at both the cathode and anode [295,296]. At each voltage, the operation at 55^{o}C shows lower ohmic resistance compared to the 45^{o}C electrolysis operation.

Similar trends regarding the effect of temperature on the resistances of an AEM electrolyzer can be found in some of the AEM electrolysis studies. One study utilizing polybenzimidazole (PBI) AEM, and $NiFeO_x$ and NiFeCo catalysts for the anode and cathode respectively in 1M KOH, found that at 1.9 V the ohmic resistance decreased from 0.0178 Ω cm^{-2} at 30^{o}C to 0.0156 Ω cm^{-2} at 60^{o}C [182]. Similarly, in the same study, the activation resistance was lowered with an increase in temperature, decreasing from 0.023 Ω cm^{-2} at 30^{o}C to 0.0114 Ω cm^{-2}. Two other studies, one utilizing a Sustainion X37-50 and a NiFeCo cathode catalyst and the other a FAA3-50 with a 40%

Pt/C cathode catalyst, both in 1M KOH, similarly observed a significant decrease in both ohmic and activation resistance as the temperature increased from 30°C to 60°C [233,297].

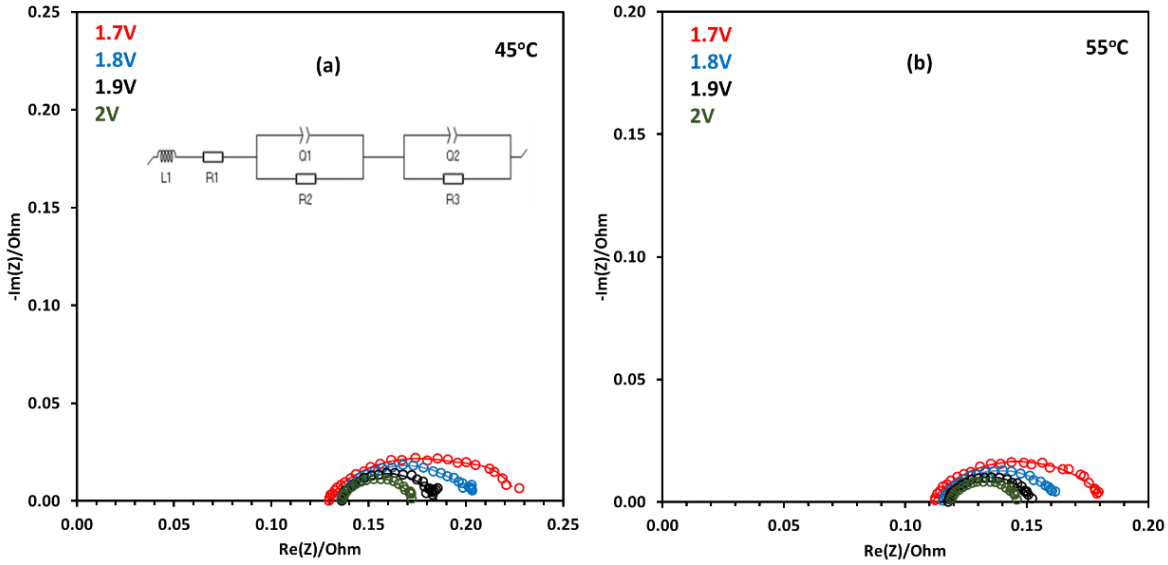


Figure 7.8. Nyquist plots for $NiFe_2O_4$ catalyst using FAA-3-50 membrane for water electrolysis at 45°C and 55°C.

Table 7.2. Results from fitting an equivalent circuit during electrolysis operations at temperatures of 45°C and 55°C using FAA-3-50 membrane, with $NiFe_2O_4$ catalyst.

Temperature	Ohmic resistance	Activation resistance
	$R_{ohm\ (\Omega)}$	$R_{anode}+ R_{cathode\ (\Omega)}$
1.7 V		
45°C	0.127	0.101
55°C	0.108	0.075
1.8 V		
45°C	0.133	0.077
55°C	0.115	0.071
1.9 V		
45°C	0.134	0.051
55°C	0.116	0.036
2 V		
45°C	0.134	0.055
55°C	0.117	0.031

7.3.5 EIS with different Anion Exchange Membranes

Figure 7.9 a-b shows the Nyquist plot at 55◦C for different membrane electrode assemblies at 1.7 V. The results of equivalent circuit fittings are presented in Table 7.3. The FAA-3-50 membrane showed the lowest activation resistance of 0.0756 Ω followed by FAS-50 with 0.0918 Ω. The other two membranes FAA-3-PK-75 had an activation resistance of 0.113 Ω and FAB-PK-130 which had very low electrolysis performance had a very high activation resistance of 0.199 Ω. Similar trends were seen in ohmic resistance with the lowest values on FAS-50 at 0.092 Ω and FAA-3-50 at 0.108 Ω. For AEM electrolysis these membranes showed a similar performance which can be due to similar resistances offered during the operation. These results showed that FAA-3-50 and FAS-50 had higher conductivity than the other AEM in similar operating conditions. It also shows that the membrane charge transfer between the membrane and catalyst layer is faster in these membranes compared to the low-performing membranes.

Among different membranes used for AEM electrolysis, X-37-50 displays considerably lower resistance possessing an activation resistance of 0.034 Ω compared to the 0.042 Ω of the FAS-50, 0.056 Ω of the PiperION, and 0.070 Ω of the FAA-3-50 at 50°C in 1M KOH using a NiFe-Based catalyst at the anode and a 20wt.% Pt/C cathode catalyst [298].

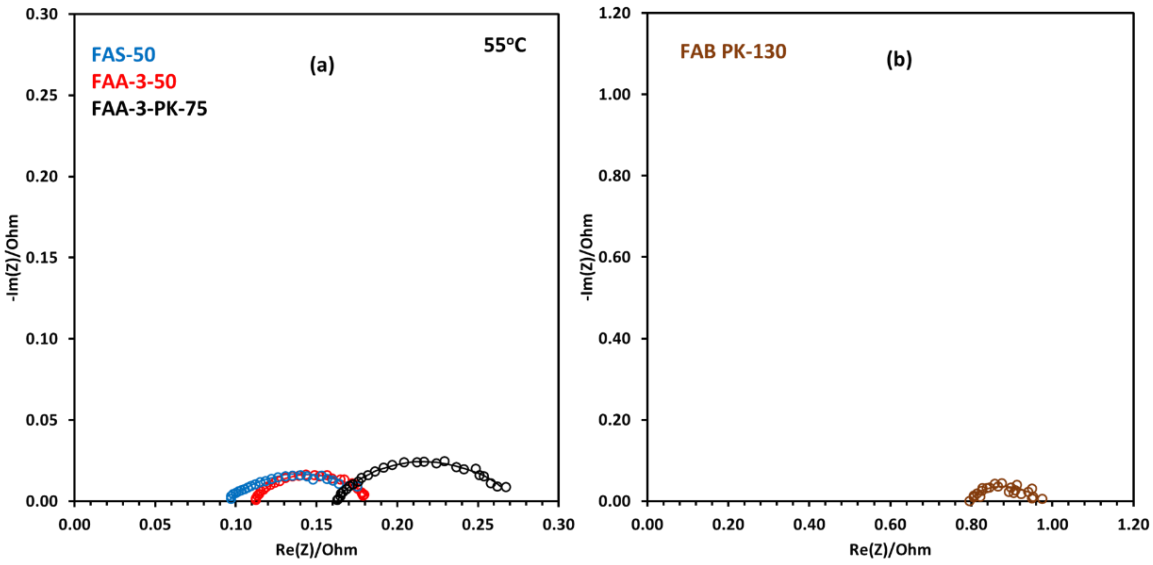


Figure 7.9. Nyquist plots for AEM electrolysis operation with different membranes at 1.7 V with $NiFe_2O_4$ catalyst at 55°C.

Table 7.3. Resistances evaluated from equivalent circuit fittings for AEM water electrolysis using different membranes with $NiFe_2O_4$ catalyst at 1.7 V.

Membranes	Ohmic resistance	Activation resistance
	$R_{ohm\ (\Omega)}$	$R_{anode} + R_{cathode\ (\Omega)}$
FAA-3-50	0.108	0.0756
FAS-50	0.092	0.0918
FAA-3-PK-75	0.16	0.113
FAB-PK-130	0.777	0.199

7.3.6 Durability Test

A durability test was performed for the AEM water electrolyzer using $NiFe_2O_4$ catalyst at the anode. The electrolyzer was operated at 400 mA/cm^2 for 12 h at 55°C. At this operating condition, the cell efficiency was 72%. A degradation rate of 0.833 mV/h was observed during the test, the initial voltage was 1.71 V which after 12 h of continuous operation increased to 1.72 V, as shown in Figure 7.10. The Faradic efficiency was 83%, calculated by dividing the amount of hydrogen

obtained from the electrolyzer by the amount of theoretical amount of hydrogen at these conditions. During the stability testing, the electrolyzer's performance remained stable.

AEM electrolyzers using $NiFe_2O_4$ catalysts show stability and durability over long-term testing. One study using a Sustainion X-37-50 membrane, and Raney nickel cathode catalyst, had a degradation rate of 0.7 μV/h at 1A cm^{-2} for over 1000 hours [279]. In that study, a 10% performance loss was reported after 298 h. Another study demonstrated no increase in voltage using a Sustainion X-37-50, NiFe metal-organic framework (MOF)-$NiFe_2O_4$ hybrid material as both anode and cathode catalysts. At 400 mA cm^{-2} the voltage decreased from 2.203 V to 2.193 V over 150 hours [299].

The durability of AEM affects the long-term testing of the electrolyzer operation, commercial membranes have been reported to show a loss in performance in long-term testing experiments in an alkaline medium [86]. Several key degradation pathways are common including, various S_N2 substitutions (benzyl, methyl), ring-opening, nucleophilic substitution, dehydroflourination of the backbone and nucleophilic addition and displacement, where specific mechanism and possibility of occurrence is determined by the composition of both functional groups and backbone, as well as testing conditions [300]. The most commonly used functional groups, quaternary ammonium groups, are particularly susceptible to Hofmann elimination and nucleophilic substitution, which result in the degradation of the cation groups and the formation of amines and olefins and alcohols respectively [301,302]. Another mechanism seen in various tetraalkylammonium hydroxides is chemical rearrangement caused by ylide formation [303–305]. Polymer backbones containing phenyl groups can experience degradation due to the oxidation of the backbone phenyl groups at OER potentials, leading to the formation of acidic phenols which can decrease solution pH and reduce conductivity [305,306]. One study by Arges et al. found that polysulfone based backbones

can become brittle and therefore mechanically unstable in alkaline solutions due to hydrolysis at both the ether and quaternary carbon groups when cation groups are attached to the benzyl position of the diphenyl propane group [303].

Catalysts can also cause an increase in voltage by deactivation, which can occur due to a variety of factors. Morphology changes are one such factor that has a significant impact on performance, where significant changes in structure can result in poor contact area between the catalyst and ionomer and significantly reduce catalyst utilization [307]. Catalyst dissolution is another significant contributing factor in the deactivation of catalysts, where the catalysts dissolve into the electrolyte solution, this effect is typically intensified or promoted with electrolyzer operation as opposed to innately when in the electrolyte [308]. Passivation is a frequently seen deactivation method, wherein an insulating layer is formed between the catalyst and electrode which inhibits the flow of electrons and therefore worsens cell performance [309,310]. In general, these factors typically depend on the specific catalyst used, however frequently many such mechanisms are present at once, increasing and contributing to overall degradation [311].

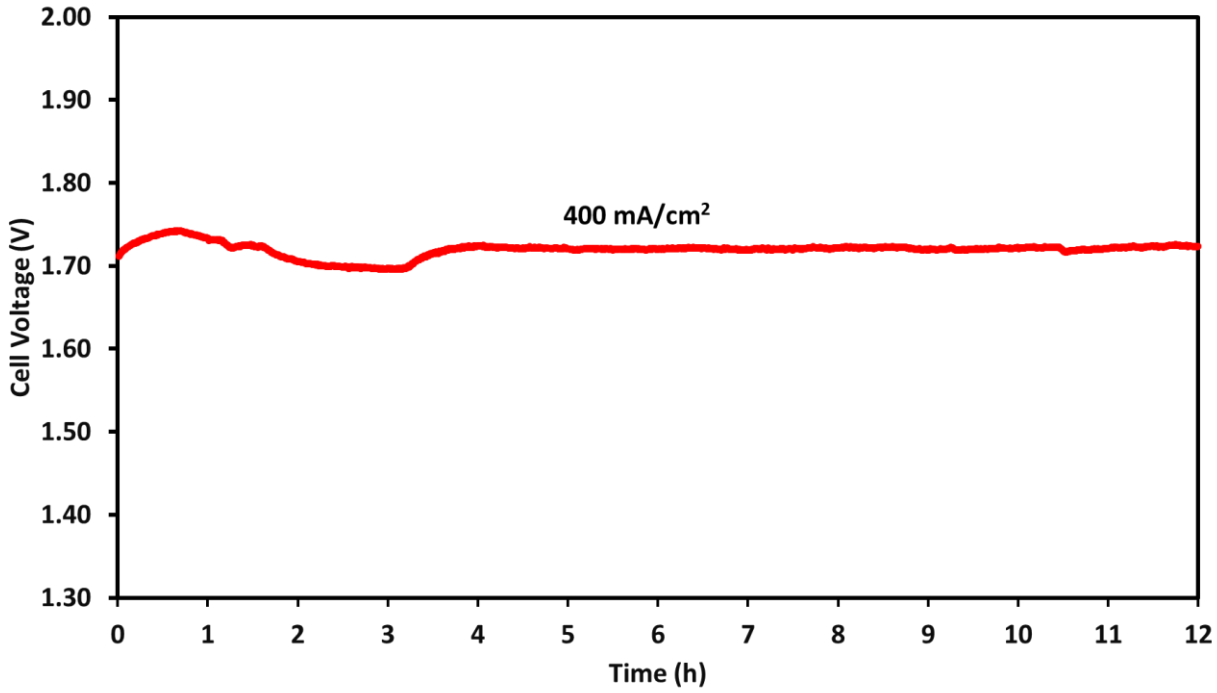


Figure 7.10. The durability test was at 400 mA/cm^2 for 12 h in 1M KOH using $NiFe_2O_4$ catalyst at the anode, electrolyzer was operated at 55^{o}C using X-37-50 grade T membrane.

7.4 Conclusion

This study has demonstrated the effectiveness of $NiFeO_x$ and $NiFe_2O_4$ catalysts for AEM water electrolysis. $NiFe_2O_4$ in stoichiometric ratio displayed the highest catalytic activity for OER achieving a current density of 135 mA cm^{-2} at 1.8 V. Similarly, it displayed the lowest Tafel slope at 124 mV dec^{-1} indicating that it possessed the most efficient electrochemical reaction kinetics. Low overpotentials of 416 and 409 mV were achieved for $NiFe_2O_4$ and $NiFeO_x$ (5%) respectively at 10 mA cm^{-2}. $NiFe_2O_4$ maintained stability and catalytic activity during the 600 h OER test at 50 mA/cm^2, over the stability testing period the degradation rate was 15 µV/h.

$NiFe_2O_4$ demonstrated the highest activity during AEM water electrolysis with a current density of 1100 mA cm^{-2} at 2.2 V at 45^{o}C. The current density increased with the increase in electrolysis temperature to 55^{o}C and all catalysts exhibited an increase in current density, with the $NiFe_2O_4$

catalyst achieving the highest current density of 1503 mA cm^{-2}. Several Fumatech membranes were tested for AEM water electrolysis, including the FAA-3-50, FAS-50, FAA-3-PK-75, and the FAB PK-130. It was shown that these membranes' activity and effectiveness strongly correlate with their ionic conductivity. The most effective membranes were the FAA-3-50 and FAS-50 which have comparable performance, the FAB PK-130 has the lowest activity compared to other membranes.

Electrochemical impedance spectroscopy and equivalent circuit fitting analysis were performed on an AEM electrolyzer to examine the impact of various operating parameters. By increasing the temperature from 40^{o}C to 55^{o}C, the ohmic resistance reduces. The observed decrease in activation resistance at both the anode and cathode, coupled with improved OH^- ion conductivity, indicates a faster reaction kinetics and lowered kinetic barriers. EIS results at 55°C and 1.7 V for various membrane electrode assemblies show distinct performance characteristics. FAA-3-50 and FAS-50 membranes showed lower activation and ohmic resistances, indicative of higher conductivity and faster membrane charge transfer. FAA-3-PK-75 exhibits intermediate performance, while FAB-PK-130 demonstrates poor AEM electrolysis performance with significantly higher resistances.

The 12 h durability test for the AEM electrolyzers demonstrated robust stability, with a minimal degradation rate of 0.833 mV/h. Throughout the test, the initial voltage of 1.71 V only increased marginally to 1.72 V. The energy efficiency, evaluated at 400 mA/cm^2, was 72%, indicating efficient hydrogen production during the entire duration of the durability test.

8 Conclusion and Future Work

This thesis provides detailed insights into the performance of various catalyst compositions and membrane types for OER and AEM water electrolysis. Catalyst durability was tested for prolonged duration of time for AEM electrolysis and OER.

In **Chapter 4**, the performance of various catalysts, including NiO, $NiFeO_x$, and $NiFeCoO_x$, for AEM water electrolysis was investigated. The results showed the superior performance of $NiFeCoO_x$ catalysts, attributed to the promotional effect of Co and Fe. Electrochemical impedance spectroscopy (EIS) analysis revealed a correlation between electrolyte concentration and electrolyzer performance, with higher concentrations leading to improved conductivity and reaction kinetics. Additionally, membrane comparison showed that X-37-50 membrane outperformed FAA-3-50, emphasizing the importance of membrane selection for enhanced electrolyzer efficiency.

Chapter 5 focused on the evaluation of different $NiCoO_x$ catalyst compositions for AEM water electrolysis. $NiCoO_x$ (1:3) with Ni to Co ratio of 1:3 emerged as the most promising catalyst, with high catalytic activity, low Tafel slope, and excellent stability over extended operation periods. EIS analysis showed the superior performance of $NiCoO_x$ (1:3) catalyst in terms of lower activation and ohmic resistances. Moreover, the increase in temperature was found to enhance electrolysis efficiency by reducing overall resistances. The durability test for OER was performed for 500 h with a very low deactivation rate, which also made this catalyst an ideal candidate for long-term operation. A long-term durability test for 30 h was performed for AEM electrolysis using the same catalyst and it had a low degradation rate of 0.68 mV/h during the electrolysis.

In Chapter 6, the catalytic activity of $NiFeCoO_x$ catalysts for AEM water electrolysis was investigated, with emphasis on the role of Fe content. Results indicated that $NiFeCoO_x$ (5% Fe) catalyst had excellent performance, showing high catalytic activity and stability. EIS analysis further confirmed the excellent performance of $NiFeCoO_x$ (5% Fe), highlighting lower activation and ohmic resistances. The durability test demonstrated stable operation, suggesting the reliability of NiFeCoOx (5% Fe) catalyst for high current density operations.

Chapter 7 examined the effectiveness of $NiFeO_x$ and $NiFe_2O_4$ catalysts for AEM water electrolysis. Among the series of $NiFeO_x$ catalysts with varied Fe composition, $NiFe_2O_4$ was the most active catalyst, demonstrating high catalytic activity, low overpotentials, and excellent stability over extended testing periods. Membrane comparison for AEM electrolysis revealed that FAA-3-50 and FAS-50 membranes displayed superior performance due to their higher ionic conductivity. EIS analysis highlighted the positive impact of higher temperatures on electrolyzer performance, with higher temperatures the resistance decreased, and overall efficiency was increased.

Future Work:

Exploration of Novel Catalyst Compositions:

Investigate additional catalyst compositions beyond those explored in this thesis, focusing on tuning the ratios of metal elements and exploring new combinations to enhance catalytic activity and stability for AEM water electrolysis. Layered double hydroxide (LDH) catalyst materials based on Ni and Co should be explored to decrease the overpotential of OER and the durability of AEM electrolysis. To improve the conductivity of the catalyst heteroatom doping of Ni and Co oxide catalysts with Mn, V, Fe, and Co should be studied in detail to improve electrocatalytic performance.

Research and Development for Advanced Membrane Materials:

Research and development of novel membrane materials with improved ion conductivity and durability to further enhance the performance of AEM electrolyzers. This could involve research on new materials, surface modifications, and fabrication techniques. Understanding of membrane degradation such as by neutrophilic and Hoffman should be understood in detail to know the interactions of hydroxyl ions with quaternary ammonium group and polymer backbone.

Long-term Durability Studies:

Perform extended durability testing under realistic operating conditions to assess catalysts and membranes' long-term stability and degradation mechanisms. Investigate strategies to decrease AEM degradation and prolong the operational lifespan of AEM electrolysis systems. Comprehensive characterization of the membrane should be performed before and after the durability test to understand the failure mechanism. Characterization of catalyst using SEM, TEM, and XPS before and after the long-term durability test to understand changes in catalyst structure during the electrolysis.

Integration with Renewable Energy Sources:

Explore the integration of AEM water electrolysis systems with renewable energy sources such as solar and wind to enable sustainable and carbon-neutral hydrogen production.

Letters of Copyright permission

ELSEVIER LICENSE
TERMS AND CONDITIONS

Sep 01, 2024

This Agreement between Khaja Wahab Ahmed ("You") and Elsevier ("Elsevier") consists of your license details and the terms and conditions provided by Elsevier and Copyright Clearance Center.

License Number	5860390022782
License date	Sep 01, 2024
Licensed Content Publisher	Elsevier
Licensed Content Publication	Progress in Energy and Combustion Science
Licensed Content Title	Recent progress in alkaline water electrolysis for hydrogen production and applications
Licensed Content Author	Kai Zeng,Dongke Zhang
Licensed Content Date	Jun 1, 2010
Licensed Content Volume	36
Licensed Content Issue	3
Licensed Content Pages	20
Start Page	307
End Page	326

Type of Use	reuse in a thesis/dissertation
Portion	figures/tables/illustrations
Number of figures/tables/illustrations	10
Format	both print and electronic
Are you the author of this Elsevier article?	No
Will you be translating?	No
Title of new work	Development and Evaluation of Nickel and Cobalt-Based Mixed Metal Oxide Catalysts for Anion Exchange Membrane Water Electrolysis
Institution name	University of Waterloo
Expected presentation date	Nov 2024
Portions	Figure 4 and Figure 10
The Requesting Person / Organization to Appear on the License	Khaja Wahab Ahmed
Requestor Location	Mr. Khaja Wahab Ahmed 300 Regina St N Waterloo, ON N2J 4H2 Canada Attn: Mr. Khaja Wahab Ahmed
Publisher Tax ID	GB 494 6272 12
Total	0.00 CAD

Terms and Conditions

INTRODUCTION

1. The publisher for this copyrighted material is Elsevier. By clicking "accept" in connection with completing this licensing transaction, you agree that the following terms and conditions apply to this transaction (along with the Billing and Payment terms and conditions established by Copyright Clearance Center, Inc. ("CCC"), at the time that you opened your RightsLink account and that are available at any time at https://myaccount.copyright.com).

GENERAL TERMS

2. Elsevier hereby grants you permission to reproduce the aforementioned material subject to the terms and conditions indicated.

3. Acknowledgement: If any part of the material to be used (for example, figures) has appeared in our publication with credit or acknowledgement to another source, permission must also be sought from that source. If such permission is not obtained then that material may not be included in your publication/copies. Suitable acknowledgement to the source must be made, either as a footnote or in a reference list at the end of your publication, as follows:

"Reprinted from Publication title, Vol /edition number, Author(s), Title of article / title of chapter, Pages No., Copyright (Year), with permission from Elsevier [OR APPLICABLE SOCIETY COPYRIGHT OWNER]." Also Lancet special credit - "Reprinted from The Lancet, Vol. number, Author(s), Title of article, Pages No., Copyright (Year), with permission from Elsevier."

4. Reproduction of this material is confined to the purpose and/or media for which permission is hereby given. The material may not be reproduced or used in any other way, including use in combination with an artificial intelligence tool (including to train an algorithm, test, process, analyse, generate output and/or develop any form of artificial intelligence tool), or to create any derivative work and/or service (including resulting from the use of artificial intelligence tools).

5. Altering/Modifying Material: Not Permitted. However figures and illustrations may be altered/adapted minimally to serve your work. Any other abbreviations, additions, deletions and/or any other alterations shall be made only with prior written authorization of Elsevier Ltd. (Please contact Elsevier's permissions helpdesk here). No modifications can be made to any Lancet figures/tables and they must be reproduced in full.

6. If the permission fee for the requested use of our material is waived in this instance, please be advised that your future requests for Elsevier materials may attract a fee.

7. Reservation of Rights: Publisher reserves all rights not specifically granted in the combination of (i) the license details provided by you and accepted in the course of this licensing transaction, (ii) these terms and conditions and (iii) CCC's Billing and Payment terms and conditions.

8. License Contingent Upon Payment: While you may exercise the rights licensed immediately upon issuance of the license at the end of the licensing process for the transaction, provided that you have disclosed complete and accurate details of your

proposed use, no license is finally effective unless and until full payment is received from you (either by publisher or by CCC) as provided in CCC's Billing and Payment terms and conditions. If full payment is not received on a timely basis, then any license preliminarily granted shall be deemed automatically revoked and shall be void as if never granted. Further, in the event that you breach any of these terms and conditions or any of CCC's Billing and Payment terms and conditions, the license is automatically revoked and shall be void as if never granted. Use of materials as described in a revoked license, as well as any use of the materials beyond the scope of an unrevoked license, may constitute copyright infringement and publisher reserves the right to take any and all action to protect its copyright in the materials.

9. Warranties: Publisher makes no representations or warranties with respect to the licensed material.

10. Indemnity: You hereby indemnify and agree to hold harmless publisher and CCC, and their respective officers, directors, employees and agents, from and against any and all claims arising out of your use of the licensed material other than as specifically authorized pursuant to this license.

11. No Transfer of License: This license is personal to you and may not be sublicensed, assigned, or transferred by you to any other person without publisher's written permission.

12. No Amendment Except in Writing: This license may not be amended except in a writing signed by both parties (or, in the case of publisher, by CCC on publisher's behalf).

13. Objection to Contrary Terms: Publisher hereby objects to any terms contained in any purchase order, acknowledgment, check endorsement or other writing prepared by you, which terms are inconsistent with these terms and conditions or CCC's Billing and Payment terms and conditions. These terms and conditions, together with CCC's Billing and Payment terms and conditions (which are incorporated herein), comprise the entire agreement between you and publisher (and CCC) concerning this licensing transaction. In the event of any conflict between your obligations established by these terms and conditions and those established by CCC's Billing and Payment terms and conditions, these terms and conditions shall control.

14. Revocation: Elsevier or Copyright Clearance Center may deny the permissions described in this License at their sole discretion, for any reason or no reason, with a full refund payable to you. Notice of such denial will be made using the contact information provided by you. Failure to receive such notice will not alter or invalidate the denial. In no event will Elsevier or Copyright Clearance Center be responsible or liable for any costs, expenses or damage incurred by you as a result of a denial of your permission request, other than a refund of the amount(s) paid by you to Elsevier and/or Copyright Clearance Center for denied permissions.

LIMITED LICENSE

The following terms and conditions apply only to specific license types:

15. **Translation**: This permission is granted for non-exclusive world **English** rights only unless your license was granted for translation rights. If you licensed translation rights you may only translate this content into the languages you requested. A professional translator must perform all translations and reproduce the content word for word preserving the integrity of the article.

16. **Posting licensed content on any Website**: The following terms and conditions apply as follows: Licensing material from an Elsevier journal: All content posted to the web site must maintain the copyright information line on the bottom of each image; A hyper-text must be included to the Homepage of the journal from which you are licensing at http://www.sciencedirect.com/science/journal/xxxxx or the Elsevier homepage for books at http://www.elsevier.com; Central Storage: This license does not include permission for a scanned version of the material to be stored in a central repository such as that provided by Heron/XanEdu.

Licensing material from an Elsevier book: A hyper-text link must be included to the Elsevier homepage at http://www.elsevier.com . All content posted to the web site must maintain the copyright information line on the bottom of each image.

Posting licensed content on Electronic reserve: In addition to the above the following clauses are applicable: The web site must be password-protected and made available only to bona fide students registered on a relevant course. This permission is granted for 1 year only. You may obtain a new license for future website posting.

17. **For journal authors:** the following clauses are applicable in addition to the above:

Preprints:

A preprint is an author's own write-up of research results and analysis, it has not been peer-reviewed, nor has it had any other value added to it by a publisher (such as formatting, copyright, technical enhancement etc.).

Authors can share their preprints anywhere at any time. Preprints should not be added to or enhanced in any way in order to appear more like, or to substitute for, the final versions of articles however authors can update their preprints on arXiv or RePEc with their Accepted Author Manuscript (see below).

If accepted for publication, we encourage authors to link from the preprint to their formal publication via its DOI. Millions of researchers have access to the formal publications on ScienceDirect, and so links will help users to find, access, cite and use the best available version. Please note that Cell Press, The Lancet and some society-owned have different preprint policies. Information on these policies is available on the journal homepage.

Accepted Author Manuscripts: An accepted author manuscript is the manuscript of an article that has been accepted for publication and which typically includes author-incorporated changes suggested during submission, peer review and editor-author communications.

Authors can share their accepted author manuscript:

- immediately
  - via their non-commercial person homepage or blog
  - by updating a preprint in arXiv or RePEc with the accepted manuscript
  - via their research institute or institutional repository for internal institutional uses or as part of an invitation-only research collaboration work-group
  - directly by providing copies to their students or to research collaborators for their personal use
  - for private scholarly sharing as part of an invitation-only work group on commercial sites with which Elsevier has an agreement
- After the embargo period

- via non-commercial hosting platforms such as their institutional repository
- via commercial sites with which Elsevier has an agreement

In all cases accepted manuscripts should:

- link to the formal publication via its DOI
- bear a CC-BY-NC-ND license - this is easy to do
- if aggregated with other manuscripts, for example in a repository or other site, be shared in alignment with our hosting policy not be added to or enhanced in any way to appear more like, or to substitute for, the published journal article.

Published journal article (JPA): A published journal article (PJA) is the definitive final record of published research that appears or will appear in the journal and embodies all value-adding publishing activities including peer review co-ordination, copy-editing, formatting, (if relevant) pagination and online enrichment.

Policies for sharing publishing journal articles differ for subscription and gold open access articles:

Subscription Articles: If you are an author, please share a link to your article rather than the full-text. Millions of researchers have access to the formal publications on ScienceDirect, and so links will help your users to find, access, cite, and use the best available version.

Theses and dissertations which contain embedded PJAs as part of the formal submission can be posted publicly by the awarding institution with DOI links back to the formal publications on ScienceDirect.

If you are affiliated with a library that subscribes to ScienceDirect you have additional private sharing rights for others' research accessed under that agreement. This includes use for classroom teaching and internal training at the institution (including use in course packs and courseware programs), and inclusion of the article for grant funding purposes.

Gold Open Access Articles: May be shared according to the author-selected end-user license and should contain a CrossMark logo, the end user license, and a DOI link to the formal publication on ScienceDirect.

Please refer to Elsevier's posting policy for further information.

18. **For book authors** the following clauses are applicable in addition to the above: Authors are permitted to place a brief summary of their work online only. You are not allowed to download and post the published electronic version of your chapter, nor may you scan the printed edition to create an electronic version. **Posting to a repository:** Authors are permitted to post a summary of their chapter only in their institution's repository.

19. **Thesis/Dissertation**: If your license is for use in a thesis/dissertation your thesis may be submitted to your institution in either print or electronic form. Should your thesis be published commercially, please reapply for permission. These requirements include permission for the Library and Archives of Canada to supply single copies, on demand, of the complete thesis and include permission for Proquest/UMI to supply single copies, on demand, of the complete thesis. Should your thesis be published commercially, please reapply for permission. Theses and dissertations which contain embedded PJAs as part of the formal submission can be posted publicly by the awarding institution with DOI links back to the formal publications on ScienceDirect.

Elsevier Open Access Terms and Conditions

You can publish open access with Elsevier in hundreds of open access journals or in nearly 2000 established subscription journals that support open access publishing. Permitted third party re-use of these open access articles is defined by the author's choice of Creative Commons user license. See our open access license policy for more information.

Terms & Conditions applicable to all Open Access articles published with Elsevier:

Any reuse of the article must not represent the author as endorsing the adaptation of the article nor should the article be modified in such a way as to damage the author's honour or reputation. If any changes have been made, such changes must be clearly indicated.

The author(s) must be appropriately credited and we ask that you include the end user license and a DOI link to the formal publication on ScienceDirect.

If any part of the material to be used (for example, figures) has appeared in our publication with credit or acknowledgement to another source it is the responsibility of the user to ensure their reuse complies with the terms and conditions determined by the rights holder.

Additional Terms & Conditions applicable to each Creative Commons user license:

CC BY: The CC-BY license allows users to copy, to create extracts, abstracts and new works from the Article, to alter and revise the Article and to make commercial use of the Article (including reuse and/or resale of the Article by commercial entities), provided the user gives appropriate credit (with a link to the formal publication through the relevant DOI), provides a link to the license, indicates if changes were made and the licensor is not represented as endorsing the use made of the work. The full details of the license are available at http://creativecommons.org/licenses/by/4.0.

CC BY NC SA: The CC BY-NC-SA license allows users to copy, to create extracts, abstracts and new works from the Article, to alter and revise the Article, provided this is not done for commercial purposes, and that the user gives appropriate credit (with a link to the formal publication through the relevant DOI), provides a link to the license, indicates if changes were made and the licensor is not represented as endorsing the use made of the work. Further, any new works must be made available on the same conditions. The full details of the license are available at http://creativecommons.org/licenses/by-nc-sa/4.0.

CC BY NC ND: The CC BY-NC-ND license allows users to copy and distribute the Article, provided this is not done for commercial purposes and further does not permit distribution of the Article if it is changed or edited in any way, and provided the user gives appropriate credit (with a link to the formal publication through the relevant DOI), provides a link to the license, and that the licensor is not represented as endorsing the use made of the work. The full details of the license are available at http://creativecommons.org/licenses/by-nc-nd/4.0. Any commercial reuse of Open Access articles published with a CC BY NC SA or CC BY NC ND license requires permission from Elsevier and will be subject to a fee.

Commercial reuse includes:

- Associating advertising with the full text of the Article
- Charging fees for document delivery or access
- Article aggregation
- Systematic distribution via e-mail lists or share buttons

Posting or linking by commercial companies for use by customers of those companies.

20. **Other Conditions**:

v1.10

Questions? customercare@copyright.com.

JOHN WILEY AND SONS LICENSE
TERMS AND CONDITIONS

Sep 01, 2024

This Agreement between Khaja Wahab Ahmed ("You") and John Wiley and Sons ("John Wiley and Sons") consists of your license details and the terms and conditions provided by John Wiley and Sons and Copyright Clearance Center.

License Number	5860390604426
License date	Sep 01, 2024
Licensed Content Publisher	John Wiley and Sons
Licensed Content Publication	ChemCatChem
Licensed Content Title	Universality in Oxygen Evolution Electrocatalysis on Oxide Surfaces
Licensed Content Author	Jan Rossmeisl, Jens K. Nørskov, Thomas F. Jaramillo, et al
Licensed Content Date	Mar 16, 2011
Licensed Content Volume	3
Licensed Content Issue	7
Licensed Content Pages	7
Type of use	Dissertation/Thesis
Requestor type	University/Academic

Format	Print and electronic
Portion	Figure/table
Number of figures/tables	2
Will you be translating?	No
Title of new work	Development and Evaluation of Nickel and Cobalt-Based Mixed Metal Oxide Catalysts for Anion Exchange Membrane Water Electrolysis
Institution name	University of Waterloo
Expected presentation date	Nov 2024
Portions	Figure 3a and Figure 4a
The Requesting Person / Organization to Appear on the License	Khaja Wahab Ahmed
Requestor Location	Mr. Khaja Wahab Ahmed 300 Regina St N Waterloo, ON N2J 4H2 Canada Attn: Mr. Khaja Wahab Ahmed
Publisher Tax ID	EU826007151
Total	0.00 CAD

Terms and Conditions

TERMS AND CONDITIONS

This copyrighted material is owned by or exclusively licensed to John Wiley & Sons, Inc. or one of its group companies (each a"Wiley Company") or handled on behalf of a society

with which a Wiley Company has exclusive publishing rights in relation to a particular work (collectively "WILEY"). By clicking "accept" in connection with completing this licensing transaction, you agree that the following terms and conditions apply to this transaction (along with the billing and payment terms and conditions established by the Copyright Clearance Center Inc., ("CCC's Billing and Payment terms and conditions"), at the time that you opened your RightsLink account (these are available at any time at http://myaccount.copyright.com).

Terms and Conditions

- The materials you have requested permission to reproduce or reuse (the "Wiley Materials") are protected by copyright.

- You are hereby granted a personal, non-exclusive, non-sub licensable (on a stand-alone basis), non-transferable, worldwide, limited license to reproduce the Wiley Materials for the purpose specified in the licensing process. This license, **and any CONTENT (PDF or image file) purchased as part of your order,** is for a one-time use only and limited to any maximum distribution number specified in the license. The first instance of republication or reuse granted by this license must be completed within two years of the date of the grant of this license (although copies prepared before the end date may be distributed thereafter). The Wiley Materials shall not be used in any other manner or for any other purpose, beyond what is granted in the license. Permission is granted subject to an appropriate acknowledgement given to the author, title of the material/book/journal and the publisher. You shall also duplicate the copyright notice that appears in the Wiley publication in your use of the Wiley Material. Permission is also granted on the understanding that nowhere in the text is a previously published source acknowledged for all or part of this Wiley Material. Any third party content is expressly excluded from this permission.

- With respect to the Wiley Materials, all rights are reserved. Except as expressly granted by the terms of the license, no part of the Wiley Materials may be copied, modified, adapted (except for minor reformatting required by the new Publication), translated, reproduced, transferred or distributed, in any form or by any means, and no derivative works may be made based on the Wiley Materials without the prior permission of the respective copyright owner.**For STM Signatory Publishers clearing permission under the terms of the STM Permissions Guidelines only, the terms of the license are extended to include subsequent editions and for editions in other languages, provided such editions are for the work as a whole in situ and does not involve the separate exploitation of the permitted figures or extracts,** You may not alter, remove or suppress in any manner any copyright, trademark or other notices displayed by the Wiley Materials. You may not license, rent, sell, loan, lease, pledge, offer as security, transfer or assign the Wiley Materials on a stand-alone basis, or any of the rights granted to you hereunder to any other person.

- The Wiley Materials and all of the intellectual property rights therein shall at all times remain the exclusive property of John Wiley & Sons Inc, the Wiley Companies, or their respective licensors, and your interest therein is only that of having possession of and the right to reproduce the Wiley Materials pursuant to Section 2 herein during the continuance of this Agreement. You agree that you own no right, title or interest in or to the Wiley Materials or any of the intellectual property rights therein. You shall have no rights hereunder other than the license as

provided for above in Section 2. No right, license or interest to any trademark, trade name, service mark or other branding ("Marks") of WILEY or its licensors is granted hereunder, and you agree that you shall not assert any such right, license or interest with respect thereto

- NEITHER WILEY NOR ITS LICENSORS MAKES ANY WARRANTY OR REPRESENTATION OF ANY KIND TO YOU OR ANY THIRD PARTY, EXPRESS, IMPLIED OR STATUTORY, WITH RESPECT TO THE MATERIALS OR THE ACCURACY OF ANY INFORMATION CONTAINED IN THE MATERIALS, INCLUDING, WITHOUT LIMITATION, ANY IMPLIED WARRANTY OF MERCHANTABILITY, ACCURACY, SATISFACTORY QUALITY, FITNESS FOR A PARTICULAR PURPOSE, USABILITY, INTEGRATION OR NON-INFRINGEMENT AND ALL SUCH WARRANTIES ARE HEREBY EXCLUDED BY WILEY AND ITS LICENSORS AND WAIVED BY YOU.

- WILEY shall have the right to terminate this Agreement immediately upon breach of this Agreement by you.

- You shall indemnify, defend and hold harmless WILEY, its Licensors and their respective directors, officers, agents and employees, from and against any actual or threatened claims, demands, causes of action or proceedings arising from any breach of this Agreement by you.

- IN NO EVENT SHALL WILEY OR ITS LICENSORS BE LIABLE TO YOU OR ANY OTHER PARTY OR ANY OTHER PERSON OR ENTITY FOR ANY SPECIAL, CONSEQUENTIAL, INCIDENTAL, INDIRECT, EXEMPLARY OR PUNITIVE DAMAGES, HOWEVER CAUSED, ARISING OUT OF OR IN CONNECTION WITH THE DOWNLOADING, PROVISIONING, VIEWING OR USE OF THE MATERIALS REGARDLESS OF THE FORM OF ACTION, WHETHER FOR BREACH OF CONTRACT, BREACH OF WARRANTY, TORT, NEGLIGENCE, INFRINGEMENT OR OTHERWISE (INCLUDING, WITHOUT LIMITATION, DAMAGES BASED ON LOSS OF PROFITS, DATA, FILES, USE, BUSINESS OPPORTUNITY OR CLAIMS OF THIRD PARTIES), AND WHETHER OR NOT THE PARTY HAS BEEN ADVISED OF THE POSSIBILITY OF SUCH DAMAGES. THIS LIMITATION SHALL APPLY NOTWITHSTANDING ANY FAILURE OF ESSENTIAL PURPOSE OF ANY LIMITED REMEDY PROVIDED HEREIN.

- Should any provision of this Agreement be held by a court of competent jurisdiction to be illegal, invalid, or unenforceable, that provision shall be deemed amended to achieve as nearly as possible the same economic effect as the original provision, and the legality, validity and enforceability of the remaining provisions of this Agreement shall not be affected or impaired thereby.

- The failure of either party to enforce any term or condition of this Agreement shall not constitute a waiver of either party's right to enforce each and every term and condition of this Agreement. No breach under this agreement shall be deemed waived or excused by either party unless such waiver or consent is in writing signed by the party granting such waiver or consent. The waiver by or consent of a party to a breach of any provision of this Agreement shall not operate or be construed as a waiver of or consent to any other or subsequent breach by such other party.

- This Agreement may not be assigned (including by operation of law or otherwise) by you without WILEY's prior written consent.
- Any fee required for this permission shall be non-refundable after thirty (30) days from receipt by the CCC.
- These terms and conditions together with CCC's Billing and Payment terms and conditions (which are incorporated herein) form the entire agreement between you and WILEY concerning this licensing transaction and (in the absence of fraud) supersedes all prior agreements and representations of the parties, oral or written. This Agreement may not be amended except in writing signed by both parties. This Agreement shall be binding upon and inure to the benefit of the parties' successors, legal representatives, and authorized assigns.
- In the event of any conflict between your obligations established by these terms and conditions and those established by CCC's Billing and Payment terms and conditions, these terms and conditions shall prevail.
- WILEY expressly reserves all rights not specifically granted in the combination of (i) the license details provided by you and accepted in the course of this licensing transaction, (ii) these terms and conditions and (iii) CCC's Billing and Payment terms and conditions.
- This Agreement will be void if the Type of Use, Format, Circulation, or Requestor Type was misrepresented during the licensing process.
- This Agreement shall be governed by and construed in accordance with the laws of the State of New York, USA, without regards to such state's conflict of law rules. Any legal action, suit or proceeding arising out of or relating to these Terms and Conditions or the breach thereof shall be instituted in a court of competent jurisdiction in New York County in the State of New York in the United States of America and each party hereby consents and submits to the personal jurisdiction of such court, waives any objection to venue in such court and consents to service of process by registered or certified mail, return receipt requested, at the last known address of such party.

WILEY OPEN ACCESS TERMS AND CONDITIONS

Wiley Publishes Open Access Articles in fully Open Access Journals and in Subscription journals offering Online Open. Although most of the fully Open Access journals publish open access articles under the terms of the Creative Commons Attribution (CC BY) License only, the subscription journals and a few of the Open Access Journals offer a choice of Creative Commons Licenses. The license type is clearly identified on the article.

The Creative Commons Attribution License

The Creative Commons Attribution License (CC-BY) allows users to copy, distribute and transmit an article, adapt the article and make commercial use of the article. The CC-BY license permits commercial and non-

Creative Commons Attribution Non-Commercial License

The Creative Commons Attribution Non-Commercial (CC-BY-NC)License permits use, distribution and reproduction in any medium, provided the original work is properly cited

and is not used for commercial purposes.(see below)

Creative Commons Attribution-Non-Commercial-NoDerivs License

The Creative Commons Attribution Non-Commercial-NoDerivs License (CC-BY-NC-ND) permits use, distribution and reproduction in any medium, provided the original work is properly cited, is not used for commercial purposes and no modifications or adaptations are made. (see below)

Use by commercial "for-profit" organizations

Use of Wiley Open Access articles for commercial, promotional, or marketing purposes requires further explicit permission from Wiley and will be subject to a fee.

Further details can be found on Wiley Online Library
http://olabout.wiley.com/WileyCDA/Section/id-410895.html

Other Terms and Conditions:

v1.10 Last updated September 2015

Questions? customercare@copyright.com.

References

[1] K. Hirose, Handbook of hydrogen storage: new materials for future energy storage, John Wiley & Sons, 2010.

[2] J.A. Turner, Sustainable hydrogen production, Science 305 (2004) 972–974. https://doi.org/10.1126/science.1103197.

[3] S. Dunn, Hydrogen futures: toward a sustainable energy system, Int. J. Hydrog. Energy 27 (2002) 235–264.

[4] J. Chi, H. Yu, Water electrolysis based on renewable energy for hydrogen production, Chin. J. Catal. 39 (2018) 390–394.

[5] T.L. LeValley, A.R. Richard, M. Fan, The progress in water gas shift and steam reforming hydrogen production technologies–A review, Int. J. Hydrog. Energy 39 (2014) 16983–17000.

[6] C. Smith, A.K. Hill, L. Torrente-Murciano, Current and future role of Haber–Bosch ammonia in a carbon-free energy landscape, Energy Environ. Sci. 13 (2020) 331–344.

[7] A. Midilli, I. Dincer, Hydrogen as a renewable and sustainable solution in reducing global fossil fuel consumption, Int. J. Hydrog. Energy 33 (2008) 4209–4222.

[8] I. Vincent, D. Bessarabov, Low cost hydrogen production by anion exchange membrane electrolysis: A review, Renew. Sustain. Energy Rev. 81 (2018) 1690–1704.

[9] H.A. Miller, K. Bouzek, J. Hnat, S. Loos, C.I. Bernäcker, T. Weißgärber, L. Röntzsch, J. Meier-Haack, Green hydrogen from anion exchange membrane water electrolysis: a review of recent developments in critical materials and operating conditions, Sustain. Energy Fuels 4 (2020) 2114–2133.

[10] D. Li, E.J. Park, W. Zhu, Q. Shi, Y. Zhou, H. Tian, Y. Lin, A. Serov, B. Zulevi, E.D. Baca, Highly quaternized polystyrene ionomers for high performance anion exchange membrane water electrolysers, Nat. Energy 5 (2020) 378–385.

[11] M.K. Cho, A. Lim, S.Y. Lee, H.-J. Kim, S.J. Yoo, Y.-E. Sung, H.S. Park, J.H. Jang, A review on membranes and catalysts for anion exchange membrane water electrolysis single cells, J. Electrochem. Sci. Technol. 8 (2017) 183–196.

[12] J. Mo, R.R. Dehoff, W.H. Peter, T.J. Toops, J.B. Green Jr, F.-Y. Zhang, Additive manufacturing of liquid/gas diffusion layers for low-cost and high-efficiency hydrogen production, Int. J. Hydrog. Energy 41 (2016) 3128–3135.

[13] G. Chisholm, P.J. Kitson, N.D. Kirkaldy, L.G. Bloor, L. Cronin, 3D printed flow plates for the electrolysis of water: an economic and adaptable approach to device manufacture, Energy Environ. Sci. 7 (2014) 3026–3032.

[14] S. Song, H. Zhang, X. Ma, Z. Shao, R.T. Baker, B. Yi, Electrochemical investigation of electrocatalysts for the oxygen evolution reaction in PEM water electrolyzers, Int. J. Hydrog. Energy 33 (2008) 4955–4961.

[15] B. Han, S.M. Steen III, J. Mo, F.-Y. Zhang, Electrochemical performance modeling of a proton exchange membrane electrolyzer cell for hydrogen energy, Int. J. Hydrog. Energy 40 (2015) 7006–7016.

[16] R.J. Ouimet, J.R. Glenn, D. De Porcellinis, A.R. Motz, M. Carmo, K.E. Ayers, The Role of Electrocatalysts in the Development of Gigawatt-Scale PEM Electrolyzers, ACS Catal. 12 (2022) 6159–6171.

[17] B. Motealleh, Z. Liu, R.I. Masel, J.P. Sculley, Z.R. Ni, L. Meroueh, Next-generation anion exchange membrane water electrolyzers operating for commercially relevant lifetimes, Int. J. Hydrog. Energy 46 (2021) 3379–3386.

[18] A.Y. Faid, A.O. Barnett, F. Seland, S. Sunde, NiCu mixed metal oxide catalyst for alkaline hydrogen evolution in anion exchange membrane water electrolysis, Electrochimica Acta 371 (2021) 137837.

[19] I. Vincent, A. Kruger, D. Bessarabov, Development of efficient membrane electrode assembly for low cost hydrogen production by anion exchange membrane electrolysis, Int. J. Hydrog. Energy 42 (2017) 10752–10761.

[20] J. Parrondo, C.G. Arges, M. Niedzwiecki, E.B. Anderson, K.E. Ayers, V. Ramani, Degradation of anion exchange membranes used for hydrogen production by ultrapure water electrolysis, Rsc Adv. 4 (2014) 9875–9879.

[21] K. Ayers, N. Danilovic, R. Ouimet, M. Carmo, B. Pivovar, M. Bornstein, Perspectives on low-temperature electrolysis and potential for renewable hydrogen at scale, Annu. Rev. Chem. Biomol. Eng. 10 (2019) 219–239.

[22] J. Durst, A. Siebel, C. Simon, F. Hasché, J. Herranz, H. Gasteiger, New insights into the electrochemical hydrogen oxidation and evolution reaction mechanism, Energy Environ. Sci. 7 (2014) 2255–2260.

[23] W. Sheng, H.A. Gasteiger, Y. Shao-Horn, Hydrogen oxidation and evolution reaction kinetics on platinum: acid vs alkaline electrolytes, J. Electrochem. Soc. 157 (2010) B1529.

[24] M. David, C. Ocampo-Martínez, R. Sánchez-Peña, Advances in alkaline water electrolyzers: A review, J. Energy Storage 23 (2019) 392–403.

[25] M. Bodner, A. Hofer, V. Hacker, H_2 generation from alkaline electrolyzer, Wiley Interdiscip. Rev. Energy Environ. 4 (2015) 365–381.

[26] F. Barbir, PEM electrolysis for production of hydrogen from renewable energy sources, Sol. Energy 78 (2005) 661–669.

[27] M. Carmo, D.L. Fritz, J. Mergel, D. Stolten, A comprehensive review on PEM water electrolysis, Int. J. Hydrog. Energy 38 (2013) 4901–4934.

[28] J.-Y. Wang, W.-T. Liu, X.-P. Li, T. Ouyang, Z.-Q. Liu, Strong hydrophilicity NiS_2/Fe_7S_8 heterojunctions encapsulated in N-doped carbon nanotubes for enhanced oxygen evolution reaction, Chem. Commun. 56 (2020) 1489–1492.

[29] J. Li, M. Yan, X. Zhou, Z.-Q. Huang, Z. Xia, C.-R. Chang, Y. Ma, Y. Qu, Mechanistic insights on ternary $Ni_{2-x}Co_xP$ for hydrogen evolution and their hybrids with graphene as highly efficient and robust catalysts for overall water splitting, Adv. Funct. Mater. 26 (2016) 6785–6796.

[30] X.-T. Wang, T. Ouyang, L. Wang, J.-H. Zhong, Z.-Q. Liu, Surface reorganization on electrochemically-induced Zn–Ni–Co spinel oxides for enhanced oxygen electrocatalysis, Angew. Chem. 132 (2020) 6554–6561.

[31] M.W. Kanan, D.G. Nocera, In situ formation of an oxygen-evolving catalyst in neutral water containing phosphate and Co^{2+}, Science 321 (2008) 1072–1075.

[32] D. Zhao, Z. Zhuang, X. Cao, C. Zhang, Q. Peng, C. Chen, Y. Li, Atomic site electrocatalysts for water splitting, oxygen reduction and selective oxidation, Chem. Soc. Rev. 49 (2020) 2215–2264.

[33] P. Shirvanian, F. van Berkel, Novel components in Proton Exchange Membrane (PEM) Water Electrolyzers (PEMWE): Status, challenges and future needs. A mini review, Electrochem. Commun. 114 (2020) 106704.

[34] T. Wang, X. Cao, L. Jiao, PEM water electrolysis for hydrogen production: fundamentals, advances, and prospects, Carbon Neutrality 1 (2022) 21.

[35] Z. Chen, L. Guo, L. Pan, T. Yan, Z. He, Y. Li, C. Shi, Z.-F. Huang, X. Zhang, J.-J. Zou, Advances in oxygen evolution electrocatalysts for proton exchange membrane water electrolyzers, Adv. Energy Mater. 12 (2022) 2103670.

[36] L. Li, P. Wang, Q. Shao, X. Huang, Recent progress in advanced electrocatalyst design for acidic oxygen evolution reaction, Adv. Mater. 33 (2021) 2004243.

[37] J. Huot, M.L. Trudeau, R. Schulz, Low hydrogen overpotential nanocrystalline Ni-Mo cathodes for alkaline water electrolysis, J. Electrochem. Soc. 138 (1991) 1316.

[38] E. Zoulias, E. Varkaraki, N. Lymberopoulos, C.N. Christodoulou, G.N. Karagiorgis, A review on water electrolysis, Tcjst 4 (2004) 41–71.

[39] G. Yang, S. Yu, J. Mo, Z. Kang, Y. Dohrmann, F.A. List III, J.B. Green Jr, S.S. Babu, F.-Y. Zhang, Bipolar plate development with additive manufacturing and protective coating for durable and high-efficiency hydrogen production, J. Power Sources 396 (2018) 590–598.

[40] A. Gago, S. Ansar, B. Saruhan, U. Schulz, P. Lettenmeier, N.A. Cañas, P. Gazdzicki, T. Morawietz, R. Hiesgen, J. Arnold, Protective coatings on stainless steel bipolar plates for proton exchange membrane (PEM) electrolysers, J. Power Sources 307 (2016) 815–825.

[41] L. Jiang, S.-J. Ji, H.-G. Xue, N.-T. Suen, HER activity of M_xNi_{1-x} (M= Cr, Mo and W; x≈ 0.2) alloy in acid and alkaline media, Int. J. Hydrog. Energy 45 (2020) 17533–17539.

[42] P. Chen, X. Hu, High-efficiency anion exchange membrane water electrolysis employing non-noble metal catalysts, Adv. Energy Mater. 10 (2020) 2002285.

[43] C. Li, J.-B. Baek, Recent advances in noble metal (Pt, Ru, and Ir)-based electrocatalysts for efficient hydrogen evolution reaction, ACS Omega 5 (2019) 31–40.

[44] S.-Y. Bae, J. Mahmood, I.-Y. Jeon, J.-B. Baek, Recent advances in ruthenium-based electrocatalysts for the hydrogen evolution reaction, Nanoscale Horiz. 5 (2020) 43–56.

[45] F. Bao, E. Kemppainen, I. Dorbandt, R. Bors, F. Xi, R. Schlatmann, R. van de Krol, S. Calnan, Understanding the Hydrogen Evolution Reaction Kinetics of Electrodeposited Nickel-Molybdenum in Acidic, Near-Neutral, and Alkaline Conditions, ChemElectroChem 8 (2021) 195–208.

[46] P. Quaino, F. Juarez, E. Santos, W. Schmickler, Volcano plots in hydrogen electrocatalysis–uses and abuses, Beilstein J. Nanotechnol. 5 (2014) 846–854.

[47] Z. Chen, X. Duan, W. Wei, S. Wang, B.-J. Ni, Recent advances in transition metal-based electrocatalysts for alkaline hydrogen evolution, J. Mater. Chem. A 7 (2019) 14971–15005.

[48] J.O. Bockris, Kinetics of activation controlled consecutive electrochemical reactions: anodic evolution of oxygen, J. Chem. Phys. 24 (1956) 817–827.

[49] E. Fabbri, A. Habereder, K. Waltar, R. Kötz, T.J. Schmidt, Developments and perspectives of oxide-based catalysts for the oxygen evolution reaction, Catal. Sci. Technol. 4 (2014) 3800–3821.

[50] Y. Matsumoto, E. Sato, Electrocatalytic properties of transition metal oxides for oxygen evolution reaction, Mater. Chem. Phys. 14 (1986) 397–426.

[51] W.H. Smyrl, J.O.M. Bockris, B.E. Conway, E. Yeager, R.E. White, Comprehensive Treatise of Electrochemistry, Plenum Press N. Y. 4 (1981) 116.

[52] R.P. Viswanath, A patent for generation of electrolytic hydrogen by a cost effective and cheaper route, Int. J. Hydrog. Energy 29 (2004) 1191–1194.

[53] K. Zeng, D. Zhang, Recent progress in alkaline water electrolysis for hydrogen production and applications, Prog. Energy Combust. Sci. 36 (2010) 307–326.

[54] K. Oldham, J. Myland, Fundamentals of electrochemical science, Elsevier, 2012.

[55] A.J. Bard, L.R. Faulkner, H.S. White, Electrochemical methods: fundamentals and applications, John Wiley & Sons, 2022.

[56] T.H. Pham, J.S. Olsson, P. Jannasch, Poly (arylene alkylene) s with pendant N-spirocyclic quaternary ammonium cations for anion exchange membranes, J. Mater. Chem. A 6 (2018) 16537–16547.

[57] J.S. Olsson, T.H. Pham, P. Jannasch, Poly (arylene piperidinium) hydroxide ion exchange membranes: synthesis, alkaline stability, and conductivity, Adv. Funct. Mater. 28 (2018) 1702758.

[58] Z. Liu, S.D. Sajjad, Y. Gao, H. Yang, J.J. Kaczur, R.I. Masel, The effect of membrane on an alkaline water electrolyzer, Int. J. Hydrog. Energy 42 (2017) 29661–29665.

[59] D. Henkensmeier, M. Najibah, C. Harms, J. Žitka, J. Hnát, K. Bouzek, Overview: State-of-the art commercial membranes for anion exchange membrane water electrolysis, J. Electrochem. Energy Convers. Storage 18 (2021) 024001.

[60] K. Min, Y. Lee, Y. Choi, O.J. Kwon, T.-H. Kim, High-performance anion exchange membranes achieved by crosslinking two aryl ether-free polymers: poly(bibenzyl N-methyl piperidine) and SEBS, J. Membr. Sci. 664 (2022) 121071. https://doi.org/10.1016/j.memsci.2022.121071.

[61] T. Huang, G. He, J. Xue, O. Otoo, X. He, H. Jiang, J. Zhang, Y. Yin, Z. Jiang, J.C. Douglin, Self-crosslinked blend alkaline anion exchange membranes with bi-continuous phase separated morphology to enhance ion conductivity, J. Membr. Sci. 597 (2020) 117769.

[62] M. Kumari, J.C. Douglin, D.R. Dekel, Crosslinked quaternary phosphonium-functionalized poly (ether ether ketone) polymer-based anion-exchange membranes, J. Membr. Sci. 626 (2021) 119167.

[63] J. Xue, X. Liu, J. Zhang, Y. Yin, M.D. Guiver, Poly (phenylene oxide) s incorporating N-spirocyclic quaternary ammonium cation/cation strings for anion exchange membranes, J. Membr. Sci. 595 (2020) 117507.

[64] J. Fan, S. Willdorf-Cohen, E.M. Schibli, Z. Paula, W. Li, T.J. Skalski, A.T. Sergeenko, A. Hohenadel, B.J. Frisken, E. Magliocca, Poly (bis-arylimidazoliums) possessing high hydroxide ion exchange capacity and high alkaline stability, Nat. Commun. 10 (2019) 2306.

[65] H.A. Kostalik IV, T.J. Clark, N.J. Robertson, P.F. Mutolo, J.M. Longo, H.D. Abruna, G.W. Coates, Solvent processable tetraalkylammonium-functionalized polyethylene for use as an alkaline anion exchange membrane, Macromolecules 43 (2010) 7147–7150.

[66] D.R. Dekel, Alkaline membrane fuel cell (AMFC) materials and system improvement-state-of-the-art, Ecs Trans. 50 (2013) 2051.

[67] N. Ataollahi, K. Vezzù, G. Nawn, G. Pace, G. Cavinato, F. Girardi, P. Scardi, V. Di Noto, R. Di Maggio, A polyketone-based anion exchange membrane for electrochemical applications: synthesis and characterization, Electrochimica Acta 226 (2017) 148–157.

[68] N. Ataollahi, F. Girardi, E. Cappelletto, K. Vezzù, V. Di Noto, P. Scardi, E. Callone, R. Di Maggio, Chemical modification and structural rearrangements of polyketone-based polymer membrane, J. Appl. Polym. Sci. 134 (2017) 45485.

[69] T.P. Pandey, A.M. Maes, H.N. Sarode, B.D. Peters, S. Lavina, K. Vezzu, Y. Yang, S.D. Poynton, J.R. Varcoe, S. Seifert, Interplay between water uptake, ion interactions, and

conductivity in an e-beam grafted poly (ethylene-co-tetrafluoroethylene) anion exchange membrane, Phys. Chem. Chem. Phys. 17 (2015) 4367–4378.

[70] V. Di Noto, G.A. Giffin, K. Vezzu, G. Nawn, F. Bertasi, T. Tsai, A.M. Maes, S. Seifert, E.B. Coughlin, A.M. Herring, Interplay between solid state transitions, conductivity mechanisms, and electrical relaxations in a [PVBTMA][Br]-b-PMB diblock copolymer membrane for electrochemical applications, Phys. Chem. Chem. Phys. 17 (2015) 31125–31139.

[71] I. Pushkareva, A. Pushkarev, S. Grigoriev, P. Modisha, D. Bessarabov, Comparative study of anion exchange membranes for low-cost water electrolysis, Int. J. Hydrog. Energy 45 (2020) 26070–26079.

[72] C.C. Pavel, F. Cecconi, C. Emiliani, S. Santiccioli, A. Scaffidi, S. Catanorchi, M. Comotti, Highly efficient platinum group metal free based membrane-electrode assembly for anion exchange membrane water electrolysis, Angew. Chem. Int. Ed. 53 (2014) 1378–1381.

[73] A. Carbone, S.C. Zignani, I. Gatto, S. Trocino, A. Aricò, Assessment of the FAA3-50 polymer electrolyte in combination with a $NiMn2O_4$ anode catalyst for anion exchange membrane water electrolysis, Int. J. Hydrog. Energy 45 (2020) 9285–9292.

[74] P. Fortin, T. Khoza, X. Cao, S.Y. Martinsen, A.O. Barnett, S. Holdcroft, High-performance alkaline water electrolysis using Aemion^{TM} anion exchange membranes, J. Power Sources 451 (2020) 227814.

[75] J.R. Varcoe, R.C. Slade, Prospects for alkaline anion-exchange membranes in low temperature fuel cells, Fuel Cells 5 (2005) 187–200.

[76] J.B. Edson, C.S. Macomber, B.S. Pivovar, J.M. Boncella, Hydroxide based decomposition pathways of alkyltrimethylammonium cations, J. Membr. Sci. 399 (2012) 49–59.

[77] D. Li, I. Matanovic, A.S. Lee, E.J. Park, C. Fujimoto, H.T. Chung, Y.S. Kim, Phenyl oxidation impacts the durability of alkaline membrane water electrolyzer, ACS Appl. Mater. Interfaces 11 (2019) 9696–9701.

[78] D. Aili, M.R. Kraglund, J. Tavacoli, C. Chatzichristodoulou, J.O. Jensen, Polysulfone-polyvinylpyrrolidone blend membranes as electrolytes in alkaline water electrolysis, J. Membr. Sci. 598 (2020) 117674.

[79] A.N. Colli, H.H. Girault, A. Battistel, Non-precious electrodes for practical alkaline water electrolysis, Materials 12 (2019) 1336.

[80] S. Grigoriev, P. Millet, S. Volobuev, V. Fateev, Optimization of porous current collectors for PEM water electrolysers, Int. J. Hydrog. Energy 34 (2009) 4968–4973.

[81] J. Mo, S. Steen, Z. Kang, G. Yang, D.A. Taylor, Y. Li, T.J. Toops, M.P. Brady, S.T. Retterer, D.A. Cullen, Study on corrosion migrations within catalyst-coated membranes of proton exchange membrane electrolyzer cells, Int. J. Hydrog. Energy 42 (2017) 27343–27349.

[82] H. Ito, T. Maeda, A. Nakano, A. Kato, T. Yoshida, Influence of pore structural properties of current collectors on the performance of proton exchange membrane electrolyzer, Electrochimica Acta 100 (2013) 242–248.

[83] S.M. Steen III, J. Mo, Z. Kang, G. Yang, F.-Y. Zhang, Investigation of titanium liquid/gas diffusion layers in proton exchange membrane electrolyzer cells, Int. J. Green Energy 14 (2017) 162–170.

[84] C.M. Hwang, M. Ishida, H. Ito, T. Maeda, A. Nakano, A. Kato, T. Yoshida, Effect of titanium powder loading in gas diffusion layer of a polymer electrolyte unitized reversible fuel cell, J. Power Sources 202 (2012) 108–113.

[85] X. Wu, K. Scott, A Li-doped Co_3O_4 oxygen evolution catalyst for non-precious metal alkaline anion exchange membrane water electrolysers, Int. J. Hydrog. Energy 38 (2013) 3123–3129.

[86] D. Li, A.R. Motz, C. Bae, C. Fujimoto, G. Yang, F.-Y. Zhang, K.E. Ayers, Y.S. Kim, Durability of anion exchange membrane water electrolyzers, Energy Environ. Sci. (2021).

[87] K. Li, S. Yu, D. Li, L. Ding, W. Wang, Z. Xie, E.J. Park, C. Fujimoto, D.A. Cullen, Y.S. Kim, Engineered thin diffusion layers for anion-exchange membrane electrolyzer cells with outstanding performance, ACS Appl. Mater. Interfaces 13 (2021) 50957–50964.

[88] S. Seetharaman, R. Balaji, K. Ramya, K. Dhathathreyan, M. Velan, Graphene oxide modified non-noble metal electrode for alkaline anion exchange membrane water electrolyzers, Int. J. Hydrog. Energy 38 (2013) 14934–14942.

[89] F. Arbabi, A. Kalantarian, R. Abouatallah, R. Wang, J. Wallace, A. Bazylak, Feasibility study of using microfluidic platforms for visualizing bubble flows in electrolyzer gas diffusion layers, J. Power Sources 258 (2014) 142–149.

[90] G.-C. Chen, T.H. Wondimu, H.-C. Huang, K.-C. Wang, C.-H. Wang, Microwave-assisted facile synthesis of cobalt iron oxide nanocomposites for oxygen production using alkaline

anion exchange membrane water electrolysis, Int. J. Hydrog. Energy 44 (2019) 10174–10181.

[91] Q. Xu, S.Z. Oener, G. Lindquist, H. Jiang, C. Li, S.W. Boettcher, Integrated reference electrodes in anion-exchange-membrane electrolyzers: impact of stainless-steel gas-diffusion layers and internal mechanical pressure, ACS Energy Lett. 6 (2020) 305–312.

[92] K.K. Rao, Y. Lai, L. Zhou, J.A. Haber, M. Bajdich, J.M. Gregoire, Overcoming hurdles in oxygen evolution catalyst discovery via codesign, Chem. Mater. 34 (2022) 899–910.

[93] M. Jafarian, O. Azizi, F. Gobal, M. Mahjani, Kinetics and electrocatalytic behavior of nanocrystalline CoNiFe alloy in hydrogen evolution reaction, Int. J. Hydrog. Energy 32 (2007) 1686–1693.

[94] F. Safizadeh, E. Ghali, G. Houlachi, Electrocatalysis developments for hydrogen evolution reaction in alkaline solutions–a review, Int. J. Hydrog. Energy 40 (2015) 256–274.

[95] X. Wu, K. Scott, A polymethacrylate-based quaternary ammonium OH− ionomer binder for non-precious metal alkaline anion exchange membrane water electrolysers, J. Power Sources 214 (2012) 124–129.

[96] S.H. Ahn, B.-S. Lee, I. Choi, S.J. Yoo, H.-J. Kim, E. Cho, D. Henkensmeier, S.W. Nam, S.-K. Kim, J.H. Jang, Development of a membrane electrode assembly for alkaline water electrolysis by direct electrodeposition of nickel on carbon papers, Appl. Catal. B Environ. 154 (2014) 197–205.

[97] S.H. Ahn, H.-Y. Park, I. Choi, S.J. Yoo, S.J. Hwang, H.-J. Kim, E. Cho, C.W. Yoon, H. Park, H. Son, Electrochemically fabricated NiCu alloy catalysts for hydrogen production in alkaline water electrolysis, Int. J. Hydrog. Energy 38 (2013) 13493–13501.

[98] M. Fang, W. Gao, G. Dong, Z. Xia, S. Yip, Y. Qin, Y. Qu, J.C. Ho, Hierarchical NiMo-based 3D electrocatalysts for highly-efficient hydrogen evolution in alkaline conditions, Nano Energy 27 (2016) 247–254.

[99] S. Chu, W. Chen, G. Chen, J. Huang, R. Zhang, C. Song, X. Wang, C. Li, K.K. Ostrikov, Holey Ni-Cu phosphide nanosheets as a highly efficient and stable electrocatalyst for hydrogen evolution, Appl. Catal. B Environ. 243 (2019) 537–545.

[100] C. González-Buch, I. Herraiz-Cardona, E. Ortega, J. García-Antón, V. Pérez-Herranz, Synthesis and characterization of macroporous Ni, Co and Ni–Co electrocatalytic deposits

for hydrogen evolution reaction in alkaline media, Int. J. Hydrog. Energy 38 (2013) 10157–10169.

[101] M. Xia, T. Lei, N. Lv, N. Li, Synthesis and electrocatalytic hydrogen evolution performance of Ni–Mo–Cu alloy coating electrode, Int. J. Hydrog. Energy 39 (2014) 4794–4802.

[102] L. Xiao, S. Zhang, J. Pan, C. Yang, M. He, L. Zhuang, J. Lu, First implementation of alkaline polymer electrolyte water electrolysis working only with pure water, Energy Environ. Sci. 5 (2012) 7869–7871.

[103] X. Tang, L. Xiao, C. Yang, J. Lu, L. Zhuang, Noble fabrication of Ni–Mo cathode for alkaline water electrolysis and alkaline polymer electrolyte water electrolysis, Int. J. Hydrog. Energy 39 (2014) 3055–3060.

[104] I. Herraiz-Cardona, E. Ortega, J.G. Antón, V. Pérez-Herranz, Assessment of the roughness factor effect and the intrinsic catalytic activity for hydrogen evolution reaction on Ni-based electrodeposits, Int. J. Hydrog. Energy 36 (2011) 9428–9438.

[105] A. Döner, İ. Karcı, G. Kardaş, Effect of C-felt supported Ni, Co and NiCo catalysts to produce hydrogen, Int. J. Hydrog. Energy 37 (2012) 9470–9476.

[106] I. Herraiz-Cardona, E. Ortega, V. Pérez-Herranz, Impedance study of hydrogen evolution on Ni/Zn and Ni–Co/Zn stainless steel based electrodeposits, Electrochimica Acta 56 (2011) 1308–1315.

[107] C. Lupi, A. Dell'Era, M. Pasquali, Nickel–cobalt electrodeposited alloys for hydrogen evolution in alkaline media, Int. J. Hydrog. Energy 34 (2009) 2101–2106.

[108] H. Suffredini, J. Cerne, F. Crnkovic, S. Machado, L. Avaca, Recent developments in electrode materials for water electrolysis, Int. J. Hydrog. Energy 25 (2000) 415–423.

[109] S. Martinez, M. Metikoš-Huković, L. Valek, Electrocatalytic properties of electrodeposited Ni–15Mo cathodes for the HER in acid solutions: Synergistic electronic effect, J. Mol. Catal. Chem. 245 (2006) 114–121.

[110] N. Krstajić, V.D. Jović, L. Gajić-Krstajić, B.M. Jović, A. Antozzi, G. Martelli, Electrodeposition of Ni–Mo alloy coatings and their characterization as cathodes for hydrogen evolution in sodium hydroxide solution, Int. J. Hydrog. Energy 33 (2008) 3676–3687.

[111] E. Navarro-Flores, Z. Chong, S. Omanovic, Characterization of Ni, NiMo, NiW and NiFe electroactive coatings as electrocatalysts for hydrogen evolution in an acidic medium, J. Mol. Catal. Chem. 226 (2005) 179–197.

[112] J. Jakšić, M. Vojnović, N. Krstajić, Kinetic analysis of hydrogen evolution at Ni–Mo alloy electrodes, Electrochimica Acta 45 (2000) 4151–4158.

[113] R. Solmaz, G. Kardaş, Electrochemical deposition and characterization of NiFe coatings as electrocatalytic materials for alkaline water electrolysis, Electrochimica Acta 54 (2009) 3726–3734.

[114] C. Fan, D. Piron, A. Sleb, P. Paradis, Study of Electrodeposited Nickel-Molybdenum, Nickel-Tungsten, Cobalt-Molybdenum, and Cobalt-Tungsten as Hydrogen Electrodes in Alkaline Water Electrolysis, J. Electrochem. Soc. 141 (1994) 382.

[115] S.L. Suib, New and future developments in catalysis: hybrid materials, composites, and organocatalysts, Newnes, 2013.

[116] A.Y. Faid, A.O. Barnett, F. Seland, S. Sunde, Optimized nickel-cobalt and nickel-iron oxide catalysts for the hydrogen evolution reaction in alkaline water electrolysis, J. Electrochem. Soc. 166 (2019) F519.

[117] J.J. Kaczur, H. Yang, Z. Liu, S.D. Sajjad, R.I. Masel, Carbon dioxide and water electrolysis using new alkaline stable anion membranes, Front. Chem. 6 (2018) 263.

[118] M.E. LYONS, The oxygen evolution reaction on passive oxide covered transition metal electrodes in alkaline solution. Part 2-Cobalt., (2008).

[119] M.E. LYONS, The oxygen evolution reaction on passive oxide covered transition metal electrodes in alkaline solution. Part III-Iron., (2008).

[120] M.E. LYONS, The oxygen evolution reaction on passive oxide covered transition metal electrodes in aqueous alkaline solution. Part 1-Nickel, (2008).

[121] M. Li, Y. Xiong, X. Liu, X. Bo, Y. Zhang, C. Han, L. Guo, Facile synthesis of electrospun MFe_2O_4 (M= Co, Ni, Cu, Mn) spinel nanofibers with excellent electrocatalytic properties for oxygen evolution and hydrogen peroxide reduction, Nanoscale 7 (2015) 8920–8930.

[122] I. Nikolov, R. Darkaoui, E. Zhecheva, R. Stoyanova, N. Dimitrov, T. Vitanov, Electrocatalytic activity of spinel related cobalties $M_xCo_{3-x}O_4$ (M= Li, Ni, Cu) in the oxygen evolution reaction, J. Electroanal. Chem. 429 (1997) 157–168.

[123] X. Liu, Z. Chang, L. Luo, T. Xu, X. Lei, J. Liu, X. Sun, Hierarchical Zn x $Co_{3-x}O_4$ nanoarrays with high activity for electrocatalytic oxygen evolution, Chem. Mater. 26 (2014) 1889–1895.

[124] H.-Y. Wang, S.-F. Hung, H.-Y. Chen, T.-S. Chan, H.M. Chen, B. Liu, In operando identification of geometrical-site-dependent water oxidation activity of spinel Co_3O_4, J. Am. Chem. Soc. 138 (2016) 36–39.

[125] R. Zhang, C. Qin, H. Bala, Y. Wang, J. Cao, Recent Progress in Spinel Ferrite (MFe_2O_4) Chemiresistive Based Gas Sensors, Nanomaterials 13 (2023) 2188.

[126] N.-T. Suen, S.-F. Hung, Q. Quan, N. Zhang, Y.-J. Xu, H.M. Chen, Electrocatalysis for the oxygen evolution reaction: recent development and future perspectives, Chem. Soc. Rev. 46 (2017) 337–365.

[127] Y. Li, P. Hasin, Y. Wu, $Ni_xCo_{3-x}O_4$ nanowire arrays for electrocatalytic oxygen evolution, Adv. Mater. 22 (2010) 1926–1929.

[128] J. Wang, T. Qiu, X. Chen, Y. Lu, W. Yang, Hierarchical hollow urchin-like $NiCo_2O_4$ nanomaterial as electrocatalyst for oxygen evolution reaction in alkaline medium, J. Power Sources 268 (2014) 341–348.

[129] H. Shi, G. Zhao, Water oxidation on spinel $NiCo_2O_4$ nanoneedles anode: microstructures, specific surface character, and the enhanced electrocatalytic performance, J. Phys. Chem. C 118 (2014) 25939–25946.

[130] H. Hu, B. Guan, B. Xia, X.W. Lou, Designed formation of Co_3O_4/$NiCo_2O_4$ double-shelled nanocages with enhanced pseudocapacitive and electrocatalytic properties, J. Am. Chem. Soc. 137 (2015) 5590–5595.

[131] W.-Y. Xia, N. Li, Q.-Y. Li, K.-H. Ye, C.-W. Xu, Au-$NiCo_2O_4$ supported on three-dimensional hierarchical porous graphene-like material for highly effective oxygen evolution reaction, Sci. Rep. 6 (2016) 1–9.

[132] S. Chen, S.-Z. Qiao, Hierarchically porous nitrogen-doped graphene–$NiCo_2O_4$ hybrid paper as an advanced electrocatalytic water-splitting material, ACS Nano 7 (2013) 10190–10196.

[133] M. Hamdani, R. Singh, P. Chartier, Co_3O_4 and Co-based spinel oxides bifunctional oxygen electrodes, Int.J.Electrochem.Sci 5 (2010) 556–577.

[134] E. Rios, J.-L. Gautier, G. Poillerat, P. Chartier, Mixed valency spinel oxides of transition metals and electrocatalysis: case of the $Mn_xCo_{3-x}O_4$ system, Electrochimica Acta 44 (1998) 1491–1497.

[135] F. Cheng, J. Shen, B. Peng, Y. Pan, Z. Tao, J. Chen, Rapid room-temperature synthesis of nanocrystalline spinels as oxygen reduction and evolution electrocatalysts, Nat. Chem. 3 (2011) 79–84.

[136] M. De Koninck, S.-C. Poirier, B. Marsan, $Cu_xCo_{3-x}O_4$ used as bifunctional electrocatalyst: II. Electrochemical characterization for the oxygen reduction reaction, J. Electrochem. Soc. 154 (2007) A381.

[137] M. De Koninck, B. Marsan, $Mn_xCu_{1-x}Co_2O_4$ used as bifunctional electrocatalyst in alkaline medium, Electrochimica Acta 53 (2008) 7012–7021.

[138] W.-S. Choi, M.J. Jang, Y.S. Park, K.H. Lee, J.Y. Lee, M.-H. Seo, S.M. Choi, Three-dimensional honeycomb-like $Cu_{0.81}Co_{2.19}O_4$ nanosheet arrays supported by Ni foam and their high efficiency as oxygen evolution electrodes, ACS Appl. Mater. Interfaces 10 (2018) 38663–38668.

[139] Z. Liu, H. Cheng, N. Li, T.Y. Ma, Y. Su, $ZnCo_2O_4$ quantum dots anchored on nitrogen-doped carbon nanotubes as reversible oxygen reduction/evolution electrocatalysts, Adv. Mater. 28 (2016) 3777–3784.

[140] A.T. Aqueel Ahmed, B. Hou, H.S. Chavan, Y. Jo, S. Cho, J. Kim, S.M. Pawar, S. Cha, A.I. Inamdar, H. Kim, Self-assembled nanostructured $CuCo_2O_4$ for electrochemical energy storage and the oxygen evolution reaction via morphology engineering, Small 14 (2018) 1800742.

[141] S.K. Bikkarolla, P. Papakonstantinou, $CuCo_2O_4$ nanoparticles on nitrogenated graphene as highly efficient oxygen evolution catalyst, J. Power Sources 281 (2015) 243–251.

[142] X. Wu, K. Scott, $Cu_xCo_{3-x}O_4$ ($0 \leq x < 1$) nanoparticles for oxygen evolution in high performance alkaline exchange membrane water electrolysers, J. Mater. Chem. 21 (2011) 12344–12351.

[143] X. Wang, T. Ouyang, L. Wang, J. Zhong, T. Ma, Z. Liu, Redox-Inert Fe^{3+} Ions in Octahedral Sites of Co-Fe Spinel Oxides with Enhanced Oxygen Catalytic Activity for Rechargeable Zinc–Air Batteries, Angew. Chem. 131 (2019) 13425–13430.

[144] H. Cheng, M. Li, C. Su, N. Li, Z. Liu, Cu–Co Bimetallic Oxide Quantum Dot Decorated Nitrogen-Doped Carbon Nanotubes: A High-Efficiency Bifunctional Oxygen Electrode for Zn–Air Batteries, Adv. Funct. Mater. 27 (2017) 1701833.

[145] L. Trotochaud, J.K. Ranney, K.N. Williams, S.W. Boettcher, Solution-cast metal oxide thin film electrocatalysts for oxygen evolution, J. Am. Chem. Soc. 134 (2012) 17253–17261.

[146] M.E. Lyons, M.P. Brandon, A comparative study of the oxygen evolution reaction on oxidised nickel, cobalt and iron electrodes in base, J. Electroanal. Chem. 641 (2010) 119–130.

[147] X. Li, F.C. Walsh, D. Pletcher, Nickel based electrocatalysts for oxygen evolution in high current density, alkaline water electrolysers, Phys. Chem. Chem. Phys. 13 (2011) 1162–1167.

[148] P. Oliva, J. Leonardi, J. Laurent, C. Delmas, J. Braconnier, M. Figlarz, F. Fievet, A. De Guibert, Review of the structure and the electrochemistry of nickel hydroxides and oxy-hydroxides, J. Power Sources 8 (1982) 229–255.

[149] S. Cordoba, R. Carbonio, M.L. Teijelo, V. Macagno, The electrochemical response of binary mixtures of hydrous transition metal hydroxides co-precipitated on conducting substrates with reference to the oxygen evolution reaction, Electrochimica Acta 31 (1986) 1321–1332.

[150] D.A. Corrigan, The catalysis of the oxygen evolution reaction by iron impurities in thin film nickel oxide electrodes, J. Electrochem. Soc. 134 (1987) 377.

[151] M.B. Stevens, L.J. Enman, E.H. Korkus, J. Zaffran, C.D. Trang, J. Asbury, M.G. Kast, M.C. Toroker, S.W. Boettcher, Ternary Ni-Co-Fe oxyhydroxide oxygen evolution catalysts: Intrinsic activity trends, electrical conductivity, and electronic band structure, Nano Res 12 (2019) 2288–2295.

[152] X. Bo, Y. Li, R.K. Hocking, C. Zhao, NiFeCr hydroxide holey nanosheet as advanced electrocatalyst for water oxidation, ACS Appl. Mater. Interfaces 9 (2017) 41239–41245.

[153] Y. Jin, S. Huang, X. Yue, H. Du, P.K. Shen, Mo-and Fe-modified $Ni(OH)_2$/NiOOH nanosheets as highly active and stable electrocatalysts for oxygen evolution reaction, ACS Catal. 8 (2018) 2359–2363.

[154] K.N. Dinh, P. Zheng, Z. Dai, Y. Zhang, R. Dangol, Y. Zheng, B. Li, Y. Zong, Q. Yan, Ultrathin porous NiFeV ternary layer hydroxide nanosheets as a highly efficient bifunctional electrocatalyst for overall water splitting, Small 14 (2018) 1703257.

[155] I.C. Man, H.-Y. Su, F. Calle-Vallejo, H.A. Hansen, J.I. Martínez, N.G. Inoglu, J. Kitchin, T.F. Jaramillo, J.K. Nørskov, J. Rossmeisl, Universality in oxygen evolution electrocatalysis on oxide surfaces, ChemCatChem 3 (2011) 1159–1165.

[156] E. Cossar, A.O. Barnett, F. Seland, R. Safari, G.A. Botton, E.A. Baranova, Ionomer content optimization in nickel-iron-based anodes with and without ceria for anion exchange membrane water electrolysis, J. Power Sources 514 (2021) 230563.

[157] E. López-Fernández, C. Gómez-Sacedón, J. Gil-Rostra, J. Espinós, A. González-Elipe, F. Yubero, A. de Lucas-Consuegra, Ionomer-Free Nickel-Iron bimetallic electrodes for efficient anion exchange membrane water electrolysis, Chem. Eng. J. (2021) 133774.

[158] Y. Zhang, B. Cui, Z. Qin, H. Lin, J. Li, Hierarchical wreath-like Au–$Co(OH)_2$ microclusters for water oxidation at neutral pH, Nanoscale 5 (2013) 6826–6833.

[159] J.A. Koza, C.M. Hull, Y.-C. Liu, J.A. Switzer, Deposition of β-$Co(OH)_2$ films by electrochemical reduction of tris (ethylenediamine) cobalt (III) in alkaline solution, Chem. Mater. 25 (2013) 1922–1926.

[160] M. Tahir, L. Pan, F. Idrees, X. Zhang, L. Wang, J.-J. Zou, Z.L. Wang, Electrocatalytic oxygen evolution reaction for energy conversion and storage: a comprehensive review, Nano Energy 37 (2017) 136–157.

[161] D. Xu, M.B. Stevens, M.R. Cosby, S.Z. Oener, A.M. Smith, L.J. Enman, K.E. Ayers, C.B. Capuano, J.N. Renner, N. Danilovic, Earth-abundant oxygen electrocatalysts for alkaline anion-exchange-membrane water electrolysis: effects of catalyst conductivity and comparison with performance in three-electrode cells, ACS Catal. 9 (2018) 7–15.

[162] F. Song, X. Hu, Exfoliation of layered double hydroxides for enhanced oxygen evolution catalysis, Nat. Commun. 5 (2014) 4477.

[163] B. Zhang, X. Zheng, O. Voznyy, R. Comin, M. Bajdich, M. García-Melchor, L. Han, J. Xu, M. Liu, L. Zheng, Homogeneously dispersed multimetal oxygen-evolving catalysts, Science 352 (2016) 333–337.

[164] X. Li, H. Wang, Z. Cui, Y. Li, S. Xin, J. Zhou, Y. Long, C. Jin, J.B. Goodenough, Exceptional oxygen evolution reactivities on $CaCoO_3$ and $SrCoO_3$, Sci. Adv. 5 (2019) eaav6262.

[165] H. Ito, N. Kawaguchi, S. Someya, T. Munakata, Pressurized operation of anion exchange membrane water electrolysis, Electrochimica Acta 297 (2019) 188–196.

[166] N. Lee, D.T. Duong, D. Kim, Cyclic ammonium grafted poly (arylene ether ketone) hydroxide ion exchange membranes for alkaline water electrolysis with high chemical stability and cell efficiency, Electrochimica Acta 271 (2018) 150–157.

[167] J.E. Park, M.-J. Kim, M.S. Lim, S.Y. Kang, J.K. Kim, S.-H. Oh, M. Her, Y.-H. Cho, Y.-E. Sung, Graphitic carbon nitride-carbon nanofiber as oxygen catalyst in anion-exchange membrane water electrolyzer and rechargeable metal–air cells, Appl. Catal. B Environ. 237 (2018) 140–148.

[168] S. Marini, P. Salvi, P. Nelli, R. Pesenti, M. Villa, M. Berrettoni, G. Zangari, Y. Kiros, Advanced alkaline water electrolysis, Electrochimica Acta 82 (2012) 384–391.

[169] K.W. Ahmed, M.J. Jang, M.G. Park, Z. Chen, M. Fowler, Effect of Components and Operating Conditions on the Performance of PEM Electrolyzers: A Review, Electrochem 3 (2022) 581–612.

[170] M.J. Jang, J. Yang, J. Jeong, G.H. Kim, C.Y. Kwon, N.V. Myung, K.H. Lee, S.M. Choi, Promotion Effect of Modified Ni/C by La–Ce Oxide for Durable Hydrogen Evolution Reaction, ACS Sustain. Chem. Eng. 9 (2021) 12508–12513.

[171] M.J. Jang, J. Yang, J. Lee, Y.S. Park, J. Jeong, S.M. Park, J.-Y. Jeong, Y. Yin, M.-H. Seo, S.M. Choi, Superior performance and stability of anion exchange membrane water electrolysis: pH-controlled copper cobalt oxide nanoparticles for the oxygen evolution reaction, J. Mater. Chem. A 8 (2020) 4290–4299.

[172] F. Song, L. Bai, A. Moysiadou, S. Lee, C. Hu, L. Liardet, X. Hu, Transition metal oxides as electrocatalysts for the oxygen evolution reaction in alkaline solutions: an application-inspired renaissance, J. Am. Chem. Soc. 140 (2018) 7748–7759.

[173] F. Lu, M. Zhou, Y. Zhou, X. Zeng, First-row transition metal based catalysts for the oxygen evolution reaction under alkaline conditions: basic principles and recent advances, Small 13 (2017) 1701931.

[174] R. Subbaraman, D. Tripkovic, K.-C. Chang, D. Strmcnik, A.P. Paulikas, P. Hirunsit, M. Chan, J. Greeley, V. Stamenkovic, N.M. Markovic, Trends in activity for the water electrolyser reactions on 3 d M (Ni, Co, Fe, Mn) hydr (oxy) oxide catalysts, Nat. Mater. 11 (2012) 550–557.

[175] Y. Leng, G. Chen, A.J. Mendoza, T.B. Tighe, M.A. Hickner, C.-Y. Wang, Solid-state water electrolysis with an alkaline membrane, J. Am. Chem. Soc. 134 (2012) 9054–9057.

[176] L. Zeng, T. Zhao, Integrated inorganic membrane electrode assembly with layered double hydroxides as ionic conductors for anion exchange membrane water electrolysis, Nano Energy 11 (2015) 110–118.

[177] L. Trotochaud, S.L. Young, J.K. Ranney, S.W. Boettcher, Nickel–iron oxyhydroxide oxygen-evolution electrocatalysts: the role of intentional and incidental iron incorporation, J. Am. Chem. Soc. 136 (2014) 6744–6753.

[178] M. Gong, Y. Li, H. Wang, Y. Liang, J.Z. Wu, J. Zhou, J. Wang, T. Regier, F. Wei, H. Dai, An advanced Ni–Fe layered double hydroxide electrocatalyst for water oxidation, J. Am. Chem. Soc. 135 (2013) 8452–8455.

[179] Y.-F. Li, A. Selloni, Mechanism and activity of water oxidation on selected surfaces of pure and Fe-doped NiO x, Acs Catal. 4 (2014) 1148–1153.

[180] Z. Kang, S. Yu, G. Yang, Y. Li, G. Bender, B.S. Pivovar, J.B. Green Jr, F.-Y. Zhang, Performance improvement of proton exchange membrane electrolyzer cells by introducing in-plane transport enhancement layers, Electrochimica Acta 316 (2019) 43–51.

[181] M.J. Jang, S.H. Yang, M.G. Park, J. Jeong, M.S. Cha, S.-H. Shin, K.H. Lee, Z. Bai, Z. Chen, J.Y. Lee, Efficient and Durable Anion Exchange Membrane Water Electrolysis for a Commercially Available Electrolyzer Stack using Alkaline Electrolyte, ACS Energy Lett. 7 (2022) 2576–2583.

[182] I. Vincent, E.-C. Lee, H.-M. Kim, Comprehensive impedance investigation of low-cost anion exchange membrane electrolysis for large-scale hydrogen production, Sci. Rep. 11 (2021) 1–12.

[183] G. Yang, J. Mo, Z. Kang, Y. Dohrmann, F.A. List III, J.B. Green Jr, S.S. Babu, F.-Y. Zhang, Fully printed and integrated electrolyzer cells with additive manufacturing for high-efficiency water splitting, Appl. Energy 215 (2018) 202–210.

[184] B. Han, J. Mo, Z. Kang, F.-Y. Zhang, Effects of membrane electrode assembly properties on two-phase transport and performance in proton exchange membrane electrolyzer cells, Electrochimica Acta 188 (2016) 317–326.

[185] J. Ge, A. Higier, H. Liu, Effect of gas diffusion layer compression on PEM fuel cell performance, J. Power Sources 159 (2006) 922–927.

[186] S. Price, X. Ren, A. Savage, F. Beyer, Synthesis and characterization of anion-exchange membranes based on hydrogenated poly (norbornene), Polym. Chem. 8 (2017) 5708–5717.

[187] V.M. Truong, N.B. Duong, H. Yang, Comparison of Carbon Supports in Anion Exchange Membrane Fuel Cells, Materials 13 (2020) 5370.

[188] F. Razmjooei, R. Reißner, A.S. Gago, A. Ansar, Highly active binder free plasma sprayed non-noble metal electrodes for anion exchange membrane electrolysis at different reduced KOH concentrations, ECS Trans. 92 (2019) 689.

[189] E. López-Fernández, C.G. Sacedón, J. Gil-Rostra, F. Yubero, A.R. González-Elipe, A. de Lucas-Consuegra, Recent Advances in Alkaline Exchange Membrane Water Electrolysis and Electrode Manufacturing, Molecules 26 (2021) 6326.

[190] R.I. Masel, Z. Liu, S. Sajjad, Anion exchange membrane electrolyzers showing 1 A/cm2 at less than 2 V, ECS Trans. 75 (2016) 1143.

[191] A. Lim, H. Kim, D. Henkensmeier, S.J. Yoo, J.Y. Kim, S.Y. Lee, Y.-E. Sung, J.H. Jang, H.S. Park, A study on electrode fabrication and operation variables affecting the performance of anion exchange membrane water electrolysis, J. Ind. Eng. Chem. 76 (2019) 410–418.

[192] R.B. Kutz, Q. Chen, H. Yang, S.D. Sajjad, Z. Liu, I.R. Masel, Sustainion imidazolium-functionalized polymers for carbon dioxide electrolysis, Energy Technol. 5 (2017) 929–936.

[193] K. Zhang, X. Liang, L. Wang, K. Sun, Y. Wang, Z. Xie, Q. Wu, X. Bai, M.S. Hamdy, H. Chen, Status and perspectives of key materials for PEM electrolyzer, Nano Res. Energy 1 (2022) e9120032.

[194] A.Y. Faid, L. Xie, A.O. Barnett, F. Seland, D. Kirk, S. Sunde, Effect of anion exchange ionomer content on electrode performance in AEM water electrolysis, Int. J. Hydrog. Energy 45 (2020) 28272–28284.

[195] R.I. Masel, Q. Chen, Z. Liu, R. Kutz, Ion-conducting membranes, Dioxide Materials, Inc. Boca Raton, FL (United States), 2017.

[196] K. Yang, X. Li, J. Guo, J. Zheng, S. Li, S. Zhang, X. Cao, T.A. Sherazi, X. Liu, Preparation and properties of anion exchange membranes with exceptional alkaline stable polymer backbone and cation groups, J. Membr. Sci. 596 (2020) 117720.

[197] Z. Sun, B. Lin, F. Yan, Anion-exchange membranes for alkaline fuel-cell applications: the effects of cations, ChemSusChem 11 (2018) 58–70.

[198] N.J. Robertson, H.A. Kostalik IV, T.J. Clark, P.F. Mutolo, H.D. Abruña, G.W. Coates, Tunable high performance cross-linked alkaline anion exchange membranes for fuel cell applications, J. Am. Chem. Soc. 132 (2010) 3400–3404.

[199] T.J. Clark, N.J. Robertson, H.A. Kostalik IV, E.B. Lobkovsky, P.F. Mutolo, H.D. Abruna, G.W. Coates, A ring-opening metathesis polymerization route to alkaline anion exchange membranes: development of hydroxide-conducting thin films from an ammonium-functionalized monomer, J. Am. Chem. Soc. 131 (2009) 12888–12889.

[200] S. Chempath, B.R. Einsla, L.R. Pratt, C.S. Macomber, J.M. Boncella, J.A. Rau, B.S. Pivovar, Mechanism of tetraalkylammonium headgroup degradation in alkaline fuel cell membranes, J. Phys. Chem. C 112 (2008) 3179–3182.

[201] S. Chempath, J.M. Boncella, L.R. Pratt, N. Henson, B.S. Pivovar, Density functional theory study of degradation of tetraalkylammonium hydroxides, J. Phys. Chem. C 114 (2010) 11977–11983.

[202] H. Long, K. Kim, B.S. Pivovar, Hydroxide degradation pathways for substituted trimethylammonium cations: a DFT study, J. Phys. Chem. C 116 (2012) 9419–9426.

[203] Z. Si, Z. Sun, F. Gu, L. Qiu, F. Yan, Alkaline stable imidazolium-based ionomers containing poly (arylene ether sulfone) side chains for alkaline anion exchange membranes, J. Mater. Chem. A 2 (2014) 4413–4421.

[204] J. Fan, A.G. Wright, B. Britton, T. Weissbach, T.J. Skalski, J. Ward, T.J. Peckham, S. Holdcroft, Cationic polyelectrolytes, stable in 10 M KOH_{aq} at 100° C, ACS Macro Lett. 6 (2017) 1089–1093.

[205] G. Borisov, H. Penchev, K. Maksimova-Dimitrova, F. Ublekov, E. Lefterova, V. Sinigersky, E. Slavcheva, Alkaline water electrolysis facilitated via non-precious

monometallic catalysts combined with highly KOH doped polybenzimidazole membrane, Mater. Lett. 240 (2019) 144–146.

[206] G. Borisov, V. Bachvarov, H. Penchev, R. Rashkov, E. Slavcheva, Multi-metallic electrodeposited catalysts applicable for oxygen evolution reaction in AEM water electrolysis, Mater. Lett. 286 (2021) 129248.

[207] A.J. Esswein, M.J. McMurdo, P.N. Ross, A.T. Bell, T.D. Tilley, Size-Dependent Activity of Co_3O_4 Nanoparticle Anodes for Alkaline Water Electrolysis, J. Phys. Chem. C 113 (2009) 15068–15072. https://doi.org/10.1021/jp904022e.

[208] H.-C. Chien, W.-Y. Cheng, Y.-H. Wang, T.-Y. Wei, S.-Y. Lu, Ultralow overpotentials for oxygen evolution reactions achieved by nickel cobaltite aerogels, J. Mater. Chem. 21 (2011) 18180–18182.

[209] C. Wang, D. van der Vliet, K.-C. Chang, H. You, D. Strmcnik, J.A. Schlueter, N.M. Markovic, V.R. Stamenkovic, Monodisperse Pt3Co Nanoparticles as a Catalyst for the Oxygen Reduction Reaction: Size-Dependent Activity, J. Phys. Chem. C 113 (2009) 19365–19368. https://doi.org/10.1021/jp908203p.

[210] F. Hegge, F. Lombeck, E. Cruz Ortiz, L. Bohn, M. von Holst, M. Kroschel, J. Hübner, M. Breitwieser, P. Strasser, S. Vierrath, Efficient and stable low iridium loaded anodes for PEM water electrolysis made possible by nanofiber interlayers, ACS Appl. Energy Mater. 3 (2020) 8276–8284.

[211] M. Subhramannia, B.K. Balan, B.R. Sathe, I.S. Mulla, V.K. Pillai, Template-assisted synthesis of ruthenium oxide nanoneedles: Electrical and electrochemical properties, J. Phys. Chem. C 111 (2007) 16593–16600.

[212] D.U. Lee, B.J. Kim, Z. Chen, One-pot synthesis of a mesoporous $NiCo_2O_4$ nanoplatelet and graphene hybrid and its oxygen reduction and evolution activities as an efficient bi-functional electrocatalyst, J. Mater. Chem. A 1 (2013) 4754–4762.

[213] B.H. Suryanto, X. Lu, C. Zhao, Layer-by-layer assembly of transparent amorphous Co_3O_4 nanoparticles/graphene composite electrodes for sustained oxygen evolution reaction, J. Mater. Chem. A 1 (2013) 12726–12731.

[214] D. Wang, X. Chen, D.G. Evans, W. Yang, Well-dispersed Co_3O_4/Co_2MnO_4 nanocomposites as a synergistic bifunctional catalyst for oxygen reduction and oxygen evolution reactions, Nanoscale 5 (2013) 5312–5315.

[215] Y.J. Sa, K. Kwon, J.Y. Cheon, F. Kleitz, S.H. Joo, Ordered mesoporous Co_3O_4 spinels as stable, bifunctional, noble metal-free oxygen electrocatalysts, J. Mater. Chem. A 1 (2013) 9992–10001.

[216] Q. Zhao, Z. Yan, C. Chen, J. Chen, Spinels: controlled preparation, oxygen reduction/evolution reaction application, and beyond, Chem. Rev. 117 (2017) 10121–10211.

[217] B. Cui, H. Lin, J. Li, X. Li, J. Yang, J. Tao, Core–ring structured $NiCo_2O_4$ nanoplatelets: synthesis, characterization, and electrocatalytic applications, Adv. Funct. Mater. 18 (2008) 1440–1447.

[218] M. Bhushan, M. Mani, A.K. Singh, A.B. Panda, V.K. Shahi, Self-standing polyaniline membrane containing quaternary ammonium groups loaded with hollow spherical $NiCo_2O_4$ electrocatalyst for alkaline water electrolyser, J. Mater. Chem. A 8 (2020) 17089–17097.

[219] R. Kumar, $NiCo_2O_4$ nano-/microstructures as high-performance biosensors: a review, Nano-Micro Lett. 12 (2020) 1–52.

[220] K.W. Ahmed, M.J. Jang, S. Habibpour, Z. Chen, M. Fowler, $NiFeO_x$ and $NiFeCoO_x$ Catalysts for Anion Exchange Membrane Water Electrolysis, Electrochem 3 (2022) 843–861.

[221] S. Trasatti, Electrocatalysis in the anodic evolution of oxygen and chlorine, Electrochimica Acta 29 (1984) 1503–1512.

[222] B. Chi, J. Li, Y. Han, Y. Chen, Effect of temperature on the preparation and electrocatalytic properties of a spinel $NiCo_2O_4$/Ni electrode, Int. J. Hydrog. Energy 29 (2004) 605–610.

[223] K.-H. Chang, Y.-F. Lee, C.-C. Hu, C.-I. Chang, C.-L. Liu, Y.-L. Yang, A unique strategy for preparing single-phase unitary/binary oxides–graphene composites, Chem. Commun. 46 (2010) 7957–7959.

[224] N. Garg, M. Basu, K. Upadhyaya, S. Shivaprasad, A.K. Ganguli, Controlling the aspect ratio and electrocatalytic properties of nickel cobaltite nanorods, RSC Adv. 3 (2013) 24328–24336.

[225] L. Zeng, T.S. Zhao, R.H. Zhang, J.B. Xu, $NiCo_2O_4$ nanowires@ MnO_x nanoflakes supported on stainless steel mesh with superior electrocatalytic performance for anion exchange membrane water splitting, Electrochem. Commun. 87 (2018) 66–70.

[226] G. Zhang, H. Wang, J. Yang, Q. Zhao, L. Yang, H. Tang, C. Liu, H. Chen, Y. Lin, F. Pan, Temperature effect on Co-based catalysts in oxygen evolution reaction, Inorg. Chem. 57 (2018) 2766–2772.

[227] O. Diaz-Morales, I. Ledezma-Yanez, M.T. Koper, F. Calle-Vallejo, Guidelines for the rational design of Ni-based double hydroxide electrocatalysts for the oxygen evolution reaction, ACS Catal. 5 (2015) 5380–5387.

[228] P. Wang, Y. Lin, L. Wan, B. Wang, Autologous growth of Fe-doped $Ni(OH)_2$ nanosheets with low overpotential for oxygen evolution reaction, Int. J. Hydrog. Energy 45 (2020) 6416–6424.

[229] R. Ding, L. Qi, M. Jia, H. Wang, Simple hydrothermal synthesis of mesoporous spinel $NiCo_2O_4$ nanoparticles and their catalytic behavior in CH_3OH electro-oxidation and H_2O_2 electro-reduction, Catal. Sci. Technol. 3 (2013) 3207–3215.

[230] C. Jin, F. Lu, X. Cao, Z. Yang, R. Yang, Facile synthesis and excellent electrochemical properties of $NiCo_2O_4$ spinel nanowire arrays as a bifunctional catalyst for the oxygen reduction and evolution reaction, J. Mater. Chem. A 1 (2013) 12170–12177.

[231] Y. Li, Z. Zhou, H. Xu, X. Liao, G. Cheng, M. Sun, L. Yu, Controllable synthesis of $Ni_xCo_{3-x}O_4$-rGO with enhanced oxygen reduction/evolution activity, J. Mater. Sci. Mater. Electron. 30 (2019) 18424–18431.

[232] C. Busacca, S.C. Zignani, A. Di Blasi, O. Di Blasi, M.L. Faro, V. Antonucci, A.S. Aricò, Electrospun $NiMn_2O_4$ and $NiCo_2O_4$ spinel oxides supported on carbon nanofibers as electrocatalysts for the oxygen evolution reaction in an anion exchange membrane-based electrolysis cell, Int. J. Hydrog. Energy 44 (2019) 20987–20996.

[233] A. Caprì, I. Gatto, C. Lo Vecchio, S. Trocino, A. Carbone, V. Baglio, Anion Exchange Membrane Water Electrolysis Based on Nickel Ferrite Catalysts, ChemElectroChem 10 (2023) e202201056.

[234] A.S. Pushkarev, I.V. Pushkareva, S.P. du Preez, D.G. Bessarabov, PGM-free electrocatalytic layer characterization by electrochemical impedance spectroscopy of an

anion exchange membrane water electrolyzer with Nafion ionomer as the bonding agent, Catalysts 13 (2023) 554.

[235] T.E. Springer, T.A. Zawodzinski, M.S. Wilson, S. Gottesfeld, Characterization of polymer electrolyte fuel cells using AC impedance spectroscopy, J. Electrochem. Soc. 143 (1996) 587.

[236] Z. Kang, J. Mo, G. Yang, S.T. Retterer, D.A. Cullen, T.J. Toops, J.B. Green Jr, M.M. Mench, F.-Y. Zhang, Investigation of thin/well-tunable liquid/gas diffusion layers exhibiting superior multifunctional performance in low-temperature electrolytic water splitting, Energy Environ. Sci. 10 (2017) 166–175.

[237] P.K. Giesbrecht, M.S. Freund, Investigation of Water Oxidation at IrO_2 Electrodes in Nafion-Based Membrane Electrode Assemblies Using Impedance Spectroscopy and Distribution of Relaxation Times Analysis, J. Phys. Chem. C 126 (2022) 17844–17861.

[238] J.E. Park, S.Y. Kang, S.-H. Oh, J.K. Kim, M.S. Lim, C.-Y. Ahn, Y.-H. Cho, Y.-E. Sung, High-performance anion-exchange membrane water electrolysis, Electrochimica Acta 295 (2019) 99–106.

[239] N. Du, C. Roy, R. Peach, M. Turnbull, S. Thiele, C. Bock, Anion-exchange membrane water electrolyzers, Chem. Rev. 122 (2022) 11830–11895.

[240] F. Zeng, C. Mebrahtu, L. Liao, A.K. Beine, R. Palkovits, Stability and deactivation of OER electrocatalysts: A review, J. Energy Chem. 69 (2022) 301–329.

[241] R.A. Krivina, G.A. Lindquist, S.R. Beaudoin, T.N. Stovall, W.L. Thompson, L.P. Twight, D. Marsh, J. Grzyb, K. Fabrizio, J.E. Hutchison, Anode catalysts in anion-exchange-membrane electrolysis without supporting electrolyte: conductivity, dynamics, and ionomer degradation, Adv. Mater. 34 (2022) 2203033.

[242] A. Singh, R. Singh, Effect of V substitution at B-site on the physicochemical and electrocatalytic properties of spinel-type $NiFe_2O_4$ towards O_2 evolution in alkaline solutions, Int. J. Hydrog. Energy 35 (2010) 3243–3248.

[243] W.G. Hardin, J.T. Mefford, D.A. Slanac, B.B. Patel, X. Wang, S. Dai, X. Zhao, R.S. Ruoff, K.P. Johnston, K.J. Stevenson, Tuning the electrocatalytic activity of perovskites through active site variation and support interactions, Chem. Mater. 26 (2014) 3368–3376.

[244] J. Qi, W. Zhang, R. Xiang, K. Liu, H. Wang, M. Chen, Y. Han, R. Cao, Porous nickel–iron oxide as a highly efficient electrocatalyst for oxygen evolution reaction, Adv. Sci. 2 (2015) 1500199.

[245] M.K. Bates, Q. Jia, H. Doan, W. Liang, S. Mukerjee, Charge-transfer effects in Ni–Fe and Ni–Fe–Co mixed-metal oxides for the alkaline oxygen evolution reaction, ACS Catal. 6 (2016) 155–161.

[246] J.B. Gerken, S.E. Shaner, R.C. Massé, N.J. Porubsky, S.S. Stahl, A survey of diverse earth abundant oxygen evolution electrocatalysts showing enhanced activity from Ni–Fe oxides containing a third metal, Energy Environ. Sci. 7 (2014) 2376–2382.

[247] J. Landon, E. Demeter, N. Inoglu, C. Keturakis, I.E. Wachs, R. Vasic, A.I. Frenkel, J.R. Kitchin, Spectroscopic characterization of mixed Fe–Ni oxide electrocatalysts for the oxygen evolution reaction in alkaline electrolytes, Acs Catal. 2 (2012) 1793–1801.

[248] Y.S. Park, J.-Y. Jeong, M.J. Jang, C.-Y. Kwon, G.H. Kim, J. Jeong, J. Lee, J. Lee, S.M. Choi, Ternary layered double hydroxide oxygen evolution reaction electrocatalyst for anion exchange membrane alkaline seawater electrolysis, J. Energy Chem. 75 (2022) 127–134.

[249] M. Gao, W. Sheng, Z. Zhuang, Q. Fang, S. Gu, J. Jiang, Y. Yan, Efficient water oxidation using nanostructured α-nickel-hydroxide as an electrocatalyst, J. Am. Chem. Soc. 136 (2014) 7077–7084.

[250] M.W. Louie, A.T. Bell, An investigation of thin-film Ni–Fe oxide catalysts for the electrochemical evolution of oxygen, J. Am. Chem. Soc. 135 (2013) 12329–12337.

[251] E. Guerrini, M. Piozzini, A. Castelli, A. Colombo, S. Trasatti, Effect of FeO_x on the electrocatalytic properties of $NiCo_2O_4$ for O_2 evolution from alkaline solutions, J. Solid State Electrochem. 12 (2008) 363–373.

[252] E.L. Miller, R.E. Rocheleau, Electrochemical behavior of reactively sputtered iron-doped nickel oxide, J. Electrochem. Soc. 144 (1997) 3072.

[253] A.Y. Faid, A.O. Barnett, F. Seland, S. Sunde, Ternary NiCoFe nanosheets for oxygen evolution in anion exchange membrane water electrolysis, Int. J. Hydrog. Energy 47 (2022) 23483–23497.

[254] K.W. Ahmed, S. Habibpour, Z. Chen, M. Fowler, Investigation of $NiCoO_x$ catalysts for anion exchange membrane water electrolysis: Performance, durability, and efficiency analysis, J. Energy Storage 79 (2024) 110149.

[255] T.A. Zegeye, W.-T. Chen, C.-C. Hsu, J.A.A. Valinton, C.-H. Chen, Activation energy assessing potential-dependent activities and site reconstruction for oxygen evolution, ACS Energy Lett. 7 (2022) 2236–2243.

[256] S. Siracusano, S. Trocino, N. Briguglio, V. Baglio, A.S. Aricò, Electrochemical impedance spectroscopy as a diagnostic tool in polymer electrolyte membrane electrolysis, Materials 11 (2018) 1368.

[257] J.C. Garcia-Navarro, M. Schulze, K.A. Friedrich, Measuring and modeling mass transport losses in proton exchange membrane water electrolyzers using electrochemical impedance spectroscopy, J. Power Sources 431 (2019) 189–204.

[258] Z. Xie, S. Holdcroft, Polarization-dependent mass transport parameters for orr in perfluorosulfonic acid ionomer membranes: an EIS study using microelectrodes, J. Electroanal. Chem. 568 (2004) 247–260.

[259] Z.-G. Ye, H.-M. Meng, D.-B. Sun, Electrochemical impedance spectroscopic (EIS) investigation of the oxygen evolution reaction mechanism of Ti/IrO_2+ MnO_2 electrodes in 0.5 M H_2SO_4 solution, J. Electroanal. Chem. 621 (2008) 49–54.

[260] Q. Chen, Y. Yu, J. Li, H. Nan, S. Luo, C. Jia, P. Deng, S. Zhong, X. Tian, Recent Progress in Layered Double Hydroxide-Based Electrocatalyst for Hydrogen Evolution Reaction, ChemElectroChem 9 (2022) e202101387.

[261] F. Dionigi, P. Strasser, NiFe-based (oxy) hydroxide catalysts for oxygen evolution reaction in non-acidic electrolytes, Adv. Energy Mater. 6 (2016) 1600621.

[262] Z. Liu, N. Li, H. Zhao, Y. Zhang, Y. Huang, Z. Yin, Y. Du, Regulating the active species of $Ni(OH)_2$ using CeO_2: 3D CeO_2/Ni $(OH)_2$/carbon foam as an efficient electrode for the oxygen evolution reaction, Chem. Sci. 8 (2017) 3211–3217.

[263] P. Tian, Y. Yu, X. Yin, X. Wang, A wafer-scale 1 nm $Ni(OH)_2$ nanosheet with superior electrocatalytic activity for the oxygen evolution reaction, Nanoscale 10 (2018) 5054–5059.

[264] B. Kim, A. Oh, M.K. Kabiraz, Y. Hong, J. Joo, H. Baik, S.-I. Choi, K. Lee, NiOOH exfoliation-free nickel octahedra as highly active and durable electrocatalysts toward the

oxygen evolution reaction in an alkaline electrolyte, ACS Appl. Mater. Interfaces 10 (2018) 10115–10122.

[265] Y. Dong, P. Zhang, Y. Kou, Z. Yang, Y. Li, X. Sun, A first-principles study of oxygen formation over NiFe-layered double hydroxides surface, Catal. Lett. 145 (2015) 1541–1548.

[266] S. Yin, W. Tu, Y. Sheng, Y. Du, M. Kraft, A. Borgna, R. Xu, A Highly Efficient Oxygen Evolution Catalyst Consisting of Interconnected Nickel–Iron-Layered Double Hydroxide and Carbon Nanodomains, Adv. Mater. 30 (2018) 1705106.

[267] C. Tang, H. Wang, H. Wang, Q. Zhang, G. Tian, J. Nie, F. Wei, Spatially confined hybridization of nanometer-sized NiFe hydroxides into nitrogen-doped graphene frameworks leading to superior oxygen evolution reactivity, Adv. Mater. 27 (2015) 4516–4522.

[268] A.G. Wright, J. Fan, B. Britton, T. Weissbach, H.-F. Lee, E.A. Kitching, T.J. Peckham, S. Holdcroft, Hexamethyl-p-terphenyl poly (benzimidazolium): a universal hydroxide-conducting polymer for energy conversion devices, Energy Environ. Sci. 9 (2016) 2130–2142.

[269] S.Y. Kang, J.E. Park, G.Y. Jang, O.-H. Kim, O.J. Kwon, Y.-H. Cho, Y.-E. Sung, High-performance and durable water electrolysis using a highly conductive and stable anion-exchange membrane, Int. J. Hydrog. Energy 47 (2022) 9115–9126. https://doi.org/10.1016/j.ijhydene.2022.01.002.

[270] N. Dalai, B. Mohanty, A. Mitra, B. Jena, Highly Active Ternary Nickel–Iron oxide as Bifunctional Catalyst for Electrochemical Water Splitting, ChemistrySelect 4 (2019) 7791–7796. https://doi.org/10.1002/slct.201901465.

[271] G. Liu, K. Wang, X. Gao, D. He, J. Li, Fabrication of mesoporous $NiFe_2O_4$ nanorods as efficient oxygen evolution catalyst for water splitting, Electrochimica Acta 211 (2016) 871–878. https://doi.org/10.1016/j.electacta.2016.06.113.

[272] G. Liu, X. Gao, K. Wang, D. He, J. Li, Uniformly mesoporous $NiO/NiFe_2O_4$ biphasic nanorods as efficient oxygen evolving catalyst for water splitting, Int. J. Hydrog. Energy 41 (2016) 17976–17986. https://doi.org/10.1016/j.ijhydene.2016.07.268.

[273] Z. Feng, P. Wang, Y. Cheng, Y. Mo, X. Luo, P. Liu, R. Guo, X. Liu, Recent progress on $NiFe_2O_4$ spinels as electrocatalysts for the oxygen evolution reaction, J. Electroanal. Chem. 946 (2023) 117703. https://doi.org/10.1016/j.jelechem.2023.117703.

[274] J. Zhu, Q. Zhang, P. Zhao, L. Chen, S. Yang, Q. Yan, H. Li, $NiFe_2O_4$@Co_3O_4 heterostructure with abundant oxygen vacancies as a bifunctional electrocatalyst for overall water splitting, J. Alloys Compd. 918 (2022) 165705. https://doi.org/10.1016/j.jallcom.2022.165705.

[275] D. Navadeepthy, A. Rebekah, C. Viswanthan, N. Ponpandian, Boosting the kinetics of oxygen and hydrogen evolution in alkaline water splitting using nickel ferrite /N-graphene nanocomposite as a bifunctional electrocatalyst, Int. J. Hydrog. Energy 46 (2021) 21512–21524. https://doi.org/10.1016/j.ijhydene.2021.03.244.

[276] G. Liu, Y. Wu, M. Wang, R. Yao, N. Li, Y. Zhao, F. Zhao, J. Li, Phosphate ions-functionalized and wettability-tuned nickel ferrite for boosted oxygen evolution performance, Int. J. Hydrog. Energy 44 (2019) 26992–27000. https://doi.org/10.1016/j.ijhydene.2019.08.132.

[277] Y. Chu, Y. Chen, N. Chen, F. Wang, H. Zhu, A new method for improving the ion conductivity of anion exchange membranes by using TiO2 nanoparticles coated with ionic liquid, RSC Adv. 6 (2016) 96768–96777. https://doi.org/10.1039/C6RA21355C.

[278] H.-J. Liu, R.-N. Luan, L.-Y. Li, R.-Q. Lv, Y.-M. Chai, B. Dong, Sulphur-dopant induced breaking of the scaling relation on low-valence Ni sites in nickel ferrite nanocones for water oxidation with industrial-level current density, Chem. Eng. J. 461 (2023) 141714. https://doi.org/10.1016/j.cej.2023.141714.

[279] B. Motealleh, Z. Liu, R.I. Masel, J.P. Sculley, Z. Richard Ni, L. Meroueh, Next-generation anion exchange membrane water electrolyzers operating for commercially relevant lifetimes, Int. J. Hydrog. Energy 46 (2021) 3379–3386. https://doi.org/10.1016/j.ijhydene.2020.10.244.

[280] M. Chen, M. Mandal, K. Groenhout, G. McCool, H.M. Tee, B. Zulevi, P.A. Kohl, Self-adhesive ionomers for durable low-temperature anion exchange membrane electrolysis, J. Power Sources 536 (2022) 231495. https://doi.org/10.1016/j.jpowsour.2022.231495.

[281] A.M.I. Noor Azam, T. Ragunathan, N.N. Zulkefli, M.S. Masdar, E.H. Majlan, R. Mohamad Yunus, N.S. Shamsul, T. Husaini, S.N.A. Shaffee, Investigation of Performance

of Anion Exchange Membrane (AEM) Electrolysis with Different Operating Conditions, Polymers 15 (2023) 1301. https://doi.org/10.3390/polym15051301.

[282] F.E. Chakik, M. Kaddami, M. Mikou, Optimization of physico-chemical parameters of hydrogen production by electrolysis of water, in: 2018 Renew. Energ. Power Syst. Green Incl. Econ. REPS-GIE, 2018: pp. 1–6. https://doi.org/10.1109/REPSGIE.2018.8488777.

[283] C. Santoro, A. Lavacchi, P. Mustarelli, V. Di Noto, L. Elbaz, D.R. Dekel, F. Jaouen, What is Next in Anion-Exchange Membrane Water Electrolyzers? Bottlenecks, Benefits, and Future, ChemSusChem 15 (2022) e202200027. https://doi.org/10.1002/cssc.202200027.

[284] C. Lo Vecchio, A. Carbone, I. Gatto, V. Baglio, Investigation of Fumasep® FAA3-50 Membranes in Alkaline Direct Methanol Fuel Cells, Polymers 15 (2023) 1555. https://doi.org/10.3390/polym15061555.

[285] Fumasep FAA-3-50, (n.d.). https://www.fuelcellstore.com/fumasep-faa-3-50 (accessed October 27, 2023).

[286] Fumasep FAS-50, (n.d.). https://www.fuelcellstore.com/fumasep-fas-50 (accessed October 27, 2023).

[287] S.A. Lee, J. Kim, K.C. Kwon, S.H. Park, H.W. Jang, Anion exchange membrane water electrolysis for sustainable large-scale hydrogen production, Carbon Neutralization 1 (2022) 26–48. https://doi.org/10.1002/cnl2.9.

[288] Fumasep FAA-3-PK-75, (n.d.). https://www.fuelcellstore.com/fumasep-faa-3-pk-75 (accessed October 27, 2023).

[289] Fumasep FAB-PK-130, (n.d.). https://www.fuelcellstore.com/fumasep-fab (accessed October 27, 2023).

[290] A. Caprì, A. Martínez-Lázaro, J. Béjar, I. Gatto, L. Álvarez-Contreras, M.P. Gurrola, J. Ledesma-García, V. Baglio, L.G. Arriaga, Three-dimensionally ordered macroporous trimetallic spinel for anion exchange membrane water electrolysis, Electrochimica Acta 463 (2023) 142851. https://doi.org/10.1016/j.electacta.2023.142851.

[291] A. Lim, H. Kim, D. Henkensmeier, S. Jong Yoo, J. Young Kim, S. Young Lee, Y.-E. Sung, J.H. Jang, H.S. Park, A study on electrode fabrication and operation variables affecting the performance of anion exchange membrane water electrolysis, J. Ind. Eng. Chem. 76 (2019) 410–418. https://doi.org/10.1016/j.jiec.2019.04.007.

[292] J. van der Merwe, K. Uren, G. van Schoor, D. Bessarabov, Characterisation tools development for PEM electrolysers, Int. J. Hydrog. Energy 39 (2014) 14212–14221. https://doi.org/10.1016/j.ijhydene.2014.02.096.

[293] Z. Kang, G. Yang, J. Mo, S. Yu, D.A. Cullen, S.T. Retterer, T.J. Toops, M.P. Brady, G. Bender, B.S. Pivovar, Developing titanium micro/nano porous layers on planar thin/tunable LGDLs for high-efficiency hydrogen production, Int. J. Hydrog. Energy 43 (2018) 14618–14628.

[294] L. Zeng, T.S. Zhao, Integrated inorganic membrane electrode assembly with layered double hydroxides as ionic conductors for anion exchange membrane water electrolysis, Nano Energy 11 (2015) 110–118. https://doi.org/10.1016/j.nanoen.2014.10.019.

[295] S. Seetharaman, R. Balaji, K. Ramya, K.S. Dhathathreyan, M. Velan, Graphene oxide modified non-noble metal electrode for alkaline anion exchange membrane water electrolyzers, Int. J. Hydrog. Energy 38 (2013) 14934–14942. https://doi.org/10.1016/j.ijhydene.2013.09.033.

[296] A. Lim, M.K. Cho, S.Y. Lee, H.-J. Kim, S.J. Yoo, Y.-E. Sung, J.H. Jang, H.S. Park, A Review of Industrially Developed Components and Operation Conditions for Anion Exchange Membrane Water Electrolysis, J. Electrochem. Sci. Technol. 8 (2017) 265–273. https://doi.org/10.5229/JECST.2017.8.4.265.

[297] Z. Wu, Z. Zou, J. Huang, F. Gao, $NiFe_2O_4$ Nanoparticles/NiFe Layered Double-Hydroxide Nanosheet Heterostructure Array for Efficient Overall Water Splitting at Large Current Densities, ACS Appl. Mater. Interfaces 10 (2018) 26283–26292. https://doi.org/10.1021/acsami.8b07835.

[298] T.-H. Kong, P. Thangavel, S. Shin, S. Kwon, H. Choi, H. Lee, N. Park, J.-J. Woo, Y. Kwon, In-Situ Ionomer-Free Catalyst-Coated Membranes for Anion Exchange Membrane Water Electrolyzers, ACS Energy Lett. (2023) 4666–4673. https://doi.org/10.1021/acsenergylett.3c01418.

[299] Y.-C. Wang, S.-E. Yu, I.-C. Cheng, Y.-C. Chuang, Y.-S. Chen, J.-Z. Chen, NiFe Metal-Organic Frameworks on Carbon Paper as an Efficient Electrocatalyst for Alkaline Water Electrolysis Module, (2023). https://doi.org/10.2139/ssrn.4427030.

[300] W. E. Mustain, M. Chatenet, M. Page, Y. Seung Kim, Durability challenges of anion exchange membrane fuel cells, Energy Environ. Sci. 13 (2020) 2805–2838. https://doi.org/10.1039/D0EE01133A.

[301] S. Wierzbicki, J.C. Douglin, A. Kostuch, D.R. Dekel, K. Kruczała, Are Radicals Formed During Anion-Exchange Membrane Fuel Cell Operation? J. Phys. Chem. Lett. 11 (2020) 7630–7636. https://doi.org/10.1021/acs.jpclett.0c02349.

[302] G. Couture, A. Alaaeddine, F. Boschet, B. Ameduri, Polymeric materials as anion-exchange membranes for alkaline fuel cells, Prog. Polym. Sci. 36 (2011) 1521–1557. https://doi.org/10.1016/j.progpolymsci.2011.04.004.

[303] C.G. Arges, V. Ramani, Two-dimensional NMR spectroscopy reveals cation-triggered backbone degradation in polysulfone-based anion exchange membranes, Proc. Natl. Acad. Sci. U. S. A. 110 (2013) 2490–2495. https://doi.org/10.1073/pnas.1217215110.

[304] G. Merle, M. Wessling, K. Nijmeijer, Anion exchange membranes for alkaline fuel cells: A review, J. Membr. Sci. 377 (2011) 1–35. https://doi.org/10.1016/j.memsci.2011.04.043.

[305] D. Li, E.J. Park, W. Zhu, Q. Shi, Y. Zhou, H. Tian, Y. Lin, A. Serov, B. Zulevi, E.D. Baca, C. Fujimoto, H.T. Chung, Y.S. Kim, Highly quaternized polystyrene ionomers for high performance anion exchange membrane water electrolysers, Nat. Energy 5 (2020) 378–385. https://doi.org/10.1038/s41560-020-0577-x.

[306] D.P. Leonard, M. Lehmann, J.M. Klein, I. Matanovic, C. Fujimoto, T. Saito, Y.S. Kim, Phenyl-Free Polynorbornenes for Potential Anion Exchange Ionomers for Fuel Cells and Electrolyzers, Adv. Energy Mater. 13 (2023) 2203488. https://doi.org/10.1002/aenm.202203488.

[307] C. Lei, K. Yang, G. Wang, G. Wang, J. Lu, L. Xiao, L. Zhuang, Impact of Catalyst Reconstruction on the Durability of Anion Exchange Membrane Water Electrolysis, ACS Sustain. Chem. Eng. 10 (2022) 16725–16733. https://doi.org/10.1021/acssuschemeng.2c04855.

[308] R. Chen, S.-F. Hung, D. Zhou, J. Gao, C. Yang, H. Tao, H.B. Yang, L. Zhang, L. Zhang, Q. Xiong, H.M. Chen, B. Liu, Layered Structure Causes Bulk NiFe Layered Double Hydroxide Unstable in Alkaline Oxygen Evolution Reaction, Adv. Mater. 31 (2019) 1903909. https://doi.org/10.1002/adma.201903909.

[309] H. Jang, S. Chung, J. Lee, In situ demonstration of anodic interface degradation during water electrolysis: Corrosion and passivation, Electrochimica Acta 365 (2021) 137276. https://doi.org/10.1016/j.electacta.2020.137276.

[310] S.K. Singh, K. Takeyasu, B. Paul, S.K. Sharma, J. Nakamura, CoO_x electro-catalysts anchored on nitrogen-doped carbon nanotubes for the oxygen evolution reaction, Sustain. Energy Fuels 5 (2021) 820–827. https://doi.org/10.1039/D0SE01285H.

[311] R. Berenguer, A. La Rosa-Toro, C. Quijada, E. Morallón, Origin of the Deactivation of Spinel $Cu_xCo_{3-x}O_4$/Ti Anodes Prepared by Thermal Decomposition, J. Phys. Chem. C 112 (2008) 16945–16952. https://doi.org/10.1021/jp804403x.

Appendix

Efficiency calculations

Sample calculations for cell efficiency for water electrolysis at current density of 0.25 A/cm^2. With an area of electrodes 3.24 cm^2 and a hydrogen production rate of 4.6 ml/min.

j = 0.25 A/cm^2

A = 3.24 cm^2

V = 4.6 ml/min

Cell efficiency is defined as the ratio of energy stored as hydrogen to the energy input to the electrolyzer.

Cell efficiency (%) = molar flow rate of hydrogen x ΔH x 100

AEM electrolyzer power input

$$\text{Cell efficiency (\%)} = \frac{n \times \Delta H \text{ x } 100}{j \times A \times V}$$

Where,

n is the molar flow rate of hydrogen (mol/sec)

ΔH (285000 kj/mol) is the higher heating value of hydrogen at standard conditions.

j is the current density

V is the voltage of the electrolyzer

Molar flow rate of hydrogen can be calculated from the volumetric flow rate as follows

V is the volumetric flowrate of hydrogen per minute (ml/min)

$$n = \frac{4.60 \ \frac{ml}{min}}{60 \text{ s/min} \times 22400 \text{ ml/mol}}$$

n = 3.42 x10^{-6} mol/s

$$\text{Cell efficiency (\%)} = \frac{3.42\ \text{x}0^{-6} \times 285000 \times 100}{0.25\frac{\text{A}}{\text{cm}^2} \times 3.24\ \text{cm}^2 \times 1.717\ \text{V}}$$

$$\text{Cell efficiency (\%)} = 70.3\%$$

Faradic efficiency calculations

Sample calculations for Faradic efficiency for water electrolysis at 0.8 A/cm^2. With an area of electrodes 3.24 cm^2 and a hydrogen production rate of 15.7 ml/min.

j = 0.8 A/cm^2

A = 3.24 cm^2

V = 15.7 ml/min

Using Faraday's law, we can write the following equation.

$$n = \frac{j \times A}{\text{z} \times \text{F}}$$

n is the number of moles of hydrogen formed per second

j is the current density

A is the area of electrodes.

z is the number of electrons

F is the Faraday constant

$$n = \frac{0.8 \times 3.24}{2 \times 96485}$$

n = 1.34 x10^{-5} mol/s

V_{the} = 1.34 x10^{-5} mol/s x 22400 ml/mol

V_{the} = 0.301 ml/s x 60 s/min

V_{the} = 18.06 ml/min

Where V_{the} is the theoretical volumetric flow rate of hydrogen at these working conditions.

Faradic efficiency can be calculated by dividing the actual volumetric flow rate by the theoretical volumetric flow rate.

$$Faradic\ efficency\ (\%) = \frac{15.7\ \text{ml/min x } 100}{18.06\ \text{ml/min}}$$

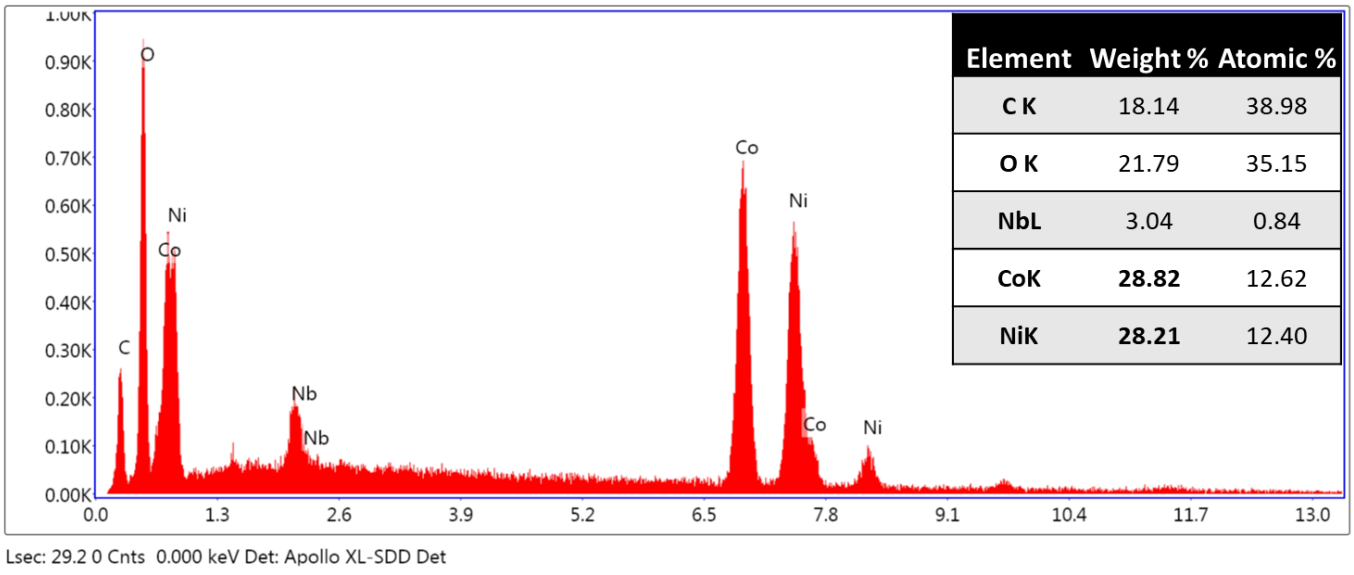
$$Faradic\ efficency\ (\%) = 86.93\%$$

Energy-dispersive X-ray spectroscopy (EDS)

Supplementary Information

Investigation of $NiCoO_x$ Catalysts for Anion Exchange Membrane Water Electrolysis: Performance, Durability, and Efficiency Analysis

EDS spectra for $NiCoO_x$ catalyst series, conforming the Ni to Co ratio.



Element	Weight %	Atomic %
C K	18.14	38.98
O K	21.79	35.15
NbL	3.04	0.84
CoK	**28.82**	12.62
NiK	**28.21**	12.40

Figure A5.1. EDS spectra of $NiCoO_x$ (1:1).

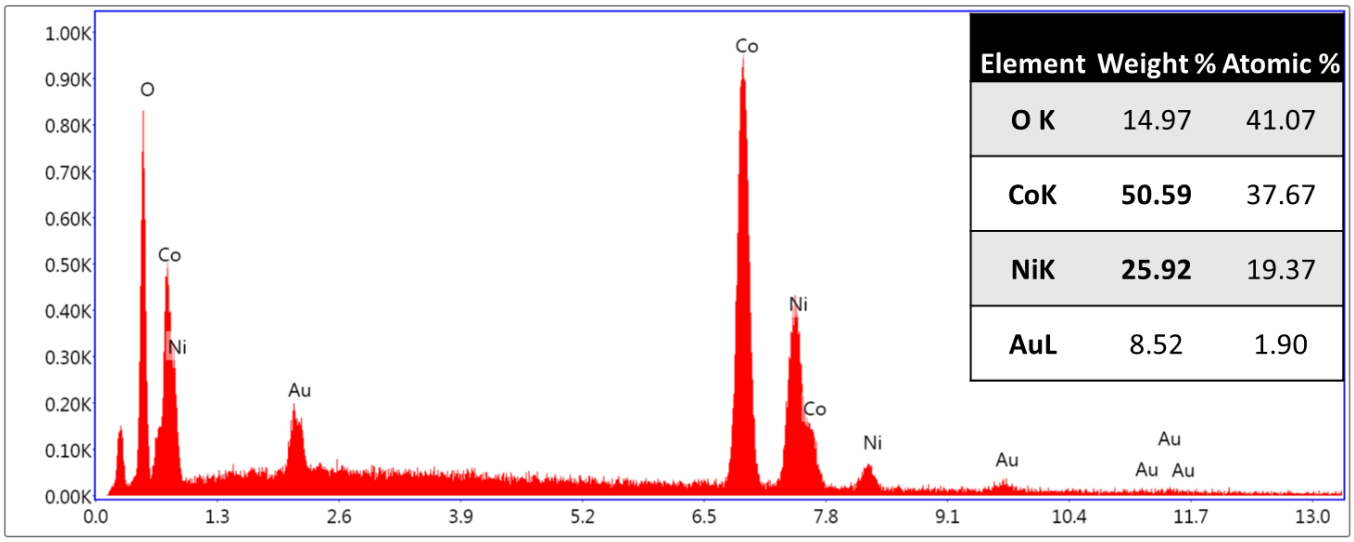


Figure A5.2. EDS spectra of $NiCoO_x$ (1:2).

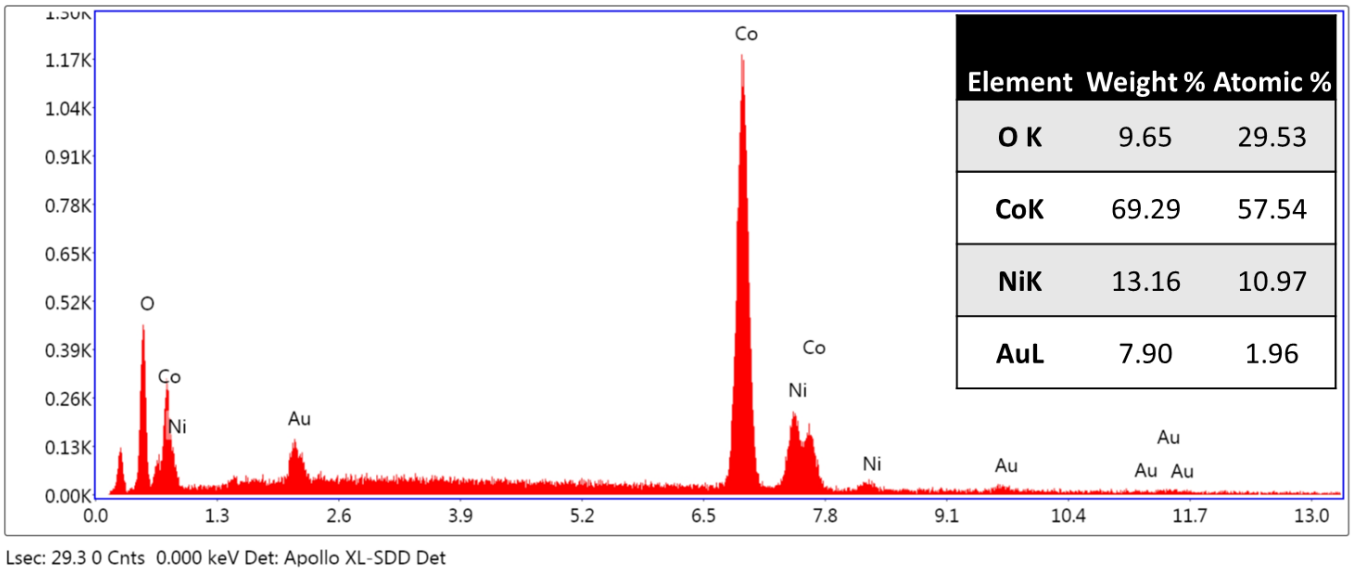


Figure A5.3. EDS spectra of $NiCoO_x$ (1:5).

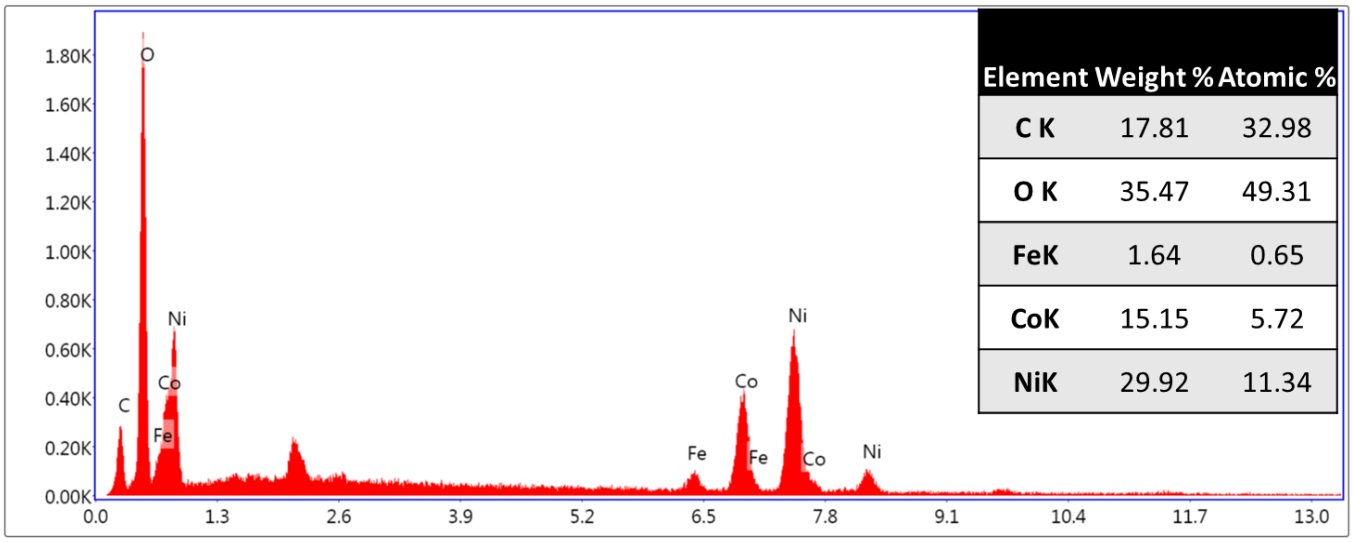


Figure A5.4. EDS spectra of $NiCoO_x$ (2:1).

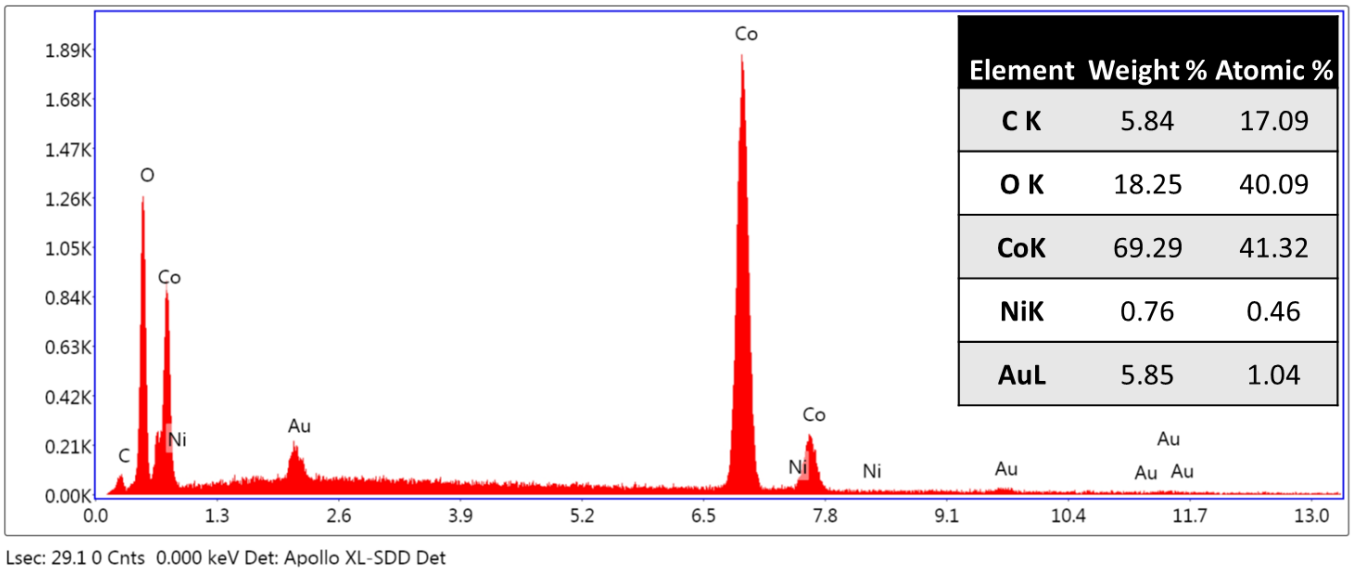


Figure A5.5. EDS spectra of Co_3O_4.

Performance Evaluation and Durability Analysis of $NiFeCoO_x$ Catalysts for Alkaline Water Electrolysis in AEM Electrolyzers

EDS spectra for $NiFeCoO_x$ catalyst series, which confirm the ratio of Ni, Fe and Co.

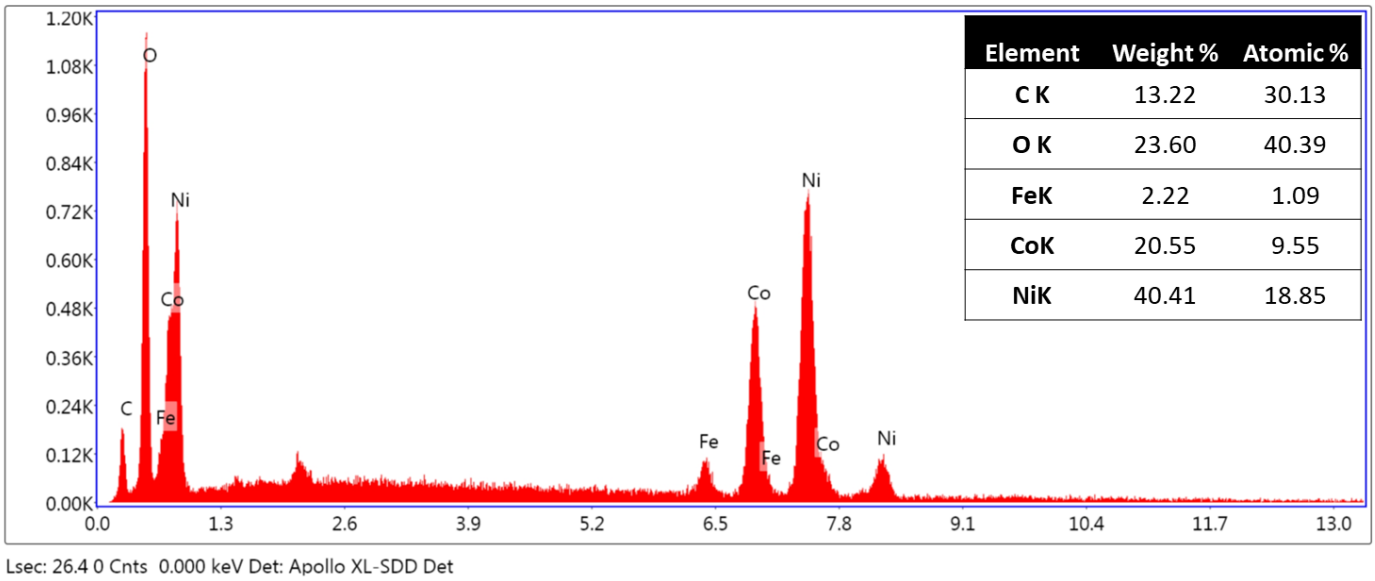


Figure A6.1. EDS spectra of $NiFeCoO_x$ (2.5% Fe).

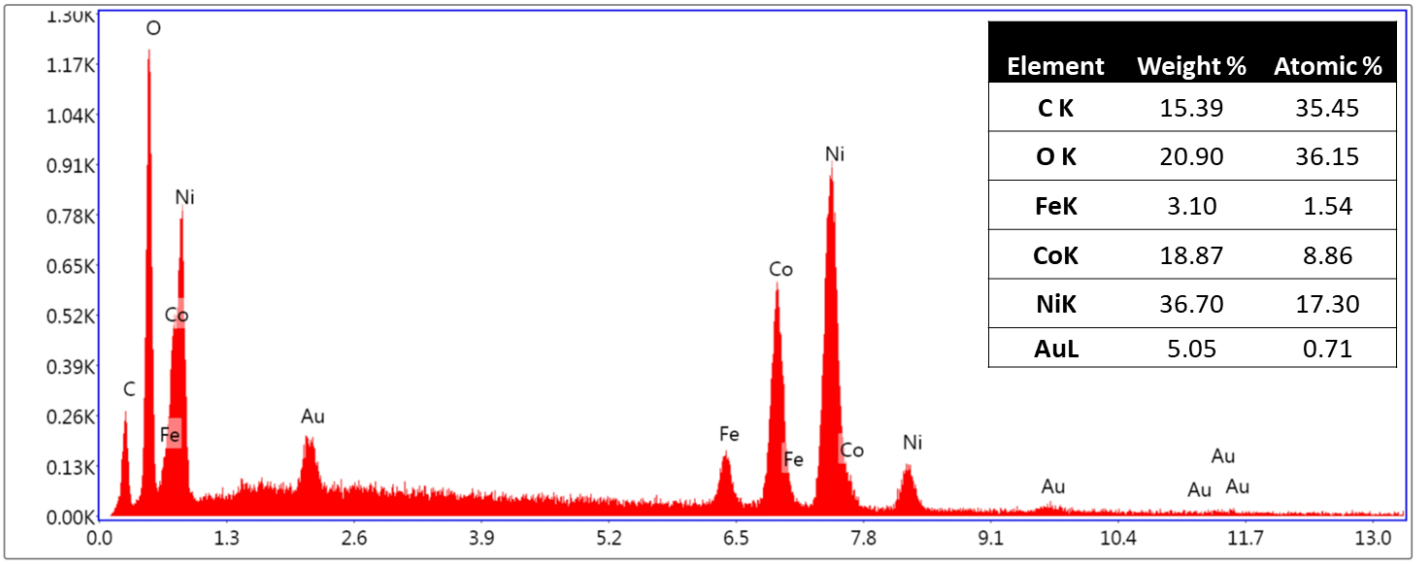


Figure A6.2. EDS spectra of $NiFeCoO_x$ (5% Fe).

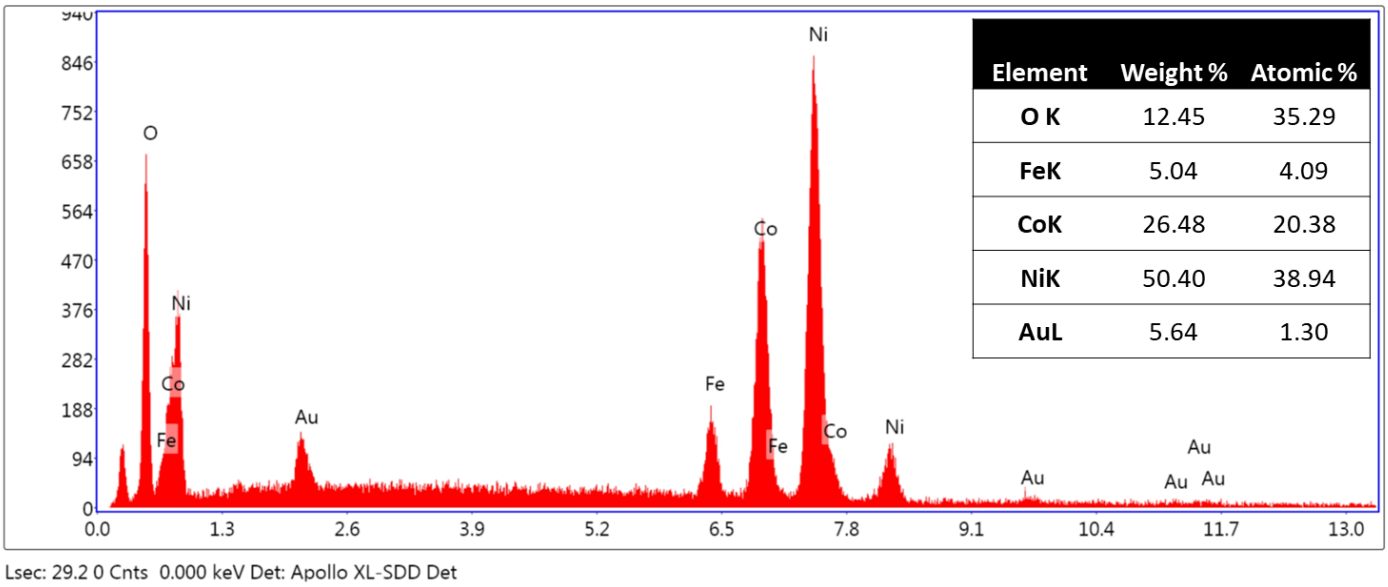


Figure A6.3. EDS spectra of $NiFeCoO_x$ (7.5% Fe).

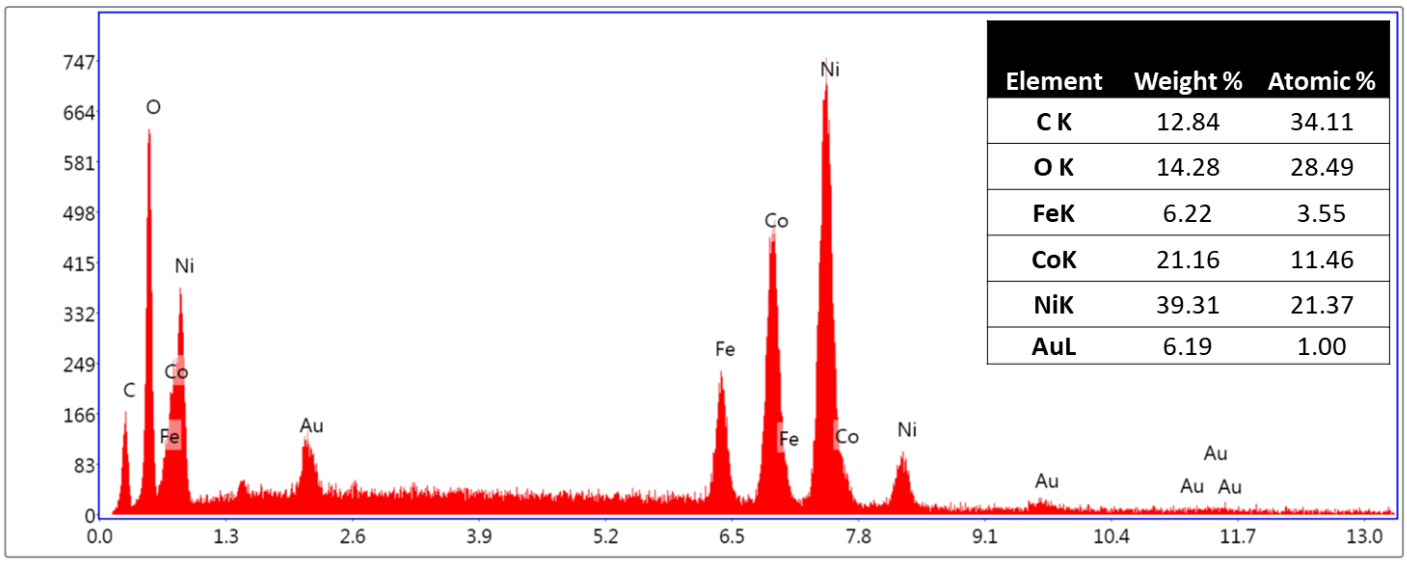


Figure A6.4. EDS spectra of $NiFeCoO_x$ (10% Fe).

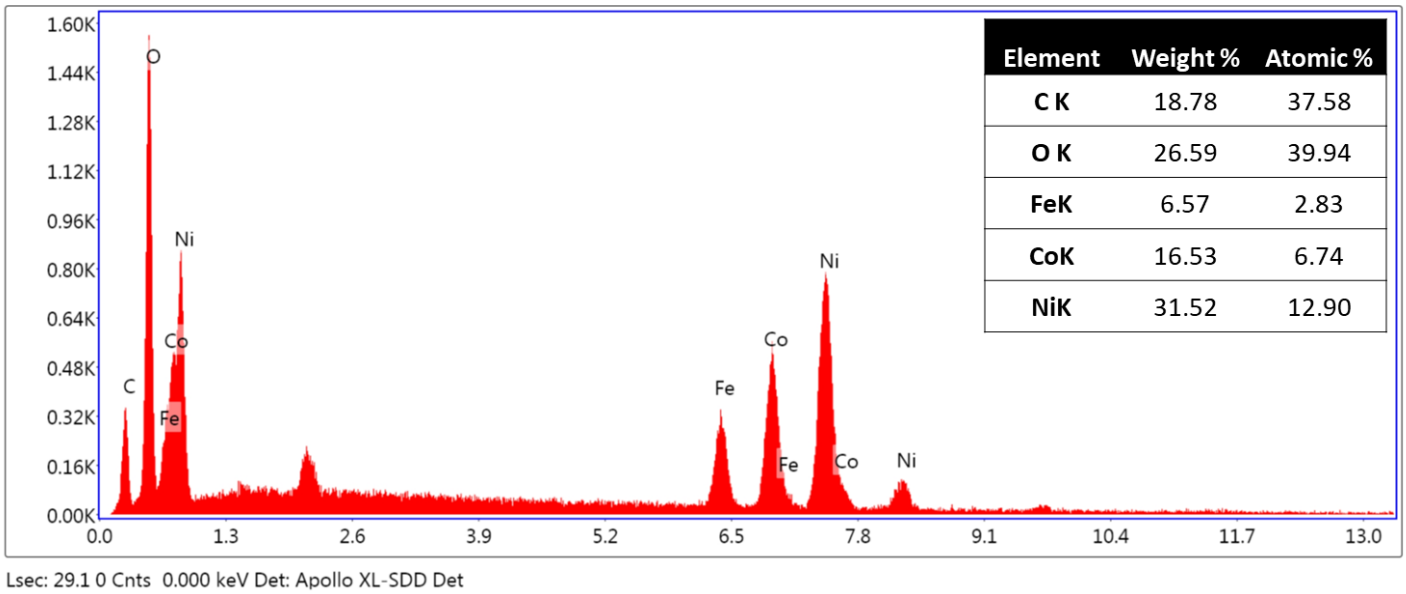


Figure A6.5. EDS spectra of $NiFeCoO_x$ (12.5% Fe).

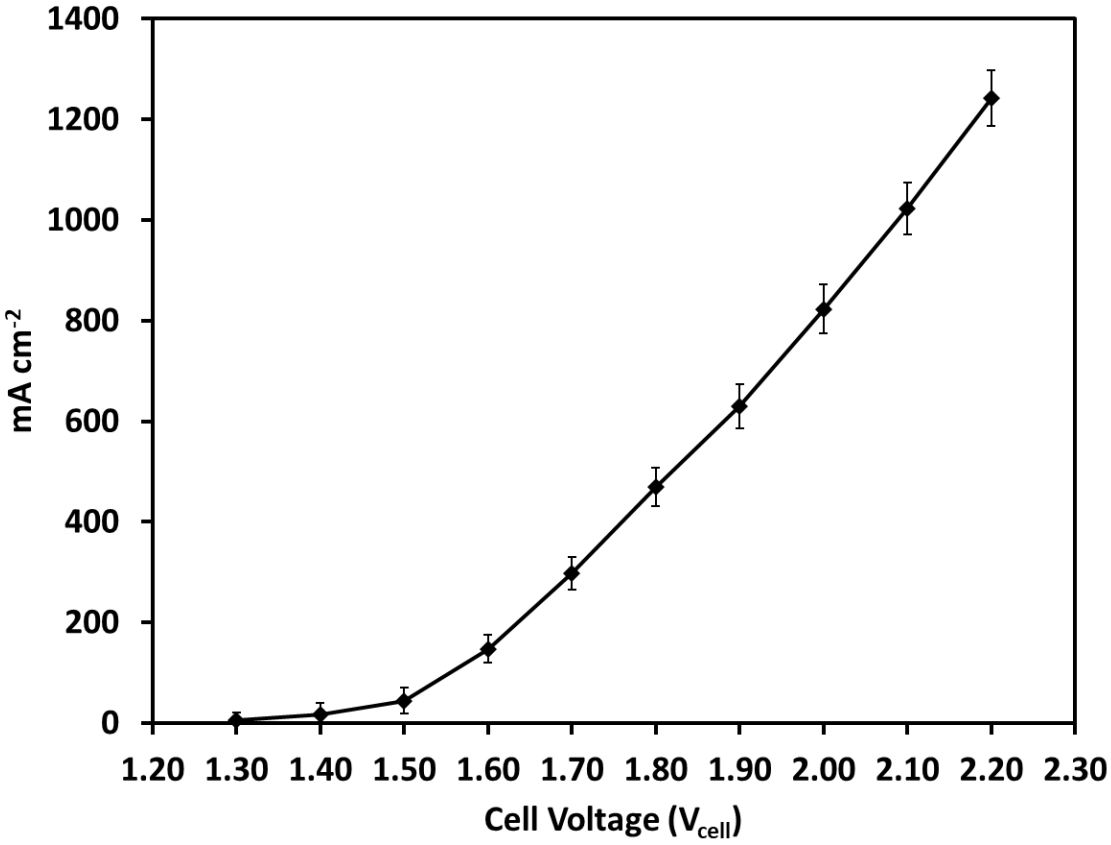


Figure A6.6. Polarization curve for AEM water electrolyzer at 45^{o}C. The error bars indicate the standard deviation among the measured points. The electrolyzer was tested for reproducibility and the membrane electrode assembly was tested three times with the same $NiFeCoO_x$ (5% Fe catalyst) and Pt/C catalyst using the new X-37-50 T membrane each time.

Supplementary Information

Enhanced Performance and Stability of $NiFe_2O_4$ Catalysts in Anion Exchange Membrane Water Electrolysis: Influence of Iron Content, Membrane Selection, and Electrolyte Concentration.

EDS spectra for $NiFeO_x$ catalyst series, which confirms the ratio of Ni to Fe.

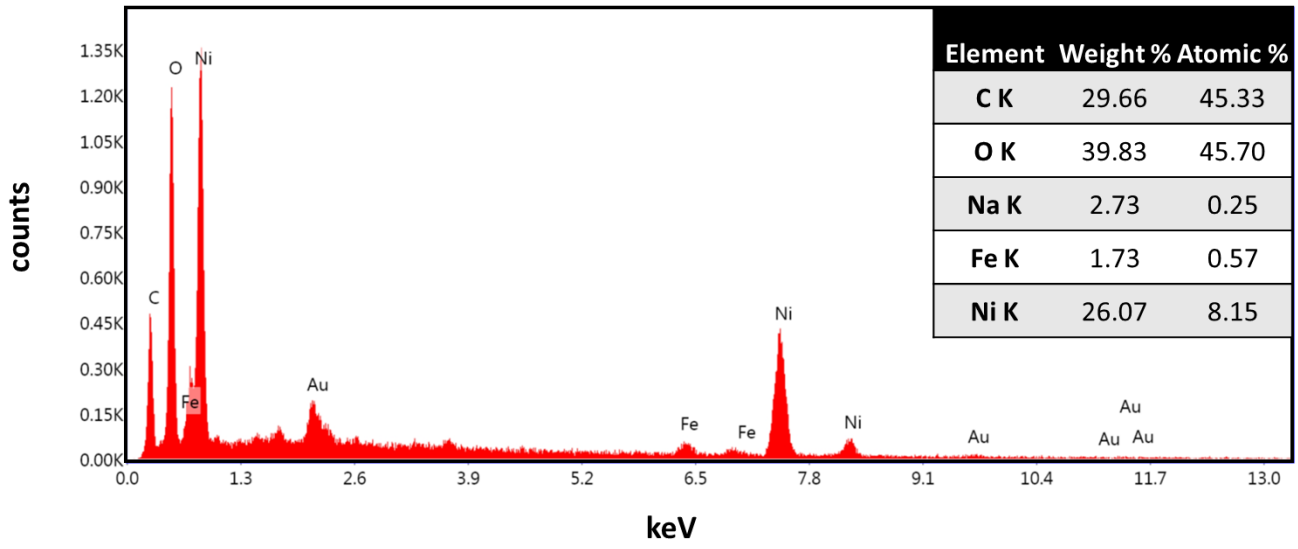


Figure A7.1. EDS spectra of $NiFeO_x$ (5% Fe).

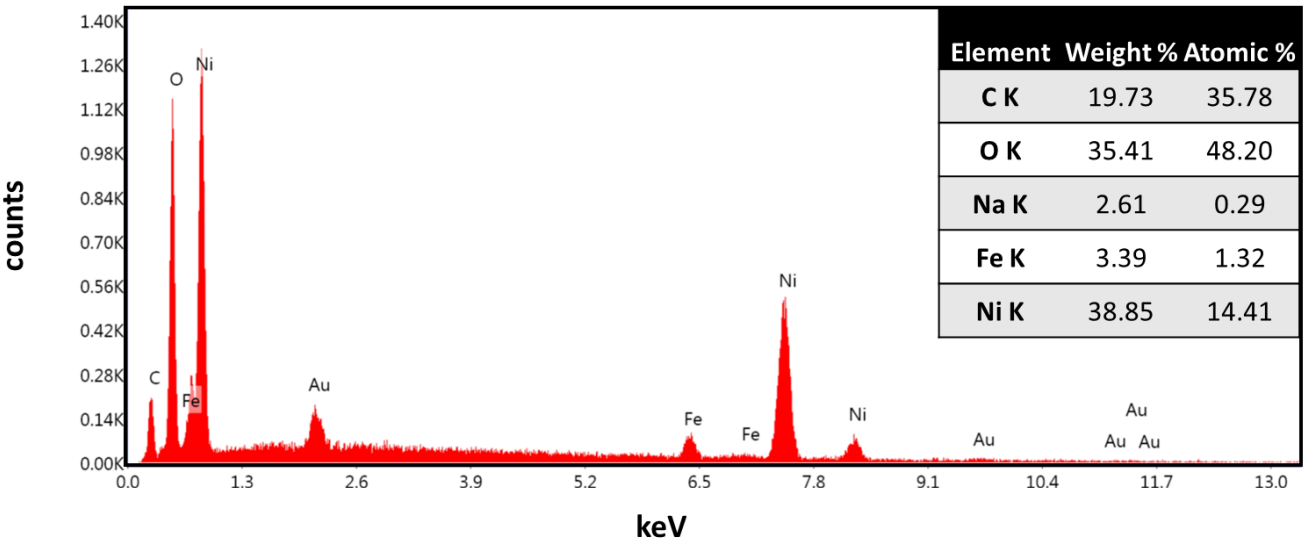


Figure A7.2. EDS spectra of $NiFeO_x$ (7.5% Fe).

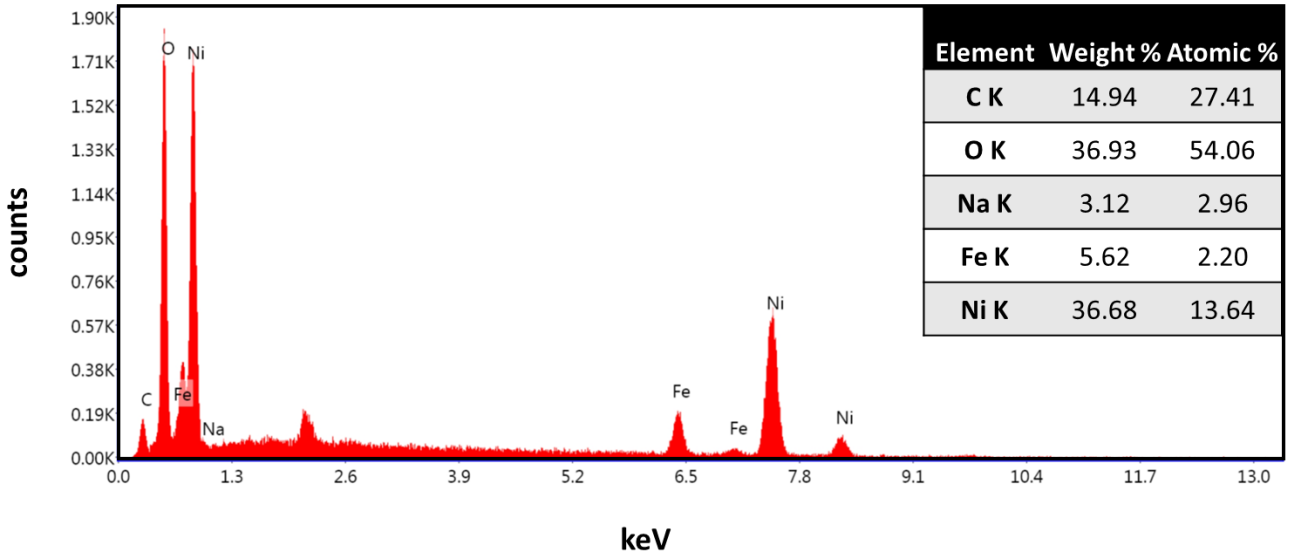


Figure A7.3. EDS spectra of $NiFeO_x$ (12.5% Fe).